Multifunctional
Spin Crossover Complexes

Dissertation

zur Erlangung des akademischen Grades

„Doktor der Naturwissenschaften"

im Promotionsfach Chemie

am Fachbereich Chemie, Pharmazie,

Geographie und Geowissenschaften

der Johannes Gutenberg-Universität Mainz

vorlegt von

Elvira Bergen

geboren in Archipowka

Mainz, 2020

Die vorliegende Arbeit wurde in der Zeit von Juli 2017 bis November 2020 am Department für Chemie der Johannes Gutenberg-Universität Mainz unter Betreuung von ■■■■■■■ ■■■■■■■ angefertigt.

Ich versichere, dass ich diese Arbeit selbständig und keine anderen Hilfsmittel als die angegebenen Quellen und Hilfsmittel benutzt habe.

Mainz, den 20.11.2020

Dekan:

Erste Berichterstatterin:

Zweite Berichterstatterin:

Prüfer:

Tag der mündlichen Prüfung:

D77

Danksagung

Kurzzusammenfassung

Der Spinübergang (engl. *spin crossover*, SCO) bezeichnet den durch Temperatur-/ Druckänderung oder Lichteinstrahlung induzierten Übergang zwischen dem *high-spin* und *low-spin* Zustand von oktaedrischen $3d^n$ (n = 4 – 7) Übergangsmetallkomplexen. Systeme mit hoher Kooperativität weisen einen abrupten Übergang, teilweise mit Hysterese, auf und werden daher als Schlüsselelemente in molekularen Schaltern, Datenspeichermedien oder Sensoren diskutiert. In diesem Rahmen zeichnen sich SCO Komplexe über ihre Fähigkeit aus, andere relevante Aspekte wie die elektrische Leitfähigkeit, sowie die magnetischen und luminszenten Eigenschaften gezielt zu schalten. In diesem Kontext liefert diese Arbeit einen Einblick in die Synergie des Spinübergangs und der magnetischen Austauschwechselwirkung, sowie der langsamen Relaxation der Magnetisierung von Einzelionenmagneten (engl. *single-ion magnets*, SIMs).

Der Einfluss der magnetischen Austauschwechselwirkung auf das *Spin Crossover* Verhalten wurde im ersten Teil dieser Arbeit untersucht. Dazu wurden zunächst mehrkernige Kupfer(II)-Modellkomplexe synthetisiert und mittels Röntgenstrukturanalyse sowie magnetischen Messungen analysiert, um einen Einblick in die strukturellen und elektronischen Einflüsse zu erhalten und diese auf die entsprechenden Eisen(II)- und Kobalt(II)-Komplexe zu übertragen. Die zwei entwickelten Ligandensysteme basieren auf 1,3,4-Oxadiazol- und bis-1,3,4-Thiadiazol-Einheiten. Die Darstellung von ein-, zwei- und mehrkernigen Übergangsmetallkomplexen auf Basis von Kupfer(II)-, Eisen(II)- und Kobalt(II)-Ionen mit unterschiedlichen Austauschpfaden konnte über die entsprechende Dentizität sowie Anzahl an Donoratomen gezielt gesteuert werden.

Im zweiten Teil wurde die Synergie zwischen dem Spinübergang und der langsamen Relaxation von Einzelionenmagneten anhand von trinuklearen Komplexen untersucht. In dieser Arbeit werden in diesem Zusammenhang zwei synthetische Methoden zur Verknüpfung von *Spin Crossover* Komplexen und Einzelionenmagneten vorgestellt. In beiden Fällen dient eine zentrale Kobalt(II)-bis-Terpyridin-Einheit als *Spin Crossover* Komplex, welche für den entsprechenden synthetischen Ansatz mit geeigneten Substituenten funktionalisiert wurde.
Die erste Methode beschreibt die Verknüpfung über die Kupfer(I)-katalysierte Azid-Alkin Cycloaddition, weshalb am zentralen Kobalt(II)-bis-Terpyridin-Komplex Azid-Substituenten und am Kobalt(II)-basierten Einzelionenmagneten eine Alkin-Funktionalität eingeführt wurden. Der erhaltene trinukleare Kobalt(II)-Komplex konnte mittels IR- und UV-Vis Spektroskopie charakterisiert und das magnetische Verhalten über Suszeptibilitäts- sowie Magnetisierungs-messungen analysiert werden.
Im zweiten synthetischen Ansatz wurde ein Ligand mit zwei unterschiedlichen Koordinations-taschen verwendet. Die Terpyridin-Einheit dient auch hier zur die Bildung des zentralen Kobalt(II)-bis-Terpyridin-Komplexes mit *Spin Crossover* Verhalten. Über eine kovalent gebundene 15-Krone-5 Koordinationstasche sollten Kobalt(II)- bzw. Dysprosium(III)-Ionen koordiniert werden, welche den Einzelionenmagneten darstellen.

Abstract

The spin crossover phenomenon (SCO) describes the transition between the high-spin and low-spin state of octahedral $3d^n$ (n = 4 − 7) transition metal complexes by temperature or pressure change as well as light irradiation. Highly cooperative systems with abrupt or even hysteretic transitions are discussed for the application as key elements in molecular switches, storage devices or sensors. The combination of the SCO phenomenon with further relevant aspects for such applications as for example electric conductivity, luminescence or other magnetic properties leads to highly valuable structures, that can be adjusted easily by changing the spin state. The research in the field of spin crossover has therefore focused on the investigation of the interplay between the spin transition and the named properties. In this context, this thesis provides an insight into the synergy between the spin crossover phenomenon and the magnetic exchange coupling as well as slow relaxation of magnetization of single-ion magnets (SIMs).

The influence of magnetic exchange interactions on the spin crossover behavior was analyzed in the first part of the thesis. Simple multinuclear copper(II) model complexes were synthesized and characterized by X-ray structure analysis as well as magnetic measurements to investigate the structural and electronic aspects of the magnetic exchange coupling and to transfer the information to the appropriate iron(II) and cobalt(II) spin crossover complexes. Therefore, two ligand systems based on 1,3,4-oxadiazole and bis-1,3,4-thiadiazole moieties were developed. The different denticity and number of donor atoms enabled the targeted formation of mono-, di- and polynuclear complexes with various magnetic exchange pathways.

In the second part, the synergy between the spin crossover phenomenon and the slow relaxation of magnetization was investigated on discrete trinuclear complexes. Therefore, two different synthetic methods were developed to combine spin crossover complexes with single-ion magnets. In both cases, a central cobalt(II) bis-terpyridine moiety serves as spin crossover complex which was functionalized according to the requirements of the synthetic approach.
The first method describes the linkage by using the well-known copper(I)-catalyzed azide-alkyne cycloaddition. Therefore, an azide substituent was introduced to the central cobalt(II) bis-terpyridine complex and an alkyne functionality to the cobalt(II)-based single-ion magnet. The obtained trinuclear cobalt(II) complex was characterized by IR and UV-Vis spectroscopy and the magnetic behavior was investigated by susceptibility and magnetization measurements.
In the second approach, the linkage of spin crossover complexes and single-ion magnets was performed by the usage of a ligand with two different coordination pockets. The central cobalt(II) bis-terpyridine spin crossover complex is formed by two ligands *via* the terpyridine moiety. Cobalt(II) or dysprosium(III) ions should be further coordinated by the 15-crown-5 coordination pocket to form the single-ion magnets.

Content

List of Compounds

Ligands

L1   2,5-bis[(4-*tert*-butyl-1*H*-1,2,3-triazol-1-yl)methyl]-1,3,4-oxadiazole

L1'   dianion of 1,2-di(4-*tert*-butyl-1,2,3-triazol-1-ylacetyl)hydrazine

L2   2,2'-bismethyl-5,5'-di-1,3,4-thiadiazole

L3   4'-azido-2,2':6',2''-terpyridine

L4   4'-ethynyl-2,2':6',2''-terpyridine

L3-4 1,4-bis[4'-(2,2':6',2''-terpyridyl)]-1,2,3-triazole

L5   4'-(4'''-benzo-15-crown-5)-methyloxy-2,2'-6',2''-terpyridine

Complexes

C1 $\{[Cu^{II}(\mu\text{-}\textbf{L1})Cl_2]\cdot MeCN\}_n$

C1' $[Cu_2^{II}(\textbf{L1'})Cl_2(MeOH)_2]$

C2 $\{[Cu^{II}(\mu\text{-}\textbf{L2})_3(H_2O)((CH_3)_2CO)](ClO_4)_2\cdot H_2O\}_n$

C3 $\{[Fe^{II}(trans\text{-}\mu\text{-}\textbf{L2})_2(H_2O)_4](ClO_4)_2\cdot 2H_2O\}_n$

C3' $\{[Fe^{II}(\mu\text{-}\textbf{L2})_4(H_2O)_2](ClO_4)_2\cdot\textbf{L2}\}_n$

C4 $\{Fe^{II}(trans\text{-}\mu\text{-}\textbf{L2})_2(\textbf{L2})(SCN)_2\}_n$

C5 $[Fe^{II}(\textbf{L2})_3](BF_4)_2\cdot 3CHCl_3$

C6 $\{[Co^{II}(cis\text{-}\mu\text{-}\textbf{L2})(H_2O)_4](ClO_4)_2\}_n$

C7 $[Co^{II}(\textbf{L3})_2](ClO_4)_2$

C8 $[Co^{II}(\textbf{L3})_2](PF_6)_2$

C9 $[Co^{II}(\textbf{L3})_2]Br_2$

C10 $[Co^{II}(\textbf{L3})_2]Cl_2$

C11 $[Co^{II}(\textbf{L3})_2](SCN)_2\cdot H_2O$

C12 $[Co^{II}(\textbf{L3})_2]SO_4$

C13 $[Co^{II}(\textbf{L3})_2](BF_4)_2$

C14 $[Zn^{II}(\textbf{L3})_2](ClO_4)_2$

C15 $[Co^{II}(Brterpy)_2](ClO_4)_2$

C16 $[Co^{II}(Brterpy)_2](PF_6)_2$

C17 $[Co^{II}(oda)(\textbf{L4})]$

C18 $[Co^{II}(dipic)(\textbf{L4})]\cdot 3H_2O$

C19 $[Co_3^{II}(\textbf{L3-4})_2(oda)_2](ClO_4)_2$

C20 $[Co^{II}(\textbf{L5})_2](BF_4)_2$

C21 $[Co^{III}(\textbf{L5})_2]_2[Co^{II}(NCS)_4]_3\cdot 6MeCN$

C22 $[Dy^{III}(\textbf{L5})(\eta^2\text{-}NO_3)_2(\eta^1\text{-}NO_3)(H_2O)]$ $\cdot MeCN$

1 Introduction

1.1 Spin Crossover

The spin crossover (SCO) phenomenon describes the change of the spin state from the low-spin (LS) to the high-spin (HS) state of a suitable transition metal ion and *vice versa* as a result of external stimuli such as temperature, pressure or light irradiation. The transition is accompanied by magnetic, optical, electronic, and structural changes, thus making SCO compounds favorable for possible applications as key elements in molecular sensors or switches.[1]

The unusual behavior of the magnetic moment was first observed by Cambi and Szegö[2–4] in the early 1930s on Fe(III) dithiocarbamate complexes. In the upcoming years, similar octahedral Fe(III) SCO complexes with a $\{N_2S_2O_2\}$ donor set as well as Schiff base ligands providing $\{N_4O_2\}$ or $\{N_3O_3\}$ donor sets attained more attention.[5–10] In the 1960s, the first Fe(II) spin crossover complexes containing bis-1,10-phenanthroline (phen) and 2,2'-bipyridine (2,2'-bipy) as well as analogue *N*-heterocycles in combination with pseudohalides were studied intensively.[11–14] Next to Fe(III) and Fe(II) ions, spin crossover occurs in Co(II),[15] Co(III),[16] Ni(II),[17] Mn(III)[18] and Cr(II)[19] complexes. The major milestones in the understanding of the SCO phenomenon were achieved especially by König,[12,20,21] Gütlich[22–25] and Kahn.[26]

In the following, the theoretical aspects of the spin crossover will be explained exemplarily for octahedral Fe(II) ($3d^6$) complexes.

1.1.1 Ligand Field Theory

On the molecular level, the spin crossover phenomenon can be described by the ligand field theory.[27] In general, transition metal ions with an electronic configuration of $3d^n$ with $n = 4 - 7$ are present in the LS or HS state, depending on the ligand field strength and the spin pairing energy P. In an ideal octahedral coordination sphere, the five d-orbitals are split into the weak-to non-bonding t_{2g} (d_{xy}, d_{xz} and d_{yz}) and the anti-bonding e_g^* (d_{z^2} and $d_{x^2-y^2}$) orbitals. The energy difference refers to the octahedral ligand field splitting Δ_O.[28,29] In systems with more than one d-electron, the t_{2g} and e_g^* sets will be occupied following Hund's rule with a maximal spin multiplicity.[30] If the spin pairing energy is larger than Δ_O, the paramagnetic HS state $^5T_{2g}$ with $t_{2g}^4 e_g^2$ and a total spin of $S = 2$ represents the ground state of the $3d^6$ system. A large ligand field splitting leads to the full occupation of the t_{2g} orbitals, resulting in the diamagnetic LS state $^1A_{1g}$ with $t_{2g}^6 e_g^0$ and $S = 0$ (see Figure 1).
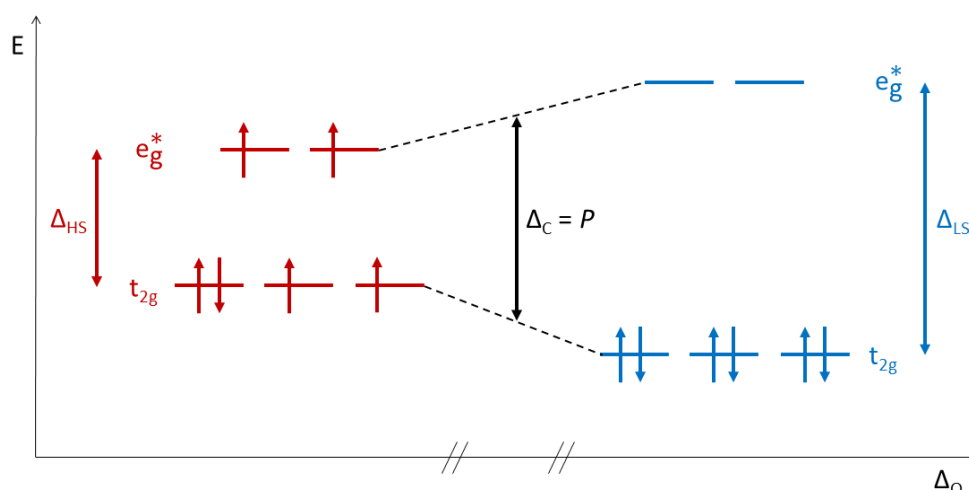
Figure 1 Energy diagram of a 3d⁶ ion in an ideal octahedral coordination sphere. Left in red: The HS state $^5T_{2g}$ is occupied, when the spin pairing energy P is larger than the ligand field Δ_{HS}. Right in blue: As the ligand field Δ_{LS} is larger than P, the LS state $^1A_{1g}$ is occupied. Δ_C describes the critical ligand field strength.[33]

The effect of the ligand field strength is further visualized in the corresponding Tanabe-Sugano diagram, where the energy of the ground and excited state terms are plotted against the ligand field strength in the units of the Racah parameter *B* of the electron-electron repulsion.[31] The terms result from the Russel-Saunders coupling scheme ^{2S+1}L with the spin multiplicity $2S+1$ and the orbital moment *L*.[32] Figure 2 shows the Tanabe-Sugano diagram for a 3d⁶ system in an ideal octahedral ligand field.
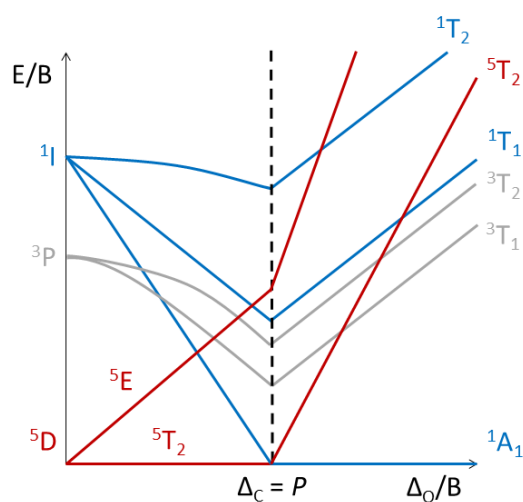
Figure 2 Tanabe-Sugano diagram for a 3d⁶ ion in an ideal octahedral ligand field. The energy of the ligand field states is plotted against the ligand field strength Δ_O, given in the units of the Racah parameter B of the electron-electronic repulsion. For clarity, only the relevant states are emphasized.[36]

The free ion ground state of a 3d^6 system is the ^{5}D state. In an octahedral ligand field, the ^{5}D state splits into the ^{5}T$_2$ ground state with an occupation of $t_{2g}^4 e_g^2$ and the ^{5}E excited state with $t_{2g}^3 e_g^3$. This state remains to be the ground state up to a critical ligand field strength Δ_C, where the ligand field is equal to the spin pairing energy P. In a ligand field with $\Delta_O > \Delta_C$, the ^{1}A$_1$ state, arising from the excited ^{1}I state, is energetically stabilized and becomes the ground state. Due to the Franck-Condon principle,[33] the d-d transitions of metal complexes can be directly read off the Tanabe-Sugano diagram as vertical transitions. Typical ligand field values are $\Delta_{HS} <$ 11 000 cm^{-1} for HS and $\Delta_{LS} >$ 21 500 cm^{-1} for LS complexes. The d-d transitions of spin crossover complexes are in the range of Δ_{HS} = 11 500 − 12 500 cm^{-1} and Δ_{LS} = 19000 − 21000 cm^{-1} for the HS and LS species, respectively.[27]

In order to understand the critical ligand field strength and the spin transition, the discussion of the Tanabe-Sugano diagram is insufficient as it only considers the energy difference between the ground and excited states in relation to the ground state. The ligand field strength Δ_O furthermore depends on the metal-ligand distance Fe–L by:[34,35]

$$\Delta_O = \frac{\mu}{(Fe-L)^6} \tag{1}$$

with the dipole moment μ of the neutral ligand. The Fe–L bond lengths in a HS complex are much larger than those in the corresponding LS complex due to the occupation of the anti-bonding e_g^* orbitals. Typical values for Fe(II) SCO complexes with a {N$_6$} donor set are 1.95 − 2.00 Å for the LS and 2.12 − 2.18 Å for the HS state, hence the difference Δ(Fe–L) is of about 0.2 Å.[27,35,36] For a better understanding, the adiabatic potentials of the ^{5}T$_{2g}$ and the ^{1}A$_{1g}$ ground states are plotted depending on their energy and the totally symmetric r_{Fe-L} stretch vibration.
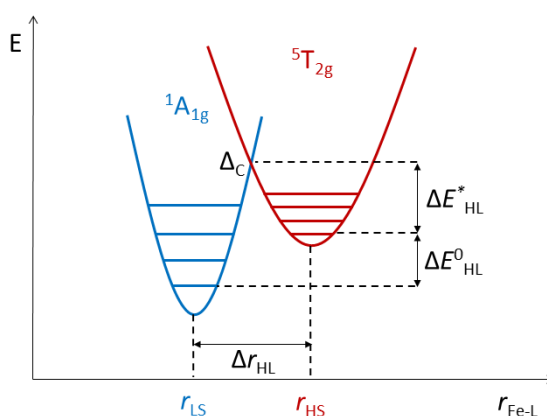
Figure 3 Adiabatic potentials for the ^{1}A$_{1g}$ LS (left in blue) and the ^{5}T$_{2g}$ HS (right in red) state along the totally symmetric metal-ligand stretch vibration r_{Fe-L}. The horizontal lines represent the vibrational energy levels, ΔE_{HL}^0 the zero-point energy difference and ΔE_{HL}^* the activation energy.[37]

Due to the occupation of the anti-bonding e_g^* orbitals, the adiabatic potential of the HS state ^{5}T$_{2g}$ is shifted towards higher energy and larger r_{Fe-L} in comparison to the LS state ^{1}A$_{1g}$, irrespective of the ligand. In contrast, the properties of the ligand determine the potential

energies of both states. The zero-point energy difference ΔE^0_{HL} between the two states is determined by the difference of $E^0_{HS} - E^0_{LS}$ and the activation enegery ΔE^*_{HL} by the energy difference of the crossing point Δ_C and E^0_{HS}. The energy of the vibrational levels E^{vib}_i (i = HS or LS) is determined by:

$$E^{vib}_i = h\left(n + \frac{1}{2}\right)\frac{1}{2\pi}\sqrt{f_i/M} \qquad (2)$$

with the vibrational force contant f_i ($f_{LS} > f_{HS}$) and the reduced mass M, resulting in higher vibrational energy for the HS state. At low temperatures, the LS state is occupied, and thermal energy leads to the population of excited vibrational levels up to the crossing point Δ_C of the adiabatic potentials where both states have the same geometry. According to the Franck-Condon principle the transformation takes place.[37] This singluar point refers to a transition state and cannot be isolated and investigated.[34]

The main driving force of the thermally activated spin transition is the change of the entropy ΔS. At low temperatures, the Gibbs free energy G is determined by the enthalphy H.

$$\Delta G = \Delta H - T\Delta S \qquad (3)$$

The contribution to the entropy change ΔS for the population of the HS state derives from vibrational and electronic contributions:

$$\Delta S = \Delta S_{el} + \Delta S_{vib} \qquad (4)$$

The spin and orbit contribute to the electronic entropy change ΔS_{el}, but the latter is often quenched and can be neglected. Hence, the electronic contribution derives from the 15-fold degenerated $^5T_{2g}$ state is in comparison to the single $^1A_{1g}$ ground state. The change of the spin multiplicity ΔS_{mag} amounts:

$$\Delta S_{mag} = R[\ln(2S+1)_{HS} - \ln(2S+1)_{LS}] = 13.4 \text{ J K}^{-1} \text{ mol}^{-1} \qquad (5)$$

and represents approximately 25% of the total entropy gain.[27,38]

1.1.2 Inducing Spin Crossover

A well-established method to induce spin crossover is the variation of the temperature as heating and cooling is possible on a large number of devices (see Chapter 1.1.3) and the transition temperature $T_{1/2}$ is commonly in the range of thermal energy. Consequently, the change of the temperature is the most used method to investigate the nature of the spin crossover.[34,39] In addition, application of pressure of irradiation with visible light is feasible.

Pressure

In contrast to the entropy-driven thermal spin transition, the effect of the pressure is determined by the large difference of the bond lengths of $\Delta(Fe–L) \approx 0.2$ Å and can be understood in terms of the LS and HS potential wells (see Figure 4). The application of mechanical or chemical pressure destabilizes the HS state because of its larger molecular volume and causes a vertical displacement of the potential well.[37,40] The zero-point energy difference ΔE^0_{HS} is increase by the term $p\Delta V^0_{HS}$ whereas the activation energy ΔE^*_{HL} is decreased.[40] Therefore, the LS state is favored and the transition temperature $T_{1/2}$ is shifted towards higher temperatures.[41,42]
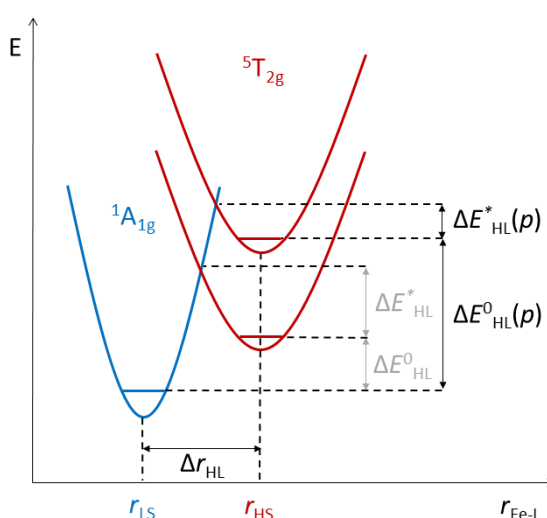
Figure 4 Pressure effect on the adiabatic potential wells of the HS and LS state. The HS potential well is shifted towards higher energy due to the larger bond lengths and volume. The zero-point energy $\Delta E^0_{HL}(p)$ is increased whereas the activation energy $\Delta E^*_{HL}(p)$ is decreased.[40]

Light Irradiation

Changing the spin state by irradiation with visible light was first observed in the early 1980s by McGarvey,[43] when he irradiated LS Fe(II) and Fe(III) complexes in solution to populate the metastable HS^* state with a lifetime of microseconds. Decurtins et al.[44] followed this observation by the possibility of trapping the metastable HS^* state of the Fe(II) complex [Fe^{II}(1-propyltetrazole)$_6$](BF_4)$_2$ at very low temperatures in the solid state. Subsequently, the term LIESST effect (Light Induced Spin State Trapping) was introduced to describe this phenomenon. The mechanistic studies revealed, that the excitation with pulsed green light (λ = 514 nm) results in the spin-allowed transition to the excited $^1T_{1g}$ and $^1T_{2g}$ states or to the metal-to-ligand charge transfer (MLCT) depending on the extended π-system of the ligand. The fast double intersystem crossing (ISC) *via* the $^3T_{1g}$ and $^3T_{2g}$ states leads to relaxation to the LS or to the metastable HS^* state.[45] With sufficient irradiation time, the photoexcited HS^* state

can be populated with a long lifetime at cryogenic temperatures because the $^5T_{2g} \rightarrow {}^1A_{1g}$ transition is forbidden. The relaxation temperature T(LIESST) describes the temperature, above which the excitation to the metastable HS* state is no longer observable.[46,47] The reverse-LIESST effect occurs by the usage of red light (λ = 820 nm), where the metastable HS* state is excited to the ^5E_g state. Relaxation to the $^1A_{1g}$ state takes place by intersystem crossing *via* the $^3T_{2g}$ and $^3T_{1g}$ states.[48]
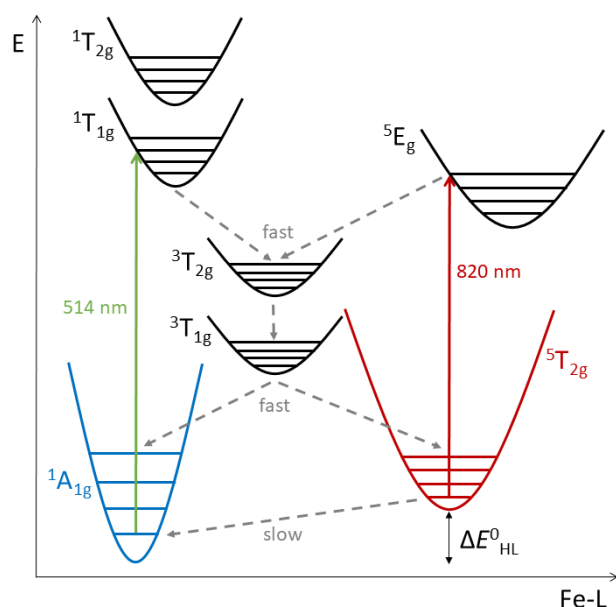
Figure 5 Mechanism of the LIESST and reverse-LIESST effects.[37]

The lifetime of the photoinduced HS* state and the relaxation to the LS state as well as the activation energy and relaxation process can be determined by analyzing the kinetics. Hauser et al.[49,50] identified an independent tunneling region and a thermally activated relaxation pathway, which is crucial in especially highly cooperative systems with self-acceleration and non-linear behaviors.

1.1.3 Investigation of Spin Crossover Behavior

The LS and HS species of a spin crossover complex exhibit differences, among others in the molecular structure and the magnetic moment due to the different occupation of the e_g^* orbitals. These differences and the simple variation of temperature for most analytical measurement devices are used to get more information about the spin state of the investigated 3d metal complexes.

Magnetic Measurements

Measurements of the magnetic susceptibility are standardly performed with SQUID (Superconducting QUantum Interference Device) magnetometers due to the high sensitivity and the ability to use samples in milligram scale as well as single crystals. Furthermore, air and water sensitive samples can be measured under inert atmosphere, pressure-dependent spin transitions can be investigated, and light irradiation is possible with customized sample holders. The determination of the magnetic susceptibility is suitable for all 3d metal ions, which show spin crossover behavior, as the change of the magnetic susceptibility arises from the different number of unpaired spins in the LS and HS state, respectively. It is especially pronounced in Fe(II) systems as the LS state is diamagnetic with $S = 0$ and the HS state highly paramagnetic with $S = 2$. For spin crossover compounds the magnetic susceptibility χ involves the contributions χ_{HS} and χ_{LS} of both states:[1,34]

$$\chi(T) = \gamma_{HS} \cdot \chi_{HS} + (1 - \gamma_{HS}) \cdot \chi_{LS} \qquad (6)$$

With the known susceptibility values for each state, either the molar HS fraction γ_{HS} or the molar susceptibility can be plotted as a function of the temperature T to obtain spin transition curves (see Chapter 1.1.4).[1,34]

In solution, the magnetic susceptibility can be determined by ^{1}H-NMR spectroscopy using the Evan's method.[51–54] The sample solution is placed in the inner tube of a special double walled NMR tube and the solvent is located in the outer tube as external reference. The signals of the sample are shifted by Δv in relation to the diamagnetic reference as a result of the additional magnetic field induced by the paramagnetic substance:[52,55–57]

$$\chi_m = \frac{3\Delta v}{4\pi v m} + \chi_0 + \frac{\chi_0 (\rho_0 - \rho_S)}{m} \qquad (7)$$

χ_m is the magnetic mass susceptibility, v the spectrometer frequency, ρ_0 the density of of the solvent and ρ_S the density of the solution.

Single Crystal X-Ray Diffraction

Single crystal X-ray diffraction is most appropriate as the molecular structures of the HS and LS state differ in bond lengths and angles. In Fe(II) complexes with a $\{N_6\}$ donor set, the Fe–N bond lengths change of about $\Delta(Fe–L) \approx 0.20$ Å, which causes a change in the total volume of the cell of up to 5% and a distortion of the metal coordination sphere.[58] The deviation from the perfect $\{M–N_6\}$ octahedron can be described using the octahedral distortion parameter Σ_0, which is the sum of the deviations from 90° of all twelve *cis*-angles φ_i:[57,59,60]

$$\Sigma_0 = \Sigma_{i=1}^{12} |\varphi_i - 90°| \qquad (8)$$

Fe(II) HS complexes show large deviations with values of $\Sigma_0 > 100°$ whereas the LS complexes are closer to the perfect octahedron with $\Sigma_0 < 80°$.[60]

By determining the crystal structure of a given sample above and below the transition temperature, the structures can be compared directly and a potential crystallographic phase change can be illustrated.[34] Furthermore, possible intra- and intermolecular interactions such as hydrogen bonding or π-π-stacking can be determined.[1]

UV-Vis Spectroscopy

As the spin transition is typically accompanied by a color change, temperature-dependent optical spectroscopy is suitable for the investigation. The transition of the mainly colorless HS Fe(II) complexes to the red to violet LS species is observed as the spin- and parity-allowed charge transfer and d-d transitions appear in the ultraviolet-visible region (UV-Vis).[1] The spin-allowed d-d transition $^5T_{2g} \rightarrow {}^5E_g$ of HS Fe(II) complexes appear in the near-infrared region of 12 500 cm^{-1} to 10 000 cm^{-1} while for the LS state the $^1A_{1g} \rightarrow {}^1T_{1g}$ and $^1A_{1g} \rightarrow {}^1T_{2g}$ transitions are found between 22 000 cm^{-1} and 18 000 cm^{-1}.[27]

^{57}Fe Mössbauer Spectroscopy

The Mössbauer spectroscopy describes the recoilless nuclear resonance absorption of γ-radiation and is especially suitable for the characterization of Fe(II) and Fe(III) spin crossover complexes, as the relaxation times of the HS and LS states are much longer than the time scale of the Mössbauer spectroscopy (10^{-7} s). The two most important parameters, the isomer shift δ and the quadrupole splitting ΔE_Q, significantly differ for the two states of Fe(II) and Fe(III) complexes. The isomer shift δ describes the d-electron density at the nucleus and provides information about the spin and oxidation state. A quadrupole splitting ΔE_Q is observed when an inhomogeneous electric field is present at the nucleus. This occurs for non-symmetric electron distribution such as in HS Fe ions as the non-bonding e_g^* orbitals are occupied in contrast to the LS state. Typical values of Fe(II) spin crossover complexes are $\delta^{LS} \leq 0.5$ mms^{-1} and $\Delta E_Q^{LS} \leq 1$ mms^{-1} as well as $\delta^{HS} \approx 1$ mms^{-1} and $\Delta E_Q^{HS} = 2-3$ mms^{-1}.[28,61]

IR Spectroscopy

Another possible characterization method is the infrared (IR) spectroscopy. The reduced occupation of the antibonding e_g^* orbitals in the LS state strengthens the M–L bonds, which causes a shift towards higher frequencies in comparison to the HS state. The stretching frequencies of M–L bonds lie in the far infrared (FIR) range of approximately 250 cm^{-1} to 500 cm^{-1}.[62] Moreover, the shift of a characteristic ligand band, e.g. NCS$^-$ or NCSe$^-$, can be a hint for a spin crossover. The stronger Fe–N bond of the LS species increases the π-back bonding towards the ligand, therefore the antibonding π^*(N-C) orbitals are depopulated and the N=C stretching mode frequency rises in order to compensate the charge deficit at the central metal ion.[1,63]

Differential Scanning Calorimetric Measurements

Differential scanning calorimetric (DSC) measurements are used to determine the transition enthalpy and entropy as well as the transition temperature when the HS→LS transition is assumed as a phase transition. The maximum in the C_p (heat capacity) versus T plot represents the spin transition.[64] The integration leads to the values of the enthalpy (C_p vs. T) and entropy (C_p/T vs. T) change.[1,65] The enthalpy and entropy changes $\Delta H = H_{HS} - H_{LS}$ and $\Delta S = S_{HS} - S_{LS}$ are positive and the Gibbs energy change ΔG (see Equation 3) becomes negative at the transition temperature $T_{1/2} = \Delta H/\Delta S$.[66] Typical values of Fe(II) systems are $\Delta H \approx 10 - 20$ kJ mol^{-1} and $\Delta S \approx 50 - 85$ J K^{-1} mol^{-1}.[65]

Further methods are Electron Paramagnetic Resonance (EPR),[67–69] X-ray Absorption Spectroscopy (XAS)[70,71] and Nuclear Forward Scattering (NFS).[72,73]

1.1.4 Occurence of Spin Crossover

In order to describe the spin crossover behavior, the HS fraction γ_{HS} or the $\chi_M T$ product is plotted against the temperature T. Even though the spin crossover phenomenon takes place in single metal centers, different types of transitions are possible depending on the degree of cooperativity. Cooperative interactions between the molecules refer to the ability to propagate the information of the spin transition, especially the changes of the M–L distances, within the crystal lattice to the next metal center. The communication of the volume change of the single SCO center leads to long-range interactions, which are facilitated by intra- and intermolecular interactions.[34,39]
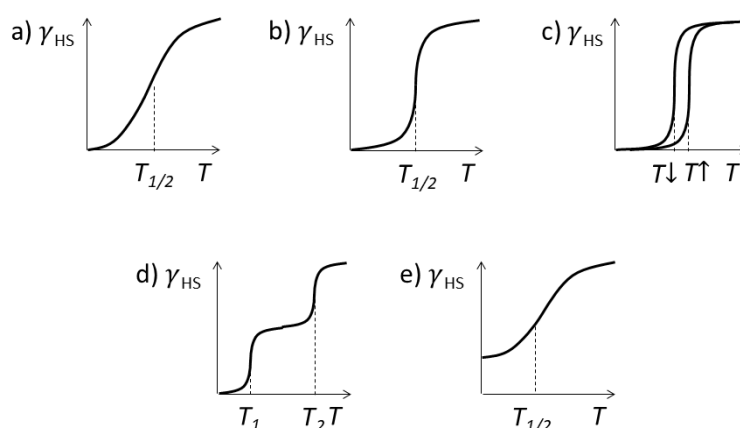

Figure 6 The HS fraction γ_{HS} is plotted against the temperature T. The curves describe different types of the spin transition: a) gradual, b) abrupt, c) hysteretic, d) stepwise and e) incomplete. $T_{1/2}$ describes the transition temperature, T↑ and T↓ describe two different transition temperatures in hysteretic systems depending on prior heating or cooling.[34]

The SCO occurs gradually when the transition takes place over a wide temperature range up to several hundred Kelvin (Figure 6a). Such a transition often occurs in solution, where the spin transition simply follows the Boltzmann law. The cooperative interactions are weak.[1]

An abrupt spin transition (Figure 6b) is an indication for the presence of (strong) cooperativity within the crystal structure. Abrupt transitions can show hysteresis effects (c), which appears in form of the two different transition temperatures $T_{1/2}\uparrow$ and $T_{1/2}\downarrow$. The bistability arises from the two electronic states, which are present in the same temperature range depending on prior heating or cooling. This memory effect is crucial concerning possible applications such as memory devices or molecular switches.[74] According to Gütlich, either a phase change or a strong communication between neighboring molecules cause the hysteresis.[1] A structural phase change of the lattice results from the drastic change of the M–L bond lengths and consequently of the molecular volume, which can be considered as a point defect. The induced chemical pressure tremendously effects the lattice and is communicated *via* elastic phonon interactions.[75–77] The intermolecular interactions are facilitated by hydrogen bonds directly between the complexes or *via* anions or solvent molecules and π-π-stacking between aromatic moieties.[1,34,38] The cooperative interactions can be investigated by the incorporation of non-active spin crossover ions in an isostructural environment. For example the dilution with diamagnetic Zn(II) ions leads to a more gradual spin transition curve as it reflects a system in solution with a simple Boltzmann distribution of the states.[78–80]

Figure 6d shows a stepwise spin crossover, which occurs for example in dinuclear complexes (*vide infra*). Also, mononuclear complexes can show this behavior when the spin transition is accompanied with a preferential 'HS/LS' pairing due to short-range interactions.[81–83]

An incomplete transition (Figure 6e) can have various origins. Some of the metal ions could sit in different lattice sites in form of defects and this particular ligand field is too strong or weak to induce a spin transition. Otherwise, a part of the HS complexes is frozen, as the HS→LS conversion rate gets smaller for very low temperatures. Rapid cooling from room to liquid nitrogen temperatures state this kinetic effect and is referred as the TIESST effect (Temperature Induced Spin State Trapping).[84–87]

1.1.5 Influences on the Spin Crossover Behavior

The spin crossover is generally induced or suppressed by the type of ligand providing a (non-) suitable ligand field. The transition temperature can be altered by the variation of the ligands or substituents as a result of different ligand field strengths. The ligand field can for example be fine-tuned by different substituents on the ligand, changing the ring size, as five-membered rings reduce the σ-donor and π-acceptor properties in relation to six-membered rings, or replacing aromatic moieties with aliphatic ones.[88] The cooperativity strongly depends on the intra- and intermolecular interactions, hence varying anions or solvents can crucially influence the abruptness of the spin transition.

Optimization of the Ligand

The variation of the substituents of a given ligand can influence the spin transition electronically and/or sterically. For example, a 4'-substituent with variable electronic influence such as a chloro-, hydroxyl- or alkyl-functionality does not lead to the desired spin crossover of the LS Fe(II) bis-2,2':6',2''-terpyridine complex.[89,90] However, the HS analogues can be obtained with sterically demanding substitutents at the 6- and 6''-position by forcing strong distortion directly in the Fe(II) environment.[91]

A systematic analysis of electronic effects was reported by Halcrow et al.[92] on the series of substituted $[Fe^{II}(1\text{-bpp}^{X,Y})_2]^{2+}$ complexes (1-bpp = 2,6-di(pyrazol-1-yl)pyridine) where **X** describes the pyridyl substituent on the 4'-position and **Y** the pyrazolyl substituent on the 4- and 4''-position. To quantify the electronic and exclude crystal-packing effects, the spin states were measured in solution by the variable-temperature Evan's method.[55] Furthermore, either the **X** or **Y** substituent was changed while the proton remained on the other substituent site. Among others, halogen, hydroxy, amine, thiol as well as (thiol-)ether, carboxylic acid, and sulfoxide substituents were investigated. Different alkyl, ester and halogen functionalities were introduced on the pyrazoles. The analysis revealed a strong dependence of the transition temperature $T_{1/2}$ on the σ- and π-bonding effects. On the one hand, electron-withdrawing substituents decrease the energy of the ligand's lone pairs, thus weakening the σ-ligand field and stabilizing the HS state. On the other hand, the Fe–bpp π-backbonding is strengthened by the reduced energy of the π^* orbitals, favoring the LS state. It was found, that the spin state of the $[Fe^{II}(bpp^{X,H})_2]^{2+}$ series strongly depends on the π-bonding effects, as electron-withdrawing **X** substituents strongly stabilize the t_{2g} manifold which increases the ligand field and raises $T_{1/2}$. In contrast to that, the σ-bonding influences the spin state of the $[Fe^{II}(bpp^{H,Y})_2]^{2+}$ series. Electron-withdrawing **Y** substituents stabilize the e_g^* manifold, thus favoring the HS state and lowering $T_{1/2}$.

Anions and Solvent Molecules

Solvent molecules or anions can have a crucial influence on the spin crossover behavior, resulting in a shift the transition temperature or even the absence of the transition as well as in a change the nature of the transition from gradual to abrupt or even hysteretic. As discussed before, solvent molecules and/or non-coordinating anions can influence especially the cooperativity for example by the formation of hydrogen bonds or a change in the crystal packing.[89,93,94] This behavior was observed for the dinuclear Fe(II) complex series $[Fe_2(\mu_2\text{-}PMOD)_2]X_4$ (PMOD = 4-amino-3,5-bis{[(2-pyridyl-methyl)amino]methyl}-4H-1,3,4-oxadiazole; X = ClO_4^-, BF_4^- and $CF_3SO_3^-$) reported by our group.[95] The variation of the counterion led to different spin crossover behavior due to varying intermolecular interactions. The [HS-HS] state was observed with the tetrafluoroborate anion, an abrupt [HS-LS]→[HS-HS] spin transition at 150 K with perchlorate and a 26 K wide hysteresis with the triflate anion. In contrast to the BF_4^- complex, hydrogen bonds are found between the ClO_4^- and $CF_3SO_3^-$ anions and the secondary amine proton forming one-dimensional coordination chains. These induce strong inter-molecular interaction and enable an abrupt transition as it is mediated directly to the next

Fe(II) centers. In the latter, two cation complexes are connected by two counter ions leading to a stronger cooperativity and hysteretic behavior.[95]

1.1.6 Cobalt(II) Spin Crossover Complexes

The aforementioned theoretical aspects of the spin crossover phenomenon were described on Fe(II) complexes as they are able to show gradual, abrupt and hysteretic SCO and can be investigated by a large number of methods. In this thesis, Co(II) complexes are intensively discussed and thus the main differences and characteristics are explained in this chapter.

The first Co(II) based SCO compound was investigated by Figgins and Busch[96] on diamine and terimine systems forming hexa-coordinated Co(II) complexes. Co(II) ions provide an electron configuration of $3d^7$ with a LS ^2E ($t_{2g}^6 e_g^1$) and a HS $^4T_1$ ($t_{2g}^5 e_g^2$) state. In contrast to Fe(II), Co(II) ions show less tendency for oxidation and the LS state is strongly influenced by the Jahn-Teller-distortion arising from the singly occupied e_g^* orbitals. Additionally, the magnetic moment changes less with $\Delta S = 1$ according to the LS ($S = 1/2$) and HS ($S = 3/2$) states. Therefore, the magnetic entropy change of $\Delta S_{mag} = 5.8$ J K^{-1} mol^{-1} between the LS and HS state is much smaller than for Fe(II) with $\Delta S_{mag} = 13.4$ J K^{-1} mol^{-1}.[97] The spin transition leads to typical values of $\chi_M T = 0.4 - 0.6$ cm³ K mol^{-1} ($\mu_{eff} = 1.8 - 2.2$ μ_B) for the LS and $\chi_M T = 2.8 - 3.4$ cm³ K mol^{-1} ($\mu_{eff} = 4.7 - 5.2$ μ_B) for the HS state due to the contribution of the unquenched orbital angular momentum.[98] Furthermore, Co(II) ions require a stronger intrinsic ligand field to enable spin crossover.[99,100] Ligands based on imines, 2,2'-bipyridines (bipy) and 2,2':6',2''-terpyridines (terpy) provide a suitable ligand field and the ability to generate hexa-coordinated Co(II) complexes. In comparison to Fe(II) or Fe(III) spin crossover compounds, Co(II) complexes exhibit a smaller change in the M–L distance with only approximately Δ(Co–L) = 0.10 Å and a lower change in the molecular volume which implicates a more gradual spin transition.[98]

A large family of Co(II) SCO compounds is based on the mononuclear bis-terpyridine complex series [Co^{II}(terpy)$_2$]X$_2$·nH$_2$O (X = Br$^-$, Cl$^-$, I$^-$, F$^-$, ClO$_4^-$, BF$_4^-$, NCS$^-$, NO$_3^-$, [Co(CN)$_4$]$^{2-}$, SO$_4^{2-}$, BPh$_4^-$ and n = 0 − 6) with a large variety of anions and number of solvent molecules.[97] Already the first observations by Hogg and Wilkins[89] revealed a high anion and solvation dependency of the spin state. For example, the bromide complex with a magnetic moment of $\mu_{eff} = 2.7 - 3.0$ μ_B at room temperature is reported to be in both the LS and HS state due to disordered bromide anions.[93,94,101,102] Otherwise, the magnetic moment of [Co^{II}(terpy)$_2$](ClO$_4$)$_2$·0.5H$_2$O amounts $\mu_{eff} = 4.1$ μ_B at room temperature and the structure exhibits longer Co–N distances than for the appropriate bromide complex.[93] Both aspects are pointing towards the HS species.[103] The [Co(terpy)$_2$]I$_2$ complex exhibits a partial spin transition from 120 K to 295 K. The low-temperature structure confirmed the LS state with Co–N$_{central}$ and Co-N$_{distal}$ bond lengths of 1.912 Å and 2.083 Å and a magnetic moment of $\mu_{eff} = 2.2$ μ_B. The magnetic moment of $\mu_{eff} = 3.2$ μ_B at 295 K indicates a mixture of both states.[101,104] Further investigations on the structure of such Co(II) complexes illustrated the correlation of the Co–N bond distances to the observed spin state. The predominant change occurs for the Co–N$_{central}$ distance with about

0.21 Å in contrast to $\Delta(\text{Co–N}_{\text{distal}})$ = 0.07 Å, which correlates to the Jahn-Teller-effect of the LS state.[105]

Furthermore, the group of Real[106,107] reported the complex series $[\text{Co}^{\text{II}}(\text{OH-terpy})_2]\text{SO}_4$, $[\text{Co}^{\text{II}}(\text{OH-terpy})_2]\text{Cl}_2\cdot\text{H}_2\text{O}$ and $[\text{Co}^{\text{II}}(\text{OH-terpy})_2](\text{ClO}_4)_2\cdot\text{H}_2\text{O}$ where the hydroxyl groups form hydrogen bonds with the non-coordinating anions and the water molecules. Depending on the anion and the possibility to form hydrogen bonds, the spin crossover does not occur (SO_4^{2-}), shows a gradual (Cl^-) or an abrupt spin transition (ClO_4^-).

An interesting 'reverse' spin crossover behavior with hysteresis close to room temperature was reported by Hayami[97,108–110] and observed for Co(II) bis-terpyridine complexes with attached long alkyl chains (C12, C14, C16 and branched). The spin transition is accompanied by a structural phase change leading to a synergetic effect of the spin crossover and the flexibility of the alkyl chains.

The spin crossover behavior of the complex series $[\text{Co}(\textbf{L5})]\text{X}_2$ (**L5** = 4'-(4'''-benzo-15-crown-5)-methyloxy-2,2':6',2''-terpyridine and X = SO_4^{2-}, BF_4^-, Cl^-, Br^-, SCN^- and PF_6^-) and the potential application as chemosensor was investigated in our group by Johanna Oberhaus.[111] Gradual spin crossover was observed for all non-coordinating anions and the additional coordination of sodium cations by the 15-crown-5 moiety led to a slight change in the steepness of the spin transition.

1.1.7 Multinuclear Spin Crossover Complexes

Regarding possible applications such as memory devices, data storage, molecular switches or displays, the focus is on the production of spin crossover materials with abrupt and hysteretic transitions around room temperature.[74,88,112–114] Strong communication between the SCO active centers leads to high cooperativity and enables the desired properties.[115] The transfer of the information is facilitated by intermolecular interactions such as hydrogen bonding or π-π-stacking. In the case of polynuclear systems, communication can also occur intramolecularly *via* covalent bonds, thus making them favorable when enhancing cooperativity.[34,116,117] As dinucleear complexes form the smallest polynuclear unit and the simplest model system, they are qualified for the investigation of the intra- and intermolecular interactions.[88,117–121] In addition, the combination of different electronic properties such as spin crossover and the magnetic exchange between the metal centers can be investigated. Furthermore, dinuclear SCO complexes possibly enable switching between the three possible [LS-LS], [LS-HS] and [HS-HS] states, which provides a higher storage capability or more logical operations.[88,115]

Dinuclear Complexes

The design of dinuclear spin crossover complexes requires appropriate bridging and terminal ligands.[14] As for mononuclear complexes, heterocyclic *N*-donors such as pyridines, triazoles and tetrazoles are suitable as uni-, bi- or multidentate ligands especially in combination with

unidentate *N*-bonded NCX⁻ (X = O, S, Se, BH₃) co-ligands. Next to the ligand's nature, the denticity and chelating function influence the ligand field strength. The rigidity/flexibility of the ligands further influences the accessibility of the [LS-LS], [LS-HS] and [HS-HS] states.[14,116]

The first dinuclear complex showing a stepwise spin crossover *via* the [LS-HS] state was investigated by Kahn and coworker.[118] In the Fe(II) complex [Fe^{II}(bt)(NCS)$_2$]$_2$bpym **1** (bt = 2,2'-bi-2-thiazoline and bpym = 2,2'-bipyrimidine), the bpym ligand acts as a bridging unit. The magnetic interaction between the Fe(II) centers was determined by the comparison with the related [HS-HS] system [Fe^{II}(bpym)(NCS)$_2$]$_2$bpym, indicating a weak antiferromagnetic exchange coupling of J = −2 to −2.5 cm^{-1}.[122] ^{57}Fe Mössbauer studies and dilution experiments confirmed the intermediate [LS-HS] state by contributions to the isomer shift and quadrupole splitting of both the HS and LS state. Kahn furthermore emphasized the energetic stabilization by short- and long-range intermolecular interactions.[123,124]
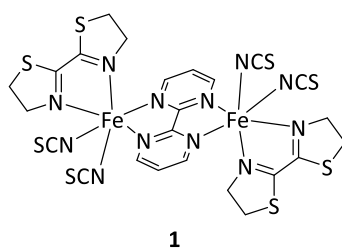

1

*Figure 7 Molecular structure of the dinuelcar Fe(II) complex [Fe(bt)(NCS)$_2$]$_2$bpym **1** (bt = 2,2'-bi-2-thiazoline and bpym = 2,2'-bipyrimidine).[118]*

In general, the [LS-LS], [LS-HS] and [HS-HS] spin states are separated by the energy differences Δ_1 and Δ_2, which are dominated by the orbital angular momentum and the crystal field. The energetic level of the [LS-HS] state is stabilized by the intra- and intermolecular interactions, resulting in the ground state, the highest energetic level or inbetween the [LS-LS] and [HS-HS] states.[125]
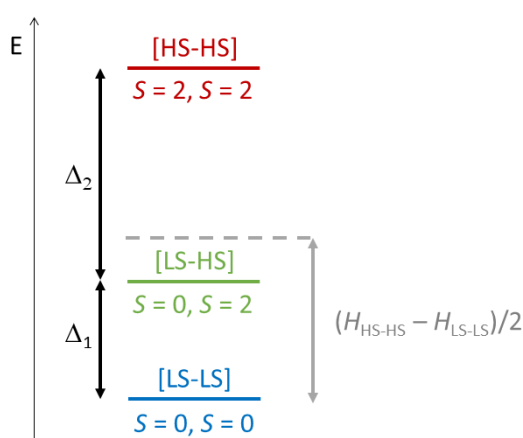

Figure 8 Energetic levels of the [LS-LS], [LS-HS] and [HS-HS] states of a dinuclear Fe(II) SCO complex.[125]

The population of the intermediate [LS-HS] state requires the enthalpy H_{LS-HS} to be slightly lower than $(H_{HS-HS} - H_{LS-LS})/2$ and strong intramolecular interactions.[126] In case of dinuclear Fe(II) complexes, only the [HS-HS] state can couple antiferro- or ferromagnetically, whereas in Fe(III) and Co(II) systems all states can show magnetic exchange coupling. The antiferro- or ferromagnetic interactions shift the energetic levels of the [LS-LS], [LS-HS] and [HS-HS] states depending on the strength and sign of the exchange interaction. The energetic level of well separated [LS-LS], [LS-HS] and [HS-HS] states is not perturbed much by weak magnetic exchange coupling, hence a spin transition can occur (Figure 9 left). Conversely, a strong antiferromagnetic interaction causes mixing of the $S_{HS-HS} = 0$ ground state with the $S_{LS-LS} = 0$ and $S_{LS-LS} = 1$ states when the [LS-LS] ground state is not well separated from the [HS-HS] state (Figure 9 right). Thus there will be never a full [HS-HS]→[LS-LS] conversion.[125] To date, only a few related studies are known in the literature, mostly based on theoretical studies of [Fe^{II}-Fe^{II}] and [Fe^{III}-Fe^{III}][39,125–127] as well as further dinuclear transition metal complexes such as Cu(II), Ni(II), Mn(II) and Co(II).[128]
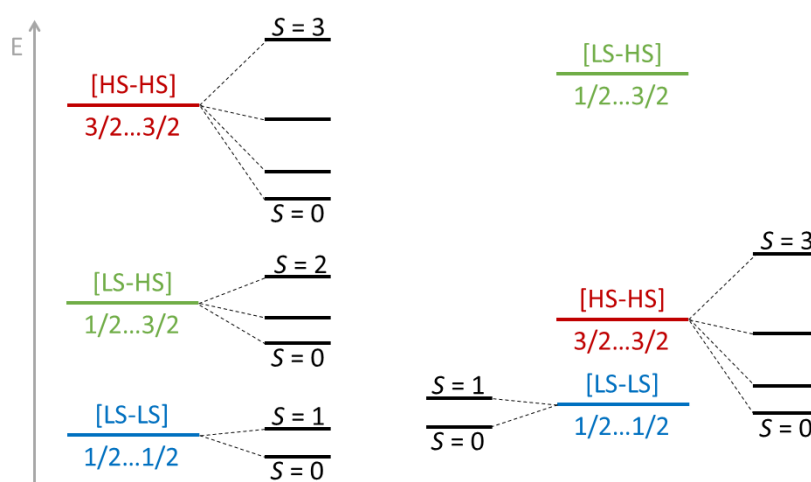

Figure 9 Electronic states of an antiferromagnetically coupled dinuclear Co(II) complex. Left: all well-separated [LS-LS], [LS-HS] and [HS-HS] states can be populated due to weak magnetic exchange coupling. Right: the [LS-LS] ground state mixes with the [HS-HS] state because of strong antiferromagnetic exchange coupling.[125]

The synthesis of dinuclear SCO complexes is followed by two different approaches. The [Fe^{II}(bt)(NCS)$_2$]$_2$bpym complex **1** is an example for the 'supramolecular' approach, where simple blocking and capping ligands (see Figure 10) are used and no laborious organic synthesis is needed. The synthesis of the dinuclear complexes is controlled by the geometrical requirements of the metal ion, the denticity of the ligand and the molar ratios. Nonetheless, the control of the desired dinuclear compound over the possible mono- or polynuclear side products remains challenging.[116,129]
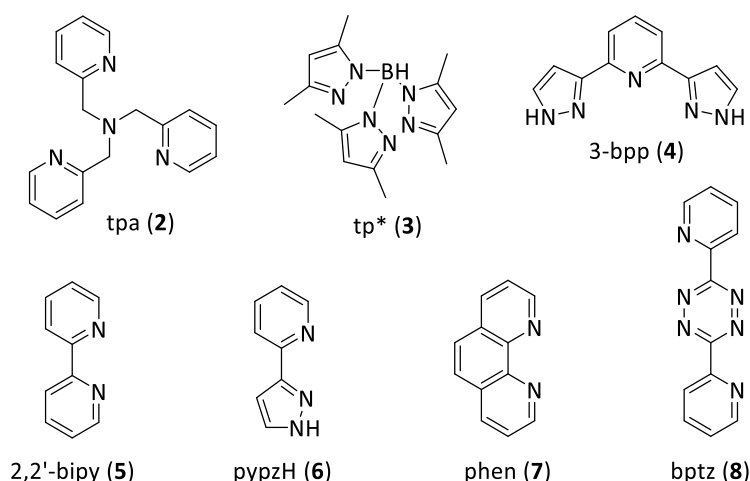
Figure 10 Examples for blocking and bridging ligands that are used for the 'supramolecular' approach to synthesize dinuclear Fe(II) spin crossover complexes:[116] tpa = tris(2-pyridylmethyl)amine (2),[130] tp* = hydrotris(pyrazolyl)borate (3),[131] 3-bpp = 2,6-bis(pyrazol-3-yl)pyridine (4),[132] 2,2'-bipy = 2,2'-bipyridine (5),[133] pypzH = 2-pyrazolylpyridine (6),[134] phen = 1,10-phenanthroline (7)[12] and bptz = 3,6- bis(2-pyridyl)tetrazine (8).[129]

Another possibility to create dinuclear SCO complexes is the 'designer-ligand' approach, where polydentate ligands with the desired number of binding pockets and denticity are synthesized. The bridging units consist of five-membered *N*-heterocycles, aromatic or conjugated moieties while the side arms are built up by other six- or five-membered *N*-heterocycles, which provide a suitable ligand field. Such systems are well-investigated, for example by the groups of Murray,[135] Meyer,[136] Brooker,[137] and Rentschler.[95,138]
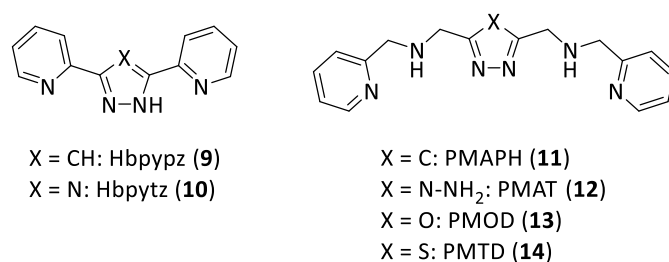

Figure 11 Examples of bridging ligand that are used for the 'designer-ligand' approach to synthesize dinuclear Fe(II) spin crossover complexes:[116] Hbpypz = 3,5-bis(2-pyridyl)-pyrazole (9),[139] Hbpytz = 3,5-bis(2-pyridyl)-triazole (10),[135] PMAPH = 3,5-bis{[N-(2-pyridylmethyl)amino]methyl}-1H-pyrazole (11),[140] PMAT = 4-amino-3,5-bis{[(2-pyridylmethyl)amino]methyl}-4H-1,2,4-triazole (12),[137] PMOD = 3,5-bis{[(2-pyridylmethyl)amino]methyl}-1,3,4-oxadiazole (13),[95] PMTD = 3,5-bis{[(2-pyridyl-methyl)amino]methyl}-1,3,4-thiadiazole (14).[138]

The dinuclear Fe(II) complex [Fe$_2$(PMAT)$_2$](BF$_4$)$_4$·DMF (PMAT = 4-amino-3,5-bis{[(2-pyridyl-methyl)amino]methyl}-4*H*-1,2,4-triazole **12**) was reported by Brooker[141] and shows an abrupt spin crossover from the [LS-HS] to the [HS-HS] state with increasing temperature. The [LS-HS] state could be confirmed by magnetic and applied field ^{57}Fe Mössbauer measurements as well

as the first crystal structure of a distinct [LS-HS] state. Further modifications were achieved by the variation of **X** (including CH, *N*-NH$_2$, *N*-phenyl, *N*-pyrrolyl),[140,142] changing the non-coordinating anion (Cl$^-$, PF$_6^-$, SbF$_6^-$, CF$_3$SO$_3^-$, B(Ph)$_4^-$ and C$_{16}$H$_{33}$SO$_3^-$)[143] and substitutions of the secondary amine with toluenesulfonyl[144] or using a thioether bridge.[145] Related dinuclear systems with central 1,3,4-thiazole[128,138,146–149] and 1,3,4-oxadiazole[95,150] cores were reported by our group. The influence of the non-coordinating anions (BF$_4^-$, ClO$_4^-$ and CF$_3$SO$_3^-$), the solvent content as well as the variation of the *N*-heterocyclic side-arms (pyridine, imidazole, thiazole) were investigated with regard to the magnetic properties.

1D, 2D and 3D Spin Crossover Complexes

Fundamental research on the one-dimensional complex series [Fe^{II}(Rtrz)$_3$]X$_2$·nSolv **15** (Rtrz = 4-substituted-1,2,4-triazole, X = monovalent anion) was performed by Kahn already in the early 90s.[114] These compounds provide a sharp transition close to room temperature, have shown to be robust and offer a modular approach towards a high variety of substituents for a large number of possible applications.
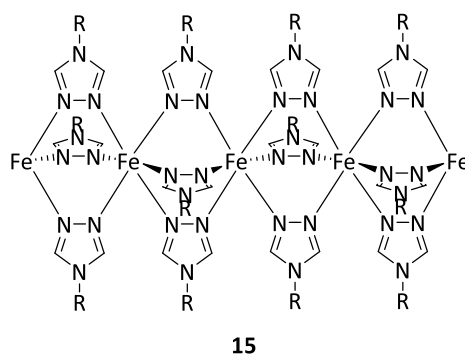

15

Figure 12 Structure of the one-dimensional [Fe^{II}(Rtrz)$_3$]$^{2+}$ coordination chain **15**.[114]

The 1,2,4-triazoles form an octahedral {N$_6$} coordination sphere around the Fe(II) centers and act as bridging ligand *via* the N1 and N2 donor atoms. The high cooperativity is attributed to the short-range intramolecular interaction between the neighboring Fe(II) ions (d(Fe–Fe) = 3.6 – 3.7 Å) mediated by the triazole bridge. The cooperativity strongly depends on the substituents R, the non-coordinating anions and solvent molecules.[151] Numerous substituents have been introduced on the N4 nitrogen atom, such as alkyl chains, aromatic moieties as well as ionic and bulky functionalities, in order to influence the packing of the one-dimensional chain, the abruptness of the transition and the transition temperature itself.[152] This system was already incorporated into supramolecular gels,[153,154] thin films[155,156] as well as liquid crystals[157] and represents the prototype of a switchable optical device[158] which is an important step towards daily used applications.

Two- and three-dimensional networks in form of [Fe^{II}(**L**)$_6$]$^{2+}$[159–161] and [Fe^{II}(**L**)$_4$(NCX)$_2$][162–164] with connecting aromatic ligands such as **L** = pyridyl, pyrrolyl, pyrazolyl, triazolyl, imidazolyl

moieties and X = S, Se, BH_3, CH_3 as well as the Hofmann Clathrates [$Fe^{II}L_2M^{II}(CN)_4$]x{guest} (**L** = pyridine, pyrazine and M = Ni, Pd, Pt)[165,166] have been intensively investigated. Depending on the bridging ligand and choice of the co-ligands, the size of the cavities as well as intermolecular interactions can be adjusted, which enables the functions as 'molecular sponges' due to reversible dehydration/rehydration, molecular separators, catalysts or chemical sensors.[88]

1.1.8 Hybrid Spin Crossover Complexes

The combination of the spin crossover phenomenon with other functional materials or properties is of high interest because these compounds are suitable for applications in various fields, e.g. in spintronics or high-density storage. Spin crossover complexes were already successfully combined with porosity, electrical conductivity, exchange coupling and long-range magnetic order, liquid crystals, gels or nonlinear optics.[14] In this context, the combination with single-molecule magnets (SMMs) is of upmost interest in terms of molecular magnetism. SMMs show slow relaxation of magnetization due to an effective energy barrier U_{eff} (further details will be discussed in Chapter 1.2).

Until now, only a few examples of complexes showing both SCO and SMM behavior are reported in the literature. The first examples are based on mononuclear Fe(III), Fe(II) or Co(II) complexes. In 2012, Mossin, Mayer and Mindiola[167] reported the tetra-coordinated [$Fe^{III}(PNP)Cl_2$] complex (PNP = N[2-P($CHMe_2$)$_2$-4-methylphenyl]$_2^-$) with a transition of S = 3/2 to S = 5/2 above 80 K and an effective energy barrier of U_{eff} = 47 − 52 K. The SMM properties can be switched ON and OFF by light irradiation in the well-known tetrazole-based spin crossover complexes [Fe^{II}(1-propyl-tetrazole)$_6$](BF_4)$_2$ with U_{eff} = 22 K (λ = 505 nm and λ = 850 nm)[168] and [Fe^{II}(1-methyl-tetrazole)$_6$](CF_3SO_3)$_2$ with U_{eff} = 55 K (λ = 500 − 650 nm and λ = 650 − 900 nm)[169] as well as [$PhB(MesIm)_3Fe^{II}$-N=PPh_3] (Mes = 2,4,6-$Me_3C_6H_2$) with U_{eff} = 22 K (white light).[170] Another interesting example is the square pyramidal coordinated complex [Co^{II}(3,4-lut)$_4$Br]Br (3,4-lut = 3,4-lutidine), where the thermally induced spin crossover from S = 1/2 to S = 3/2 in the range of 150 − 290 K is combined with SMM behavior of the LS state.[171] The combination of SCO and slow relaxation of magnetization can be also provided by different metal ions within the structure. One example was reported by Mathoière and Clérac[172] in 2013. The single chain magnet {Mn^{III}(saltmen)}$_2$ (saltmen = N,N'-(1,1,2,2-tetramethylethylene)-bis-(salicylidene-iminate)) with U_{eff} = 13.9 K was combined with the spin crossover moiety {Fe^{II}(**L**)(CN)$_2$} (**L** = 2,13-dimethyl-3,6,9,12,18-pentaaza-bicyclo[12.3.1]-octa-deca-1(18),2,12,14,16-pentaene) in order to switch the magnetic interaction by irradiation. Also, the Co(II)-doped Fe(II) complex [$Fe_{0.92}Co_{0.08}$(bppCOOH)$_2$](ClO_4)$_2$ combines spin crossover (Fe(II)) and field-induced SMM behavior (Co(II)) in the different metal centers.[173] Different coordination geometries of Co(II) ions in [Co(Brphterpy)$_2$][Co(NCS)$_4$]·2MeCN lead to thermally induced SCO (O_h) and field-induced slow relaxation of magnetization (T_d). Nonetheless, several questions as the influence of the SCO on the SMM properties and relaxation processes remain unclear.[174]

1.2 Single-Molecule Magnets

Single-molecule magnets (SMMs) show slow relaxation of magnetization resulting from an energy barrier of purely molecular origin. When a SMM is placed into an external magnetic field, the unpaired electrons will align along the direction of the field. After removing the external magnetic field, the spins retain their direction for a specific time period.[175] The highest temperature where the magnetization is maintained without an external magnetic field is called the blocking temperature T_B. Based on their physical properties, SMMs are highly suitable for the future application as molecular spintronics or quantum computing.[176]

The first single molecule magnet $[Mn_{12}O_{12}(O_2CCH_3)_{16}(H_2O)_4]\cdot 4H_2O\cdot 2CH_3CO_2H$ 'Mn$_{12}$' was investigated by Sessoli et al.[177] in 1993. The molecule consists of a mixed-valence $Mn_8^{III}Mn_4^{VI}$ core, where the eight Mn(III) ions form an external octagon and the four Mn(IV) ions build up an inner tetrahedron. The inner Mn(III) ions with S = 2 and the external Mn(IV) ions with S = 3/2 ferromagnetically couple among each other. The antiferromagnetic interaction between the Mn(III) and Mn(IV) ions results in the total S = 10 ground state. The zero-field splitting parameter of D = –0.50 cm^{-1} relies on the single-ion anisotropy of the Jahn-Teller distorted Mn(III) ions. Below 2 K, the magnetization retains for two months.[178]

1.2.1 Zero-Field Splitting and Magnetic Anisotropy

The origin of the slow relaxation of magnetization lies in a paramagnetic spin ground state S and a strong magnetic anisotropy D. Magnetic anisotropy occurs in an external magnetic field (Zeeman effect) or *via* zero-field splitting (ZFS) without an applied field. In both cases, the degeneracy of the spin ground state is removed and an energy gap is created.[175,179] Zero-field splitting is ascribed to the electrostatic field of the ligands and pronounced spin-orbit coupling.[180,181] The ZFS Hamiltonian $\hat{H}_{ZFS}$ is expressed by the following equation:[26]

$$\hat{H}_{ZFS} = \mathbf{D}\cdot\mathbf{S^2} = D[S_z^2 - S(S+1)/3] + E(S_x^2 - S_y^2) \tag{9}$$

with the diagonal and traceless **D**-tensor. This tensor consists of both the axial and rhombic ZFS parameter D and E. These parameters reflect the symmetry around the magnetic center and are related by $|D| \geq 3E \geq 0$.[127,182] The axial parameter is defined as $D = D_{zz} - D_{xx}/2 - D_{yy}/2$ and the transverse as $E = (D_{xx} - D_{yy})/2$.[183] In a cubic symmetry, D_{zz} equals D_{xx} and D_{yy}, hence D is zero. In an axial symmetric system, the transverse parameter E is zero as D_{xx} equals D_{yy}. This results in the simplified spin Hamiltonian of:

$$\hat{H}_{ZFS} = D \cdot S_z^2 \tag{10}$$

A complex with a total spin of $S > 1/2$ has $2S+1$ possible spin states in the range of $M_S = +S$ to $M_S = -S$. A negative D value leads to the $M_S = \pm S$ ground state. A positive D value has the opposite effect, the $M_S = 0$ for a system with integer or $M_S = \pm 1/2$ for half-integer number of spins is the lowest energetic state.[184] The direction of the axial magnetic anisotropy is described as the *easy-axis*, also known as the Ising-type of magnetic anisotropy ($D < 0$). A positive D value describes an *easy-plane* type of magnetic anisotropy.[175,179]

1.2.2 Energy Barrier and Relaxation Processes

For an *easy-axis* magnetic anisotropy the energy barrier U for the reorientation of the magnetization is for integer and half-integer spin systems:[179]

$$U = |D| \cdot S^2 \tag{11}$$

$$U = |D| \cdot (S^2 - 1/4) \tag{12}$$

The energy diagram of a SMM is visualized in a so-called double-well potential (see Figure 13). In a system with $M_S = \pm S$ states, the $M_S = +S$ and $M_S = -S$ states are separated by the energy barrier U. When applying an external magnetic field, one potential well is more favored due to the alignment of the spins in the magnetic field. The energies of these states decrease, and a magnetization takes place. After removing the magnetic field, the magnetization remains, and the reorientation of the spins occurs slowly by overcoming the energy barrier U.
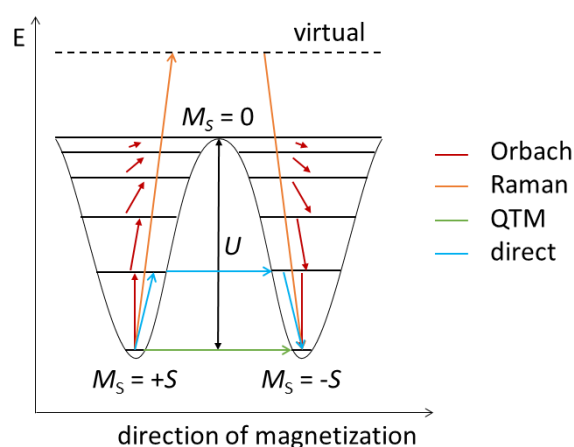

Figure 13 The double-well potential giving an overview of the different relaxation processes. The red arrows describe the Orbach process where the single M_S states are populated by phonon interaction. In the temperature-dependent Raman process (orange arrows) the excitation occurs to a virtual state. The green arrow represents the quantum tunnelling process which occurs between the two resonant $M_S = +S$ and $M_S = -S$ ground states. In the direct (blue arrows) process, the tunneling occurs between excited M_S states of the same energy.

In the literature, four different relaxation processes are discussed. The Orbach, Raman and direct processes as well as the quantum tunneling of magnetization (QTM) are divided into temperature- and field-dependent processes. The relaxation time τ consists of the following contributions:

$$\tau^{-1} = A_1 \cdot H^4 \cdot T + A_2 \cdot H^2 \cdot T + \frac{B}{1 + F \cdot H^2} + C \cdot T^n + \tau_0^{-1} \cdot \exp\left(-\frac{\Delta E}{k_B T}\right) \tag{13}$$

$$\text{direct process} \qquad \text{QTM} \quad \text{Raman} \qquad \text{Orbach}$$

The temperature-dependent Orbach process follows the Arrhenius law. The electron is excited to the next energetically higher M_S state by excitation of a phonon upon lattice interaction and overcoming the barrier by following relaxation. Typical values of the pre-exponential factor τ_0 are $10^{-6} - 10^{-13}$ s. In case of the temperature-dependent Raman process, the excitation of the phonon occurs to a virtual energetic level and relaxation to a real spin state. The exponent n is in the range of 2 < n < 9, where n = 2 are valid at high and n = 5 at low temperatures. A large value of n = 9 is attributed to a large energy difference between the Kramers' levels.[185] The excitation of a phonon with simultaneous spin-flip is referred to the direct process and depends on both the temperature and the field.[186] Resonant quantum tunneling of magnetization (QTM) occurs within the lowest lying energetically degenerate M_S states and strongly depends on the magnetic field.[183] It is facilitated by the presence of transversal anisotropy E, hyperfine coupling and dipole-dipole interaction.[186–188] The application of an external magnetic field can reduce or even suppress QTM.

1.2.3 Measuring the Energy Barrier and Relaxation Processes

In order to investigate the SMM behavior, frequency-dependent alternating current (ac) magnetic susceptibility measurements are performed at zero-field or an applied dc field. The magnetic susceptibility χ consist of two components, the real in-phase susceptibility χ' and the imaginary out-of-phase χ'' susceptibility, which depend on the angular frequency ω of the magnetic field.[183]

$$\chi(\omega) = \chi'(\omega) - i\chi''(\omega) \tag{14}$$

The in-phase and out-of-phase components are measured in dependence of the ac frequency and the temperature. The magnetic ac susceptibility is further described by the generalized Debye equation:

$$\chi(\omega) = \chi_S + \frac{\chi_T - \chi_S}{1 + (i\omega\tau)^{1-\alpha}} \tag{15}$$

χ_S and χ_T are the adiabatic and isothermal susceptibilities. For a single relaxation process, the Cole-Cole parameter α is zero, values up to one hint to further relaxation processes.[189] The out-of-phase signal χ'' is plotted against the in-phase-signal χ' in the so-called Cole-Cole plot displayed by semi-circles, that depend on the temperature and the frequency.
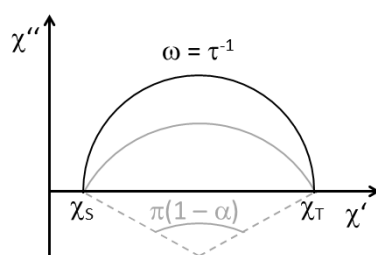
Figure 14 Representation of the Cole-Cole plot, indicating the adiabatic and isothermal susceptibilities χ_S and χ_T as well as the Cole-Cole parameter α.[183]

At the maximum of each semi-circle, the angular frequency ω is related to the relaxation time τ by $2\pi\nu = \omega = \tau^{-1}$. In case of several relaxation processes, the semi-circle becomes an arc of a circle. The term $\pi(1 - \alpha)$ describes the deduced angle between χ_S and χ_T in relation to the center of the circle. A significant difference of the relaxation times can lead to an additional semi-circle, where two relaxation times τ_1 and τ_2 are present.

In the Arrhenius plot ($\ln(\tau)$ versus $1/T$, see Figure 15), the relevant relaxation processes can be determined. Typically, tunneling processes dominate the linear low-temperature region and the thermally activated Orbach process the high-temperature region. The Raman process is dominant in the temperature region of $15 - 30$ K in particular.[190] The effective energy barrier U_{eff} is extracted from the fit using Equation 13.
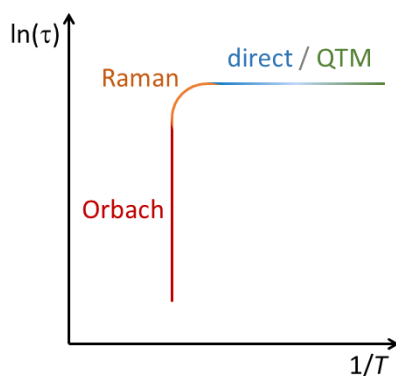

Figure 15 Representation of the Arrhenius plot. The linear curve in the low-temperature region can be assigned to QTM and the direct process whereas the Orbach process dominates the high-temperature region. The Raman process is attributed to the exponential part of the curve.[191]

1.2.4 Increasing the Energy Barrier

1.2.1.1 Polynuclear Transition Metal SMMs

As the energy barrier depends on both the spin ground state S and the magnetic anisotropy D (see Equation 9), there are different strategies to increase the effective energy barrier U_{eff}.[192,193] Based on the squared dependence on S, the synthesis of polynuclear 3d metal complexes with ferromagnetically coupled magnetic moments was tremendously studied in the early research.[192,194,195] Especially Mn(III), Fe(III) and V(III) ions were investigated due to their high spin and anisotropic ground state.[176,196–198] The highest effective energy barrier of U_{eff} = 89.2 K and blocking temperature of T_B = 4.5 K was achieved for the hexanuclear Mn(III) complex [$Mn_6O_2(sao)_6(O_2CPh)_2(EtOH)_4$] ($H_2sao$ = 2-hydroxybenz-aldehyde oxime) with a total ground state of S = 12.[199] Manganese based clusters with record spin ground states of S = 51/2[200] and S = 81/2[201] are reported but no pronounced anisotropy and the lack of slow relaxation of magnetization was observed for these examples.[182] It was further found, that D is inversely proportional to S^2 which appears antagonistic in order to create SMMs with high energy barriers.[202]

1.2.1.2 Lanthanide(III) based Single-Ion Magnets

Starting in 2003, the focus was directed towards lanthanide ions as they reveal strong single-ion magnetic anisotropy and high spin ground states. Dy(III), Tb(III), Ho(III) and Er(III) ions are suitable for designing single-ion magnets (SIM).[175] Especially the Kramers ion Dy(III) benefit from the high m_J = ±15/2 ground state and pronounced magnetic anisotropy. The spin-orbit coupling is much higher than for 3d metals giving rise to an unquenched total angular momentum J. This is then perturbed by the small but significant ligand field leading to the ($2J+1$) m_J microstates. In case of 4f-ions, the $\pm m_J$ rather than $\pm M_S$ levels form the well-known double well.[203]

The free Dy(III) ion has a sixteen-fold degenerated ground state with m_J = ±15/2, ±13/2, …, ±1/2. Each m_J state interacts differently with the crystal field, which leads to the splitting of the Kramers doublets. For lanthanide ions, the magnetic anisotropy D is described by the energy difference of the m_J ground and the lowest lying excited states. In SIMs based on lanthanides, the QTM occurs within the ground doublet but can be blocked by high symmetry. Relaxation of the magnetization must then occur *via* thermally activated processes. For this reason, the crystal field plays a crucial role when designing complexes with high magnetic anisotropy and large energy barriers.[203–205]
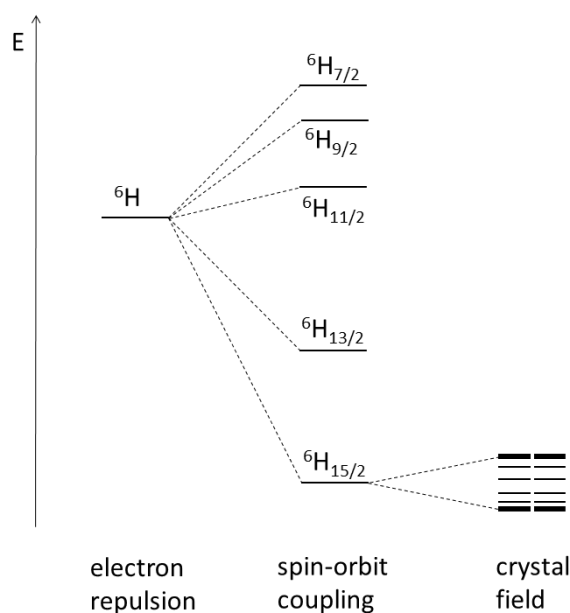
Figure 16 Electronic structure of a Dy(III) ion with perturbations of the free ions electronic ground state. Electronic repulsion, spin-orbit coupling and the crystal field lead to splitting of the ground state ^6H. For clarity, only the low-lying $^6H_{x/2}$ (x = 7 – 15) states and the splitting of the $^6H_{15/2}$ ground state is visualized.[203]

Depending on the 4f-ion, the total f-electron charge density can either have a prolate (axially elongated), oblate (equatorially expanded) or isotropic (spherical) shape. As the electron charge density of the m_J = ±15/2 state of a free Dy(III) has an oblate shape, the ligand should be located above and below the ion in the *xy*-plane, for example in a sandwich-type geometry, as already shown by Ishikawa's mononuclear [LnPc$_2$]^n (with n = 0, ±1 and Pc = phthalocyanine) doubledeckers.[194] Sandwich-like complexes with eight nitrogen donor atoms providing a square antiprismatic coordination sphere are exceedingly suitable and lead to high energy barriers of up to 652 cm^{-1} for [Tb(Pc)(OC$_6$H$_4$-*p*-^{t}Bu-Pc)].[206]
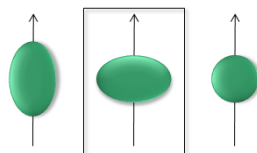

Figure 17 Possible shapes based on the quadrupol approximation of the 4f-shell electron distribution for lanthanide(III) ions. Left: prolate, middle: oblate, right: isotropic. Dysprosium(III) ions reveal an oblate shape for the f-electron density.[203]

In this context, Sessoli and coworkers[207] reported the magnetic properties of a {N$_4$O$_4$} donor macrocycle dysprosium(III) complex (Na[Dy(DOTA)(H$_2$O)]·4H$_2$O with H$_4$DOTA = 1,4,7,10-tetraazacyclododecene-1,4,7,10-tetra-acetic acid) with a square antiprismatic coordination

geometry which is capped by one water molecule. The presence of the water molecule and the position of the hydrogen atoms have shown to crucially influence the SIM behavior as the direction of the uniaxial anisotropy changes.[208] The record holder with the highest effective energy barriers are [Dy(O^{t}Bu)$_2$(py)$_5$][BPh$_4$] with U_{eff} = 1 815 K[209] and Dy(III) complexes with cyclopentadiene derivatives [Dy^{III}(Cp^{ttt})$_2$][B(Ph)$_4$] (Cp^{ttt} = 1,2,4-^{t}Bu$_3$C$_5$H$_2$) with U_{eff} = 1 837 K,[210] [Dy^{III}{Cp(^{i}Pr)$_4$(Me)}$_2$][B(C$_6$F$_5$)$_4$] with U_{eff} = 2 112 K[211] and [Dy^{III}{Cp(Me)$_3$(Cp(^{i}Pr)$_3$)}][B(C$_6$F$_5$)$_4$] with U_{eff} = 2 217 K.[212] The highly desirable axial D_{5h} symmetry of the former is provided by the five pyridine ligands in equatorial (weak ligand field) and two $tert$-butoxy ligands in axial position (strong ligand field). In the latter examples, the two Cp ligands provide a strong axial crystal field which increases the magnetic anisotropy of the Dy(III) ion.

1.2.1.3   3d Transition Metal based Single-Ion Magnets

The interest on single-ion magnets based on 3d transition metal ions started ten years ago. The focus is on understanding and maximizing the single-ion anisotropy instead of increasing the spin ground state. First row transition metal complexes with a low number of ligands provide a weak ligand field compared to a relatively large spin-orbit coupling, which makes them suitable for the investigation of their dynamic magnetic properties.[213,214]

The first monometallic 3d SIM K[(tpa^{Mes})Fe^{II}] (H$_3$tpa^{Mes} = tris((5-mesityl-1H-pyrrol-2-yl)methyl)-amine) was published by Chang and Long in 2010.[215] The trigonal pyramidal geometry and {N$_4$} coordination sphere is promoted by the bulky N-heterocyclic ligand. The unequal occupation of the 1e orbital of the HS Fe(II) ion leads to an unquenched orbital angular momentum and with an applied dc field of 1500 Oe, an out-of-phase signal was observed. The effective energy barrier was determined by U_{eff} = 42 cm^{-1} with an axial and rhombic ZFS parameter of D = −39.6 cm^{-1} and E = −0.4 cm^{-1}. Many other examples based on Fe(III),[167] Fe(I),[216] Mn(III)[217–219] and Ni(II)[220] were reported.[221]

Furthermore, a huge part of 3d SIMs is provided by HS Co(II) compounds due to their unquenched first-order orbital angular momentum. The first Co(II) based single-ion magnet that shows a slow relaxation of magnetization in the absence of an applied field was reported by Long[222] in 2011. The high zero-field splitting parameter of D = −70 cm^{-1} of the tetrahedrally coordinated Co(II) complex [Co(SPh)$_4$](Ph$_4$P)$_2$ with S = 3/2 results in an effective energy barrier of U_{eff} = 21 cm^{-1}. In the same year Murugesu and Richeson[223] reported a mononuclear penta-coordinated Co(II) complex with SIM behavior under an applied dc field. The bulky substituents of the [{ArN=CPh}$_2$(NPh)]Co(NCS)$_2$ complex (Ar = 2,6-^{i}PrC$_6$H$_3$) lead to a highly distorted square-pyramidal geometry and pronounced spin-orbit coupling.

These examples show the favorable tetra- and penta-coordination modes where the spin-orbit coupling is strong in comparison to the ligand field because of the low coordination numbers. This leads to zero-field splitting and pronounced magnetic anisotropy. However, the first example of a hexa-coordinated Co(II) based single-ion magnet was reported by Cano and Pardo in 2012.[224] The sterically hindered dmphen (2,9-dimethyl-1,10-phenanthroline) ligand of the cis-[Co(dmphen)$_2$(NCS)$_2$]·0.25 EtOH complex enforces a highly rhombically distorted octahedral coordination sphere, which causes the high values of the axial D and rhombic E

zero-field splitting parameters with D = +98 cm^{-1} and E = +8.4 cm^{-1}. This leads to an effective energy barrier in the range of U_{eff} = 16.2 − 18.1 cm^{-1} depending on the applied dc field. In contrast to the tetra- and penta-coordinated Co(II) complexes, the possibility of hexa-coordinated compounds to show SIM behavior lies in the unquenched orbital angular contributions due to strong symmetry lowering of the central metal ion. An axial distortion splits the $^4T_{1g}$ ground state into the $^4A_{2g}$ and ^4E_g states, which are separated by the energy gab Δ. A positive sign is attributed to an axial compressed and a negative sign to an elongated octahedral coordination sphere. Further second-order spin-orbit coupling leads to zero-field splitting of the two Kramers doublets m_S = ±3/2 and m_S = ±1/2 with an energy separation of $|2D|$. In case of a compressed octahedron ($\Delta > 0$), the m_S = ±1/2 is the ground state and the axial anisotropy D is of positive sign. Additional transverse anisotropy (E) causes loss of the degeneracy and an energy difference of $|2D'|$:[196,198]

$$|2D'| = 2 \sqrt{D^2 + 3E^2} \qquad (16)$$

The special feature of the reported hexa-coordinated Co(II) SIMs is the present *easy-plane* anisotropy in contrast to the *easy-axis* of single-ion magnets based on lanthanide(III) ions or low-coordinated 3d metal ions.
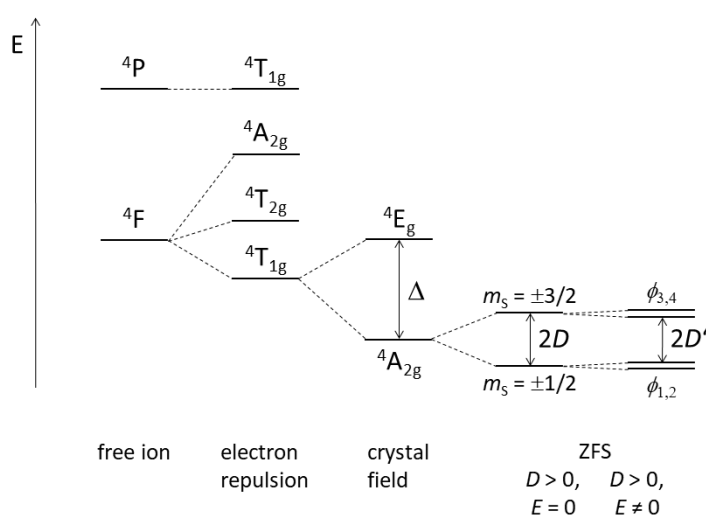

Figure 18 The energy diagram of the ground state of a high-spin cobalt(II) ion with S = 3/2: influence of the electron repulsion and the crystal field (here Δ > 0) in an octahedral coordination sphere, zero-field splitting (ZFS) with D > 0, E = 0 and D > 0, E ≠ 0.[26,225,226]

The compressed octahedral structure of [Co^{II}(abpt)$_2$(tcm)$_2$] complex (abpt = 4-amino-3,5-bis(2-pyridyl)-1,2,4-traizole and tcmH = tricyanomethane) causes an *easy-plane* anisotropy with D = +48 cm^{-1} and E/D = 0.27. The effective energy barrier U_{eff} amounts 59.9 cm^{-1}.[227] Other examples were reported by our group.[228,229] [Co(oda)(**L3**)] (H$_2$oda = oxydiacetic acid, **L3** = 4′-azido-2,2′:6′,2″-terpyridine) and [Co(oda)(**L4**)] **C17** (**L4** = 4′-ethynyl-2,2′:6′,2″-terpyridine) are heteroleptic Co(II) complexes with a distorted octahedral coordination sphere. The effective energy barriers were found to be U_{eff} = 6.2 cm^{-1} at 1500 Oe[228] and 19.50 cm^{-1} at 1000 Oe.[229]

1.3 Click Chemistry

In 2001, the green concept of *click chemistry* was introduced by Sharpless et al.[230] and is based on the effective and selective formation of carbon-heteroatom over carbon-carbon bonds preferred by nature. The best example is the formation and usage of carbon dioxide in the biological cycle. Nucleic acids, proteins and polysaccharides are only a few examples of nature's variety of possible products starting from carbon dioxide.[230] This strategy of very selective reactions under mild conditions can further be used by chemists to form stereospecific target molecules in a simple way. The characteristics of a click reaction are high or even quantitative yields, the toleration of aqueous and open-flask conditions as well as straight-forward purification methods.[231–233] Fast and highly exergonic reactions such as 1,3-dipolar cycloaddition and Diels-Alder-reactions as well as ring-opening reactions of strained heterocycles are examples for click reactions. Furthermore, reactions of some carbonyl compounds such as the formation of (thio)ureas, aromatic heterocycles or amides and addition reactions to carbon-carbon double/triple bonds such as epoxidations are used in this context.[230]

The copper(I)-catalyzed azide-alkyne cycloaddtion (CuAAC) is one of the most used click reactions in synthetic and biological chemistry.[230] Next to the CuAAC, thiol-ene (TEC),[234,235] thiol-yne (TYC)[236] and *N*-oxide alkyne/alkene (NNoC)[237] cycloadditions are frequently used in the synthesis of *N*-heterocyclic building blocks.

1.3.1 Copper(I)-catalyzed Azide-Alkyne Cycloaddition

1,3-Dipolar cycloadditions between a 1,3-dipole and a dipolarophile, that form five-membered *N*-heterocycles, are known as Huisgen reactions.[238,239] A well established and investigated example is the formation of 1,2,3-triazoles starting from two compounds containing an azide and alkyne moiety. The first example was published by Michael[240] in 1893, who reacted phenyl azide and dimethyl acetylenedicarboxylate to form a trisubstituted 1,2,3-triazole. The reaction between organic azides and acetylenes to form 1,2,3-triazoles is highly exothermic. However, a high activation barrier requires harsh reaction conditions, long reaction times and yields in a mixture of regioisomers **18** and **19** (see Scheme 1) causing tedious purification.[238,241] A more efficient synthesis of 1,2,3-triazoles under copper(I) catalysis was investigated independently by the groups of Fokin and Sharpless[242] as well as Meldal[243] in 2002. The former introduced a catalyst consisting of copper(II) sulfate pentahydrate which is *in situ* reduced by ascorbic acid or sodium ascorbate (NaAsc) to the active copper(I) species. The reactions coud be performed under mild conditions and with low catalyst loadings of up to 2%.[242] The direct use of Cu(I) salts such as copper(I) iodide also gave the desired 1,4-disubstituted 1,2,3-triazoles **18** in high

yields. Meldal reported the effective cycloaddition of terminal alkynes and azides on solid-phase catalyzed by copper(I) halides.[243]

1,3-dipolar cycloaddition (Huisgen reaction):
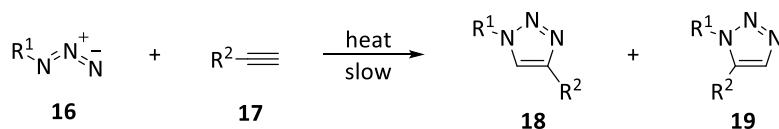

CuAAC click reaction:
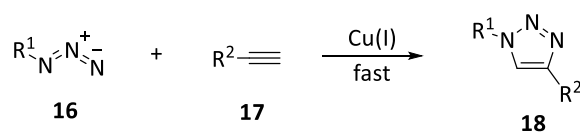
*Scheme 1 Reaction scheme of the 1,3-dipolar cycloaddition (Huisgen reaction) forming the 1,4- and 1,5-disubstituted regioisomers **18** and **19** (top) and the CuAAC click reaction selectively forming the 1,4-regio isomer **18** (bottom).[238,244]*

The CuAAC works with most of the common azide and acetylene compounds tolerating electron-rich, electron-poor, aromatic, primary, secondary, or tertiary aliphatic substituents. In most reactions, water or aqueous mixtures are used due to the stabilization of the reactive copper(I) acetylide species. Furthermore, possible side-products that result from a copper-mediated oxidation are suppressed as the produced oxygen is directly reduced under aqueous conditions.[241] The active catalyst in these transformations is a Cu(I) salt, that is generated *in situ* by using Cu(II) salts and an appropriate reducing agent (e.g. $CuSO_4$ and NaAsc) or provided as stable Cu(I) salts as copper(I) halides, copper(I) acetate or Cu(I) complexes such as $[Cu^I(CH_3CN)_4]PF_6$ or $[Cu^I(CH_3CN)_4]OTf$.[241,244]

In order to understand the high reactivity and selectivity of the CuAAC in comparison to the Huisgen reaction, the mechanism was intensively investigated. The mechanism proposed by Fokin[241] is based on DFT calculations and shown in Scheme 2 (green box).

First, the Cu(I) species **20** reacts with the terminal acetylene **17** to form the Cu(I) acetylide **21** (step A). This reaction is exothermic as the formation of the preorganized π-alkyne copper intermediate complex facilitates the deprotonation of the terminal proton by lowering the pK_a value and thus the formation of the σ-acetylide. Afterwards the organo azide **16** is coordinated to the Cu(I) acetylide by the proximal N^1 donor atom due to the negative partial electron density (**22**, step B). A coordination to the terminal N^3 is energetically unfavorable. Due to this coordination mode, the terminal N^3 of the organic azide becomes more electrophilic and the acetylide more nucleophilic. Step C describes the subsequent forming of the C–N bond under formation of the six-membered copper metallacycle **23**. This step is rate-determining and slightly endothermic. However, the activation barrier of the catalyzed reaction is drastically reduced in comparison to the uncatalyzed cycloaddition. Based on the copper activation, the formation of copper triazolide **24** (step D) is highly favored over the 1,5-regioisomer. In the last step (E) the catalyst **20** is recovered and the 1,2,3-triazole **18** is formed by protonation.[241]
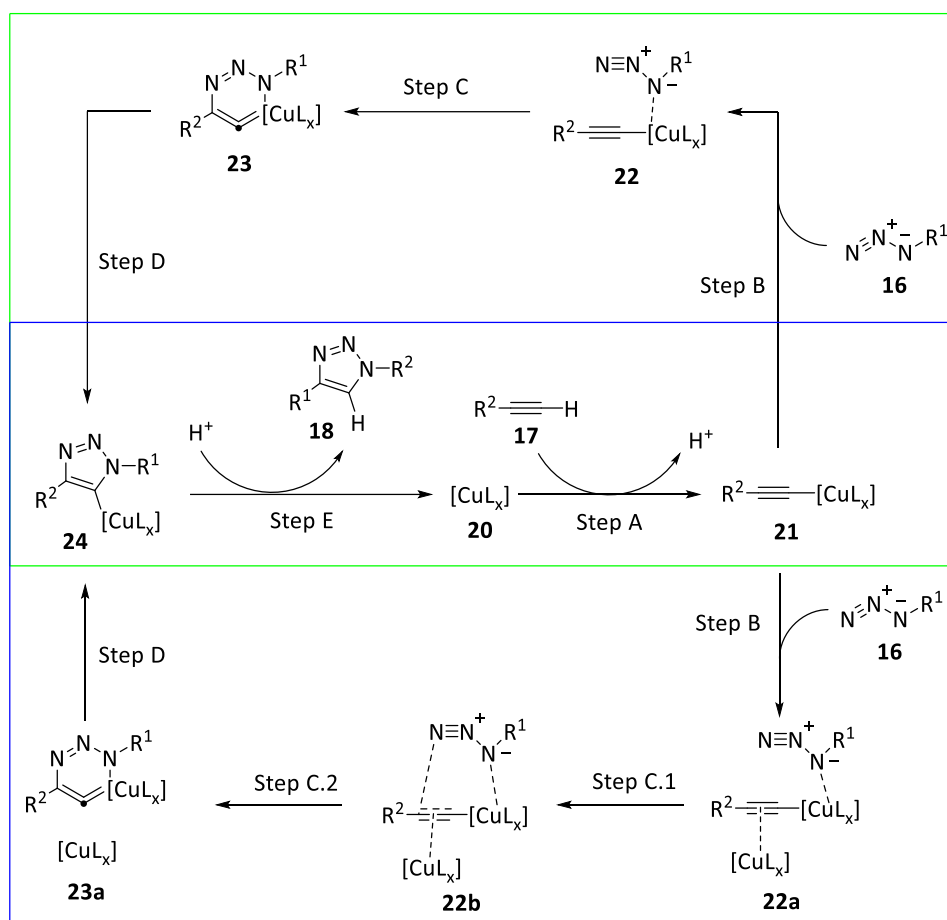
Scheme 2 Proposed mechanism of the CuAAC reaction based on DFT calculations. Green box: first-order mechanism, blue box: second-order mechanism.[241,245]

In further control experiments, the reaction was found to be second-order dependent on the catalyst concentration (see Scheme 2 blue box). In the rate-determining step of the cyclization the dinuclear Cu(I) acetylide species **22a** further decreases the activation barrier by a π-coordination of the second Cu(I) ion to the C≡C triple bond.[241,244,245]

1.3.2 CuAAC in Coordination Chemistry

Based on the simple handling and variability of the CuAAC, different fields of chemical research incorporated such reactions in the routine work. It is utilized in preparative organic chemistry, polymer chemistry, for the formation of dendrimers/rotaxanes/catenanes, the synthesis and functionalization of natural products such as peptides, enzymes or DNA as well as surface applications in general.[241,244] Furthermore, the CuAAC is used to synthesize ligands in the field of coordination chemistry or even combine metal complexes with other building blocks.

The first example of a CuAAC clicked complex in the literature is the mononuclear Fe(II) complex [Fe^{II}(4'-(4-phenyl-1H-1,2,3-triazol-1-yl)-2,2':6',2''-terpyridine)$_2$](PF$_6$)$_2$ **26**, which was reported by Constable and Housecroft.[246] The azido-functionalized precursor complex [Fe^{II}(4'-azido-2,2':6',2''-terpyridine)$_2$](PF$_6$)$_2$ **25** was clicked with phenylacetylene in the presence of copper(I) iodide and NaAsc in dimethylformamide (DMF) (Scheme 3). The successful click reaction of the LS Fe(II) complex was confirmed by IR spectroscopy, ^{1}H-NMR spectroscopy and single crystal X-ray crystallography. The characteristic N=N=N stretching of the azide substituent at 2 110 cm^{-1} vanished, whereas the signal of the 1,2,3-triazole proton appeared at 9.35 ppm in the ^{1}H-NMR spectrum.
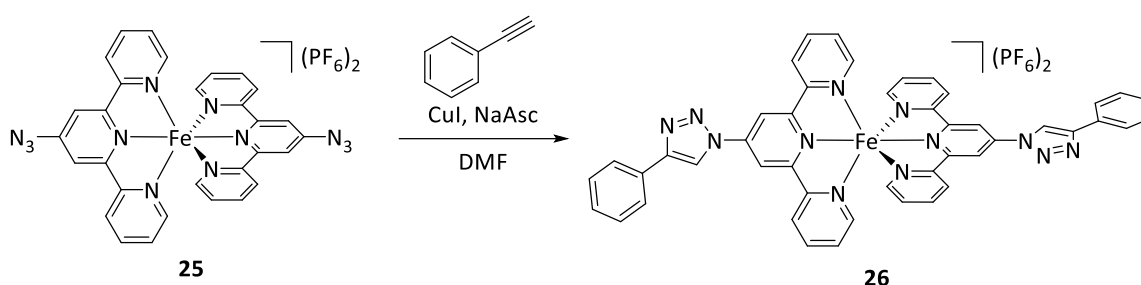
*Scheme 3 Reaction scheme of the CuAAC click reaction between [Fe(4'-azido-2,2':6',2''-terpyridine)$_2$](PF$_6$)$_2$ **25** and phenylacetylene forming [Fe(4'-(4-phenyl-1H-1,2,3-triazol-1-yl)-2,2':6',2''-terpyridine)$_2$](PF$_6$)$_2$ **26**.[246]*

Further copper(I)-catalyzed azide-alkyne cycloadditions were performed in our group by Christian Plenk[247] and Jasmin Krause.[229] Plenk used the CuAAC approach as organic coupling tool to assemble paramagnetic building blocks, especially to link single-ion magnets. The 1,2,3-triazole linkage is highly suitable as it provides a conjugated bridge and enables magnetic communication between the building blocks. The fourfold alkyne-functionalized Cu(II) metallacrown [Cu^{II}(12-MC$_{Cu(II)N(eshi)}$-4)](TMA)$_2$ **27** (H$_3$eshi = 4-ethynyl-salicylhydroxamic acid and TMA$^+$ = tetramethylammonium) forms the paramagnetic building block. The aforementioned mononuclear azido-functionalized Co(II) complex [Co^{II}(**L3**)(oda)] **28** features the SIM. The CuAAC click reaction was catalyzed by copper(I) iodide and performed in dimethylsulfoxide (DMSO) at 80 °C for 24 h. The click reaction with the appropriate azide-functionalized Zn(II) complex was performed in DMSO-d_6 to monitor the reaction by ^{1}H-NMR spectroscopy. The signal of the acetylene's proton at 4.17 ppm disappeared, whereas a simultaneaous increase of the signal at 8.35 ppm was observed, indicating the formation of the 1,2,3-triazole. Furthermore, ESI mass spectrometry and UV-Vis studies confirmed the completed click reaction. These characterization methods furthermore affirm the stability and structural integrity in solution.
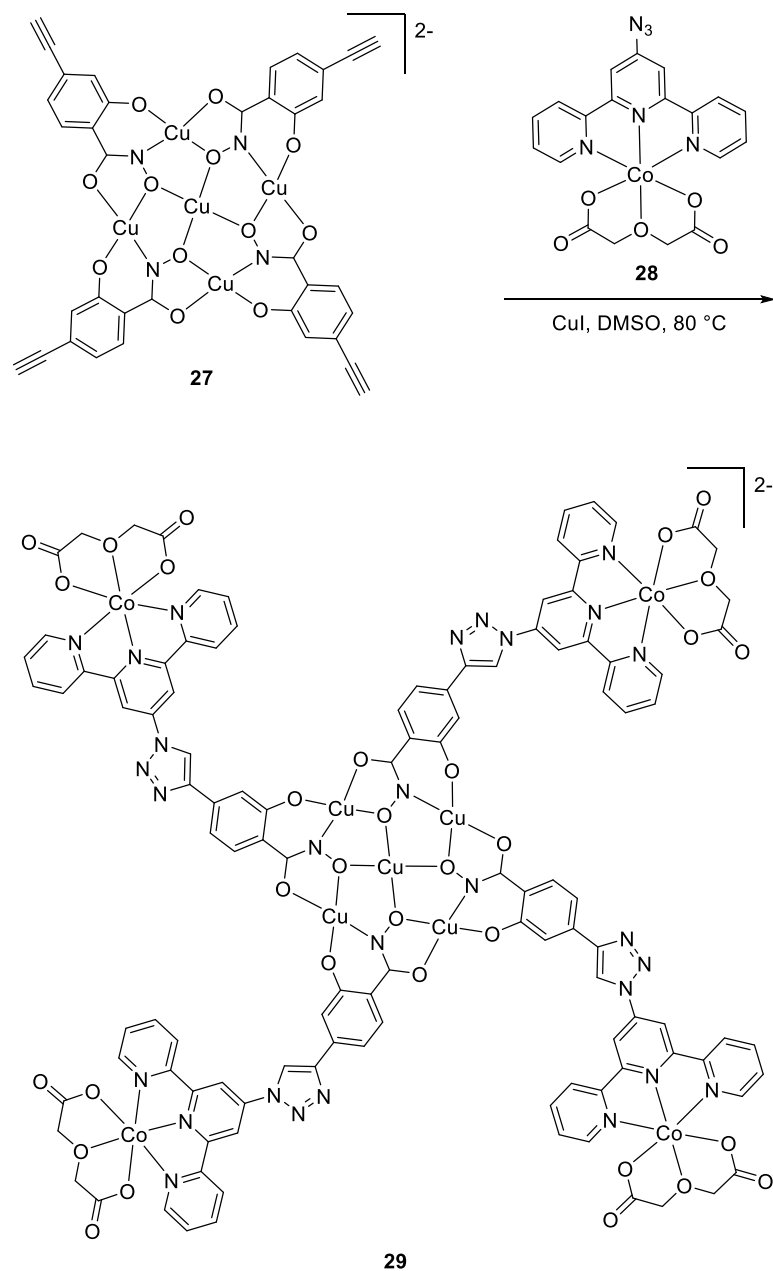
*Scheme 4 CuAAC click reaction of the alkyne-functionalized copper(II) metallacrown **27** with the azide-functionalized cobalt(II) SIM **28** using CuI in DMSO.[247]*

Krause followed this approach to covalently connect two single-ion magnets and to investigate the entanglement of the spins, a key factor for the implementation of qubits in quantum computers.[248] Therefore, the previous described Co(II) SIM [Co^{II}(**L3**)(oda)] **28** was connected to the appropriate to the similar alkyne-functionalized SIM [Co^{II}(**L4**)(oda)] **C17**. The 'click then chelate' and 'chelate then click' concepts were pursued. The ligand **L3-4** was synthesized by reacting 4'-azido-2,2':6',2''-terpyridine **L3** and 4'-ethynyl-2,2':6',2''-terpyridine **L4** with copper(II) sulfate pentahydrate and sodium ascorbate in a water/dichloromethane mixture. The formation of the product was confirmed by IR spectroscopy, NMR spectroscopy and ESI-MS. The clicked ligand was subsequently reacted with the [Co^{II}(oda)(H$_2$O)$_3$] precursor complex to form the desired dinuclear Co(II) complex **30**.[229]

1.) 'click then chelate'
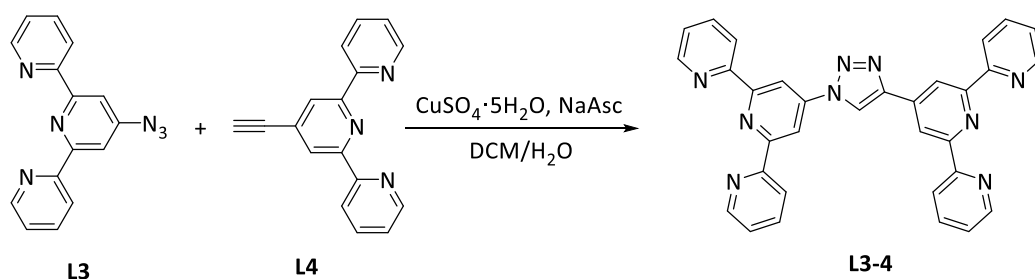
2.) 'chelate then click'
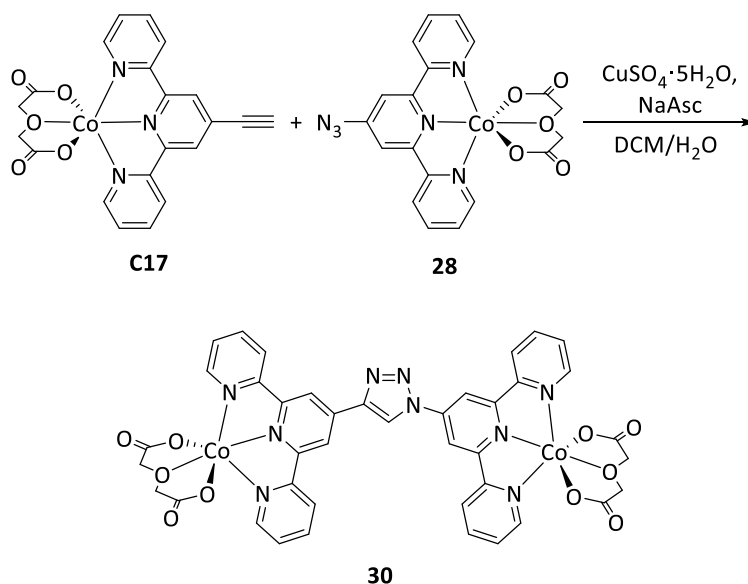
Scheme 5 The two concepts 'click then chelate' and 'chelate then click' to covalently connect two Co(II) SIMs are presented.[229]

Next to the successful click reaction of ligand **L3-4**, the appropriate dinuclear Co(II) complex was synthesized following the 'chelate then click' concept. The CuAAC click reaction between the mononuclear Co(II) complexes [Co(**L3**)(oda)] **28** and [Co(**L4**)(oda)] **C17** yielded in the appropriate dinuclear compound [Co$_2$(**L3-4**)(oda)$_2$] **30**. The reaction was successful when using copper(II) sulfate pentahydrate and sodium ascorbate to *in situ* generate the active Cu(I) species as well as copper(I) iodide. The conversion was monitored by IR spectroscopy as well as ^{1}H-NMR spectroscopy in case of the Zn(II) complex. The 1,2,3-triazole bridge ensured magnetic communication by weak antiferromagnetic exchange interaction between the two Co(II) ions.[228,229]

2 Aim of this Work

The thesis deals with the synthesis and characterization of multifunctional spin crossover complexes. The synergy of SCO behavior and magnetic exchange interaction shall be investigated in the first part. Secondly, spin crossover complexes shall be linked to single-ion magnets to study the influence of the spin transition on the slow relaxation of magnetization.

The first part of the thesis deals with di- and polynuclear complexes and the correlation between spin crossover and magnetic exchange interaction. The exchange interaction will be first investigated on appropriate di- and polynuclear Cu(II) model complexes. The results give insight into the strength and sign of the intramolecular interaction and shall be transferred to the magnetically more complicated di- and polynuclear Fe(II) and Co(II) SCO complexes.
In order to synthesize discrete dinuclear 3d metal complexes, the 'designer-ligand' approach is pursued. Therefore, the novel ligand **L1** based on two different *N*-heterocycles providing two bidentate coordination pockets is synthesized. The two metal ions are bridged by the central 1,3,4-oxadiazole moiety and additionally coordinated by the terminal 1,2,3-triazoles. Spin crossover complexes based on 1,3,4-oxadiazole ligands are rarely known in literature to date, making ligand **L1** a valuable starting point for the investigation of this lead structure. The ligand field can be easily fine-tuned when applying the CuAAC in a modular approach. Variation of the acetylene starting material may lead to a straightforward generation of a library of different 4'-substituted 1,2,3-triazole groups.
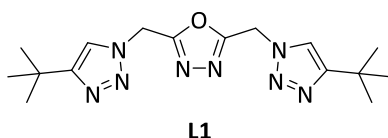

L1

*Figure 19 Molecular structure of the ligand **L1**.*

Following the 'supramolecular' approach, a variety of mono- and polynuclear spin crossover complexes should be synthesized using a bis-1,3,4-thiadiazole system (ligand **L2**, see Figure 20). Ligand **L2** offers the unique possibility to both chelate metal ions *via* the central bidentate pocket and/or the terminal nitrogen donor atoms. Depending on the chelating and/or bridging coordination mode, different exchange pathways seem feasible (highlighted in red in Figure 20). Similar to **L1**, the coordination behavior and the intramolecular exchange coupling will be first investigated for the Cu(II) model complexes and then transferred to the appropriate Fe(II) and Co(II) complexes. Polynuclear complexes containing **L2** as bridging ligand might also induce high cooperativity into such systems leading to very sharp and hysteretic transitions that are required for application in future devices.

*Figure 20 Possible coordination modes and exchange pathways of mono- and polynuclear transition metal complexes with ligand **L2**. a) chelating mode, b) chelating and bridging mode and c) bridging mode by end-to-end coordination. Possible intramolecular exchange pathways are colored in red.*

The second part of the thesis deals with the combination of spin crossover and single-ion magnets. The influence of the spin transition on the slow relaxation of magnetization and the relaxation processes as well as the effect of intramolecular interaction shall be investigated on trinuclear complexes. To date, no di- or trinuclear complex combining SCO and SIM behavior of two discrete metal ions in one molecule is known in the literature. This thesis presents two synthetic approaches where the central SCO unit connects the SIMs. The Co(II) bis-terpyridine complex is envisioned as the central spin crossover unit. The SIM complex is attached using suitable substituents (azide and alkyne) at the 4'-position of the terpyridine ligands.
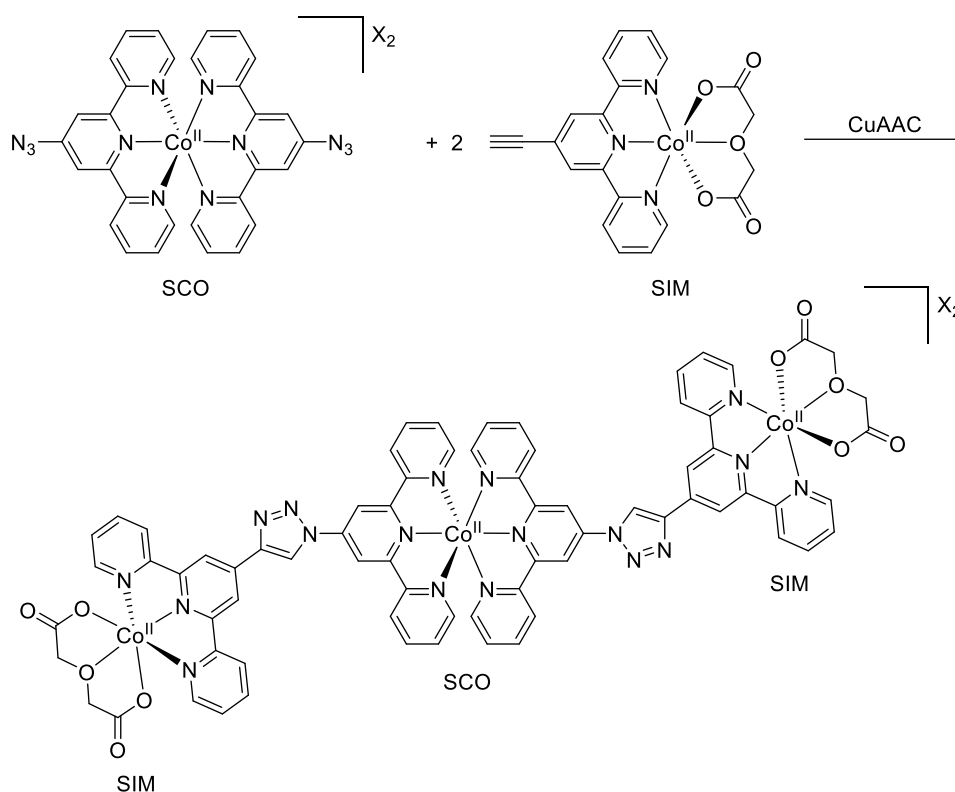
*Scheme 6 The first synthetic approach towards trinuclear SIM-SCO-SIM complexes using the CuAAC. Click reaction between the SCO complex [Co^{II}(**L3**)_2]X_2 (**L3** = 4'-azido-2,2':6',2''-terpyridine and X = monovalent anion) and the SIMs [Co^{II}(**L4**)(oda)] (**L4** = 4'-ethynyl-2,2':6',2''-terpyridine).*

The first approach incorporates the CuAAC for the connection of the SCO complex with the SIMs. Therefore, the terpyridine ligand of the spin crossover complex is functionalized with an azide substituent on the 4'-position forming the Co(II) complex [Co^{II}(**L3**)$_2$]X$_2$ with **L3** = 4'-azido-2,2':6'2''-terpyridine. The aforementioned Co(II) SIM [Co^{II}(**L4**)(oda)] **C17** on the other hand provides a suitable acetylene-substituent.[229] This approach seems promising as the first examples of click reactions with transition metal complexes were successful.[229,246,247] Furthermore, the SCO properties and SIM behavior could be compared to the single components, thus the intramolecular interaction can be determined as the investigations on the previous described clicked complex Co$_3^{II}$(**L3-4**)$_2$(oda)$_2$](ClO$_4$)$_2$ **30** already hint to weak antiferromagnetic exchange coupling.[229] The intramolecular interactions will be compared and the influence on the magnetic behavior investigated.

The second synthetic approach connects the SCO and SIM moieties by employing 'designer' ligand **L5** with two different coordination pockets to form trinuclear SIM-SCO-SIM complexes. The spin crossover of the Co(II) bis-terpyridine complex is ensured, also with the additional complexation of metal ions by the 15-crown-5 moiety.[111] The crown-ether provides a suitable geometry to enable SIM behavior with Co(II) or Dy(III) ions.[249,250] Similar to the first approach, the single SCO and SIM complexes will be synthesized and investigated separately. The influences of the spin transition on the SIM bahvior will be determined by the comparison with the precursor complexes. In contrast to the CuAAC approach, magnetic exchange coupling can be neglected, as the ligand system does not provide a conjugated system.

Approach II:
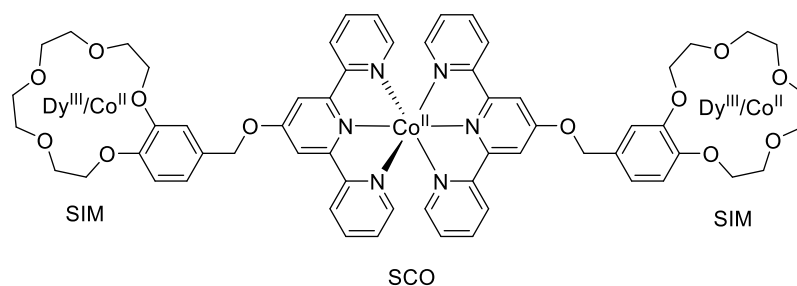
*Scheme 7 Schematic visualization of the trinuclear SIM-SCO-SIM complex with 'designer' ligand **L5** of the second synthetic approach.*

3 Results and Discussion: Spin Crossover and Magnetic Exchange Coupling

In the first part of this thesis, the influence of the magnetic exchange interaction on the spin crossover behavior in di- and polynuclear transition metal complexes was investigated on the basis of Cu(II) model complexes. To facilitate such investigations, two ligand systems based on a central 1,3,4-oxadiazole (**L1**) and a bis-1,3,4-thiadiazole moiety (**L2**) were envisioned. The ligand **L1** possesses two bidentate coordination pockets provided by the central 1,3,4-oxadiazole and the 1,2,3-triazole side arms which should enable a suitable magnetic exchange pathway for the dinuclear complex. Mono- and polynuclear transition metal complexes were envisioned with the bis-1,3,4-thiadiazole based ligand **L2** by chelation *via* the bidentate pocket or the bridging mode *via* end-to-end coordination.

3.1 Magnetic Properties of di- and polynuclear Copper(II) Complexes

The synthesis of the new symmetric ligand system based on a central 1,3,4-oxadiazole core is discussed in the following. The two bidentate coordination pockets are completed by the 1,2,3-triazole side arms which can be easily attached using the CuAAC approach. The properties of the ligand like the ligand field strength and the spin crossover behavior of the corresponding transition metal complexes highly depend on the substituent, which can be easily adjusted by variation of the appropriate alkyne starting material.
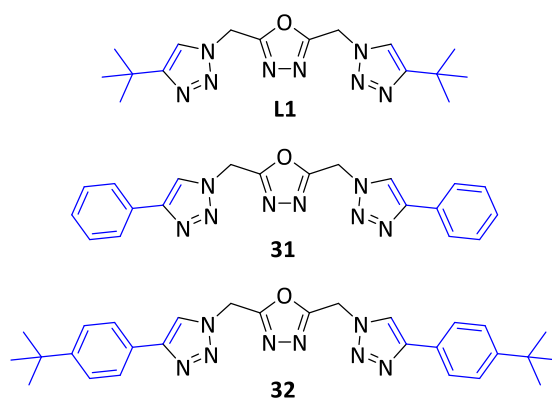

*Figure 21 Molecular structures of the ligands **L1, 31** and **32**.*[251]

3.1.1 Synthesis of Ligand L1

The ligands **31** and **32** were already synthesized during the Master thesis using phenylacetylene and 4-*tert*-butylphenylacetylene as starting materials.[251] To prevent possible π-π-stacking and drastically increase the solubility in common organic solvents, the *tert*-butyl group was attached directly on the 1,2,3-triazole by ■■■■■■■■■■■■■■■■■■■ in his Bachelor thesis.[252] The synthesis route for **L1** is illustrated in Scheme 8.

Scheme 8 Four-step synthesis route of L1.[251–254]

The central 1,3,4-oxadiazole was synthesized by treating chloroacetyl chloride **33** with hydrazine hydrate to form 1,2-dichloroacetyl hydrazine **34**. The perchloric acid mediated cyclization at 60 °C yielded in the 2,5-bis(chloromethyl)-1,3,4-oxadiazole **35** with a moderate yield of 65%.[253] To enable the click reaction, the chloride functionalities were substituted with azide groups.[254] In the final step, the CuAAC approach was pursued to synthesize **L1**. In a water/*tert*-butanol solvent mixture, 2,5-bis(azidomethyl)-1,3,4-oxadiazole **36** and *tert*-butyl-acetylene were reacted to form the 1,2,3-triazole units on both side arms. The reactive Cu(I) species was generated *in situ* by using copper(II) sulfate pentahydrate (0.3 eq) and sodium ascorbate (0.1 eq). The ligands **31** and **32** were synthesized at room temperature in quantitative yield.[251] However, the reaction with *tert*-butylacetylene for the synthesis of **L1** did not show full conversion using these conditions. Consequently, the reaction temperature was increased to 60 °C to yield in the desired product in quantitative yield.[252] This result can be easily understood by the higher spatial demand of the *tert*-butyl group in comparison to the planar phenyl substituent, which results in a higher activation barrier for the formation of the six-membered transition state during the CuAAC (see Scheme 2 Step C).

3.1.2 Copper(II) Complexes with L1

In order to investigate the synergy between spin crossover behavior and magnetic interactions, the synthesis of dinuclear Cu(II), Fe(II) and Co(II) complexes with **L1** were envisioned. Figure 22 shows the desired coordination motif. **L1** provides two bidentate coordination pockets with nitrogen donor atoms of the 1,3,4-oxadiazole and the 1,2,3-triazoles. Two ligands should form a dinuclear complex by coordinating opposite to each other in equatioral position, while different co-ligands **L**, such as thiocyanate, coordinate axial in *trans*-position.
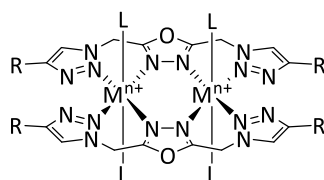
*Figure 22 Desired coordination mode of a dinuclear 3d metal complex with **L1**.*

Two different Cu(II) complexes, **C1** and **C1'**, were obtained as single crystals. The investigations of the structures and magnetic properties will be discussed in the following chapters.

The One-Dimensional Chain

By using copper(II) chloride dihydrate and the ligand **L1** in a stoichiometric reaction in an acetonitrile/methanol solvent mixture, violet single crystals of $\{[Cu^{II}(\mu\text{-}\mathbf{L1})Cl_2]\cdot MeCN\}_n$ **C1** were obtained after three days. The crystal structure was determined at 120 K. The complex **C1** crystallizes in the orthorhombic space group *Pnma*. The asymmetric unit consists of one Cu(II) ion, half of the ligand **L1**, one chlorido co-ligand and a non-coordinating acetonitrile molecule.
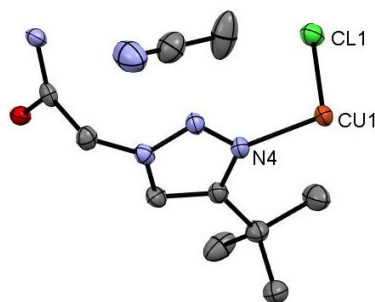
*Figure 23 Asymmetric unit of **C1** consisting one copper(II) ion, half of the ligand **L1** and one chlorido co-ligand as well as a non-coordinating acetonitrile molecule. Color code: grey – C, violet – N, red – O, orange – Cu(II), green – Cl. Hydrogen atoms are omitted for clarity. ORTEP representation with atomic displacement parameters at 50% level of probability.*

The Cu(II) ion is coordinated by the N4 nitrogen donor atoms of two ligands in *trans*-position forming a one-dimensional chain. The square planar coordination sphere is saturated by two chlorido co-ligands. The bond lengths are Cu1–N4 = 1.999(4) Å and Cu1–Cl1 = 2.2528(12) Å and the N4–Cu1–Cl1 angles (88.99(12)° and 91.01(12)°) are close to the ideal value of 90°. The one-dimensional chain has the curvature of a sine wave, where the 1,3,4-oxadiazole moiety of **L1** forms the top and bottom, respectively. It propagates in the direction of the *b*-axis as shown in Figure 24. It is noteworthy that the coordination occurs solely by the N4 nitrogen atom of the 1,2,3-triazoles and not by the bidentate pocket provided by the central 1,3,4-oxadiazole and the 1,2,3-triazole sidearms as envisioned. Either this could be a kinetic effect, because this coordination mode is preferred, or the bidentate pocket is not suitable for the coordination of Cu(II) in particular. Although Fe(II) and Co(II) ions favor an octahedral coordination sphere, this could be the reason for the missing complexes with **L1**.
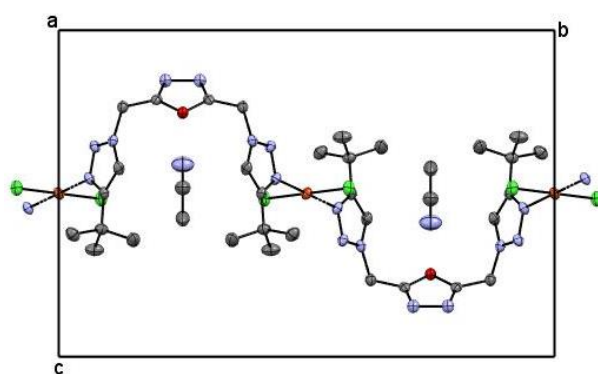
*Figure 24 One-dimensional structure of **C1**, the chain propagates in the direction of the b-axis. Color code: grey – C, violet – N, red – O, orange – Cu(II), green – Cl. Hydrogen atoms are omitted for clarity. ORTEP representation with atomic displacement parameters at 50% level of probability.*

In order to investigate the magnetic properties, the temperature-dependent magnetic susceptibility is visualized as $\chi_M T$ versus T plot in Figure 25. The molar susceptibility is calculated for one repetition unit. The experimental data were evaluated with JulX.[255]
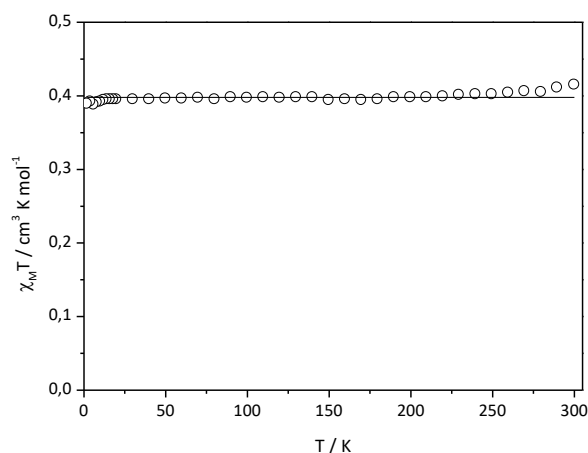
*Figure 25 Temperature-dependent magnetic behavior of **C1** for one repetition unit, $\chi_M T$ vs. T plot. ○ experimental data, – theoretical spin-only value with g = 2.06.*

For 3d metals, the orbital contribution can be neglected in most cases and the theoretical $\chi_M T$ value is calculated using the spin-only formula:

$$\mu_{eff} = g \cdot \sqrt{S(S+2)}\ \mu_B \tag{17}$$

$$\chi_M T = \frac{N_A \mu_B^2}{3k_B} \cdot (\mu_{eff})^2 = \left(\frac{\mu_{eff}}{2.82787}\right)^2 \tag{18}$$

The $\chi_M T$ value of 0.40 cm^3 K mol^{-1} is slightly higher than the expected spin-only value of $\chi_M T = 0.38$ cm^3 K mol^{-1} with $s = 1/2$ and g = 2.0. However, this can be explained by a higher anisotropic g-value of 2.06 due to the interaction of the singly occupied $d_{x^2-y^2}$ orbital with the p-orbitals of the ligand and the distorted surrounding.[256,257] The constant value over the whole temperature range indicates magnetically isolated Cu(II) ions, which is in good agreement with the structure of **C1** as the Cu–Cu distances are large with 10.072 Å and the ligand does not offer a conjugated system for a magnetic exchange pathway.

The Dinuclear Complex

As the crystals of **C1** were kept in the mother liquor for further investigations, the violet crystals turned into green needles after two days, which were suitable for single crystal X-ray crystallography. The obtained dinuclear complex [Cu$_2^{II}$(**L1'**)Cl$_2$(MeOH)$_2$] **C1'** crystallizes in the orthorhombic space group *Pbca* (120 K).
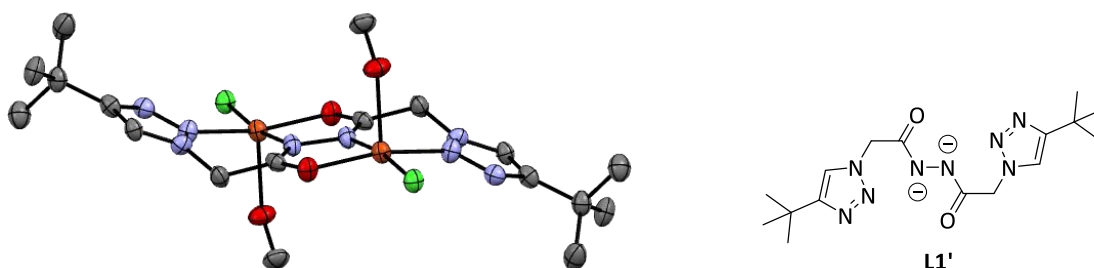
*Figure 26 Left: Molecular structure of the dinuclear Cu(II) complex **C1'**. Color code: grey – C, violet – N, red – O, orange – Cu(II), green – Cl. Hydrogen atoms are omitted for clarity. ORTEP representation with atomic displacement parameters at 50% level of probability. Right: Molecular structure of the ring-opened ligand **L1'**.*

The molecular structure of the complex contains the ligand **L1'** which has formed by a ring opening of the 1,3,4-oxadiazole of **L1** (see Scheme 9). The ligand **L1'** provids two tridentate coordination pockets for the two Cu(II) ions. Each metal ion is additionally coordinated by a chlorido co-ligand and methanol molecule forming a square pyramidal coordination sphere where the solvent molecule is located in the apical position. It is further interesting, that the reaction from **C1** to **C1'** causes loss of the non-coordinating acetonitrile and even the coordination of a methanol molecule which was not present in the structure of **C1**.

Furthermore, the molecular structure of **C1'** displays a strong bend of the 1,2,3-triazoles of 29.63° in relation to the planar central Cu–N–N–Cu moiety. Ligand **L1'** is much more flexible than **L1** because of the rigid 1,3,4-oxadiazole, hence the coordination of two metal ions with **L1** would cause a larger deformation of the side arms. The strong deviation could explain the non-existent dinuclear complexes with **L1**.
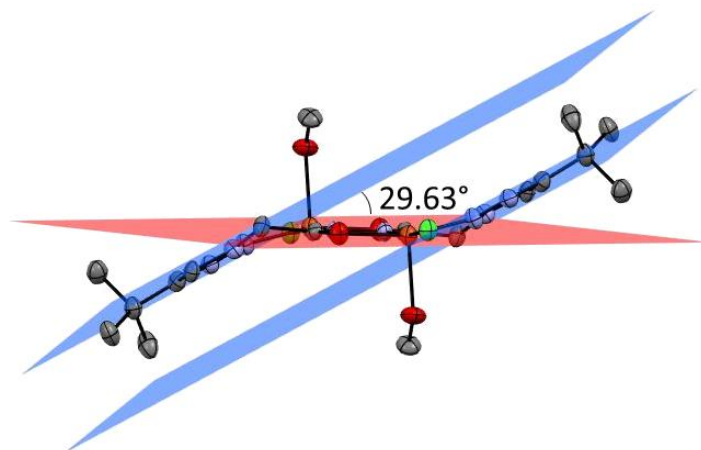

*Figure 27 Molecular structure of **C1'**, highlighting the deformation of the 1,2,3-triazole side arms. Color code: grey – C, violet – N, red – O, white – H, orange – Cu(II), green – Cl. ORTEP representation with atomic displacement parameters at 50% level of probability. The red plane is referred to the planar Cu–N–N–Cu moiety and the blue plane to the 1,2,3-triazoles.*

Ligand **L1'** has formed by a ring-opening reaction of the central 1,3,4-oxadiazole unit of **L1** leading to a central twice negatively charged [R–(CO)–N–N–(CO)–R] moiety. Ring-opening reactions of 1,3,4-oxadiazoles are known in literature and well investigated. These reactions normally occur under acidic or basic conditions.[258] In this case, it is assumed, that the copper(II) chloride acts as a Lewis acid which catalyzes the ring-opening reaction.
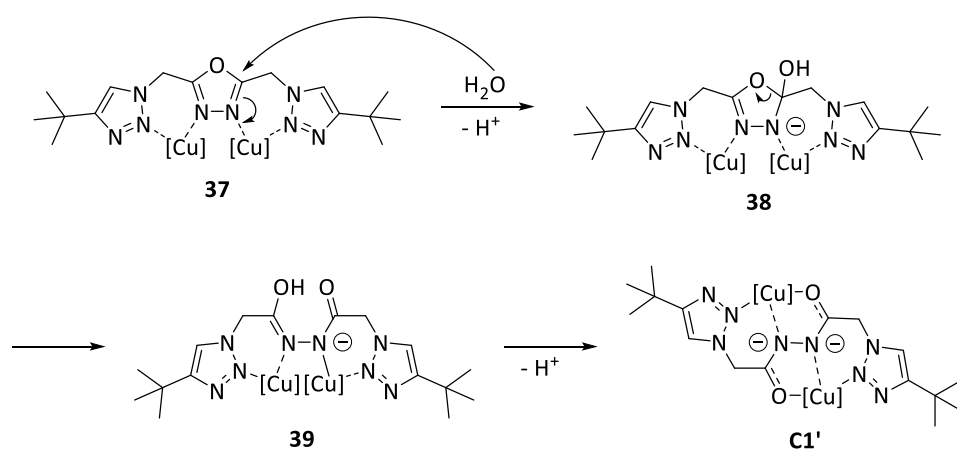
*Scheme 9 Putative mechanism of the ring-opening reaction of **L1** forming **L1'** and **C1'**.*

Although the structure of $\{[Cu^{II}(\mu\text{-}\textbf{L1})Cl_2]\cdot MeCN\}_n$ **C1** shows the coordination of the Cu(II) ion to the N4 donor atom of the 1,2,3-triazole, in solution various complexes could be present. It is assumed, that two Cu(II) ions are chelated by the bidentate pocket provided by the 1,2,3-triazole and the 1,3,4-oxadiazole (**37**). This coordination mode intensively reduces the electron density of the electron-rich 1,3,4-oxadiazole, especially at the carbon atom. The reaction solution contains water due to the utilized copper(II) chloride dihydrate, the non-dried solvents and the open-flask conditions. The water molecule adds into the activated imine bond forming hemiacetal **38**, that further fragments into the ring opened ligand **L1'** (**39**), which is twice deprotonated to act as dianionic ligand. Rotation of the N–N bond finally leads to the molecular structure of **C1'**.

The complex molecule of **C1'** is neutral as the four positive charges of the two Cu(II) ions are compensated each by two chlorido co-ligands and the twice negatively charged ligand **L1'**. The complex is centrosymmetric with an inversion center located within the hydrazine bond. The base of the square pyramidal coordination sphere of the two Cu(II) ions is formed by the N1 donor atom of the 1,2,3-triazole, the N14 of the hydrazine unit, the amide's O12 and the chlorido co-ligand. In apical position, the O14 donor atom is provided by the methanol molecule.
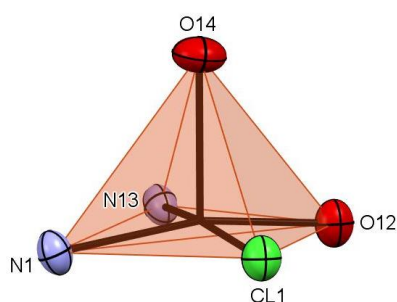
*Figure 28 Square pyramidal coordination sphere of the Cu(II) ion in **C1'**. Color code: violet – N, red – O, green – Cl. ORTEP representation with atomic displacement parameters at 50% level of probability.*

*Table 1 Selected bond lengths and angles of **C1'** at 120 K.*

		C1'
Cu1–L [Å]	Cu1–Cl1	2.237(2)
	Cu1–N1	2.033(6)
	Cu1–N13	1.937(6)
	Cu1–O12	1.985(5)
	Cu1–O14	2.245(5)
L–Cu1–L [°]	O14–Cu1-Cl1	94.38(16)
	O14–Cu1–O12	95.3(2)
	O14–Cu1–N13	92.8(2)
	O14–Cu1–N1	99.7(2)

The Cu–L bond lengths and L–Cu–L angles are listed in Table 1. Due to the rigidity of the ligand, the Cu–O and Cu–N bond lengths of the square base are short with Cu1–N13 = 1.937(6) Å, Cu1–O12 = 1.985(5) Å and Cu1–N1 = 2.033(6) Å. The distance to the monodentate coordinating chlorido co-ligand is much larger with 2.237(2) Å. The Cu1–O14 bond length is in the same range with 2.245(5) Å. The Cu(II) ion coordinates out-of-plane as the O14–Cu1–L angles are larger than 90°. The N13–N13 and C11–O12 bond distances are 1.410(11) Å and 1.282(9) Å, which indicates a N–N single and a C=O double bond.[259,260] The bond length of C11–N13 = 1.316(9) Å is between a single and double bond. This indicates that the negative charge is delocalized over the whole N–C–O moiety with a high electron density on the nitrogen N13 atom. The two Cu(II) ions are bridged by the hydrazine bond with a Cu–Cu distance of 4.623 Å.
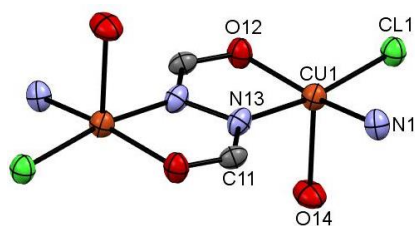
*Figure 29 Central coordination mode of **C1'**. Color code: grey – C, violet – N, red – O, orange – Cu(II), green – Cl. Hydrogen atoms are omitted for clarity. ORTEP representation with atomic displacement parameters at 50% level of probability.*

Besides, there are O–H···Cl short contacts between the complex molecules provided by the coordinated methanolic hydroxy group and the chlorido co-ligand of the next complex. The bond lengths are O–Cl = 3.123 Å and H–Cl = 2.288 Å and the O–H···Cl angle is 160.43°. This results in a one-dimensional chain coordination polymer connected by two hydrogen bonds.
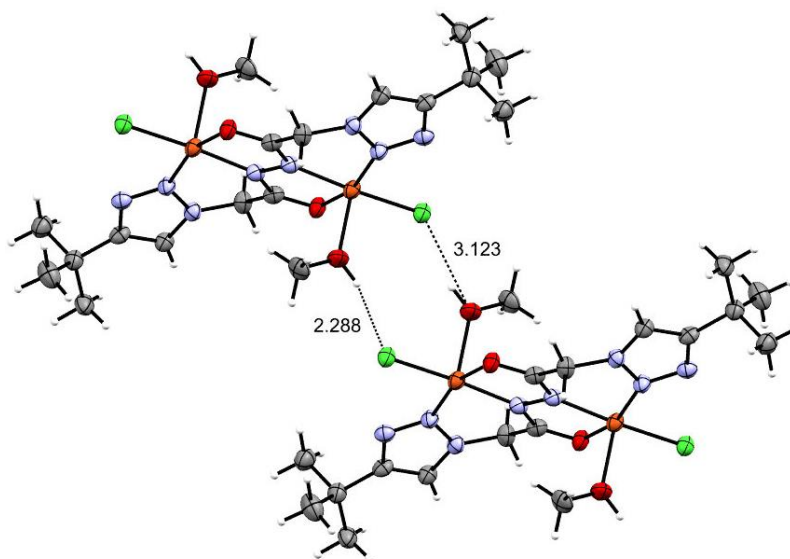
*Figure 30 Short O–H···Cl contacts between the dinuclear **C1'** complexes. Color code: grey – C, violet – N, red – O, white – H, orange – Cu(II), green – Cl. ORTEP representation with atomic displacement parameters at 50% level of probability. Dashed lines represent the O–H···Cl short contacts between the complex molecules.*

The temperature-dependent $\chi_M T$ product of **C1'** is shown in Figure 32. At 300 K, the $\chi_M T$ value amounts 0.87 cm³ K mol⁻¹. This is slightly higher than the spin-only value of $\chi_M T = 0.75$ cm³ K mol⁻¹ for two Cu(II) ions with $s_1 = s_2 = 1/2$, but in good agreement with the literature assuming a larger g-value.[256,257,261] The $\chi_M T$ value slowly decreases towards 100 K and then strongly diminishes to zero for lower temperatures, which is an indication for strong antiferromagnetic exchange coupling between the two Cu(II) ions. Exchange coupling leads to the $S = 0$ and $S = 1$ states where the former describes the ground state in case of an

antiferromagnetic interaction. The energy gap $\Delta E = E(S = 1) - E(S = 0)$ amounts $2J$.[26] At low temperatures, only the ground state is thermally populated which leads to a $\chi_M T$ value of zero.
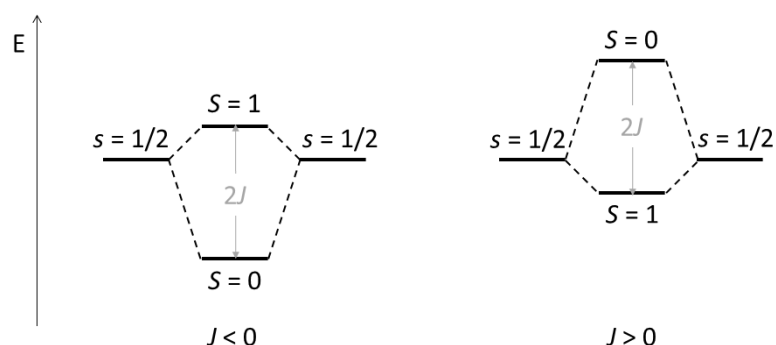
Figure 31 Energy diagram of two coupled spins with s = 1/2. Left: Antiferromagnetic coupling (J < 0) with the S = 0 ground state. Right: Ferromagnetic coupling (J > 0) with the S = 1 ground state. The energy difference between the S = 0 and S = 1 states is 2J.

This is confirmed by the χ_M versus T plot (see Figure 33) as the magnetic susceptibility rapidly decreases for low temperatures. The further rise in the range of $12 - 2$ K hints to an impurity which could be explained by an incomplete reaction from **C1** to **C1'**. The $\chi_M T$ and χ_M versus T data were fitted with the program PHI.[262] The anisotropic g-factor with g_x, g_y and g_z as well as the exchange coupling were fitted using the following Hamiltonian:[26]

$$\hat{H} = -2J \cdot S_1 \cdot S_2 - g\mu_B HS \qquad (19)$$

with $g = (g_x + g_y + g_z)/3$. The Heisenberg-Dirac-van Vleck Hamiltonian on the left describes the isotropic exchange coupling between the two spins of the Cu(II) ions[263] and the right part is ascribed to the Zeeman effect as a small magnetic field of $H = 1000$ Oe is applied.
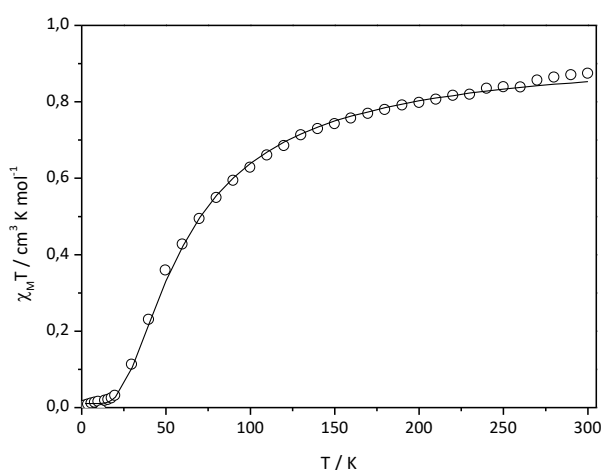
*Figure 32 Temperature-dependent magnetic behavior of **C1'**, $\chi_M T$ versus T plot. ○ experimental data, − fit including exchange interaction and paramagnetic impurity.*
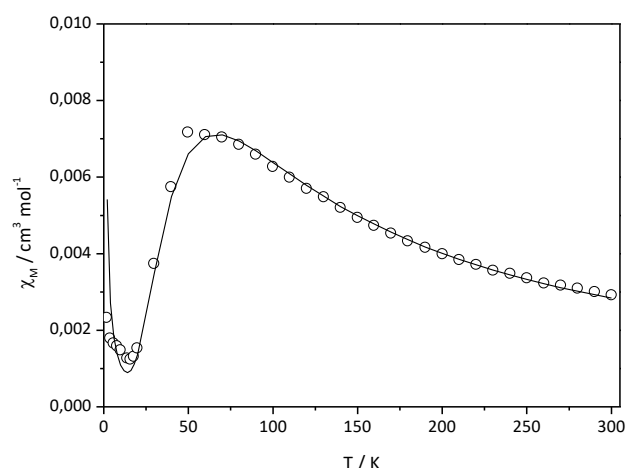
*Figure 33 Temperature-dependent magnetic behavior of **C1'**, χ_M versus T plot. ○ experimental data, − fit including exchange interaction and paramagnetic impurity.*

The paramagnetic impurity is added to the susceptibility of the sample by IMP·χ_{IMP}, where IMP is the molar fraction and χ_{IMP} is the field- and temperature-dependent magnetic susceptibility of the impurity:[262]

$$\chi = \chi_{calc} + IMP \cdot \chi_{IMP} \tag{20}$$

The impurity is assumed to contain pure spin centers with $s = 1/2$ and g = 2.0. The fitted values are $J = -37.53(36)$ cm^{-1}, g_x = 2.368(12), g_y = 2.400(6), g_z = 2.000(6) and IMP = 2.89(5)%. The residual R is calculated by the sum of squares approach:

$$R = \sum_{i=1}^{points} (\chi_{exp} - \chi_{calc})^2 \tag{21}$$

and reaches $R = 3.56 \cdot 10^{-3}$ for the best fitting. The strength and sign of the exchange interaction depends on several parameter such as the geometry, the ligand type, the bond lengths, and angles.[264] In case of **C1'**, the coordination geometry is distorted square pyramidal which leads to an energetic preference of the d-orbitals with z-character, thus $d_{x^2-y^2}$ being the singly occupied magnetic orbital.[257] The Cu1–N13 bond length is short with 1.937(6) Å providing a large orbital overlap and strong exchange interaction. In contrast to that, the N13–N13 distance is 1.410(11) Å and larger than literature known comparable pyrazole bridged complexes leading to a weaker exchange coupling.[265] In literature many examples of dinuclear Cu(II) complexes exhibiting a N–N bridge provided by the aromatic diazine,[266] pyridazine,[267] or pyrazole[265] moieties as well as aliphatic open chain diazine ligands are reported.[266] The Cu–N–N and Cu–N–N–Cu torsion angles seem to be the crucial parameters for the description of the superexchange in these complexes. In **C1'**, the Cu–N–N–Cu torsion angle is 180° giving rise to a strong antiferromagnetic interaction.[268] For example the Cu(II) complex [Cu$_2$(pahapH)(dpa)$_2$](NO$_3$)$_4$·4H$_2$O (pahap = picolinamide azine, Hdap = 1,3-diamino-2-propanol) provides a torsion angle of 175.7° and antiferromagnetically couples with $J = -93.2$ cm^{-1}.[267] Hence, for **C1'** the coupling of $J = -37.53$ cm^{-1} should be stronger. The difference to the mentioned example could be found in the type of the ligands as **L1'** is a flexible aliphatic twice

negatively charged ligand in contrast to the mostly rigid neutral aromatic ligands reported in the literature. As discussed before, the negative charge is delocalized over the whole N–C–O moiety of the ligand, which can be described as a mixture of the two extreme cases shown in Figure 34, where the negative charge is completely located on the oxygen (**40**) or on the nitrogen atom (**41**).
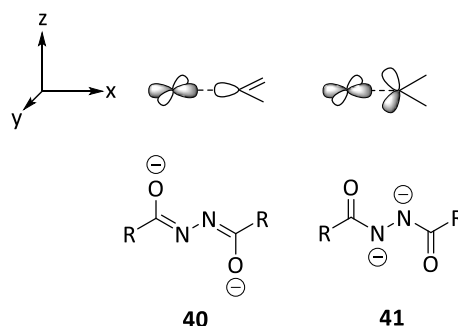

*Figure 34 Localization of the $d_{x^2-y^2}$ orbital with respect of the free electron pair of the nitrogen donor atom. Left: iminol form **40**, the free electron pair is directed towards the $d_{x^2-y^2}$-orbital along the x-axis providing a large overlap and strong exchange interaction. Right: amide form **41**, the two electron pairs with z-character show minor overlap with the $d_{x^2-y^2}$-orbital providing a weak interaction.*

The former describes the iminol form with a C=N double bond and a negatively charged oxygen atom. The free electron pair of the nitrogen is localized within the *xy* plane of the N–C–O moiety due to the sp²-hybridization. The Cu–N–N angle is 113.64° and close to the perfect 120° leading to an almost 180° angle between the $d_{x^2-y^2}$ orbital and the lone pair of the nitrogen donor atom, which results in strong antiferromagnetic exchange interaction.[26,269,270] The second case describes the amide form with a C=O double bond and a negatively charged nitrogen atom. This results in a sp³-hybridization due to the additional free lone pair of the nitrogen. In this situation, the two lone pairs are directed above and below the *xy* plane, consequently having *z*-character. Even with the perfect Cu–N–N angle of 120° and Cu–N–N–Cu torsion angle of 180°, the $d_{x^2-y^2}$ orbital of the Cu(II) ion and the free lone pairs show only minor overlap, which strongly decreases the strength of the antiferromagnetic coupling. For **C1'**, the situation is assumed to be somewhere between the two cases, thus causing a less pronounced exchange interaction than primarily expected.[267]

3.1.3 Evaluation of Ligands L1 and L1'

Although hitherto no Fe(II) or Co(II) complexes with **L1** could be synthesized, the investigations on both copper(II) complexes reveal interesting insight into the structure and the magnetic interactions of ligands **L1** and **L1'**. No magnetic exchange was observed for complex {[Cu^{II}(μ-**L1**)Cl$_2$]·MeCN}$_n$ **C1** due to the coordination *via* the N4 donor atom of the 1,2,3-triazoles

and the large Cu–Cu distance. In contrast, the dinuclear complex $[Cu_2^{II}(\textbf{L1'})Cl_2(MeOH)_2]$ **C1'** features antiferromagnetic exchange interaction, which could be transferred to the corresponding Fe(II) or Co(II) spin crossover complexes with a central **L1'** ligand. Furthermore, the molecular structure of complex **C1'** already shows a large distortion concerning the methylene bridge of the ligand **L1'**. The 1,3,4-oxadiazole in **L1** would cause an even higher strain which explains the lacking dinuclear transition metal complexes with **L1**, thus making **L1'** more suitable for the study of the SCO complexes. Besides, the Cu(II) complex **C1'** shows the possibility to form the LS Fe(II) or Co(II) species as the observed Cu(II)–L bond lengths towards the donor atoms of **L1'** are shorter than 2.0 Å. In contrast, the distortion of the ligand would facilitate the formation of the HS state, thus providing a suitable geometry for both states.

3.2 Mono- and polynuclear 3d Metal Complexes

The ligand 2,2'-bismethyl-5,5'-di-1,3,4-thiadiazole **L2** was envisioned to form mono- and polynuclear transition metal complexes with Cu(II), Fe(II) and Co(II) ions. The possibility to chelate the metal ion *via* the bidentate pocket (Figure 35a+b) as well as to bridge two metal ions *via* end-to-end coordination (Figure 35c) made ligand **L2** a suitable candidate to investigate the synthesis of variable supramolecular coordination compounds. Depending on the coordination mode, a magnetic exchange coupling could occur *via* the N–N bridge of one 1,3,4-thiadiazole moiety or the entire ligand.
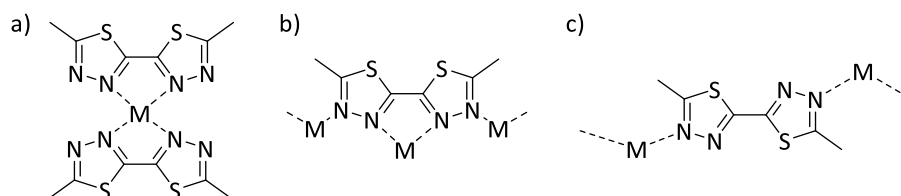
*Figure 35 Possible coordination modes of mono- and polynuclear transition metal complexes with ligand **L2**. a) chelating mode, b) chelating and bridging mode and c) bridging mode by end-to-end coordination.*

Next to the synthesis of the ligand, the structural and magnetic aspects of the appropriate Cu(II) model complex were investigated to get an insight into the intramolecular interactions. Furthermore, the versatile multi-dimensional structures of the obtained Fe(II) complexes as well as the magnetic behavior of the Co(II) coordination chain are discussed in the following.

3.2.1 The bis-1,3,4-Thiadiazole Ligand System

The ligand **L2** was synthesized in three steps with straightforward reaction and purification methods. Starting from diethyl oxalate **42** and hydrazine hydrate, the oxalyl dihydrazide **43** was obtained in quantitative yield.[271] The addition of acetic anhydride in a water/ethanol solvent mixture led to the *N,N'*-diacetyloxal dihydrazide **44** with a good yield of 78%.[272] The conversion to 2,2'-bismethyl-5,5'-di-1,3,4-thiadiazole **L2** with tetraphosphorus decasulfide is already known in the literature.[273,274] In this thesis, the yield could almost be doubled to 68% by using 2.2 equivalents of the Lawesson's reagent under inert atmosphere.
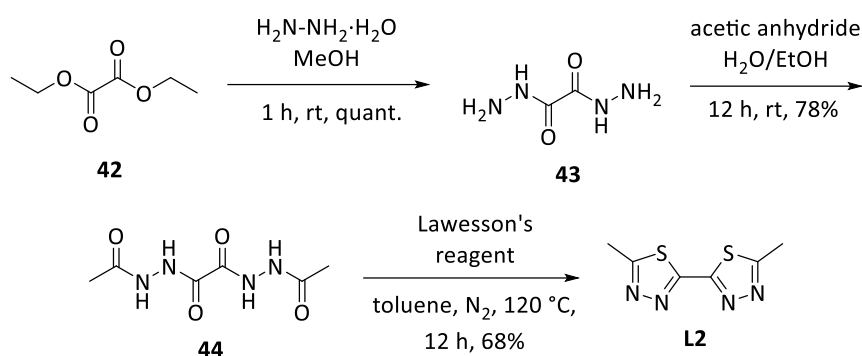
Figure 36 Three-step synthesis route of L2.[271,272]

To synthesize 3d metal complexes, the ligand was reacted with various Cu(II), Fe(II) and Co(II) salts. All reactions with Fe(II) were performed under inert atmosphere in order to prevent the oxidation of Fe(II) to Fe(III). Due to the solubility properties of **L2**, the reactions were performed in dichloromethane, chloroform, or solvent mixtures. Solvents such as alcohols or acetonitrile mostly produced insoluble precipitates probably because the directly formed polynuclear complexes are not soluble in these polar solvents. However, reactions in dichloromethane/ acetone mixtures yielded in the formation of single crystals. The Cu(II) complex **C2**, the four different Fe(II) complexes **C3**, **C3'**, **C4** and **C5** as well as one Co(II) complex **C6** were obtained as crystals suitable for single crystal X-ray diffraction. The magneto-structural properties of the Cu(II) complex **C2** are presented hereafter. Based on these results, the Fe(II) complexes were investigated structurally. Due to the insufficient material, no magnetic measurements could be performed. Finally, the structural and magnetic properties of the Co(II) complex **C6** are discussed.

3.2.2 The Copper(II) Complex: A Two-Dimensional Network

The Cu(II) complex {[Cu^{II}(μ-**L2**)$_3$(H_2O)((CH_3)$_2$CO)](ClO$_4$)$_2$(H_2O)}$_n$ **C2** was synthesized by dissolving the ligand **L2** in dichloromethane and adding to a solution of copper(II) perchlorate hexahydrate in acetone. Intensive blue single crystals have formed after several hours. The crystal structure was investigated at 173 K. The complex crystallizes in the triclinic space group $P\bar{1}$. The Cu(II) ion is coordinated by three ligands **L2**, one water and one acetone molecule, forming a square pyramidal coordination sphere. Two non-coordinating perchlorate anions per Cu(II) ion balancing the charge and one lattice water molecule are found within the structure.
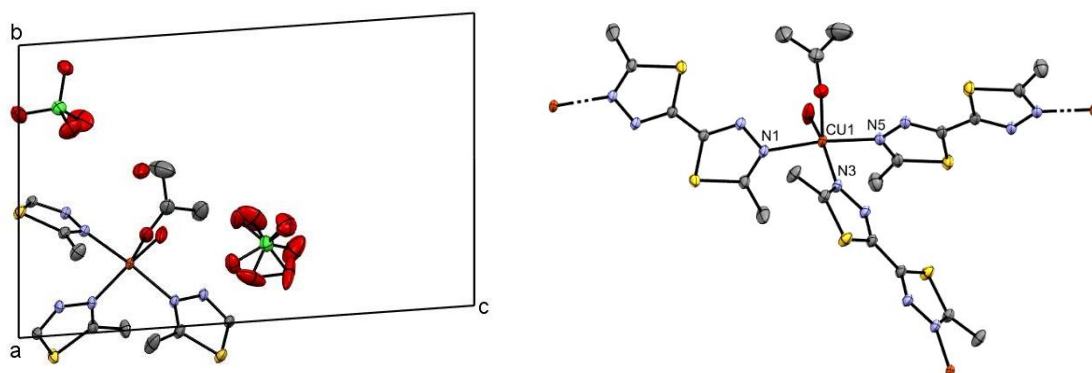
*Figure 37 Left: Asymmetric unit of **C2**. Right: One repetition unit of **C2** highlighting the three bridging ligands **L2** to form the two-dimensional network. Color code: grey – C, violet – N, yellow – S, red – O, orange – Cu(II). Hydrogen atoms are omitted for clarity. ORTEP representation with atomic displacement parameters at 50% level of probability.*

The asymmetric unit represents one repetition unit of the coordination polymer with one Cu(II) ion and three 'half' ligands as an inversion center is found in each C–C bond of the ligand molecules. It is noticeable, that **L2** solely coordinates *via* the terminal nitrogen donors and functions as briding unit between two Cu(II) ions. The two-dimensional network has formed within the *bc* plane which is visualized in Figure 38.
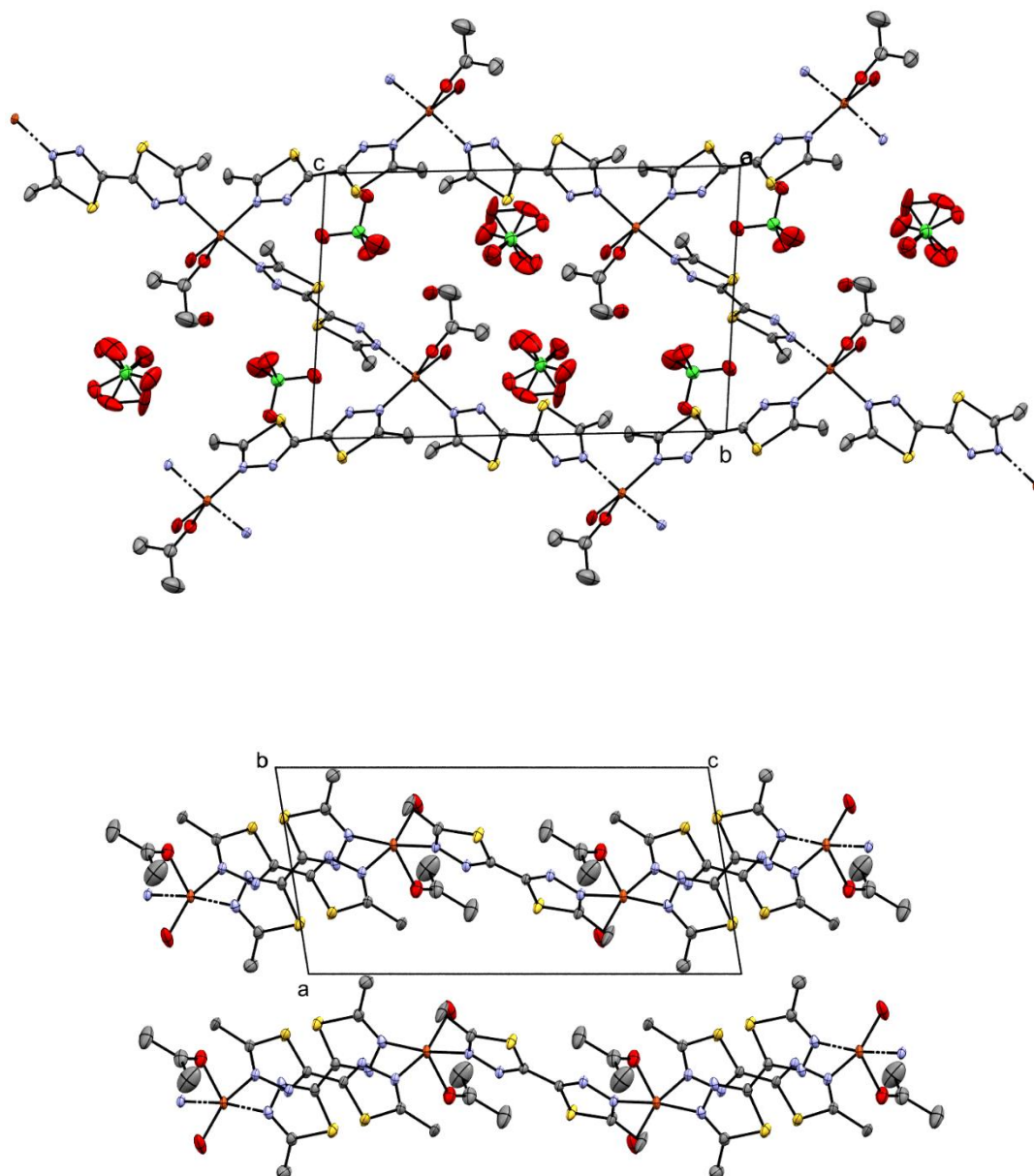
*Figure 38 Top: Top view of the two-dimensional network of **C2** highlighting the cavity. Hydrogen atoms are omitted for clarity. Bottom: Side view of the two-dimensional network of **C2**. Hydrogen atoms, perchlorate anions and solvent molecules are omitted for clarity. Color code: grey – C, violet – N, yellow – S, red – O, orange – Cu(II). ORTEP representation with atomic displacement parameters at 50% level of probability.*

Within the cavity, the opposite lying repetition units are connected *via* the coordinated water molecules forming a three-dimensional hydrogen bonding network. The hydrogen bonds between the water molecules and perchlorate anions are illustrated in Figure 39.
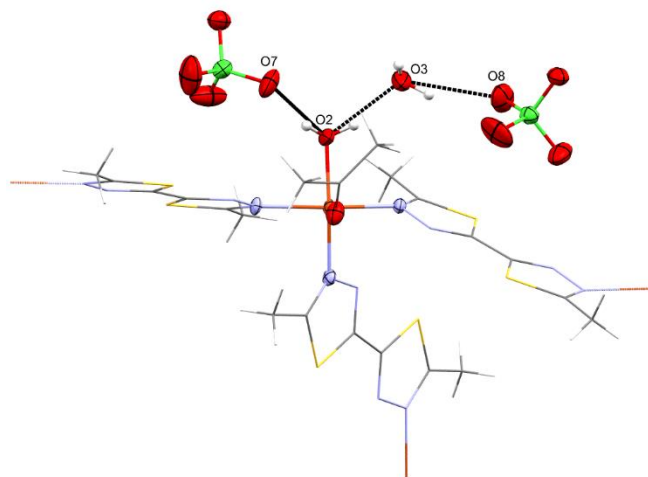
*Figure 39 Molecular structure of **C2** highlighting the the hydrogen bonds between the water molecules and perchlorate anions within the cavity. Color code: grey – C, violet – N, yellow – S, red – O, orange – Cu(II). ORTEP representation with atomic displacement parameters at 50% level of probability of the relevant atoms.*

The penta-coordinated Cu(II) ions form a square pyramidal coordination sphere. The three ligands and the water molecule form the base and the oxygen donor atom of the acetone molecule is located in the apical position of the pyramide. The bond lengths of the square base are in the range of 1.9512(15) – 2.0282(14) Å. The Cu1–O1 distance is larger with 2.1942(14) Å leading to an elongation of the pyramide. The O1–Cu1–L angles are in the range of 91.34(6)° to 101.25(6)°, much higher than 90°, leading to an out-of-plane coordination of the Cu(II) ion.
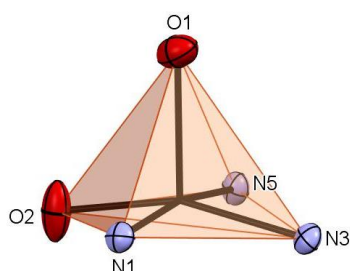
*Figure 40 Square pyramidal coordination sphere of the Cu(II) ion in **C2**. Color code: violet – N, red – O. ORTEP representation with atomic displacement parameters at 50% level of probability.*

*Table 2 Selected bond lengths and angles of **C2** at 120 K.*

		C2
	Cu1–O1	2.1942(14)
	Cu1–O2	1.9512(15)
Cu1–L [Å]	Cu1–N1	2.0278(14)
	Cu1–N3	2.1068(15)
	Cu1–N5	2.0083(14)
	O1-Cu1-O2	99.74(7)
L–Cu1–L [°]	O1-Cu1-N1	91.34(6)
	O1-Cu1-N3	101.25(6)
	O1-Cu1-N5	99.24(6)

The temperature-dependent magnetic susceptibility is plotted as $\chi_M T$ versus T plot for one repetition unit in the temperature range of 2 – 100 K in Figure 41. The comparable large $\chi_M T$ value of 0.52 cm³ K mol^{-1} can be explained by the higher g-value of 2.35 caused by the square pyrdamidal coordination sphere and the pronounced axial elongation.[261] No intramolecular interaction between the Cu(II) ions is observed as the $\chi_M T$ value is constant over the whole temperature range.
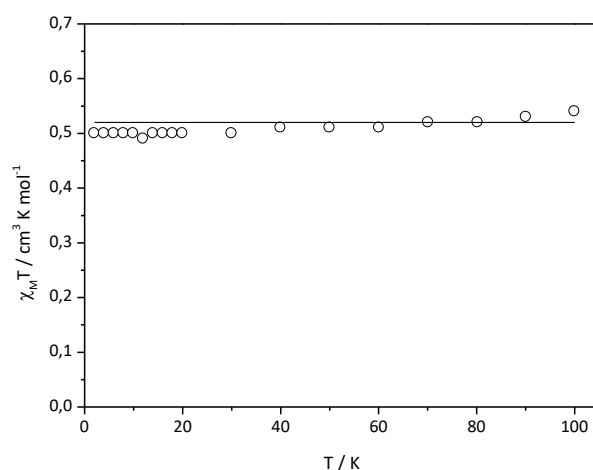
*Figure 41 Temperature-dependent magnetic behavior of **C2**, $\chi_M T$ vs. T plot. ○ experimental data, – theoretical spin-only value with g = 2.35.*

In this complex, the coordination of the Cu(II) ions solely occurs *via* the bridging mode of the ligand **L2**. Regarding the relevant Cu1–N–N and Cu1–N–N'–Cu1' angles, which are listed in Table 3, the values of 114.04(11) to 120.63(11)° and 180° provide a suitable orbital overlap between the $d_{x^2-y^2}$ orbital of the Cu(II) ion and the p-orbital of the nitrogen donor atoms N1, N3 and N5. The missing magnetic exchange coupling is therefore presumably based on the large bond lengths of Cu1–N > 2.0 Å and the large Cu1–Cu1' distances (> 9.2 Å) over the extended ligand system.[275]

*Table 3 Selected bond lengths and angles of **C2** at 173 K describing the magnetic exchange interaction.*

Angles [°]		Torsion angles [°]	
Cu1–N1–N2	120.63(11)	Cu1–N1–N1'–Cu1'	180
Cu1–N3–N4	114.15(11)	Cu1–N3–N3'–Cu1'	180
Cu1–N5–N6	116.04(11)	Cu1–N5–N5'–Cu1'	180
Bond lengths [°]			
Cu1–Cu1'(N1)	9.476	Cu1–N1	2.0278(14)
Cu1–Cu1'(N3)	9.293	Cu1–N3	2.1068(15)
Cu1–Cu1'(N5)	9.283	Cu1–N5	2.0083(14)

For corresponding Fe(II) and Co(II) complexes with a similar bridging coordination of ligand **L2**, the intramolecular exchange interaction is negligible. The strength of the interaction *via* the M–N–N–M pathway could not be determined as no appropriate Cu(II) complex was obtained throughout the study.

3.2.3 Iron(II) Complexes: A Variety of 0D, 1D and 2D Coordination Networks

In order to synthesize 3d metal complexes with possible spin crossover behavior, the ligand **L2** was reacted with various Fe(II) salts. The reaction of **L2** and iron(II) perchlorate yielded in the yellow co-crystallizing block and plate shaped crystals {[Fe^{II}(*trans*-μ-**L2**)$_2$(H$_2$O)$_4$](ClO$_4$)$_2$·2H$_2$O}$_n$ **C3** and {[Fe^{II}(μ-**L2**)$_4$(H$_2$O)$_2$](ClO$_4$)$_2$·**L2**}$_n$ **C3'** after one day by evaporation of the solvent. Iron(II) thiocyanate was *in situ* generated by the reaction of iron(II) perchlorate and potassium thiocyanate in acetone which was layered over a solution of **L2** in dichloromethane. Evaporation of the solvent gave complex {Fe^{II}(*trans*-μ-**L2**)$_2$(**L2**)(SCN)$_2$}$_n$ **C4** as red single crystals. Complex [Fe^{II}(**L2**)$_3$](BF$_4$)$_2$·3CHCl$_3$ **C5** was obtained by the reaction of the ligand and iron(II) tetrafluoroborate in a dichloromethane/acetone solvent mixture. After evaporation of the solvent, brown single crystals were obtained. Due to the co-crystallization of **C3/C3'** and the low yields of **C4** and **C5**, the crystal structures but not the magnetic properties could be determined.
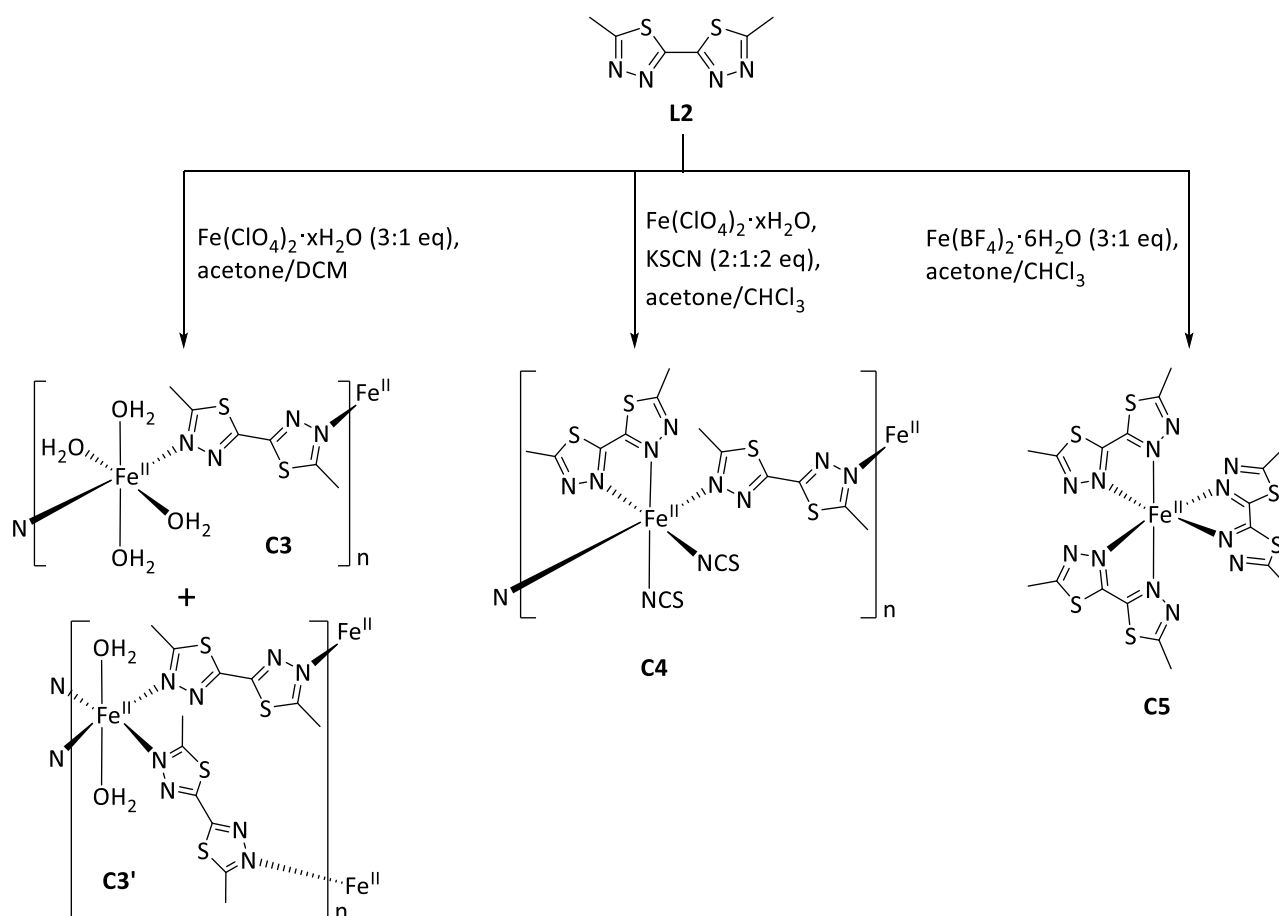
*Scheme 10 Overview of the reactions with Fe(II) salts and **L2** forming the complexes **C3**, **C3'**, **C4** and **C5**.*

Complex C3

Iron(II) perchlorate hexahydrate was reacted with **L2** in a dichloromethane/acetone solvent mixture and yielded in the co-crystallizing block shaped crystals of **C3** and plates of **C3'**. The complex {[Fe^{II}(*trans*-μ-**L2**)$_2$(H$_2$O)$_4$](ClO$_4$)$_2$·2H$_2$O}$_n$ **C3** crystallizes in the monoclinic space group *P*2$_1$/*c* (120 K). The structure can be described as a one-dimensional chain, where the Fe(II) ions are bridged by the twisted ligand **L2** coordinating in *trans*-position. **L2** is planar with a twisting angle of N2–C9–C9–N2 = 180°, similar to the Cu(II) complex **C2**. Four water molecules saturate the octahedral coordination sphere. The charge is balanced by two non-coordinating perchlorate anions per Fe(II) ion. One lattice water molecule is present in the structure.
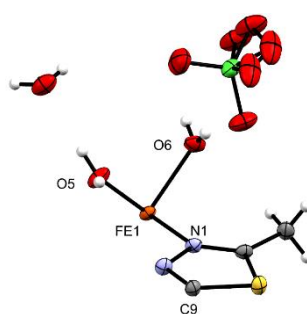
*Figure 42 Asymmetric unit of **C3**. Color code: grey – C, violet – N, yellow – S, red – O, white – H, orange – Fe(II), green – Cl. The perchlorate anion is disordered. ORTEP representation with atomic displacement parameters at 50% level of probability.*

The repetition unit of the one-dimensional coordination chain consists of the Fe(II) center, one ligand and four coordinated water molecules. Due to an inversion center within the C9–C9 bond and the Fe(II) ion, the asymmetric unit consists of half the repetition unit as well as one non-coordinating perchlorate anion and the lattice water.
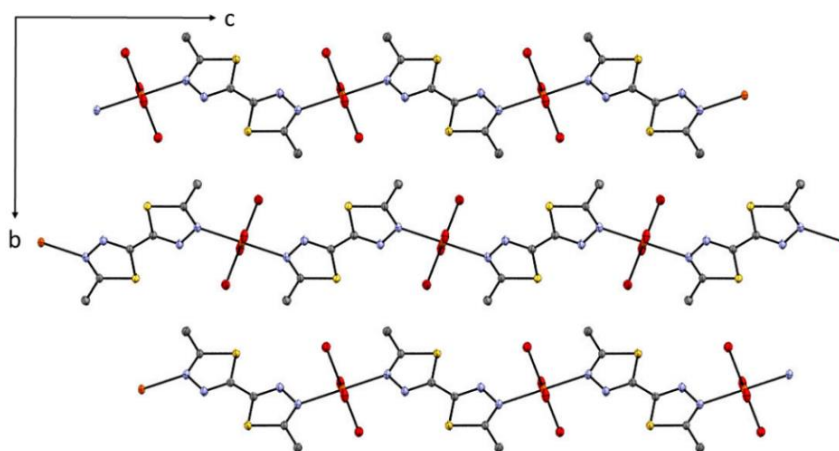
*Figure 43 One-dimensional coordination chains of **C3** propagating in the direction of the c-axis. Color code: grey – C, violet – N, yellow – S, red – O, orange – Fe(II). Hydrogen atoms, perchlorate anions and non-coordinating water molecules are omitted for clarity. ORTEP representation with atomic displacement parameters at 50% level of probability.*

The one-dimensional coordination chains propagate parallel to the *c*-axis and are aligned within the *bc* plane. Figure 44 shows the cross section of the one-dimensional coordination chains. These align in a zigzag manner with respect to the ligands. The twist angle between the ligands of two neighboring chains amounts 115.16°. The cross section further shows the alternation of the layers of the coordination chains within the *bc* plane and the layers containing the non-coordinating perchlorate anions and water molecules.
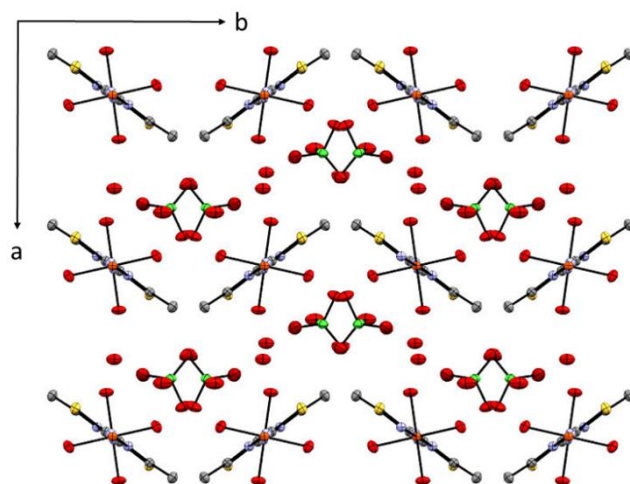
*Figure 44 Cross section of the one-dimensional chain structure of **C3**. Color code: grey – C, violet – N, yellow – S, red – O, orange – Fe(II), green – Cl. Hydrogen atoms are omitted for clarity. ORTEP representation with atomic displacement parameters at 50% level of probability.*

The coordination chains are connected by several hydrogen bonds *via* the non-coordinating perchlorate anions and water molecules as visualized in Figure 45. The extended hydrogen bonds connect the single coordination chains to a three-dimensional network.
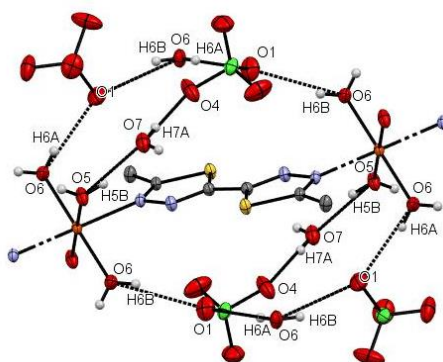
*Figure 45 Hydrogen bond network of **C3** forming a cage around the coordinated **L2**. Color code: grey – C, violet – N, yellow – S, red – O, orange – Fe(II), green – Cl, white – H. For clarity, only the relevant hydrogen atoms are shown and the relevant atoms labelled. ORTEP representation with atomic displacement parameters at 50% level of probability.*

The Fe(II) ions are hexa-coordinated forming an octahedral coordination sphere with a $\{N_2O_4\}$ donor set. As shown in Table 4, the Fe1–N1 distance is 2.1955(14) Å and the Fe1–O bond lengths are shorter with 2.0909(14) Å and 2.1343(15) Å, forming a slight rhombic distorted octahedron. The long bond lengths hint to the HS state of the Fe(II) ion. The *cis*-angles are close to 90° and accumulate to a slight deviation with the octahedral distortion parameter being $\Sigma_0 = 18.68°$. This is further confirmed by continuous shape measurements (CShM), performed with the program SHAPE 2.1,[276] as the divergence of the perfect octahedron is very low with CShM = 0.09.
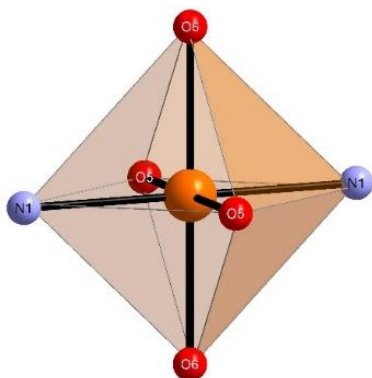
Figure 46 The $\{FeN_2O_4\}$ octahedron of **C3** compared to the perfect polyhedron calculated by CShM. Color code: violet – N, red – O, orange – Fe(II).

Table 4 Selected bond lengths and angles of **C3** at 120 K.

		C3
Fe–L [Å]	Fe1–N1	2.1955(14)
	Fe1–O5	2.0909(14)
	Fe1–O6	2.1343(15)
L–Fe–L [°]	N1–Fe1–O5	88.34(6)
	N1–Fe1–O6	92.40(6)
	O5–Fe1–O6	90.61(6)
Σ_0 [°]		18.68
CShM		0.09

In the case of **C3**, the deviation is relatively small compared to the typical values for $\{Fe–N_6\}$ spin crossover complexes as the majority consists of bi- or tridentate ligands, such as 2,2'-bipy or phen and nitrogen donor atoms. Because of their geometry and rigidity, the L–Fe–L angles have to show a large deviation compared to the LS state. Here, all six ligands are monodentate and not bulky, distortion due to avoidance of any voluminous groups is not necessary, which explains the long bond lengths typical for HS complexes but the small distortion. This is further confirmed, when comparing with literature-known complexes with comparable structures, for example with the HS Fe(II) complexes $\{[Fe^{II}(H_2PO_4)_2(\mu\text{-}4,4'\text{-bipy})_2(H_2O)_2]\cdot H_2O\cdot(4,4'\text{-bipy})\}$[277] and $[Fe^{II}(trz\text{-}tet)_2(H_2O)_4]\cdot 2H_2O$ (trz-tet = 5-(4H-1,2,4-triazol-yl)-2H-tetrazole).[278] The bond distances and deviations are Fe–L_{av} = 2.122 Å and 2.133 Å as well as Σ_0 = 39.20° and Σ_0 = 24.64°. The HS state is confirmed by magnetic measurements and ^{57}Fe Mössbauer spectroscopy. The comparable ligand field strength of 4,4'-bipy and trz-tet with **L2** confirms the HS state of **C3** and indicates no spin crossover behavior. Similar to the latter example, complex $\{[Fe^{II}(trans\text{-}\mu\text{-}\textbf{L2})_2(H_2O)_4](ClO_4)_2\cdot 2H_2O\}_n$ **C3** consists of four coordinating water molecules, which is known to exhibit a weak ligand field.[27] In general, a $\{N_2O_4\}$ donor set is not common for Fe(II) spin crossover complexes, these compounds are expected to stay in the HS state.[238] The paramagnetic HS state of the Fe(II) ions would further enable intramolecular exchange interaction. However, as the coordination mode of **L2** is similar to the Cu(II) complex **C2** and

the Fe–N and Fe–Fe distances are even larger with 2.1955(14) Å and 9.637 Å, an exchange interaction can be neglected.

Complex C3'

The complex $\{[Fe^{II}(\mu\text{-}\mathbf{L2})_4(H_2O)_2](ClO_4)_2\cdot\mathbf{L2}\}_n$ **C3'** co-crystallizes with **C3** in form of yellow plates. The crystal structure was determined at 193 K. **C3'** crystallizes in the triclinic space group $P\bar{1}$. The Fe(II) ion is coordinated by four ligands and two water molecules in *trans*-position forming an octahedral surrounding. Similar to $\{[Cu^{II}(\mu\text{-}\mathbf{L2})_3(H_2O)((CH_3)_2CO)](ClO_4)_2(H_2O)\}_n$ **C2** and $\{[Fe^{II}(\textit{trans}\text{-}\mu\text{-}\mathbf{L2})_2(H_2O)_4](ClO_4)_2\cdot2H_2O\}_n$ **C3**, **L2** functions as bridging unit between the Fe(II) centers forming a two-dimensional coordination network. The twisting angle of **L2** is 180°. The charge of each Fe(II) ion is balanced by two non-coordinating perchlorate anions. One non-coodinating ligand molecule is in the cavity. One repetition unit is found in the asymmetric unit.
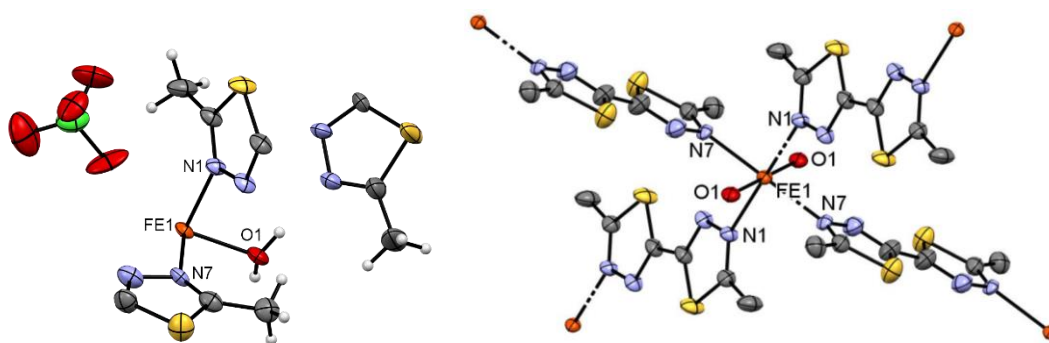
*Figure 47 Left: Asymmetric unit of **C3'**. Right: Repetition unit of the two-dimensional coordination network; hydrogen atoms, the non-coordinating ligand and perchlorate anions are omitted for clarity. Color code: grey – C, violet – N, yellow – S, red – O, orange – Fe(II), green – Cl. ORTEP representation with atomic displacement parameters at 50% level of probability.*

The two-dimensional network propagates along the *ab* directions. The size of the cavity is determined by the Fe–Fe distances of 9.590 Å and 9.709 Å resulting in an area of 93.109 Å². The cavity is large enough for an additional non-coordinating **L2**, which is located diagonally in each cavity.
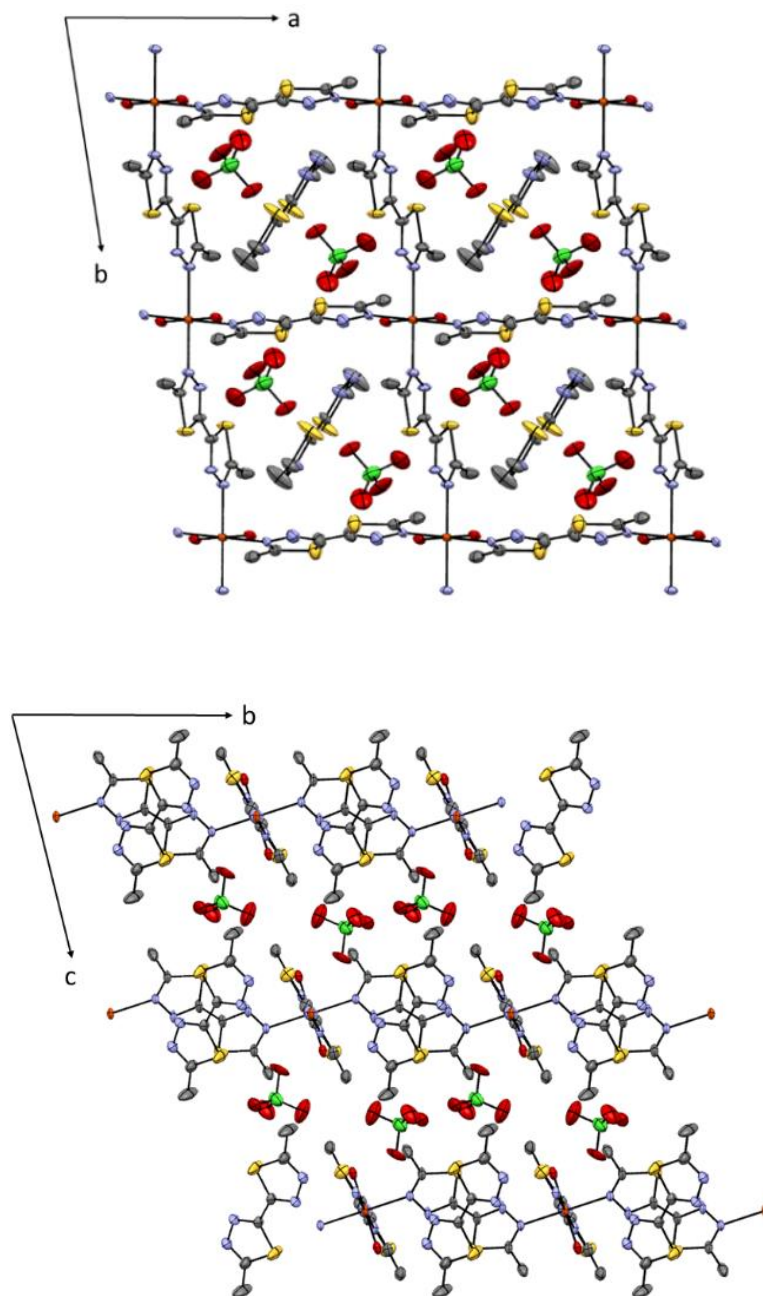
*Figure 48 Two-dimensional network structure of **C3'**. Top: Top view. Bottom: Cross section of the two-dimensional network. The perchlorate anions are located between the layers of the coordination network whereas the non-coordinating ligand are within the cavity. Color code: grey – C, violet – N, yellow – S, red – O, orange – Fe(II), green – Cl. Hydrogen atoms are omitted for clarity. ORTEP representation with atomic displacement parameters at 50% level of probability.*

As illustrated in Figure 49, there are hydrogen bonds between the coordinating water molecule and the non-coordinating perchlorate anion as well as between the lattice water and the free **L2**. The O···O/O–H···O distances and O–H···O angles are O1–H1A···O3 = 2.8 Å/2.0 Å and 153° as well as O1–H1B···N13 = 2.8 Å/1.9 Å and 172° which is in good agreement with the literature.[279–284]
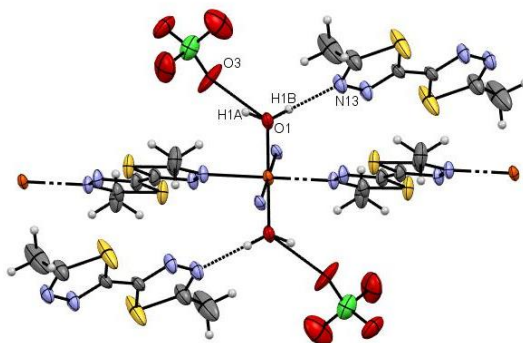
*Figure 49 Hydrogen bonds in **C3'** between the water molecules, perchlorate anions and the non-coordinating **L2** in the cavity. Color code: grey – C, violet – N, yellow – S, red – O, orange – Fe(II), green – Cl, white – H. Only the relevant atoms are labelled. ORTEP representation with atomic displacement parameters at 50% level of probability.*

The Fe1–N bond lengths are 2.240(4) Å and 2.264(4) Å, whereas the Fe1–O1 distance is much shorter with 2.058(4) Å, leading to a compressed octahedron with slight rhombic distortion. However, the bond lengths indicate the HS state of the Fe(II) ion. The L–Fe–L angles are close to 90° leading to a low deviation of Σ_0 = 16.56°. The small divergence is confirmed by continuous shape measurements, yielding in a low value of CShM = 0.23.
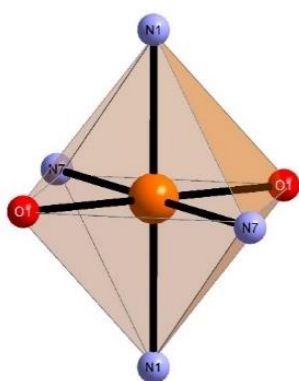
*Figure 50 The {FeN$_4$O$_2$} octahedron of **C3'** compared to the perfect polyhedron calculated by CShM. Color code: violet – N, red – O, orange – Fe(II).*

*Table 5 Selected bond lengths and angles of **C3'** at 193 K.*

		C3'
Fe–L [Å]	Fe1–N1	2.240(4)
	Fe1–N7	2.264(4)
	Fe1–O1	2.058(4)
L–Fe–L [°]	N1–Fe1–N7	86.87(15)
	N1–Fe1–O1	89.60(15)
	N7–Fe1–O1	90.61(16)
Σ_0 [°]	16.56	
CShM	0.23	

The bond lengths hint at the HS state with the average Fe–L bond length of 2.194 Å at 193 K. But similar to $\{[Fe^{II}(\textit{trans}\text{-}\mu\text{-}\mathbf{L2})_2(H_2O)_4](ClO_4)_2 \cdot 2H_2O\}_n$ $\mathbf{C3}$, the deviation factor is small and does not indicate the HS state of the Fe(II) ion as the ligand $\mathbf{L2}$ does not coordinate as bidentate ligand. In comparison to $\mathbf{C3}$, the donor set is $\{N_4O_2\}$, which is much more favorable for Fe(II) spin crossover complexes than $\{N_2O_4\}$.[285] A comparable system is represented by the spin crossover complex $[Fe^{II}(btr)_2(NCS)_2] \cdot H_2O$ (btr = 4,4'-bis-1,2,4-triazole), where the bis-1,2,4-triazole bridges the Fe(II) centers to form a two-dimensional network similar to $\mathbf{C3'}$.[163] The btr ligand provides a weaker ligand field than 2,2'-bipy or phen, thus the ligand field strength of $\mathbf{L2}$ should be between 2,2'-bipy and bis-1,2,4-triazole. The ligand field strength of the thiocyanate anions is comparable to the water co-ligands in $\mathbf{C3'}$. This gives hint to a possible spin crossover behavior of $\mathbf{C3'}$ at lower temperatures. Nevertheless, a huge difference is the occupation of the cavity. In $\mathbf{C3'}$, the cavity is filled with the non-coordinating ligand molecules whereas the cavity of the reported structure consists of only two lattice water molecules, which are much smaller than $\mathbf{L2}$. As the HS→LS transition drastically shortens the Fe–L bond lengths, the cavity gets much smaller for the LS state. This could either hinder a (full) spin transition or a phase change could take place. An intramolecular exchange interaction is negligible, as the bridging coordination of $\mathbf{L2}$ $\textit{via}$ the terminal nitrogen donor atoms and the Fe–N and Fe–Fe distances are similar to the complexes $\{[Cu^{II}(\mu\text{-}\mathbf{L2})_3(H_2O)((CH_3)_2CO)](ClO_4)_2(H_2O)\}_n$ $\mathbf{C2}$ and $\{[Fe^{II}(\textit{trans}\text{-}\mu\text{-}\mathbf{L2})_2(H_2O)_4](ClO_4)_2 \cdot 2H_2O\}_n$ $\mathbf{C3}$.

In order to confirm the HS state of the complexes $\mathbf{C3}$ and $\mathbf{C3'}$, a solid-state UV-Vis spectrum of the obtained mixed crystals was measured in barium sulfate at room temperature. The spectrum is shown in Figure 51. The UV-Vis data are evaluated qualitatively as it shows the properties of both complexes. The maximum at 38 000 cm^{-1} corresponds to the π-π^* transition of the ligand. The broad shoulder at 27 500 cm^{-1} is assigned to the $^5T_{2g} \rightarrow {}^5$MLCT transition and the maximum at 12 700 cm^{-1} to the $^5T_{2g} \rightarrow {}^5E_g$ transition of the HS species.[286] There is no local maximum in the range of 21 000 cm^{-1} to 18 000 cm^{-1} corresponding to the $^1A_{1g} \rightarrow {}^1T_{1g}$ or $^1A_{1g} \rightarrow$MLCT transition which is characteristic for the LS species pointing towards the HS state of the investigated complexes.[278]
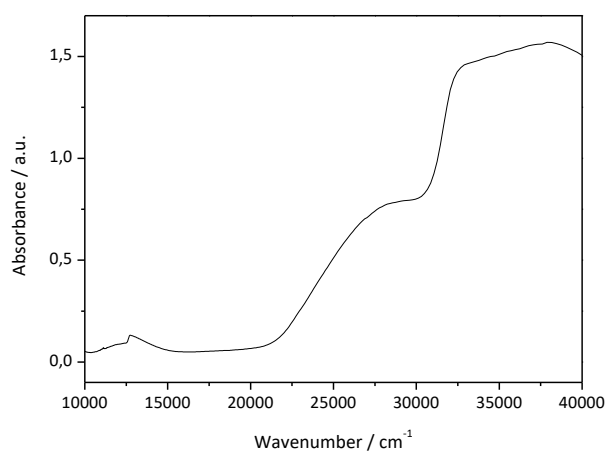

*Figure 51 Solid state UV-Vis spectrum of **C3**+**C3'** in barium sulfate at room temperature.*

Summarizing, both single crystal X-ray and UV-Vis measurements indicate the HS state for the two complexes **C3** and **C3'**. Furthermore, the $^5T_{2g} \rightarrow {}^5E_g$ transition at 12 700 cm^{-1} is close to the range of a spin crossover complex pointing towards possible SCO behavior of **C3'**.[27] Nevertheless, this is estimated to be an average value of **C3** and **C3'**, as the shift of the single $^5T_{2g} \rightarrow {}^5E_g$ transitions should differ when considering the different coordination spheres.

Complex C4

The reaction of **L2** in dichloromethane and freshly prepared 'Fe(SCN)$_2$' in acetone produced red block shaped single crystals by evaporation of the whole solvent. The structure of {Fe^{II}(*trans*-µ-**L2**)$_2$(**L2**)(SCN)$_2$}$_n$ **C4** was determined at 120 K. The complex crystallizes in the orthorhombic space group *Pna*2$_1$. The structure consists of one-dimensional coordination chains, where the Fe(II) ions are connected by **L2** with a twisting angle of 179°. The octahedral coordination sphere of the Fe(II) ion with a {N$_6$} donor set is provided by the two end-to-end coordinated **L2** in *trans*-position, a chelating **L2** and two thiocyanate anions in *cis*-position. The asymmetric unit consists of one repetition unit.
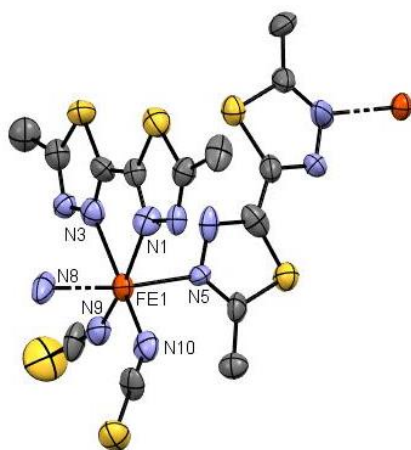
*Figure 52 Asymmetric unit of **C4**. Color code: grey – C, violet – N, yellow – S, orange – Fe(II). Hydrogen atoms are omitted for clarity. ORTEP representation with atomic displacement parameters at 50% level of probability.*

The bridging ligands and Fe(II) ions form the one-dimensional chains, which propagate diagonal to the *b*- and *c*-axes. The parallel chains are twisted by 37.78° with respect to the *b*-axis, alternating clock- and counterclockwise in each layer. As the crystals formed after the solvent was completely evaporated, the quality of the dried crystals and therefore the dataset is poor. Therefore, non-coordinating solvent molecules could not be determined precisely. The residual electron density hints to non-coordinating chloroform molecules between the layers but the available dataset does not allow getting insight into possible intermolecular contacts *via* the solvent molecules.
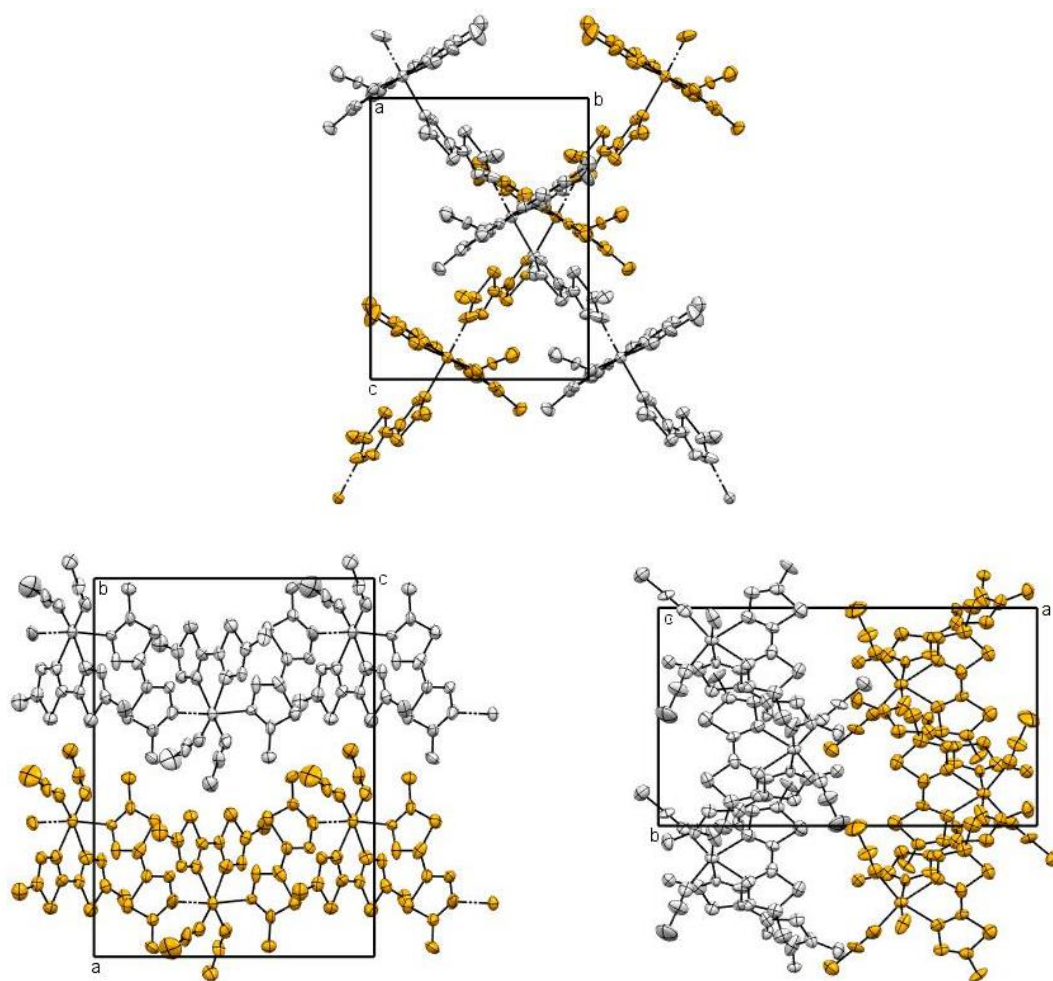
*Figure 53 Top: Arrangement of the coordination chains of **C4** along the a-axis. Bottom left: Parallel arrangement in the direction of the c-axis highlighting the sheet structure. Bottom right: Parallel arrangement in the direction of the b-axis highlighting the sheet structure. The light grey and orange colors represent each one coordination chain for better overview. Hydrogen atoms are omitted for clarity. ORTEP representation with atomic displacement parameters at 50% level of probability.*
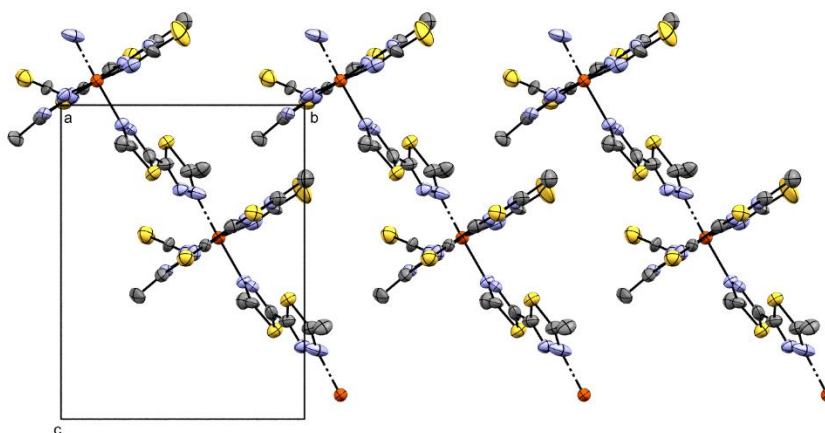
*Figure 54 Parallel array of coordination chains of **C4** within the bc plane. Hydrogen atoms are omitted for clarity. Color code: grey – C, violet – N, yellow – S, orange – Fe(II). Hydrogen atoms are omitted for clarity. ORTEP representation with atomic displacement parameters at 50% level of probability.*

The Fe1–N bond lengths of the chelating ligand are 2.20(2) Å and 2.27(2) Å, its *cis*-angle is 73.9(7)°. The bond distance to the thiocyanate anions is shorter with 2.10(3) Å and 2.07(3) Å. The small *cis*-angle of the bidentate pocket is compensated by the large *cis*-angle of the SCN^- co-ligands with 102.5(8)°. The thiocyanate anions are almost linear with N9–C13–S5 = 176(3)° and N10–C14–S6 = 178(3)°, whereas the Fe–NC linkages are strongly bent with Fe1–N9–C13 = 159(2)° and Fe1–N10–C14 = 146(2)°. The Fe–N bond lengths of the bridging ligands are 2.210(19) Å and 2.24(3) Å. The deviation of the *cis*-angles amounts Σ_0 = 63.49° and is in the range of the LS state of the Fe(II) ion with a $\{N_6\}$ donor set. This is futher confirmed by continuous shape measurements as the deviation of the perfect octahedron is larger than for **C3** and **C3'** with CShM = 0.75 and can be explained by the chelating coordination mode of the ligand. The bond lengths hint to a HS state, whereas the distortion parameter is in the range of a LS species.
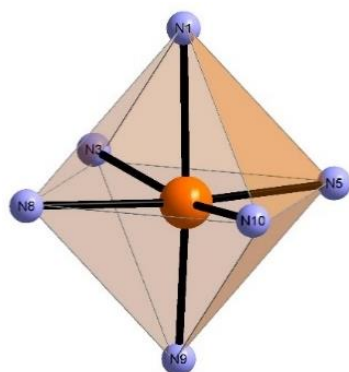
*Figure 55 The $\{FeN_6\}$ octahedron of **C4** compared to the perfect polyhedron calculated by CShM. Color code: violet – N, red – O, orange – Fe(II).*

*Table 6 Selected bond lengths and angles of **C4** at 120 K*

		C4
Fe–L [Å]	Fe1–N1	2.20(2)
	Fe1–N3	2.27(2)
	Fe1–N5	2.210(19)
	Fe1–N8	2.24(3)
	Fe1–N9	2.10(3)
	Fe1–N10	2.07(3)
L–Fe–L [°]	N1–Fe1–N3	73.9(7)
	N5–Fe1–N8	172.4(8)
	N9–Fe1–N10	102.5(8)
Σ_0 [°]		63.49
CShM		0.75

The complex $\{Fe^{II}(trans\text{-}\mu\text{-}\mathbf{L2})_2(\mathbf{L2})(SCN)_2\}_n$ **C4** can be compared with the Fe(II) spin crossover complex $[Fe^{II}(4,4'\text{-bipy})(bt)(NCX)_2]$ (X = S or Se, bt = bis-2,2'-thiazoline) reported by Bousseksou and Real.[287] This structure is similar to **C4**, as the 4,4'-bipy acts as bridging ligand, forming a one-dimensional coordination chain. The donor set is $\{N_6\}$ with the bidentate bt ligand and *cis*-coordinated thiocyanate anions and the Fe–L distances as well as L–Fe–L angles are in the same region. As the 4,4'-bipy is a stronger ligand than the bis-1,3,4-thiadiazole **L2**, complex **C4** could show spin crossover behavior at elevated temperatures. Similar to the previous discussed complexes, the Fe–Fe distance is large with 9.592 Å. Therefore, an exchange interaction is not expected to be present.

Complex C5

The reaction of the ligand **L2** and iron(II) tetrafluoroborate in an acetone/chloroform solvent mixture yielded after several months in the mononuclear complex [Fe^{II}(**L2**)$_3$](BF$_4$)$_2$·3CHCl$_3$ **C5** after the solvent was completely evaporated. The measurement was performed at 120 K. The complex crystallizes in the triclinic space group $P\bar{1}$. The three bidentate coordinating **L2** provide an octahedral coordination sphere with a {N$_6$} donor set. The asymmetric unit consists of one complex cation with two non-coordinating tetrafluoroborate anions and three chloroform molecules. The unit cell consists of both the Δ- and Λ-isomers, which are differentiated by an inversion center in the center of the unit cell. There are short contacts between the methyl groups, non-coordinating tetrafluoroborate anions and non-coordinating chloroform molecules. The C···F/C–H···F distances and C–H···F angles of 3.3 Å/2.4 Å and 146° are in good agreement with the literature.[288–293]
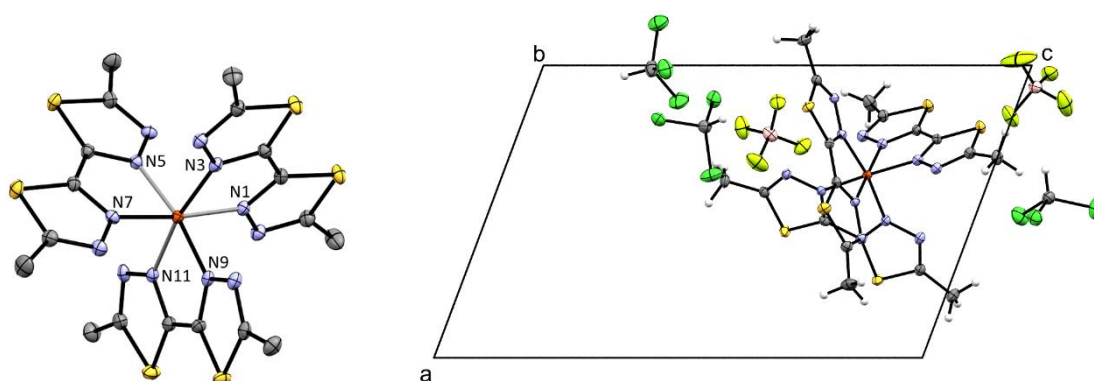
*Figure 56 Left: Molecular structure of the complex cation of **C4** (Δ-isomer). Hydrogen atoms are omitted for clarity. Right: asymmetric unit including one complex cation, two tetrafluoroborate anions and three solvent molecules. Color code: grey – C, violet – N, yellow – S, red – O, orange – Fe(II), green – Cl, light green – F, beige – B, white – H. ORTEP representation with atomic displacement parameters at 50% level of probability.*

The average Fe–L distance and N–Fe–N *cis*-angles within one ligand are 1.949(7) Å and 80.48(5)°. The short bond lengths and the low deviation of $\Sigma_0 = 58.98°$ indicate the LS state. The CShM value is low with 0.77 but higher than for {[Fe^{II}(*trans*-μ-**L2**)$_2$(H$_2$O)$_4$](ClO$_4$)$_2$·2H$_2$O}$_n$ **C3**, due to the bidentate coordination of the ligand **L2** and its rigidity. The LS state is in good agreement with comparable [Fe^{II}(2,2'-bipy)$_3$]$^{2+}$ complexes[294–297] which are in the LS state.[50] The complex could show spin crossover behavior at higher temperatures as **L2** exhibits a weaker ligand field than 2,2'-bipy.[298]
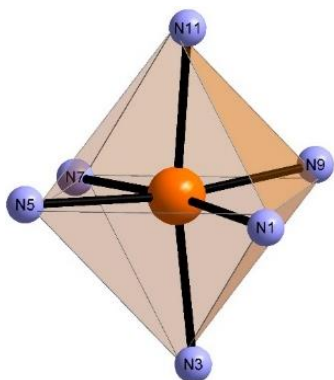
*Figure 57 The {FeN$_6$} octahedron of **C6** compared to the perfect polyhedron calculated by CShM. Color code: violet – N, red – O, orange – Fe(II).*

*Table 7 Selected Fe-L bond lengths and L-Fe-L angles of **C5** at 120 K.*

	C5	
	Fe1–N1	1.9397(18)
	Fe1–N3	1.9536(18)
Fe–L [Å]	Fe1–N5	1.9525(18)
	Fe1–N7	1.9433(18)
	Fe1–N9	1.9515(18)
	Fe1–N11	1.9499(18)
	N1–Fe1–N3	80.53(7)
L–Fe–L [°]	N5–Fe1–N7	80.49(7)
	N9–Fe1–N11	80.42(7)
Σ_0 [°]	58.98	
CShM	0.77	

3.2.4 Cobalt(II) 1D Chains: Magnetic Properties

Next to the Cu(II) and Fe(II) complexes, one Co(II) compound was obtained. The reaction of cobalt(II) perchlorate hexahydrate in acetone with the ligand **L2** in dichloromethane yielded in red single crystals after one day. The complex {[Co^{II}(cis-μ-**L2**)$_2$(H$_2$O)$_4$](ClO$_4$)$_2$}$_n$ **C6** crystallizes in the monoclinic space group P2/n at 193 K. The Co(II) ion is coordinated by two ligands **L2** in cis-position and four water molecules. The ligand connects the Co(II) ions forming a one-dimensional coordination chain. Two perchlorate anions compensate the positive charge of the divalent cation. The asymmetric unit only consists of half the repetition unit with the Co(II) ion, one ligand **L2** and two coordinated water molecules as well as one non-coordinating perchlorate anion. The structure is related to **C3** albeit the ligand is coordinating in cis-position and no solvent molecules are found within the crystal structure.
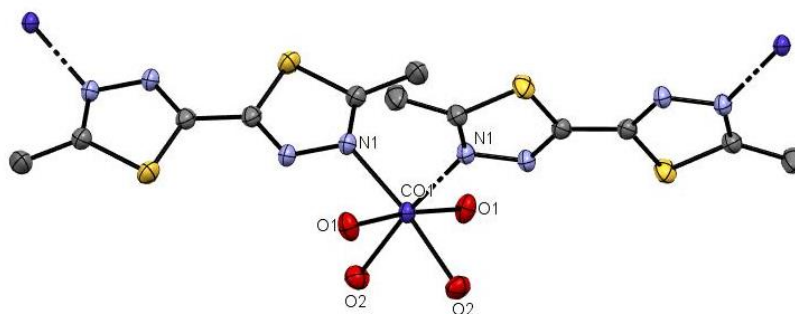
*Figure 58 Molecular structure of the coordination chain of **C5**. Color code: grey – C, violet – N, yellow – S, red – O, dark blue – Co(II), green – Cl. Hydrogen atoms are omitted for clarity. ORTEP representation with atomic displacement parameters at 50% level of probability.*

The one-dimensional chain propagates diagonal to the ac directions in a zigzag alignment. The coordinated water molecules are alternatingly directed above and below the chain. The structure consists of layers of the Co(II) coordination chains and the non-coordinating perchlorate anions, alternating along the b-axis.
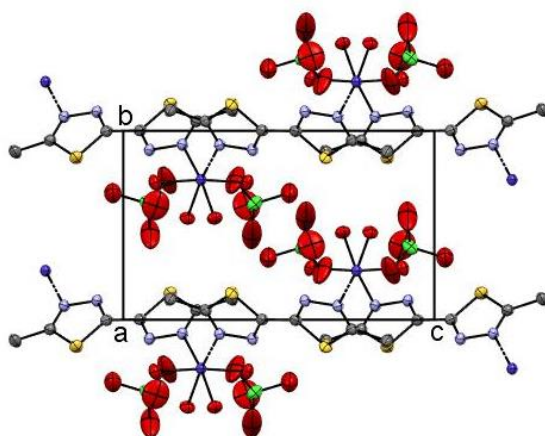
*Figure 59 One-dimensional chain structure of **C6** in the direction of the c-axis. Color code: grey – C, violet – N, yellow – S, red – O, dark blue – Co(II), green – Cl. Hydrogen atoms are omitted for clarity. ORTEP representation with atomic displacement parameters at 50% level of probability.*

The protruding water molecules allow the formation of a hydrogen bond network to the non-coordinating perchlorate anions and consequently a connection between the chains. The distances are in the range of 2.0 Å to 2.3 Å.
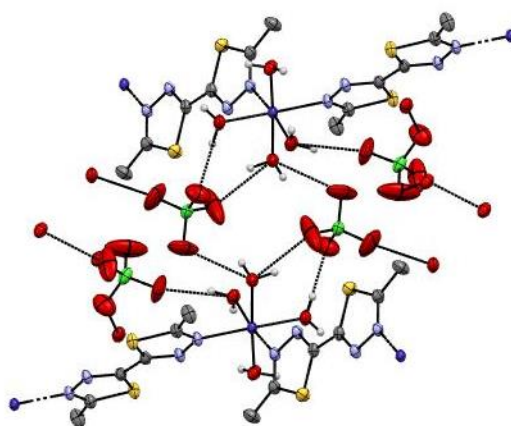
*Figure 60 Hydrogen bonding in **C6** within the 'perchlorate layer' connecting the single chains. Color code: grey – C, white – H, violet – N, yellow – S, red – O, dark blue – Co(II), green – Cl. ORTEP representation with atomic displacement parameters at 50% level of probability.*

The Co(II) ion sits in an octahedral coordination sphere provided by the two bridging ligands in *cis*-position and the four water molecules. The twisting angle of **L2** is 180°. The Co1–N1 bond length is 2.131(2) Å whereas the Co1–O1 and Co1–O2 distances are shorter with 2.063(2) Å and longer with 2.138(2) Å resulting in a rhombic distortion. The L–Co–L angles of N1–Co1–O1 and O1–Co1–O2' are close to the right angle with 90.08(10)° and 90.17(10)°. Larger deviations are found for the other angles. The slight rhombic distortion is confirmed with CShM = 0.23.
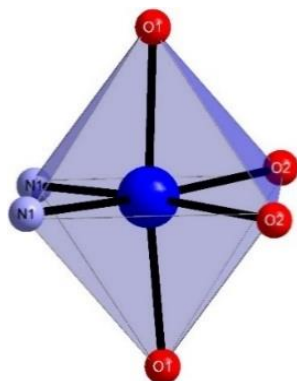
*Figure 61 The {CoN$_2$O$_4$} octahedron of **C6** compared to the perfect polyhedron calculated by CShM. Color code: violet – N, red – O, dark blue – Co(II).*

*Table 8 Selected bond lengths and angles of **C6** at 193 K.*

		C6
Co–L [Å]	Co1–N1	2.131(2)
	Co1–O1	2.063(2)
	Co1–O2	2.138(2)
L–Co–L [°]	O1–Co1–N1	90.08(10)
	O1–Co1–N1'	94.01(10)
	O1–Co1–O2	90.17(9)
	O1–Co1–O2'	85.38(10)
	N1–Co1–N1'	97.03(14)
	N1–Co1–O2	87.82(10)
	O2–Co1–O2'	87.66(13)
Σ_0 [°]		40.50
CShM		0.23

The temperature-dependent magnetic susceptibility is displayed in Figure 62 as $\chi_M T$ versus T plot. The experimental $\chi_M T$ value of 3.09 cm³ K mol^{-1} at 300 K per repetition unit hints to the HS state of the Co(II) ion with S = 3/2. This value is much higher compared to the theoretical spin-only value of $\chi_M T$ = 1.875 cm³ K mol^{-1} but in good agreement with the literature when taking an unquenched orbital angular momentum into account. With L = 3 and g = 2.0, the theoretical value amounts $\chi_M T$ = 3.38 cm³ K mol^{-1}:[98]

$$\mu_{\text{eff}} = \sqrt{g^2 \cdot S(S+2) + L(L+1)}\ \mu_B \tag{22}$$

The curve slowly decreases with lower temperatures in the range of 300 K to 100 K and more rapidly for lower temperatures down to 1.71 cm³ K mol^{-1} indicating significant zero-field splitting and the thermal depopulation of excited Kramer's doublets.[226,299] An antiferromagnetic exchange interaction between the Co(II) ions is neglected because of the findings of the appropriate Cu(II) complex **C2** with a similar coordination mode and the even larger Co–Co distance of 9.455 Å.[299]
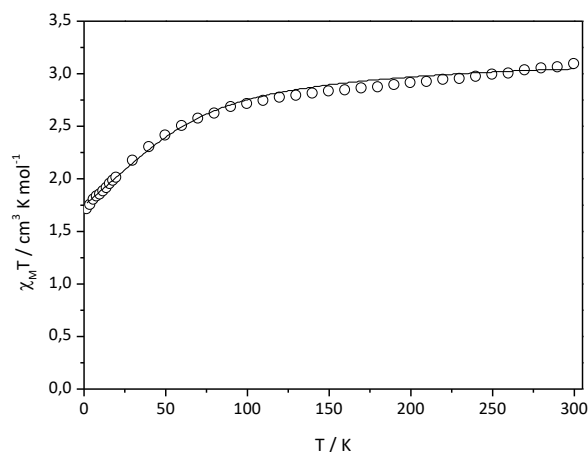
*Figure 62 Temperature-dependent magnetic behavior of **C6**, $\chi_M T$ vs. T plot. ○ experimental data, – fit including spin-orbit coupling, orbital reduction, and crystal field parameter.*

The experimental data were fitted for one repetition unit with the program PHI. The following Hamiltonian takes into account spin-orbit coupling and strong axial distortion:[262]

$$\hat{H} = -\alpha\lambda\hat{\mathbf{L}}\cdot\hat{\mathbf{S}} + \Delta[\hat{\mathbf{L}}_z^2 - L(L+1)/3] + \mu_B H(-\alpha\hat{\mathbf{L}} + g_e\hat{\mathbf{S}}) \tag{23}$$

The last term is attributed to the Zeeman splitting due to the applied magnetic field. For HS Co(II) complexes, the spin-orbit coupling parameter λ is negative, as it has more then five d-electrons, and is typically in the range of −180 and −90 cm^{-1}.[226] The parameter λ is related to the electron spin-orbit coupling constant ζ which amounts 533 cm^{-1} for Co(II) ions:[300]

$$\lambda = \frac{-\zeta}{2S} \tag{24}$$

The orbital reduction parameter α is defined as $\alpha = A \cdot \kappa$ and describes the mixing of the $^4T_{1g}(^4F)$ ground with the excited $^4T_{1g}(^4P)$ term *via* second-order spin-orbit coupling due to the same symmetry. A strong field causes a strong mixture and therefore a large orbital reduction. The value varies between A = 1 (strong field) and A = 3/2 (weak field). The delocalization of the unpaired electrons between the metal ion and the ligand reduces the orbital momentum to $L \leq 1$. The orbital reduction factor κ is in the range of $0 \leq \kappa \leq 1$. High covalency refers to a low value close to zero and a strong field, ionic bonds show higher values close to one and refer to a weak ligand field. The crystal field parameter Δ defines the energy gap between the $^4A_{2g}$ ground and the ^4E_g first excited state resulting from an axial distortion of the ideal octahedral O_h symmetry (see Chapter 1.2.1.3). The values of g = 2.0, a spin-orbit-coupling of λ = −140 cm^{-1} and an orbital reduction of α = 1.5, which refers to a weak field, were kept constant. The crystal field parameter Δ was fitted with +108(1) cm^{-1} (R = 3.42 · 10^{-2}). The positive value is in a reasonable range considering the compressed surrounding of the Co(II) ion.[226]

Next to the temperature-dependent magnetic susceptibility, the field-dependent magnetization was measured. The M versus H and M versus H/T data are shown in Figure 63 and Figure 64. The expected saturation of the magnetization M_{sat} is calculated by:[226]

$$M_{sat} = g_0 \cdot S \cdot N_A\mu_B \tag{25}$$

The experimental value of 2.32 $N_A\mu_B$ at 2 K is much lower than the expected one of M = 3 $N_A\mu_B$ for S = 3/2 and g = 2.0, but in good accordance with the literature.[226] Due to the second-order spin-orbit coupling, the degeneracy of the Kramers doublets is removed and the m_S = ±3/2 and m_S = ±1/2 states are separated by the energy difference of $|2D|$.[301] At low temperatures, only the m_S = ±1/2 ground state is assumed to be populated. Considering the effective spin of S = 1/2 and α = 1.5, the magnetization saturates to M = 2.2 μ_B with a maximal g-value of g = 4.4.[226] For higher temperatures, the magnetization is not saturated yet and the curves of the reduced magnetization do not superimpose. Both findings strengthen the presence of magnetic anisotropy. The magnetization was fitted using S = 3/2 to get insight into the energy difference of the Kramers' doublets and to obtain values for the axial (D) and rhombic (E) zero-field splitting parameter. The following Hamiltonian was applied:[262]

$$\hat{H} = D[\hat{S}_z^2 - S(S + 1)/3] + E(\hat{S}_x^2 - \hat{S}_y^2) + g\mu_B HS \tag{26}$$

The g-factor as well as the zero-field splitting parameter were fitted with g = 2.481(2), D = +47.14(62) cm^{-1} and E = –0.04(61) cm^{-1} (R = 2.76 · 10^{-3}). The values are in good agreement with the structure of the complex. The positive crystal field parameter Δ states the positive D value, which is confirmed by the fit. Simultaneous fitting of the field-dependent magnetization and the low-temperature region of the $\chi_M T$ versus T data (2 – 20 K) led to the same values and confirm the results of the individual fits (see Appendix).
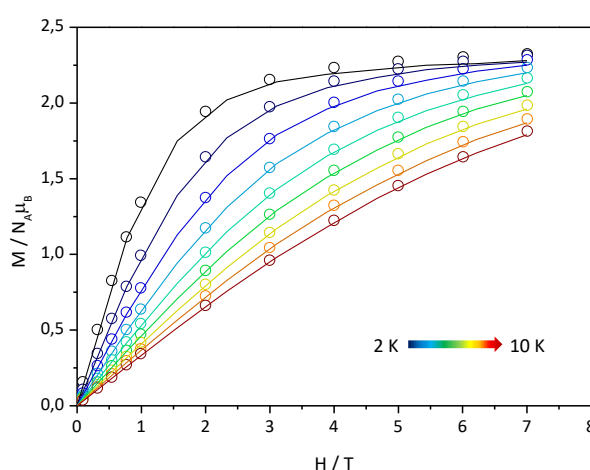

*Figure 63 Field- and temperature-dependent magnetization measurement of **C6**, M vs. H plot. ○ experimental data, – fit including the axial and rhombic zero-field splitting parameter.*
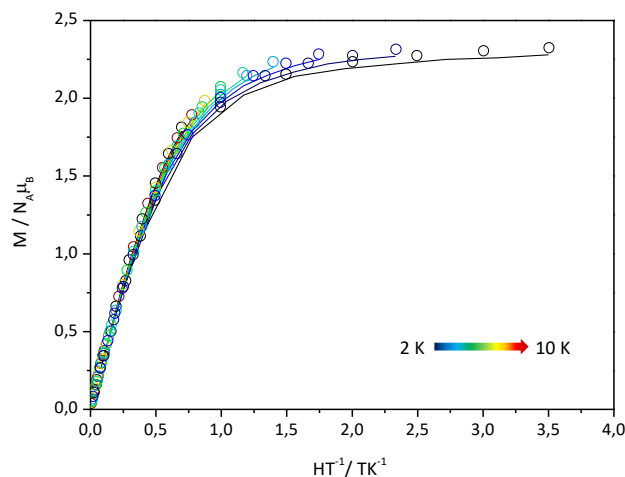
Figure 64 Field- and temperature-dependent magnetization measurement of C6, M vs. H/T plot. ○ experimental data, – fit including the axial and rhombic zero-field splitting parameter.

The positive sign of the axial zero-field splitting parameter and the high value hint at possible SIM behavior. In order to investigate the potential slow relaxation of magnetization, frequency-dependent ac magnetic susceptibility measurements were performed at 2 K.
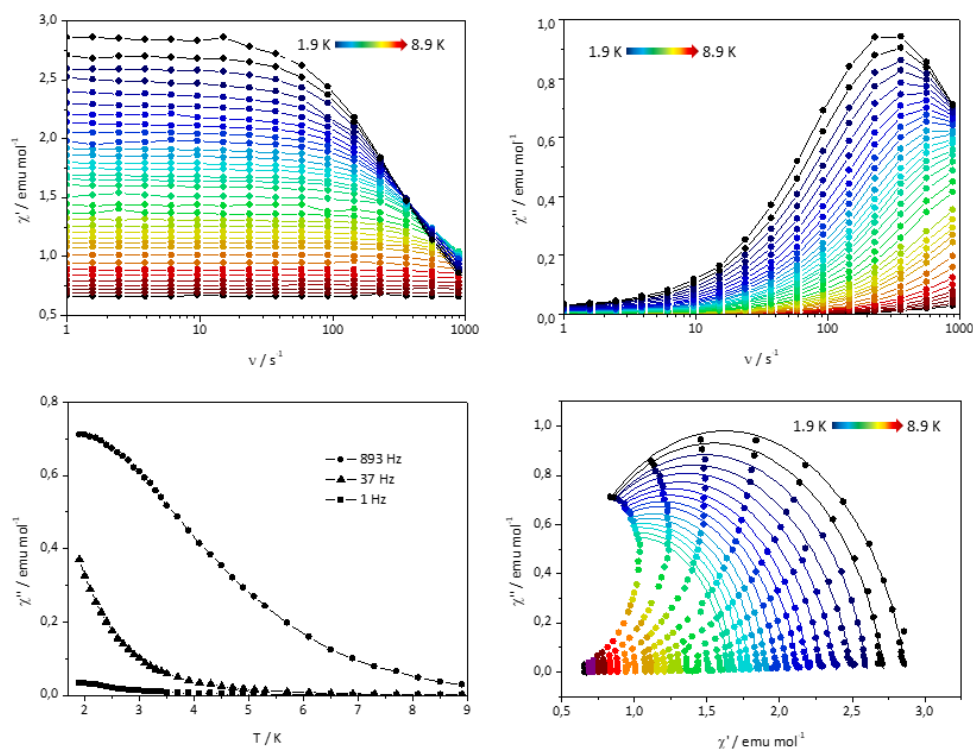

Figure 65 The ac susceptibility measurements of C6 with an applied dc field of 1000 Oe. Top left: frequency-dependent in-phase signal χ′. Top right: frequency-dependent out-of-phase signal χ′′. Bottom left: temperature-dependent out-of-phase signal χ′′ (1.9 – 8.9 K and 1 Hz to 893 Hz). -●- experimental data. Bottom right: Cole-Cole plot (1.9 – 8.9 K) ● experimental data, – fit (1.9 – 3.4 K).

At zero-field, no out-of-phase signal χ'' was observed, but for an applied dc field a non-zero signal was present. The temperature-dependent measurement was performed in the range of 1.9 – 8.9 K at 1000 Oe due to the highest χ'' signal (see Appendix). Both, the in- and out-of-phase signals χ' and χ'' show frequency- and temperature-dependent behavior, as the values for χ'' decrease for low temperatures and high frequencies. The χ'' signal shows a maximum, which lowers and slightly shifts towards larger frequencies when increasing the temperature. This hints to tunneling as well as temperature-dependent relaxation processes.[189,224] The out-of-phase signal χ'' is plotted against the in-phase signal χ' in the Cole-Cole plot and the curves with a pronounced maximum are fitted (Figure 65 bottom right). It contains the temperature range of 1.9 K to 3.4 K. The evaluation was performed with the program CC-Fit2[302] using the general Debye model (see Equation 15).[303] The subsequent data were used to display the Arrhenius plot in Figure 66. The best fit was achieved when including quantum tunneling and the thermally activated Orbach process:

$$\tau^{-1} = \tau_{QTM}^{-1} + \tau_0^{-1} \cdot \exp\left(-\frac{U_{eff}}{k_B T}\right) \tag{27}$$

The obtained values are U_{eff} = 7.5 K (5.2 cm^{-1}), τ_0 = 2.29 · 10^{-5} s and τ_{QTM} = 9.33 · 10^{-4} s.
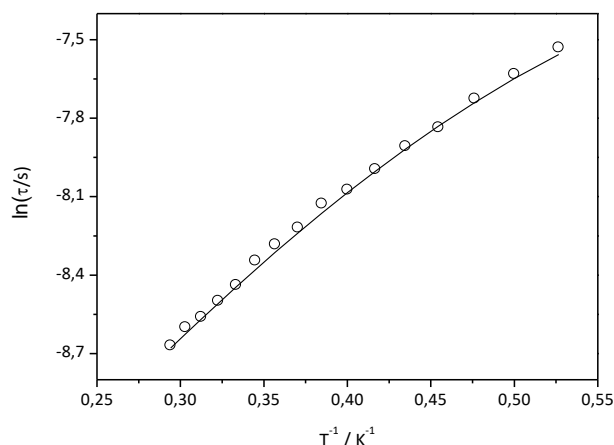
*Figure 66 Arrhenius plot of **C6**, ln(τ) versus 1/T. ○ fitted values extracted from the fit of the Cole-Cole plot, − fit of the Arrhenius plot including QTM and the Orbach process.*

The origin of the slow relaxation of magnetization and the relaxation pathways of hexa-coordinated Co(II) complexes are exceedingly discussed in literature. The coordination sphere of the metal ion clearly influences the magnetic properties as the distortion of the ideal octahedron implements the non-degeneracy of the Kramers doublets by unquenched orbital contribution and thus axial (and rhombic) anisotropy. In these cases, the *easy-plane* type of anisotropy could cause the energy barrier in agreement with the positive sign and the m_S = ±1/2 ground state.[224] The spin-flip could occur within the *easy-plane* from *x* to *-x via* the *y*-axis or *vice versa*. But for **C6**, the rhombic anisotropy parameter is negligible with E = −0.04 cm^{-1} as it would only cause an energy barrier of U_{eff} = 0.06 cm^{-1} (Equation 12) much lower than the fitted data reveal. In contrast to that, the total energy barrier of |2D'| would

amount 94.28 cm^{-1} (Equation 16), which is much higher than the fitted data, hence tunnelling processes must be considered in addition to the thermally activated Orbach process. The present hydrogen bonds or Co–Co dipolar interactions facilitate quantum tunneling as well as hyperfine coupling between the electron and nuclear spin of $I = \pm 7/2$. These interactions cause further splitting of the $m_S = \pm 1/2$ and $m_S = \pm 3/2$ states possibly leading to resonant energetic levels.[184,304] An applied field hinders these transitions but phonons with available frequency modes could still enable QTM *via* spin-lattice relaxation.[225,305] These assumptions are consistent with the fitted data, including tunneling and the thermally activated Orbach process.

3.2.5 Evaluation of Ligand L2

All complexes show the ability of ligand **L2** to chelate the metal ions *via* the bidentate pocket and to bridge the metal ions by end-to-end coordination. The crystals of complexes **C2**, **C3/C3'** and **C6** crystallize fast (hours to days) and all complexes show the same bridging coordination mode of ligand **L2**. In contrast, the crystals of **C4** and **C5** have formed after weeks or months. The end-to-end coordination of **L2** leads to the formation of kinetically stable products, which directly crystallize, whereas the chelating mode can be related to the thermodynamically favored complexes.

Furthermore, the obtained crystal structures demonstrate the high flexibility and variability of the ligand **L2**, as zero-, one- and two-dimensional networks have formed. The targeted synthesis could not be achieved by varying the metal-to-ligand ratio but improved by the usage of specific starting materials and solvent mixtures.

The obtained transition metal complexes reveal interesting magnetic behavior, starting from isolated non-interacting Cu(II) ions in **C2**, potential spin crossover behavior of the Fe(II) complexes **C3'**, **C4** and **C5**, as well as slow relaxation of magnetization of the Co(II) analogue **C6**. Although no magnetic measurements could be performed with the Fe(II) complexes, the crystal structures give an insight into the spin states of the Fe(II) ions. While the {N$_2$O$_4$} donor set is assumed to hinder the spin transition in **C3**, this donor set provides a suitable coordination sphere and ligand field to promote SIM behavior. This furthermore shows the versatile properties of complexes with **L2** when using the appropriate transition metal ion.

4 Results and Discussion: Spin Crossover and Single-Ion Magnets

In the second part of the thesis, the synergy between the spin crossover phenomenon and the slow relaxation of magnetization of single-ion magnets was investigated. Therefore, two synthetic approaches to form discrete trinuclear [SIM-SCO-SIM] complexes were pursued following the copper(I)-catalyzed azide-alkyne cycloaddition and the 'designer' ligand approach. In both cases, the Co(II) bis-terpyridine moiety serves as central spin crossover building block where the ligand backbone was decorated according to the synthetic approach.

4.1 Approach I: CuAAC

The CuAAC approach to form trinuclear Co(II) complexes showing SCO and SIM behavior was pursued on the basis of previous work from our group demonstrating successful click reactions of the apropriate building blocks (see Chapter 1.3.2). Therefore, the mononuclear Co(II) complex [Co^{II}(**L4**)(oda)] with **L4** = 4'-ethynyl-2,2':6',2''-terpyridine was intended as SIM building block.[229] To complement the crucial precursors for the CuAAC approach, 4'-azido-2,2':6',2''-terpyridine (**L3**) was envisioned as ligand for the SCO building block [Co^{II}(**L3**)$_2$]X$_2$. Such a ligand is desirable as both the synthesis routes towards 4'-functionalized terpyridines and the spin crossover behavior of the related Co(II) bis-terpyridine complexes are well described in the literature.

4.1.1 The Terpyridine Ligand Systems

The synthesis of the ligands 4'-azido-2,2':6',2''-terpyridine **L3** and 4'-ethynyl-2,2':6',2''-terpyridine **L4** was performed according to the established procedures in our group in five and six steps, respectively.[229]

Both syntheses start from the terpyridinone **48**, which was initially synthesized in a ring-building reaction sequence starting from 2-ethyl picolinate **45** and acetone **46**. A twofold Claisen condensation gave 1,5-bis-(2'-pyridyl)-pentane-1,3,5-trione **47**, which was further reacted with ammonium acetate under reflux conditions yielding in 2,2':6',2''-terpyridin-4'(1'*H*)-one **48** in overall 74% yield.[306]
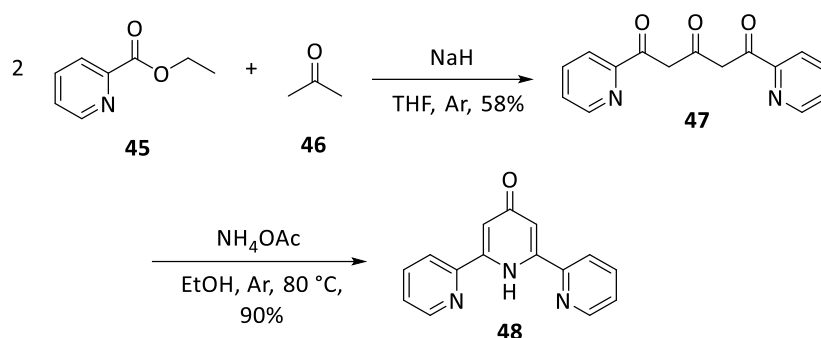
*Scheme 11 The first two steps of the synthesis of **L3** and **L4**.*[306]

L3 was synthesized in three steps starting from terpyridinone **48** (see Scheme 12). Aromatization of **48** was achieved with phosphorus pentachloride and phosphorylchloride giving the chlorinated 4'-chloro-2,2':6'2''-terpyridine **49** in 75% yield.[306] Nucleophilic substitution of the chloride function with hydrazine hydrate yielded in 4'-hydrazino-2,2':6'2''-terpyridine **50**. The azide substituted ligand **L3** was finally obtained in 91% yield by condensation of **50** with sodium nitrite under acetic acid mediation.[307]

To establish the ethynyl substituent on ligand **L4** another synthesis route starting from terpyridinone **48** was chosen. In order to implement a suitable leaving group onto the terpyridine framework for the Sonogashira coupling reaction, terpyridinone **48** was aromatized using trifluoromethanesulfonic anhydride in 79% yield.[308] The triflate group was subsequently substituted by iodide leading to 4'-iodo-2,2':6',2''-terpyridine **52**, which was afterwards subjected to a Sonogashira coupling with trimethylsilylacetylene. The reaction was catalyzed by bis(triphenylphosphine)-palladium(II) dichloride, copper(I) iodide and diisopropylamine (DIPA) under inert conditions.[309] In the last step the acetylene **53** was deprotected by potassium carbonate to yield in 4'-ethynyl-2,2':6',2''-terpyridine **L4** in quantitative yield.[310]
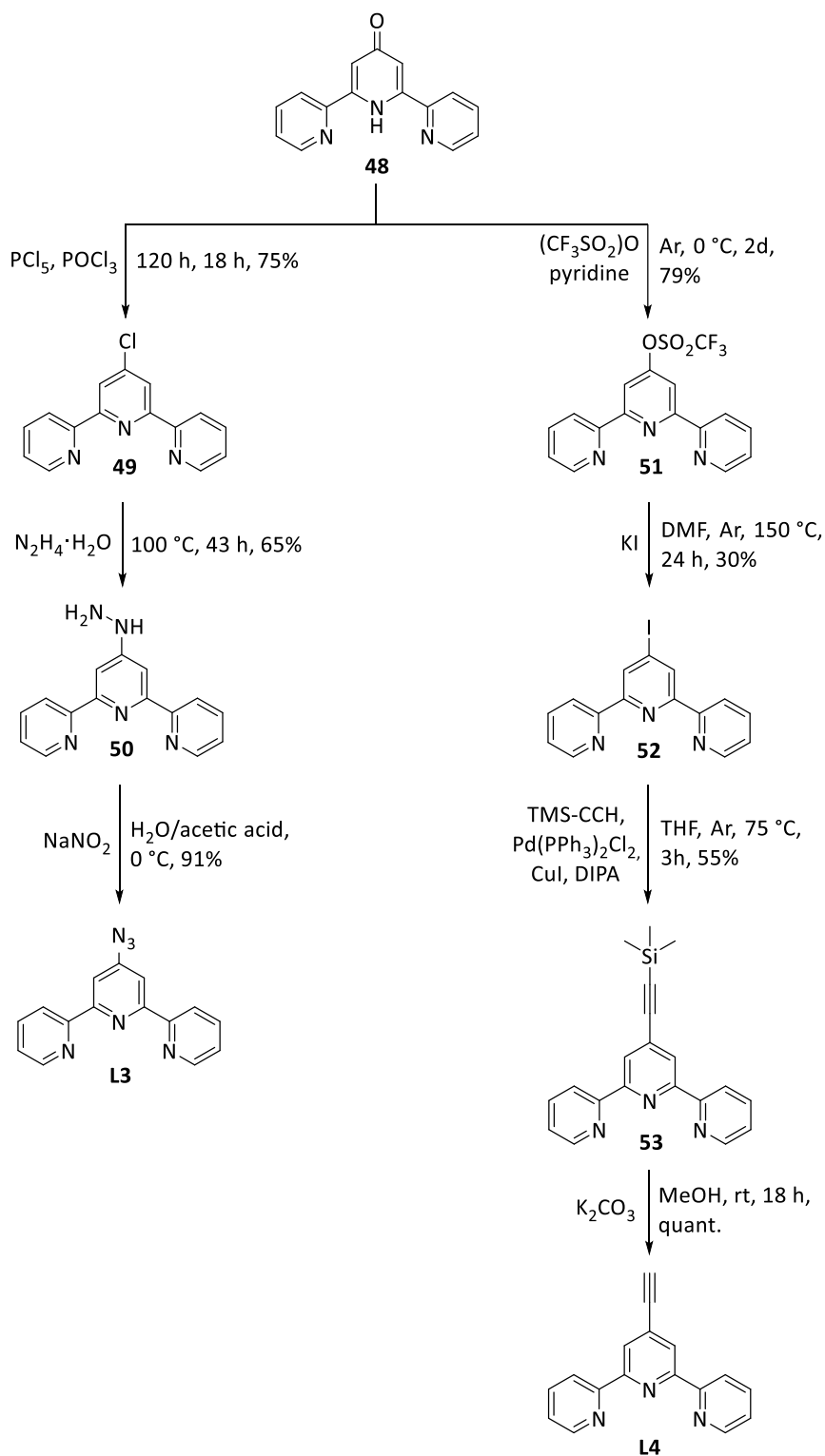
*Scheme 12 Synthesis route for the ligands 4'-azido-2,2':6'2''-terpyridine **L3** and 4'-ethynyl-2,2':6',2''-terpyridine **L4**.[306–310]*

4.1.2 The Spin Crossover Moiety

To investigate the spin crossover behavior of Co(II) complexes with **L3**, the compounds were synthesized using various anions (see Table 9). Co(II) complexes with isostructural 4'-bromo-2,2':6',2''-terpyridine (Brterpy) with a comparable strength of the inductive effect[311] and thus ligand field strength were additionally synthesized to distinguish the steric influence of the 4'-substituent on the crystal packing and the magnetic properties. The ligand Brterpy was previously synthesized in our group by ■■■■■■ and ■■■■■■.

The solutions of the ligand **L3** or Brterpy in chloroform and the appropriate Co(II) or Zn(II) salt in methanol led to the subsequent precipitation of the products. The powders were further investigated by IR and UV-Vis spectroscopy, ESI mass spectrometry and ^{1}H-NMR spectroscopy in case of the Zn(II) complex. Single crystals were obtained for the complexes **C11**, **C15** and **C16**.

*Table 9 List of the synthesized [M^{II}(**L3**)$_2$]X$_2$ and [Co^{II}(Brterpy)$_2$]X$_2$ complexes.*

C7	[Co^{II}(**L3**)$_2$](ClO$_4$)$_2$	**C12**	[Co^{II}(**L3**)$_2$]SO$_4$
C8	[Co^{II}(**L3**)$_2$](PF$_6$)$_2$	**C13**	[Co^{II}(**L3**)$_2$](BF$_4$)$_2$
C9	[Co^{II}(**L3**)$_2$]Br$_2$	**C14**	[Zn^{II}(**L3**)$_2$](ClO$_4$)$_2$
C10	[Co^{II}(**L3**)$_2$]Cl$_2$	**C15**	[Co^{II}(Brterpy)$_2$](ClO$_4$)$_2$
C11	[Co^{II}(**L3**)$_2$](SCN)$_2$	**C16**	[Co^{II}(Brterpy)$_2$](PF$_6$)$_2$

^{1}H-NMR Spectroscopy

The ^{1}H-NMR of **C14** in DMSO-d_6 is shown in Figure 67. Due to the low solubility of the complex resulting in a very low signal-to-noise ratio, further characterization of the complex using ^{13}C-NMR and related two-dimensional HSQC and HMBC experiments was not possible. The shifts in the ^{1}H-NMR were assigned according to literature known Zn(II) complexes.[247,312]

Five different aromatic signals are present in the range from 9.0 to 7.5 ppm. The *ortho-* and *para*-position of H6/H6'' and H4/H4'' in relation to the internal nitrogen atom N1 cause a downfield shift to 8.97 ppm and 7.89 ppm, stronger pronounced in the *ortho*-positions due to the strong inductive effect of the neighboring nitrogen. In contrast to that, the protons H5/H5'' in *meta*-position are weakly affected by the nitrogen leading to a shift of 7.50 ppm. The strong downfield shift of H3/H3'' and H3'/H5' to 8.81 ppm and 8.26 ppm respectively is presumably caused by the ring current of the neighbored aromatic ring.
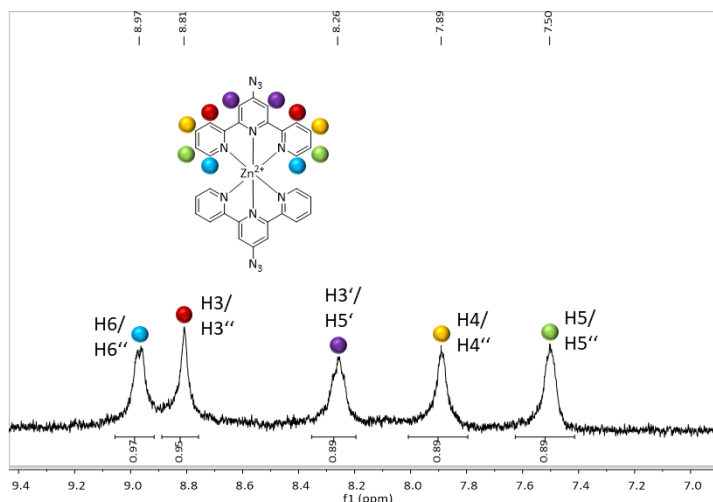
*Figure 67 ^{1}H-NMR spectrum in DMSO-d$_6$ and the molecular structure of the cation of **C14**.*

Spin Crossover Behavior

The temperature-dependent magnetic susceptibility was recorded for all Co(II) complexes with **L3** or Brterpy. The experimental data at 2 K and 300 K as well as the spin states are listed in Table 10 and the $\chi_M T$ versus T plots are shown in Figure 68.

The complexes **C7**, **C8**, **C9**, **C10**, **C13**, **C15** and **C16** show comparable spin crossover behavior as the $\chi_M T$ values gradually increase for higher temperatures. The values of 0.33 to 0.71 cm³ K mol^{-1} at 2 K confirm the LS state of all spin crossover complexes at low temperatures. The spin-only value amounts 0.38 cm³ K mol^{-1} with S = 1/2 and g = 2.0 (see Equations 17 and 18). Higher experimental values can be explained by a larger g-value, unquenched orbital angular contribution, or a partial occupation of the HS state. The complexes **C7**, **C8**, **C13** and **C15** show a steeper spin transition whereas the spin crossover is more gradual for **C9**, **C10** and **C16**. No SCO complex shows a complete transition until 300 K as the $\chi_M T$ value does not saturate. The comparison of the ligands **L3** and Brterpy does not reveal a significant influence of the substituent in 4'-position, which is consistent with the literature when considering the inductive effect and its influence on the ligand field strength.[90] In contrast, the non-coordinating anions determine the spin transition because for the complexes **C11** and **C12** no spin transition is observed. While **C12** stays in the LS state with $\chi_M T$ = 0.23 cm³ K mol^{-1}, **C11** is present in the HS state ($\chi_M T$ = 3.24 cm³ K mol^{-1}) over the whole temperature range.[90] The magnetic behavior of **C11** will be discussed in detail at the end of the chapter.

*Table 10 Experimental temperature-dependent magnetic susceptibility data of the [Co^{II}(**L3**)$_2$]X$_2$ complexes.*

		$\chi_M T$ [cm³ K mol^{-1}] at 2 K	$\chi_M T$ [cm³ K mol^{-1}] at 300 K	Spin state
C7	[Co^{II}(**L3**)$_2$](ClO$_4$)$_2$	0.64	1.79	SCO
C8	[Co^{II}(**L3**)$_2$](PF$_6$)$_2$	0.51	1.53	SCO
C9	[Co^{II}(**L3**)$_2$]Br$_2$	0.40	0.97	SCO
C10	[Co^{II}(**L3**)$_2$]Cl$_2$	0.33	0.84	SCO
C11	[Co^{II}(**L3**)$_2$](SCN)$_2$	1.78	3.24	HS
C12	[Co^{II}(**L3**)$_2$]SO$_4$	0.17	0.31	LS
C13	[Co^{II}(**L3**)$_2$](BF$_4$)$_2$	0.50	1.38	SCO
C15	[Co^{II}(Brterpy)$_2$](ClO$_4$)$_2$	0.40	1.28	SCO
C16	[Co^{II}(Brterpy)$_2$](PF$_6$)$_2$	0.71	1.47	SCO
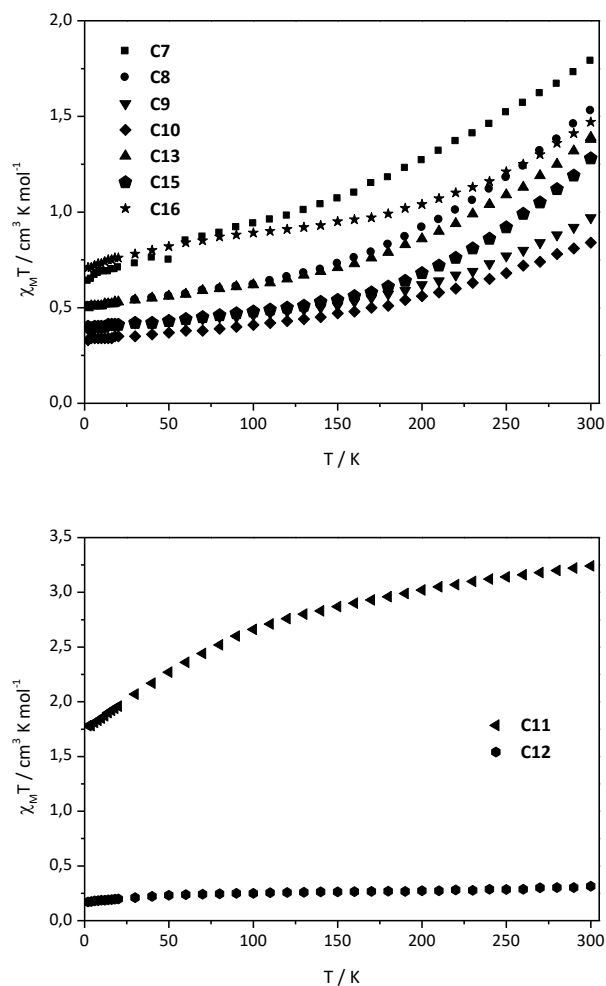
*Figure 68 Temperature-dependent magnetic behavior of the [Co^{II}(**L3**)$_2$]X$_2$ and [Co^{II}(Brterpy)$_2$]X$_2$ complex series. Top: $\chi_M T$ versus T plot of the complexes **C7**, **C8**, **C9**, **C10**, **C13**, **C15** and **C16** showing gradual spin crossover behavior. Bottom: $\chi_M T$ versus T plot of the complexes **C11** and **C12** in the HS and LS state, respectively.*

Temperature-dependent UV-Vis Spectroscopy

To confirm the spin crossover, temperature-dependent solid-state UV-Vis spectra were recorded exemplarily for **C7**, which are shown in Figure 69. The UV-Vis measurements were performed in barium sulfate in the temperature range of −30 °C to +80 °C. The maxima at 37 300 cm^{-1} and 30 900 cm^{-1} can be assigned to π-π^* and n-π^* transitions of the ligand's conjugated aromatic system.[313] The absorption maxima at 22 000 cm^{-1}, 19 400 cm^{-1} and 18 200 cm^{-1} refer to MLCT transitions of the LS Co(II) complex. The maximum at 14 500 cm^{-1} is attributed to the spin-allowed d-d transition $^2A_1 \rightarrow {}^2E$ of the LS species.[93] The decreasing intensity with increasing temperature is in good accordance with a thermal spin crossover as the content of the LS species decreases.[314] Assuming the spin-only value of 0.38 cm^3 K mol^{-1} and 3.24 cm^3 K mol^{-1} (**C11**) for 100% of the LS and HS state, respectively, at 300 K the LS:HS ratio is about 1:1 with 1.79 cm^3 K mol^{-1}, which explains the present LS characteristic bands.
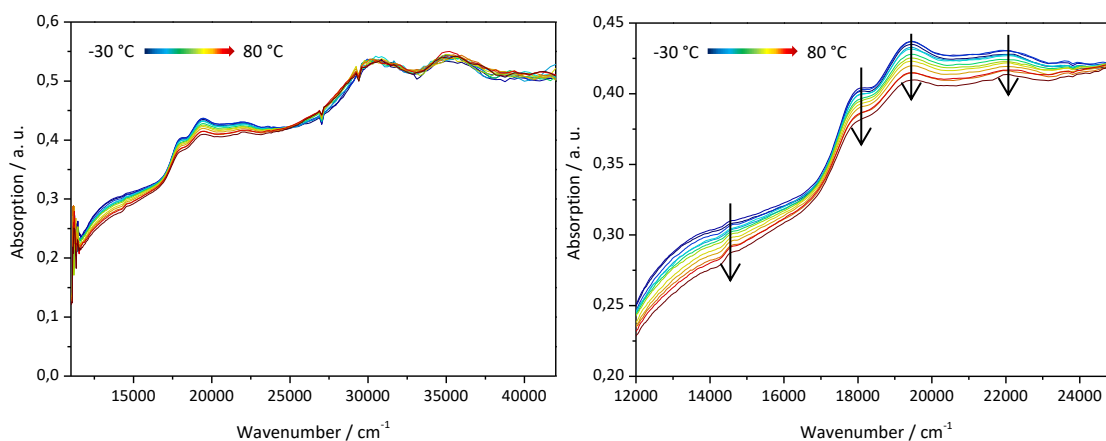
*Figure 69 Solid-state UV-Vis spectrum of **C7** in barium sulfate from −30 °C to +80 °C. Left: in the range of 42 000 cm^{-1} to 11 000 cm^{-1}. Right: in the range of 25 000 cm^{-1} to 12 000 cm^{-1}.*

Crystal Structures

Next to the magnetic properties, the crystal structures of the complexes **C11**, **C15** and **C16** were investigated.

Red crystals of [Co^{II}(**L3**)$_2$](SCN)$_2$·H$_2$O **C11** have formed after several weeks by reacting cobalt(II) thiocyanate in methanol and **L3** in chloroform followed by evaporation of the solvent. **C11** crystallizes in the space group *Pbca* at 100 K. The asymmetric unit consists of the mononuclear Co(II) complex, where two tridentate meridional **L3** ligands form the octahedral coordination sphere with a {N$_6$} donor set, two non-coordinating thiocyanate counterions and one lattice water molecule. One thiocyanate anion and the lattice water molecule are disordered.
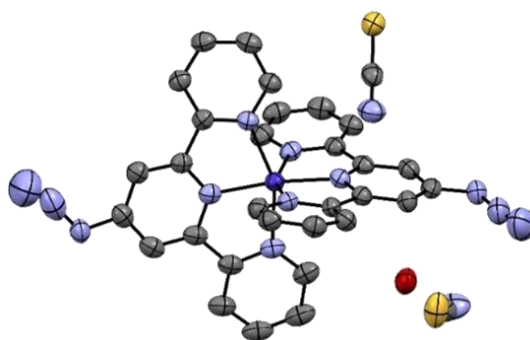
*Figure 70 Asymmetric unit of **C11**. Color code: grey – C, violet – N, yellow – S, red – O, dark blue – Co(II). Hydrogen atoms and disordered molecules are omitted for clarity. ORTEP representation with atomic displacement parameters at 50% level of probability.*

The distances to the central nitrogen donor atoms are short with Co1–N1 = 1.983(3) Å and Co1–N8 = 1.981(3) Å, whereas the distal bond lengths are larger with Co–N_{distal} > 2.1 Å, leading to a compressed octahedral coordination sphere (see Table 11). The *cis*-angles within one ligand are in the range of N–Co–N = 77.72(12) – 78.05(12)°. The deviation of 90° is large with Σ_0 = 112.83°. Continuous shape measurements approve the highly distorted octahedral surrounding with a large value of 3.48. The bond lengths, the large difference between the Co–N_{distal} and Co–$N_{central}$ distances as well as the high octahedral distortion parameter confirm the HS state of the Co(II) ion at 100 K.[105,315]

*Figure 71 The {CoN_6} octahedron of **C11** compared to the perfect polyhedron calculated by CShM. Color code: violet – N, dark blue – Co(II).*

*Table 11 Selected bond lengths and angles of **C11** at 100 K.*

		C11
Co–L [Å]	Co1–N1	2.108(3)
	Co1–N2	1.983(3)
	Co1–N3	2.101(3)
	Co1–N7	2.131(3)
	Co1–N8	1.981(3)
	Co1–N9	2.109(3)
L–Co–L [°]	N1–Co1–N2	77.72(12)
	N2–Co1–N3	77.55(12)
	N7–Co1–N8	78.05(12)
	N8–Co1–N9	77.73(12)
Σ_0 [°]	112.83	
CShM	3.48	

The non-coordinating thiocyanate anions and solvent molecules are connected by hydrogen bonds and result in anion layers within the *ab* plane as illustrated in Figure 72. The O–N

distances are 2.8 Å (red dotted line) and 3.0 Å (blue dotted line). The layers of the complex cations are separated by a short distance of 8.902 Å with respect to the Co(II) ions. There is no direct interaction between the layers.
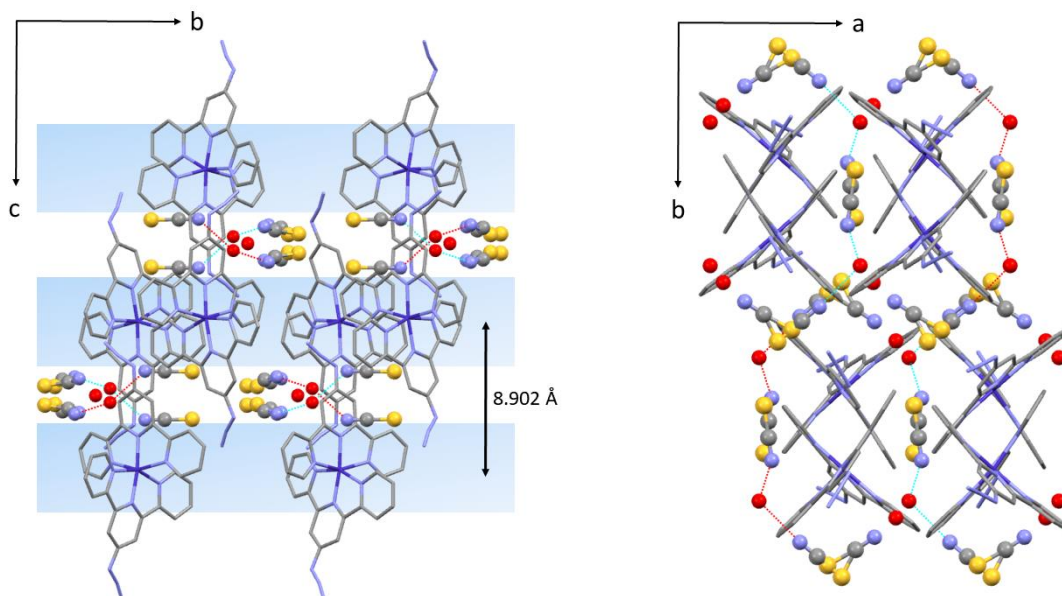

*Figure 72 Packing of **C11**. Left: view along the a-axis. Right: view along the c-axis. The thiocyanate anions and water molecules are disordered and represented as ball and stick for better overview and to highlight the hydrogen bonding (red and blue dotted lines). Color code: grey – C, violet – N, yellow – S, red – O, dark blue – Co(II).*

The reaction of Brterpy and cobalt(II) perchlorate hexahydrate in a methanol/chloroform solvent mixture yielded in red single crystals of [Co^{II}(Brterpy)$_2$](ClO$_4$)$_2$ **C15** after several months by evaporation of the solvent. The complex **C15** crystallizes in the monoclinic space group *Cc* (173 K). The asymmetric unit consists of the mononuclear Co(II) complex cation with two meridional coordinated 4'-bromo-2,2':6',2''-terpyridine ligands as well as two non-coordinating perchlorate anions for charge balance.
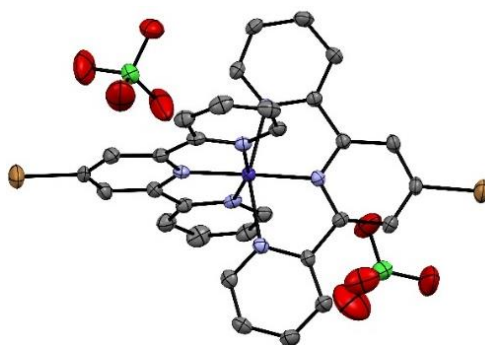
*Figure 73 Asymmetric unit of **C15**. Color code: grey – C, violet – N, red – O, brown – Br, green – Cl, dark blue – Co(II). Hydrogen atoms are omitted for clarity. ORTEP representation with atomic displacement parameters at 50% level of probability.*

The average Co–N$_{central}$ and Co–N$_{distal}$ distances are 1.902 Å and 2.078 Å. The average *cis*-angle is N–Co–N$_{av}$ = 80.1°. With Σ_0 = 89.34° and CShM = 2.23, the octahedron is less distorted than **C11**. Also, the Co–N$_{central}$ and Co–N$_{distal}$ bond lengths are shorter, which confirms the LS of **C15** state at 173 K.[104]
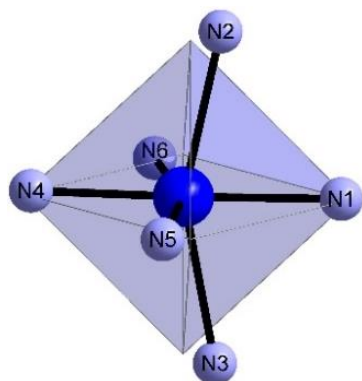

*Figure 74 The {CoN$_6$} octahedron of **C15** compared to the perfect polyhedron calculated by CShM. Color code: violet – N, dark blue – Co(II).*

*Table 12 Selected bond lengths and angles of **C15** at 173 K.*

		C15
Co–L [Å]	Co1–N1	1.934(5)
	Co1–N2	2.151(4)
	Co1–N3	2.160(5)
	Co1–N4	1.869(5)
	Co1–N5	2.005(5)
	Co1–N6	1.995(5)
L–Co–L [°]	N1–Co1–N2	78.56(18)
	N1–Co1–N3	78.99(18)
	N4–Co1–N5	81.2(2)
	N4–Co1–N6	81.5(2)
Σ_0 [°]	89.34	
CShM	2.23	

The complex cations form a layered structure within the *ab* plane. The layers are separated by the perchlorate anions as shown in Figure 75. The distance is 10.024 Å with respect to the Co(II) ions. There is no direct interaction between the layers.
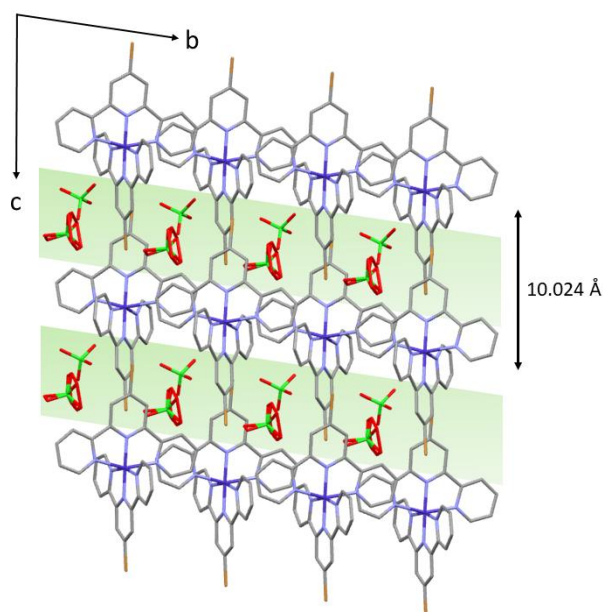
*Figure 75 Structure of **C15**, view along the a-axis highlighting the cation and anion layers. Color code: grey – C, violet – N, brown – Br, green – Cl, dark blue – Co(II). Hydrogen atoms are omitted for clarity.*

Within the cation layer, the neighboring terpyridine moieties are assembled by π-π (centroid–centroid distance = 3.534 Å) and CH-π interactions (H–centroid distance = 2.436 Å) as shown in Figure 76. Such an arrangement is typical for [M(terpy)$_2$]X$_2$ complexes as shown by the group of Figgis in 1986.[104,105]
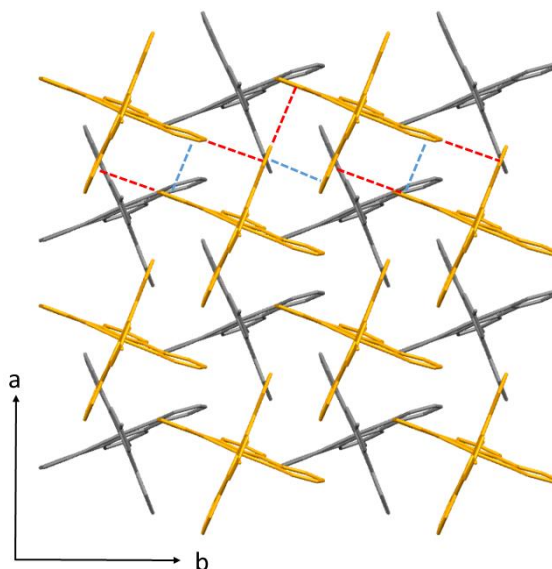

*Figure 76 Structure of **C15**. The colors highlight the layers formed by the complex cations and the π-π (blue dotted lines) as well as CH-π (red dotted line) interactions.*

The complex [Co^{II}(Brterpy)$_2$](PF$_6$)$_2$ **C16** was synthesized by mixing Brterpy and Co(II) solutions in chloroform and methanol, and subsequently adding a methanolic ammonium hexafluorophosphate solution. The obtained precipitate was dissolved in acetonitrile. Single crystals formed after two weeks by diffusion of diethyl ether into the solution. **C16** crystallizes in the tetragonal space group $P\bar{4}2_1c$ at 100 K. The asymmetric unit consists of the Co(II) bis-terpyridine complex cation and two non-coordinating hexafluorophosphate anions for charge balance. Like for **C15**, no solvent is present in the crystal structure.
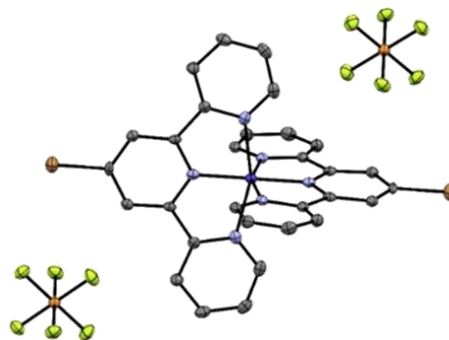
*Figure 77 Asymmetric unit of **C16**. Colour code: grey – C, violet – N, brown – Br, light green – F, orange – P, dark blue – Co(II). Hydrogen atoms are omitted for clarity. ORTEP representation with atomic displacement parameters at 50% level of probability.*

The Co-$N_{central}$ and Co-N_{distal} bond lengths are 1.890(4) Å as well as 2.088(2) Å and the *cis*-angle within the ligand is 80.15(7)°. The distortion is low with Σ_0 = 85.52° and CShM = 2.35, hinting to the LS state at 100 K which is in good accordance with the magnetic data.

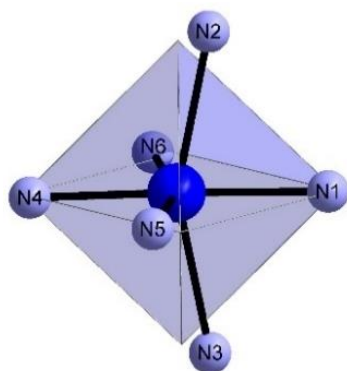*Figure 78 The {CoN$_6$} octahedron of **C16** compared to the perfect polyhedron calculated by CShM. Color code: violet – N, dark blue – Co(II).*

Table 13 Selected bond lengths and angles of **C16** at 100 K.

		C16
Co–L [Å]	Co1–N1	1.890(4)
	Co1–N2	2.088(2)
	Co1–N3	2.088(2)
	Co1–N4	1.890(4)
	Co1–N5	2.088(2)
	Co1–N6	2.088(2)
L–Co–L [°]	N1–Co1–N2	80.15(7)
	N2–Co1–N3	80.15(7)
	N4–Co1–N5	80.15(7)
	N5–Co1–N6	80.15(7)
Σ_0 [°]		85.52
CShM		2.35

Similar to **C15**, the complex cations form layers within the *ab* plane, which are separated by the hexafluorophosphate anions. There are no interactions between the layers.
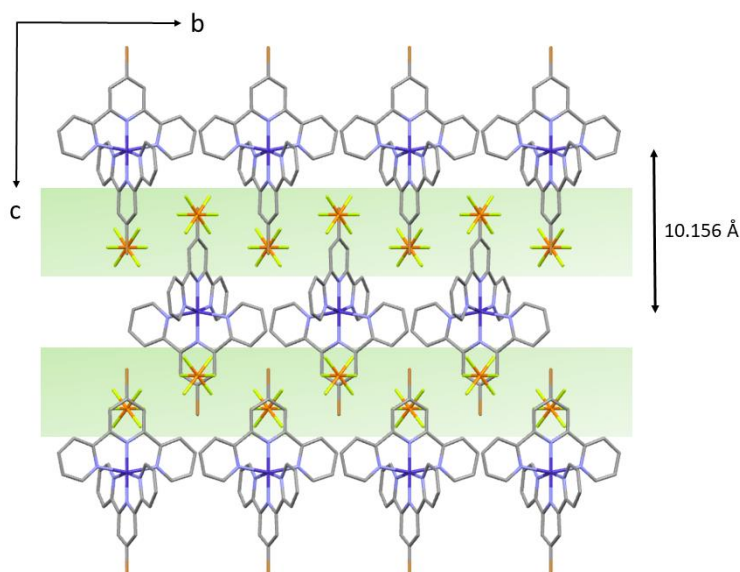
*Figure 79 Structure of **C16** along the c-axis highlighting the cation and anion layers. Colour code: grey – C, violet – N, brown – Br, light green – F, orange – P, dark blue – Co(II). Hydrogen atoms are omitted for clarity.*

Within one layer, π-π and CH-π interactions are found between two terpyridyl moieties of neighboring complex cations (centroid–centroid = 3.504 Å and H–centroid = 2.687 Å).
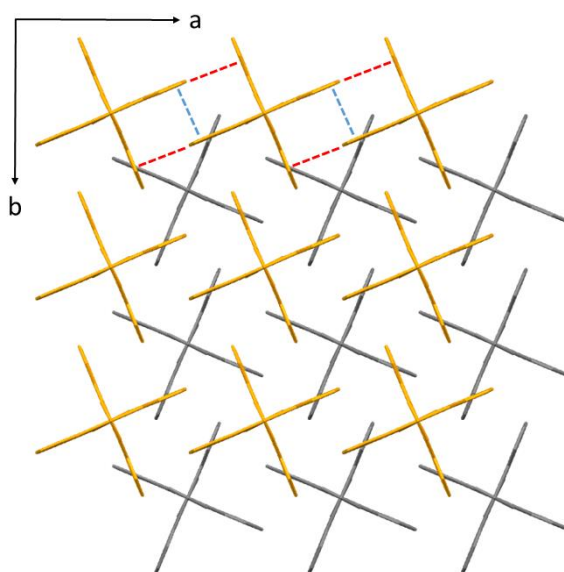

*Figure 80 Structure of **C16**. The colors highlight the layers formed by the complex cations and the π-π (blue dotted lines) as well as CH-π (red dotted line) interactions.*

The most important structural aspects of **C11**, **C15** and **C16** are summarized in Table 14. The distances of the distal and central Co–N bonds in relation to the $\chi_M T$ value are in good accordance with previous findings of [Co^{II}(terpy)$_2$]X$_2$ systems.[105] The structures of the complexes **C15** and **C16** with the ligand Brterpy are comparable regarding the layered structure as well as the π-π and CH-π interactions between the complex cations within one layer. Similar structures are found for example for the reported non-substituted [Co^{II}(terpy)$_2$](ClO$_4$)$_2$·3H$_2$O and [Co^{II}(terpy)$_2$]I$_2$·2H$_2$O complexes.[105] Hydrogen bonds between the non-coordinating water and anion molecules are found in **C11** but π-π-interactions between the complex cations are lacking. These structural aspects could be the reason for the different magnetic behavior of **C11** and **C15/C16**.

*Table 14 Structural data of **C11**, **C15** and **C16**.*

	[Co^{II}(**L3**)$_2$](SCN)$_2$·H$_2$O **C11**	[Co^{II}(Brterpy)$_2$](ClO$_4$)$_2$ **C15**	[Co^{II}(Brterpy)$_2$](PF$_6$)$_2$ **C16**
Co-N$_{distal}$ [Å]	2.121	2.078	2.088
Co-N$_{central}$ [Å]	1.981	1.902	1.890
Σ_0 [°]	112.83	89.34	85.52
CShM	3.483	2.225	2.353
T [K]	100	173	100
Spin state	HS	LS	LS

Slow Relaxation of Magnetization in C11

The structural and magnetic data of **C11** reveal the HS state over the whole temperature range of 300 – 2 K. The $\chi_M T$ value of 3.24 cm³ K mol^{-1} at 300 K is in good agreement with the literature including orbital contribution.[226] The $\chi_M T$ value decreases for lower temperatures to 1.78 cm³ K mol^{-1} pointing towards pronounced zero-field splitting.
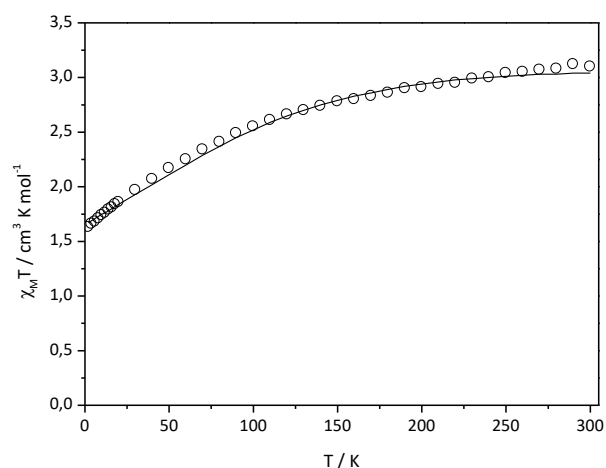

*Figure 81 Temperature-dependent magnetic susceptibility measurement of **C11**, $\chi_M T$ vs. T plot. ○ experimental data, – fit with Δ = +53 cm^{-1} (g = 2.0, α = 1.27, λ = −180 cm^{-1} were kept constant).*

The temperature-dependent magnetic susceptibility was fitted using the Hamiltonian in Equation 23.[262] The g-factor of 2.0, the orbital reduction α = 1.27 and the spin-orbit coupling λ = −180 cm^{-1} were kept constant. The crystal field parameter was fitted with Δ = +53(5) cm^{-1} (R = 4.22 · 10^{-2}). The positive value of the crystal field parameter is in good agreement with the compressed octahedral surrounding as the central Co–N distances are about 0.14 Å shorter than the distal Co–N bond lengths and each *cis*-angles highly deviate from the right angle of up to 12.45°.[226]

Next to the magnetic susceptibility, the field-dependent magnetization was measured, which is shown in Figure 82. At 2 K and 7 T, the magnetization saturates to 2.23 N$_A\mu_B$, which is in good agreement to the literature considering HS Co(II) ions with S = 3/2 and pronounce magnetic anisotropy.[316] The non-superposition of the temperature-dependent reduced magnetization confirms the presence of significant magnetic anisotropy as a result of zero-field splitting. The *M* versus *H* and *M* versus *H/T* plots were fitted with the spin Hamiltonian in Equation 26 using the S = 3/2 multiplet to describe the axial and rhombic zero-field splitting parameter. The best results of the fit were g = 2.392(3), D = +38.2(11) cm^{-1} and E = +9.16(26) cm^{-1} with R = 1.25 · 10^{-2}. The positive sign of the axial ZFS parameter D is in good accordance with the crystal field parameter Δ being larger than zero and the compressed octahedral coordination sphere.

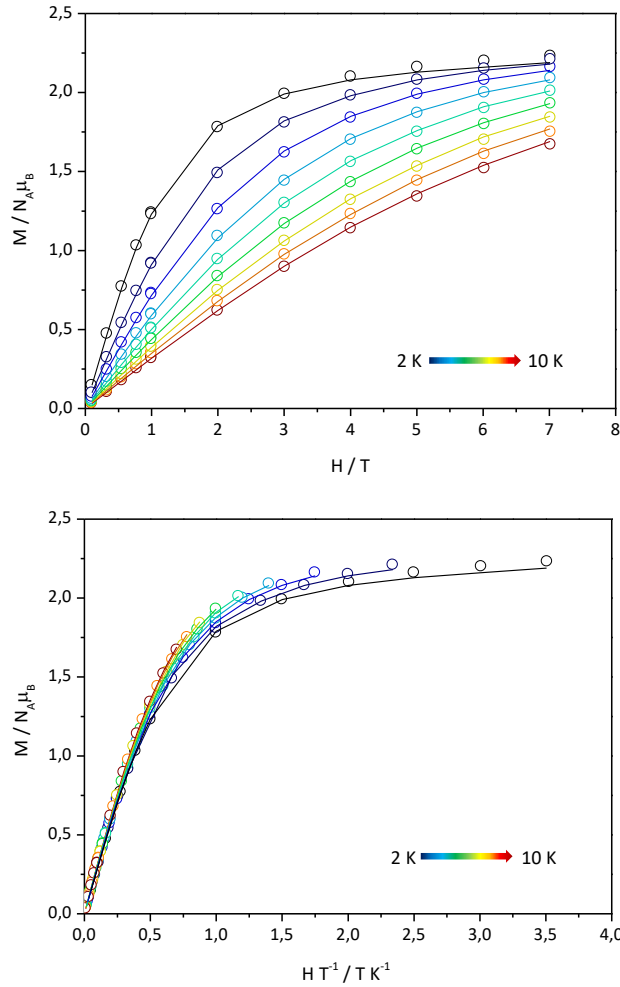*Figure 82 Field- and temperature-dependent magnetization measurement of **C11**. Top: M vs. H plot. Bottom: M vs. H/T plot. ○ experimental data, – fit with g = 2.39, D = +38.21 cm^{-1} and E = +9.16 cm^{-1}.*

As the magnetic data hint at pronounced magnetic anisotropy, ac susceptibility measurements were performed. An out-of-phase signal χ'' was not observed at zero-field but with an applied dc field. The highest signal of the out-of-phase susceptibility was found at H_{dc} = 1600 Oe. The temperature-dependent measurements were performed from 1.9 K to 3.0 K. Due to missing maxima in the Cole-Cole plot, the relaxation time could not be fitted precisely. Therefore, the effective energy barrier U_{eff} was estimated by the following relationship:[317]

$$\ln\left(\frac{\chi''}{\chi'}\right) = \ln(2\pi\nu\tau_0) + \frac{U_{eff}}{k_B}\cdot\frac{1}{T} \tag{28}$$

Here, the χ_S value of the generalized Debye model is neglected, and the relaxation time strictly follows the Arrhenius law (α = 0). This evaluation method requires several assumptions and simplifications, as the exclusion of tunneling processes, but gives an insight into the height of

the effective energy barrier U_{eff}. The $\ln(\chi''/\chi')$ term is plotted against the inverse temperature $1/T$ for various frequencies. The experimental data of the frequencies 893 Hz, 565 Hz and 361 Hz were fitted with the program Origin7.5 and plotted in Figure 83. The linear fits lead to a reasonable estimated effective energy barrier of U_{eff} = 4.4 K (3.1 cm^{-1}) with τ_0 = 5.28 · 10^{-6} s. The values of the fits are listed in Table 15.
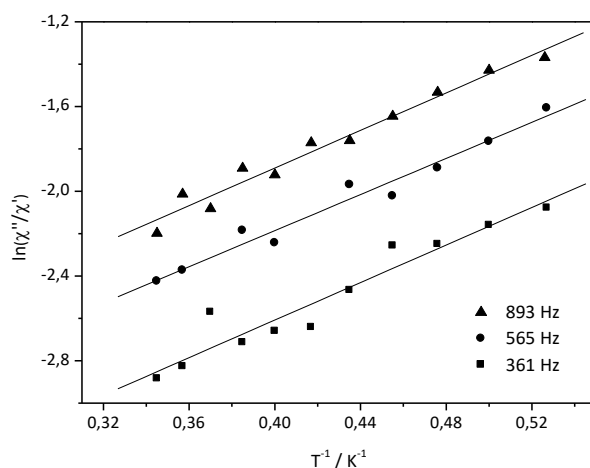

*Figure 83 $\ln(\chi''/\chi')$ vs. 1/T plot of **C11** with an applied dc field of H_{dc} = 1600 Oe. ▲ 893 Hz, ● 565 Hz, ■ 361 Hz, − linear fit.*

Table 15 Values of the linear fit for the different frequencies.

	$\ln(2\pi\nu\tau_0)$	τ_0 [s]	U_{eff}/k_B [K]	U_{eff} [cm^{-1}]	R
893 Hz	-3.6(1)	4.56 · 10^{-6}	4.4(3)	3.1	9.68 · 10^{-1}
565 Hz	-3.9(1)	5.76 · 10^{-6}	4.3(3)	3.0	9.84 · 10^{-1}
361 Hz	-4.4(2)	5.52 · 10^{-6}	4.4(4)	3.1	9.59 · 10^{-1}

The height of the effective energy barrier cannot be explained by the thermal energy barrier created by the axial and rhombic zero-field splitting. The theoretical energy difference is $|2D'|$ = 82.75 cm^{-1}, much higher than the experimental one. Thus, despite of the applied dc field, tunneling effects cannot be neglected for sure. Other processes such as a phonon bottleneck process in case of available resonant lattice vibration modes are possible,[318] but cannot be determined with the available data set.

4.1.3 The Single-Ion Magnet Building Block

The SIM building block is formed by the reported and previously described mononuclear complex [Co^{II}(**L4**)(oda)] **C17**, which shows slow relaxation of magnetization with an effective energy barrier of U_{eff} = 28 K (19.5 cm^{-1}) at an applied dc field of 1000 Oe. Due to the acetylene substituent on the 4'-position of the terpyridine ligand, the SIM is suitable for the CuAAC reaction.[229]

Additionally, the structurally similar Co(II) complex **C18** was synthesized. The oxydiacetic acid (H$_2$oda) was replaced with pyridine-2,6-dicarboxylic acid (H$_2$dipic) to increase the solubility in common organic solvents and to enable better conditions for the click reaction with the azide-substituted spin crossover moiety [Co^{II}(**L3**)$_2$](ClO$_4$)$_2$ **C7** as well as the crystallization of the clicked product. Complex **C18** was synthesized by layering an aqueous solution of H$_2$dipic, sodium carbonate and cobalt(II) chloride hexahydrate on top of a solution of 4'-ethynyl-2,2':6',2''-terpyridine **L4** in chloroform. The obtained brown precipitate was subsequently dissolved in a solvent mixture of dimethylformamide and dichloromethane to form yellow crystals by evaporation of the solvent. Due to the small amount of single crystals, the crystal structure but not the potential SIM behavior of **C18** could be investigated. The mononuclear complex crystallizes as [Co^{II}(dipic)(**L4**)]·3H$_2$O in the monoclinic space group *P*21/*c* (120 K). The asymmetric unit consists of one neutral complex molecule and three disordered water molecules. The charge of the Co(II) ion is counterbalanced by the twice deprotonated pyridine-2,6-dicarboxylic acid.
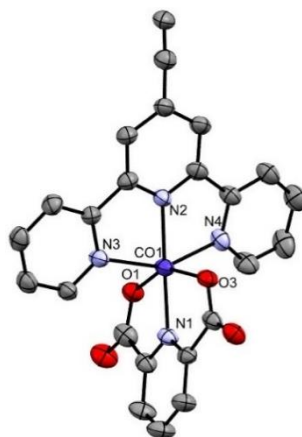

*Figure 84 Molecular structure of complex **C18**. Color code: grey – C, violet – N, red – O, dark blue – Co(II). Hydrogen atoms and non-coordinating water molecules are omitted for clarity. ORTEP representation with atomic displacement parameters at 50% level of probability.*

The Co–L bond lengths are in the range of 2.058(6) – 2.163(6) Å, whereas the Co–N$_{central}$ bond lengths are shorter than the distal distances for both ligands (see Table 16). In general, the bond lengths of **C18** are larger in comparison to **C17** with Co–L = 2.05 – 2.14 Å.[229] The *cis-*

angles within one ligand are in the range of 75.9(2) – 76.3(2)° and much smaller than 90°. The total deviation of the twelve *cis*-angles is Σ_0 = 128.96°. The high deviation parameter arises from the large tilt of 164.18° between the ligands **L4** and dipic^{2-} towards each other, which is confirmed by continuous shape measurements with CShM = 5.34. The complex is much more distorted then **C17**, as it exhibits a larger CShM value compared to 4.23.[229] The bond lengths, the deviation and the comparison with the magnetically characterized complex **C17** indicate the HS state of the Co(II) ion in **C18**.[104]
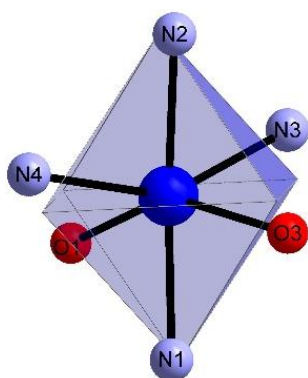
*Figure 85 The {CoN$_4$O$_2$} octahedron of **C18**, deviation of the perfect polyhedron calculated by CShM. Color code: violet – N, red – O, dark blue – Co(II).*

*Table 16 Selected bond lengths and angles of **C18** at 120 K.*

		C18
Co–L [Å]	Co1–N1	2.020(6)
	Co1–O1	2.144(5)
	Co1–O3	2.157(5)
	Co1–N2	2.058(6)
	Co1–N3	2.163(6)
	Co1–N4	2.127(6)
L–Co–L [°]	N1–Co1–O1	75.9(2)
	N1–Co1–O3	76.1(2)
	N2–Co1–N3	76.3(2)
	N2–Co1–N4	76.0(2)
Σ_0 [°]	128.96	
CShM	5.34	

Within the unit cell, the complexes align antiparallel to each other, because of π-π-stacking of bipyridyl moieties of two terpyridine ligands with a distance of 3.4 Å. The Co–Co distance is short with 7.581 Å.
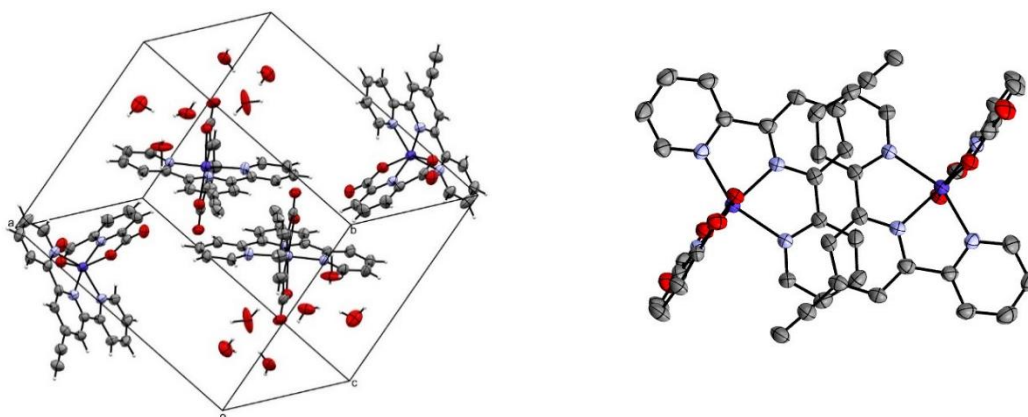

*Figure 86 Left: unit cell of **C18**. Right: molecular structure of two **C18** complexes, highlighting the π-π-stacking of the bipyridyl moieties of two terpyridine ligands; hydrogen atoms and non-coordinating water molecules are omitted for clarity. Colour code: grey – C, violet – N, red – O, dark blue – Co(II). ORTEP representation with atomic displacement parameters at 50% level of probability.*

4.1.4 CuAAC Click Reactions of SCO and SIM Complexes

Gradual spin crossover behavior was observed for the complexes [Co^{II}(**L3**)$_2$]X$_2$ with X = ClO$_4^-$, PF$_6^-$, Br$^-$, Cl$^-$ and BF$_4^-$, which was confirmed by temperature-dependent solid-state UV-Vis spectroscopy. The complex [Co(**L3**)$_2$](ClO$_4$)$_2$ **C7** shows the most abrupt spin crossover and was therefore chosen for the synthesis of the trinuclear [SIM-SCO-SIM] complex. The mononuclear Co(II) complex [Co^{II}(**L4**)(dipic)] **C18** could be synthesized in small amount and investigated structurally. Only the SIM [Co^{II}(**L4**)(oda)] **C17** was used for the click reaction, due to the insufficient material and the lacking magnetic data of **C18**. The optimal conditions for the CuAAC click reaction were found by screening different solvent mixtures and Cu(I) catalysts. The reactions with copper(II) sulfate pentahydrate and sodium ascorbate in various ratios and in water/*tert*-butanol as well as water/dichloromethane solvent mixtures did not lead to the desired product. The usage of equimolar amounts of copper(I) iodide in dimethylsulfoxide at 80 °C finally yielded in the clicked trinuclear Co(II) complex. The reaction conditions are attributed to the low solubility and the bulky terpyridine moieties of both reactants. The cyclization to the six-membered metallacycle (see Chapter 1.3.1) demonstrates the rate-determining step, which is difficult to achieve due to the steric hindrance.
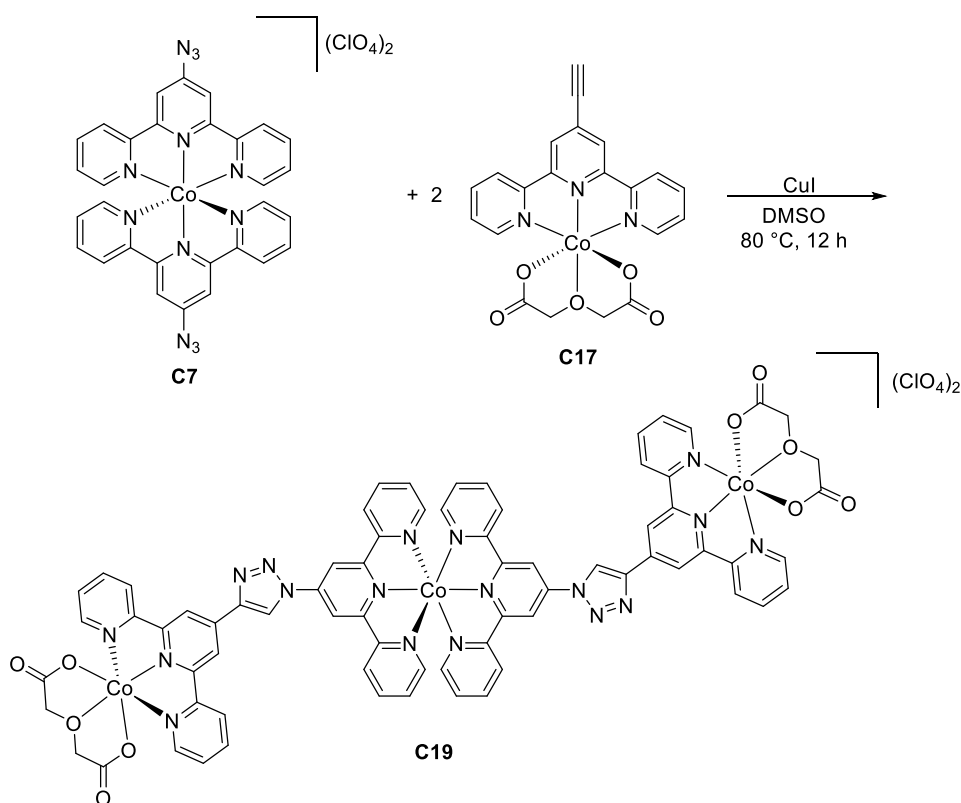

*Figure 87 CuAAC click reaction of **C7** and **C17** to form **C19** using copper(I) iodide in dimethylsulfoxide.*

Because of the low solubility, no single crystals were obtained to date. The solid product **C19** was characterized by IR spectroscopy, UV-Vis spectroscopy and magnetic measurements to investigate the SCO and SIM behavior. The verification of the successful click reaction was performed by IR spectroscopy. The relevant IR spectra of the precursor complexes $[Co^{II}(\textbf{L3})_2](ClO_4)_2$ **C7** and $[Co^{II}(\textbf{L4})(oda)]$ **C17** as well as the product **C19** are visualized in Figure 88. The characteristic asymmetric stretching frequency of the azide moiety appears at $\nu_{as} =$ 2 123 cm^{-1} in the spectrum of **C7** (Figure 88 top) and the stretch vibration of the C≡C triple bond at 2 110 cm^{-1} of **C17** (Figure 88 middle). These are not observed in the spectrum of **C19** (Figure 88 bottom), which indicates a successful click reaction and the formation of the 1,2,3-triazole.
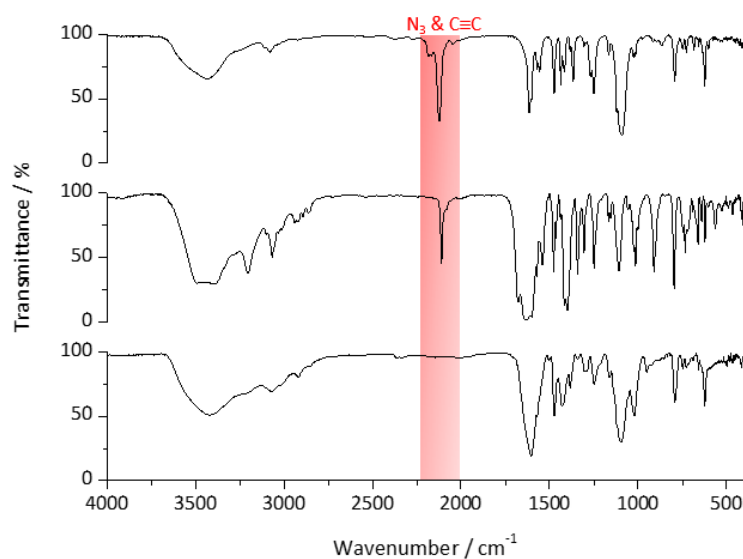
*Figure 88 IR spectra of $[Co^{II}(\textbf{L3})_2](ClO_4)_2$ **C7** (top), $[Co^{II}(\textbf{L4})(oda)]$ **C17** (middle) and [Co-Co-Co] **C19** (bottom) in KBr.*

To investigate the magnetic properties of the clicked complex **C19** and compare it with the precursor complexes **C7** and **C17**, the temperature-dependent magnetic susceptibility and the field-dependent magnetization were recorded. As the solvent was removed after the click reaction, the molar mass was calculated including copper(I) iodide in addition to the trinuclear Co(II) complex. The $\chi_M T$ versus T plot is shown in Figure 89. At 300 K, the $\chi_M T$ value amounts 7.27 cm³ K mol^{-1} and decreases for lower temperatures to 2.87 cm³ K mol^{-1}, indicating pronounced zero-field splitting and possible antiferromagnetic coupling. The $\chi_M T$ value of the Co(II) ion in **C17** is 3.18 cm³ K mol^{-1},[229] hence the residual amount of 0.91 cm³ K mol^{-1} is attributed to the central Co(II) ion. The curvature does not hint to spin crossover behavior, as the curve is less sigmoidal and more likely to saturate for higher temperatures. The comparable large $\chi_M T$ value of the central LS Co(II) ion hints to unquenched orbital angular contribution. The assumed $\{Co^{II}_{HS}\text{-}Co^{II}_{LS}\text{-}Co^{II}_{HS}\}$ complex is in good agreement with the literature as especially trinuclear HS Co(II) complexes are reported with higher values than 8.00 cm³ K mol^{-1}.[319,320] The temperature-dependent magnetic susceptibility was fitted with PHI using the following Hamiltonian:[262]

$$\hat{H} = -\alpha\lambda(L_1S_1 + L_3S_3) + \Delta(L_{1,z}^2 + L_{3,z}^2) - 2J(S_1S_2 + S_2S_3)$$
$$+ \mu_B \cdot H\{[-\alpha(L_1 + L_3) + g_e(S_1 + S_3)] + g_2S_2\}$$

(29)

The parameters of the HS species were set as $\lambda = -180$ cm^{-1}, $\alpha = 1.5$ and $g_1 = g_3 = 2.0$. The fitted parameters are $g_2 = 2.200(1)$ for the LS species, $\Delta = +80(20)$ cm^{-1} for the HS species and $J = -1.04(11)$ cm^{-1}. The fit was not satisfying with $R = 1.23$, especially in the low temperature region. The high $\chi_M T$ value points towards unquenched orbital contribution of the HS Co(II) ions which leads to pronounced zero-field splitting. The resulting anisotropic ground doublet $m_S = \pm 1/2$ causes an anisotropic exchange interaction between the Co(II) ions. The anisotropic ground state corresponds with the results of the precursor complex **C17** with $|D| = 9.75$ cm^{-1}.[229] To obtain reasonable values and to avoid overparameterization, the fit was performed with preference of the high temperature region ('residual highT/lowB' in the ****params block in the input file of the PHI program) and neglect of the exchange coupling ($J = 0$) as this is only pronounced at low temperatures. The fixed parameters of the HS species were unaffected. The crystal field parameter was fitted with $\Delta = +50(10)$ cm^{-1} and the g-factor of the central LS species with $g_2 = 2.200(1)$ resulting in a more reasonable residual value of $R = 5.5 \cdot 10^{-1}$.
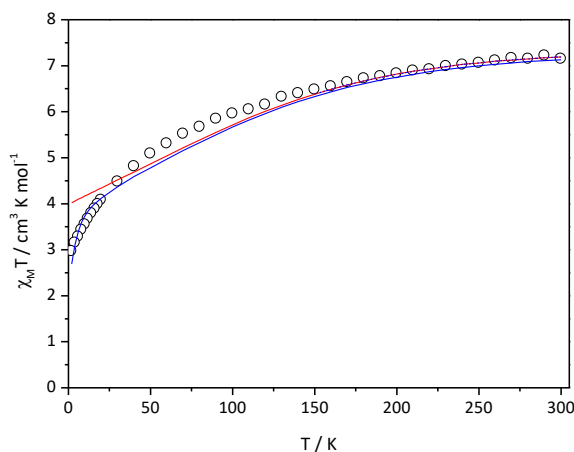

*Figure 89 Temperature-dependent magnetic behavior of **C19**, $\chi_M T$ vs. T plot. ○ experimental data, − fit 300 K to 2 K, − fit high-temperature region.*

The proposed spin states of the $\{Co_{HS}^{II}\text{-}Co_{LS}^{II}\text{-}Co_{HS}^{II}\}$ complex **C19** were further confirmed by comparing the UV-Vis spectra of the precursor complexes and the clicked trinuclear Co(II) complex, which are shown in Figure 90. The spectra were recorded in different solvents, namely acetonitrile for [Co^{II}(**L3**)$_2$](ClO$_4$)$_2$ **C7** and **C19** as well as dimethylsulfoxide for [Co^{II}(**L4**)(oda)] **C17** and are discussed qualitatively. As the spin crossover of **C7** is gradual, the LS species is still present at 300 K, which is confirmed in the UV-Vis spectrum. The characteristic MLCT bands for the LS species are found at 21 739 cm^{-1}, 19 646 cm^{-1} and 17 700 cm^{-1}. These are also present in the spectrum of the clicked complex at 22 272 cm^{-1} and 19 455 cm^{-1} indicating the presence of the LS species of the bis-terpyridine unit. The less pronounced maxima are attributed to the low solubility of **C19**. Furthermore, the UV-Vis spectrum of **C17**

shows a maximum at 19 084 cm^{-1}, which can be assigned to a d-d transition of the HS Co(II) ion.[314] Additionally, the very broad shoulder in the range of 28 000 cm^{-1} to 22 500 cm^{-1} of **C17** is also found for **C19**. Both, the UV-Vis and magnetic data hin to the proposed spin states.
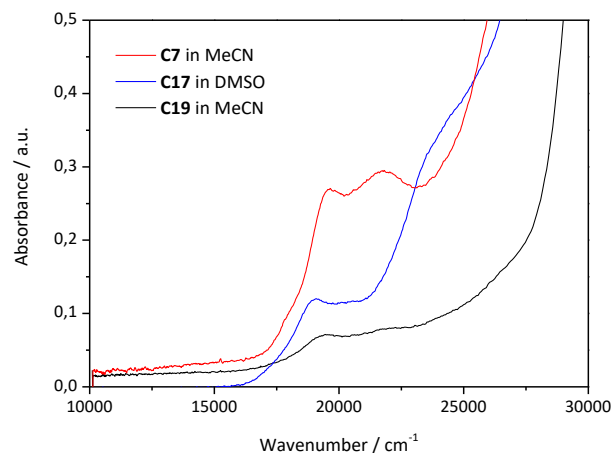

*Figure 90 UV-Vis spectra of **C7**, **C17** and **C19** in solution.*

In addition, the field-dependent magnetization was measured. At 2 K and 7 T, the experimental value is M = 4.72 N$_A\mu_B$ and consistent with the theoretical value of M = 5 N$_A\mu_B$ for the antiferromagnetic coupled system with S = 5/2 (see Equation 25). The assumed zero-field splitting is further approved by the non-superposition of the temperature curves in the M versus H/T plot. The pronounced zero-field splitting leads to the m_S = ±1/2 ground and m_S = ±3/2 excited states, which are energetically separated. To obtain reliable values and indicate the strength of the antiferromagnetic coupling, the simplified effective spin of S^{eff} = 1/2 for both HS Co(II) ions and anisotropic exchange interaction is assumed.

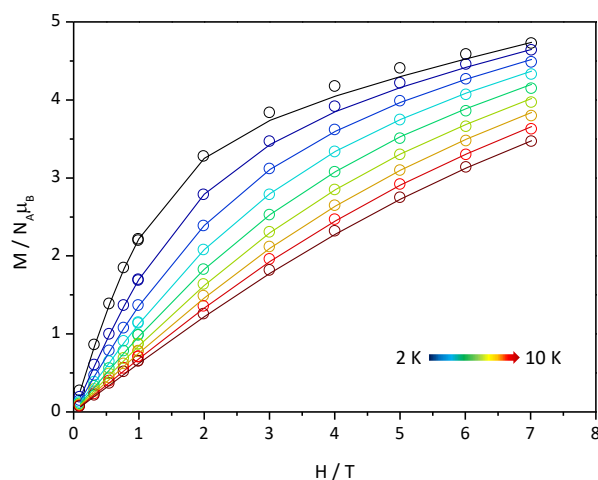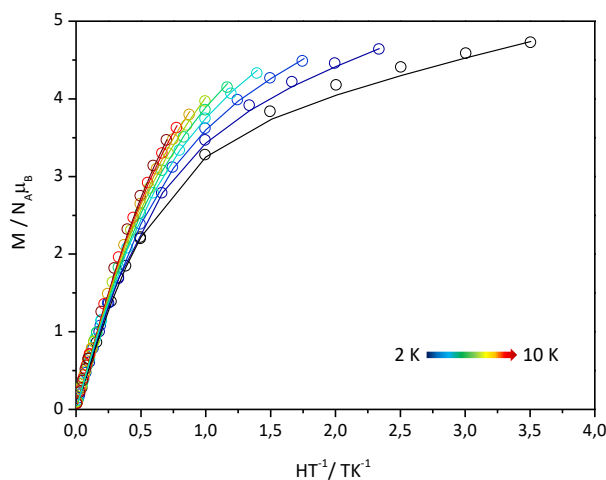*Figure 91 Field- and temperature-dependent magnetization measurement of **C19**, M vs. H plot.*
○ experimental data, − fit including exchange interaction and an effective spin of S^{eff} = 1/2.

Figure 92 Field- and temperature-dependent magnetization measurement of C19, M vs. H/T plot. ○ experimental data, – fit including exchange interaction and an effective spin of S^{eff} = 1/2.

The data were fitted according to the following Hamiltonian:

$$\hat{H} = -2J_z(S_{1,z}^{eff} \cdot S_{2,z} + S_{2,z} \cdot S_{3,z}^{eff}) - 2J_{xy}(S_{1,xy}^{eff} \cdot S_{2,xy} + S_{2,xy} \cdot S_{3,xy}^{eff}) + g\mu_B H(S_1^{eff} + S_2 + S_3^{eff}) \qquad (30)$$

The g-factor as well as the anisotropic exchange parameter J_z and J_{xy} were fitted with g = 3.894(11), J_z = +8.17(13) cm^{-1} and J_{xy} = −8.30(16) cm^{-1} (R = 8.24 · 10^{-2}) resulting in a total antiferromagnetic interaction of J = −2.81 cm^{-1} with $J = (J_z + 2J_{xy})/3$. The weak antiferromagnetic coupling between the Co(II) ions arises from the large conjugated ligand system and is consistent with the previous reported dinuclear complex [Co$_2$(**L3-4**)(oda)$_2$] **30** with J = −0.69 cm^{-1}.[229,321] Based on the present anisotropy, ac susceptibility measurements were performed but no out-of-phase signal χ'' was observed in the absence and presence of an applied dc field.

4.1.5 Evaluation of the CuAAC Approach

It is not possible to unambiguously clarify the reasons for the lacking SCO and SIM behavior as no single crystals were obtained to date and the magnetic properties could not be related to the structure. As discussed earlier, the spin crossover behavior of Co(II) bis-terpyridine complexes highly depends on the anions, solvent molecules and substituents. The attached Co(II) complex in the 4'-position could have a strong influence, especially when the crystal packing is affected and has strongly changed in comparison to the precursor complex **C7**. Furthermore, the antiferromagnetic interaction influences the energy of the LS and HS species, thus possibly leading to an energetically stabilized LS state in the case of **C19**. Next to the SCO, the molecular structure and the antiferromagnetic interaction influence the SIM behavior. The

obtained trinuclear complex could be also regarded as exchange coupled trimer instead of the two single-*ion* magnets. Then, the antiferromagnetic coupling behaves antagonistic when decreasing the spin ground state and the anisotropy, which would explain to the loss of the SMM behavior.

4.2   Approach II: The 'designer' Ligand

The 'designer' ligand 4'-(4'''-benzo-15-crown-5)-methyloxy-2,2':6',2''-terpyridine **L5** was opted to be applied in the synthesis of trinuclear [SIM-SCO-SIM] complexes as the spin crossover behavior of the appropriate [Co^{II}(**L5**)$_2$]X$_2$ complex series was maintained by the additional coordination of sodium cations *via* the 15-crown-5 moiety in previous work.[111] Furthermore, Dy(III) based SIMs with crown ether ligands and related Co(II) complexes are reported in the literature.[249,250] Based on these two findings the spin crossover behavior and slow relaxation of magnetization should be combined in the desired trinuclear complex using ligand **L5**. The synthetic attempts and the structures as well as the magnetic properties of the obtained metal complexes are described hereafter.

4.2.1   The Ligand L5

The 'designer' ligand 4'-(4'''-benzo-15-crown-5)-methyloxy-2,2':6',2''-terpyridine **L5** was synthesized in three steps starting from benzo-15-crown-5 **54** in an overall yield of 40%. The formylation of benzo-15-crown-5 **54** was carried out under Duff conditions using trifluoromethanesulfonic acid and hexamethylenetetramine at 105 °C. The aldehyde function was reduced to the primary alcohol **56** using sodium borohydride in 71% yield.[322] Subsequently, 4'-hydroxymethylbenzo-15-crown-5 **56** and 4'-bromo-2,2':6'2''-terpyridine **57** were heated to 70 °C under potassium hydroxide mediation giving the ether **L5** in 89% yield.[323]
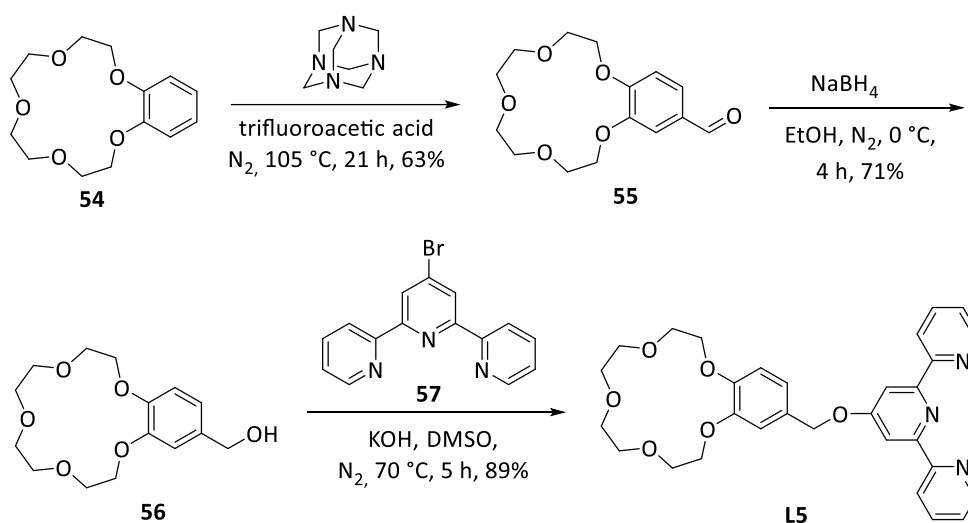

*Figure 93 Synthesis route of the ligand **L5**.*[322,323]

4.2.2 Cobalt(II) and Dysprosium(III) Complexes with L5

To prepare trinuclear Co(II) [SIM-SCO-SIM] complexes, the ligand **L5** was reacted with various Co(II) starting materials. Coordinating anions such as thiocyanate and chloride as well as non-coordinating anions such as tetrafluoroborate and perchlorate with the addition of co-ligands were screened to receive the desired complex. Either the mononuclear Co(II) bis-terpyridine complex was synthesized first and reacted with further Co(II) starting materials or the reaction was directly prepared with a metal to ligand ratio of 3:2. All reactions were performed under air and mostly in acetonitrile, methanol, or solvent mixtures due to the solubility properties of the ligand **L5**.

The attempts to synthesize the trinuclear [Dy^{III}-Co^{II}-Dy^{III}] complex was based on the preferred coordination of Co(II) ions by the tridentate terpyridine pocket to form a stable mononuclear complex.[323] For the Dy(III) ions, the crown ether moiety should be favorable as the coordination by oxygen donor atoms is thermodynamically favored over the coordination by nitrogen due to the higher electronegativity.[324] Hence, either the mononuclear Co(II) or Dy(III) complex was synthesized first and subsequently reacted with the other starting material. In the first case, the Co(II) tetrafluoroborate complex was synthesized, as the results of the former group member Johanna Oberhaus revealed the most abrupt spin transition for this compound.[111] Different Dy(III) starting materials, including nitrate, chloride, perchlorate, triflate, acetate, and pivalate, were used to prepare the trinuclear 3d-4f complex.

Following these approaches, two different complexes were obtained in form of single crystals, which will be discussed structurally and magnetically in detail in the following chapter.

The Cobalt Complex

Green single crystals were obtained after one day by reacting **L5** and cobalt(II) dithiocyanate in acetonitrile in 2:3 ratio. The structure of complex [Co^{III}(**L5**)]$_2$[Co^{II}(NCS)$_4$]$_3$·6MeCN **C21** is shown in Figure 94. The complex crystallizes in the monoclinic space group $P\bar{1}$ at 173 K. The favored central mononuclear cobalt bis-terpyridine complex is present in the crystal structure. The 15-crown-5 moieties are vacant, the additional Co(II) ions are present in form of [Co^{II}(NCS)$_4$]$^{2-}$ counterions. The central Co(II) ion was oxidized to Co(III), as both the bond lengths (see Table 17) and the presence 1.5 equivalents of [Co^{II}(NCS)$_4$]$^{2-}$ counterions per [Co^{III}(**L5**)]$^{3+}$ complex cation reveal.[325] Continuous shape measurements were performed for the two different [Co^{II}(NCS)$_4$]$^{2-}$ counter ions in the asymmetric unit. The calculated values are CShM = 0.20 for [Co2(NCS)$_4$]$^{2-}$ and CShM = 0.24 for [Co3(NCS)$_4$]$^{2-}$ with respect to the ideal tetrahedron (see Appendix).
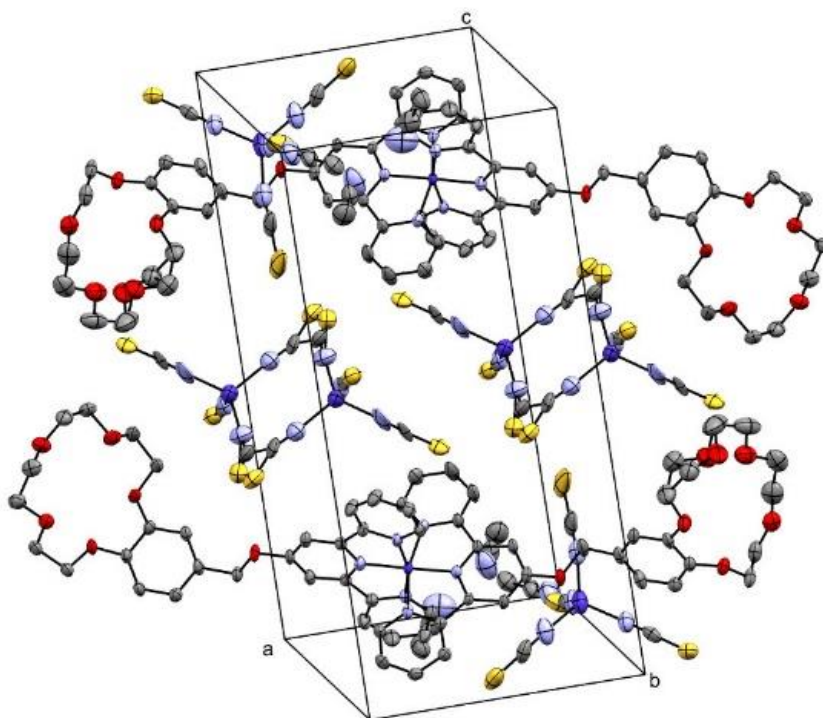
*Figure 94 Molecular structure of [Co^{III}(**L5**)]$_2$[Co^{II}(NCS)$_4$]$_3$·6MeCN **C21** where the central [Co^{II}(NCS)$_4$]$^{2-}$ anion is fourfold disordered and occupied by 25% each. Color code: grey – C, violet – N, red – O, yellow – S, dark blue – Co. Hydrogen atoms are omitted for clarity. ORTEP representation with atomic displacement parameters at 50% level of probability.*

*Table 17 Selected bond lengths and angles of **C21** at 173 K.*

Co1–L [Å]		Co2–L [Å]		Co3–L [Å]	
Co1–N1	1.872(6)	Co2–N7	1.961(9)	Co3–N11	1.99(2)
Co1–N2	1.941(6)	Co2–N8	1.951(13)	Co3–N12	1.992(19)
Co1–N3	1.945(6)	Co2–N9	1.980(9)	Co3–N13	2.09(3)
Co1–N4	1.864(6)	Co2–N10	1.962(11)	Co3–N14	1.998(18)
Co1–N5	1.941(6)	CShM	0.20	CShM	0.24
Co1–N6	1.946(6)				

The temperature-dependent magnetic susceptibility and field-dependent magnetization were investigated to verify the oxidation states of the Co(II) and Co(III) ions. The $\chi_M T$ versus T plot of **C21** is shown in Figure 95. From $\chi_M T$ = 9.10 cm³ K mol⁻¹ at 300 K, the $\chi_M T$ value decreases linearly to 7.12 cm³ K mol⁻¹ at 20 K, which hints towards temperature-independent paramagnetism (TIP). The TIP results from the Zeeman perturbation of the Co(III) ions, where the excited states are mixing with the ground state because of the small energy difference.[326] The $\chi_M T$ value of 7.12 cm³ K mol⁻¹ is in good accordance with three tetrahedral coordinated Co(II) ions taking spin-orbit coupling into account.[327] With lowering temperature the value

further decreases to 4.84 cm³ K mol^{-1} at 2 K due to zero-field splitting of the ^{4}A$_{2g}$ ground term into the $m_S = \pm1/2$ and $m_S = \pm3/2$ sublevels.[328] At 2 K and 7 T, the magnetization is 8.78 N$_A\mu_B$, which is close to the theoretical value of 9.00 N$_A\mu_B$ for three HS Co(II) ions (see Equation 25), but not saturated yet. Furthermore, the non-superposition of the curves in the *M* versus *H*/*T* plot reveals magnetic anisotropy due to zero-field splitting.
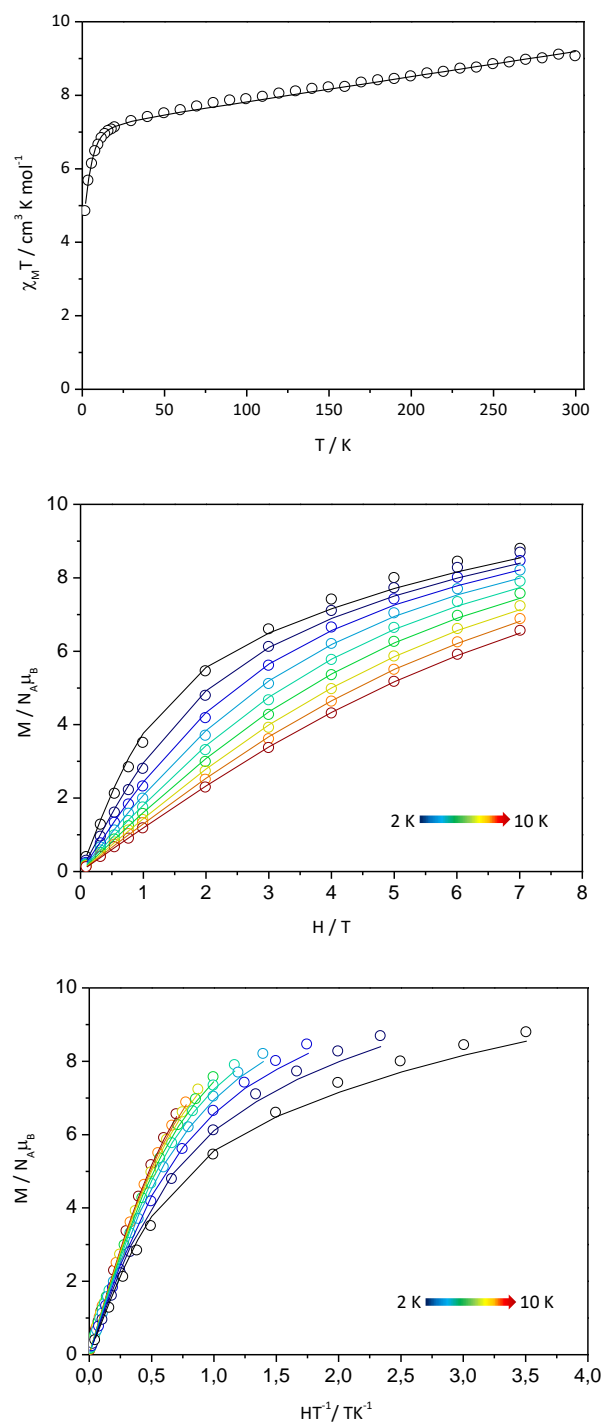

*Figure 95 Top: temperature-dependent magnetic behavior of **C21**, $\chi_M T$ vs. T plot. Field- and temperature-dependent magnetization measurement of **C21**. Middle: M vs. H plot. Bottom: M vs. H/T plot. ○ experimental data, − fit with g = 2.25 and D = −5.46 cm^{-1}.*

The susceptibility and magnetization data were fitted simultaneously using the following spin-only Hamiltonian and $S = 3/2$ for the three HS Co(II) ions.

$$\hat{H} = D[\hat{S}_z^2 - S(S + 1)/3] + g\mu_B HS \tag{31}$$

The fit of the experimental data resulted in g = 2.253(2) and $D = -5.46(7)$ cm^{-1}. The temperature-independent paramagnetism was added with $\chi_{TIP} = 6\ 827 \cdot 10^{-6}$ cm^3 mol^{-1} for two Co(III) ions, which is in the typical range for such diamagnetic metal ions.[326] The low value of the axial zero-field splitting parameter hints to low-lying excited states of the Co(II) ions, which explains the non-saturation of the magnetization. When comparing with the literature,[328] the negative value of the axial zero-field splitting parameter and the comparable deviation from the ideal tetrahedron hint to SIM behavior, but no out-of-phase signal was observed in the absence and presence of an applied dc field.

The Mononuclear Dysprosium(III) Complex

The reaction of **L5** and dysprosium(III) nitrate nonahydrate in an acetonitrile/methanol solvent mixture yielded after ten days in colorless single crystals by evaporation of the solvent. The mononuclear complex [Dy^{III}(**L5**)(η^2-NO$_3$)$_2$(η^1-NO$_3$)(H$_2$O)]·MeCN **C22** crystallizes in the monoclinic space group $P2_1/c$ at 173 K. The asymmetric unit consists of the neutral complex molecule and one non-coordinating acetonitrile molecule.
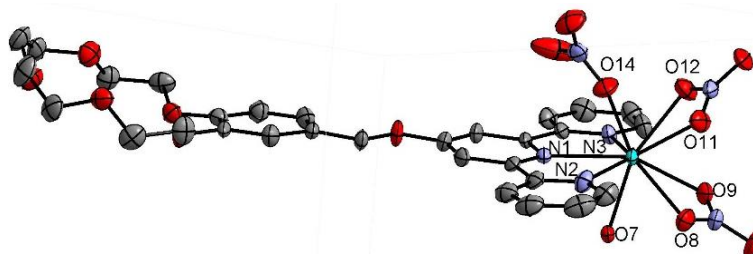

*Figure 96 Molecular structure of [Dy^{III}(**L5**)(η^2-NO$_3$)$_2$(η^1-NO$_3$)(H$_2$O)]·MeCN **C22**. Color code: grey – C, violet – N, red – O, cyan – Dy(III). Hydrogen atoms and solvent molecules are omitted for clarity. ORTEP representation with atomic displacement parameters at 50% level of probability.*

The central Dy(III) ion is coordinated by the terpyridine unit of **L5**, while the 15-crown-5 moiety is vacant. The coordination sphere of the Dy(III) ion is saturated by two η^2- and one η^1- coordinating nitrate anions as well as one water molecule. The coordinated water molecule exhibits hydrogen bonds to three oxygen atoms of the 15-crown-5 moiety, hence two neighboring complex molecules form a 'complex dimer' where head and tail are located towards each other resulting in an inversion center in the center of the dimer. The water molecule is located out-of-plane of the crown ether function and blocks one side of the possible coordination.
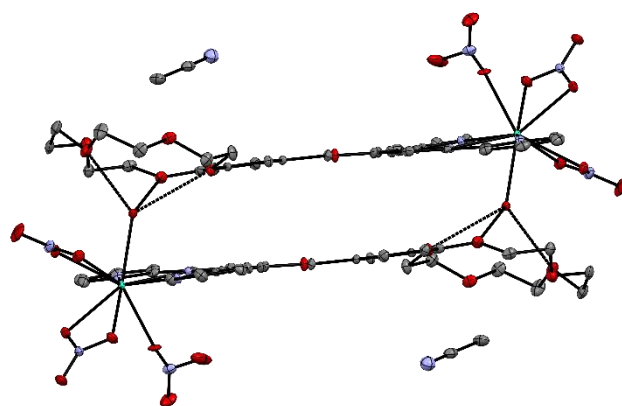
*Figure 97 Structure of the 'complex dimer' of **C22** connected by hydrogen bonds between the coordinated water molecule and the crown ether moiety of the next ligand. Color code: grey – C, violet – N, red – O, cyan – Dy(III). Hydrogen atoms and solvent molecules are omitted for clarity. ORTEP representation with atomic displacement parameters at 50% level of probability.*

The Dy(III) ion is coordinated by nine donor atoms forming a $\{N_3O_6\}$ donor set. The average Dy–O and Dy–N bond lengths are 2.458 Å and 2.426 Å, respectively. The distances to the water molecule and η^1-coordinated nitrate anion are shorter than 2.4 Å, whereas the η^2-coordinated nitrate anions show larger bond lengths (see

Table 18). Continuous shape measurements resulted in a spherical capped square antiprisma as best description of the polyhedron with a factor of CShM = 1.90 and a local C_{4v} symmetry of the Dy(III) ion. The O8 donor atom is located on top of the square antiprism. The rigidity of the terpyridine ligand as well as the given angles of the η^2-coordinated nitrate anions cause the deviation. The side and top views of the capped square antiprism further visualize the distortion of the ideal polyhedron.
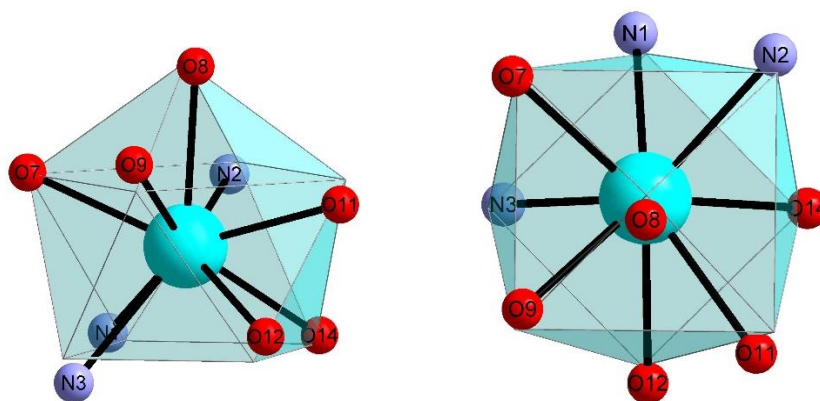

*Figure 98 The $\{DyN_3O_6\}$ core of **C22** with a spherical capped square antiprismatic structure (CSAPR-9) in comparison to the ideal polyhedron. Left: side view. Right: top view. Color code: violet – N, red – O, cyan – Dy(III).*

Table 18 Selected bond lengths of C22.

| Dy–L [Å]			
Dy1–N1	2.463(3)	Dy1–O9	2.434(3)
Dy1–N2	2.457(3)	Dy1–O11	2.435(3)
Dy1–N3	2.454(3)	Dy1–O12	2.455(3)
Dy1–O7	2.387(2)	Dy1–O14	2.378(5)
Dy1–O8	2.468(3)		

The temperature-dependent magnetic susceptibility and field-dependent magnetization measurements are shown in Figure 100. The $\chi_M T$ value of 14.07 cm³ K mol⁻¹ at 300 K is in good agreement with the expected value of $\chi_M T$ = 14.17 cm³ K mol⁻¹ for one Dy(III) ion ($^6H_{15/2}$, S = 5/2, L = 5, J = 15/2). The theoretical $\chi_M T$ for Dy(III) value is calculated by:[133]

$$g_J = 1 + \frac{J(J+1) + S(S+1) - L(L+1)}{2J(J+1)} = \frac{4}{3} \tag{32}$$

$$\mu_{eff} = g_J \cdot \sqrt{J(J+1)} = 10.65 \ \mu_B \tag{33}$$

$$\chi_M T = \left(\frac{\mu_{eff}}{2.82787}\right)^2 = 14.17 \ \text{cm}^3 \ \text{K mol}^{-1} \tag{34}$$

The $\chi_M T$ value slightly decreases upon lowering the temperature. It decreases stronger in the range of 50 K to 2 K to 9.19 cm³ K mol⁻¹, which is attributed to the thermal depopulation of the excited Stark sublevels.[329] The value indicates the m_J = ±13/2 ($\chi_M T$ = 10.84 cm³ K mol⁻¹) or ±11/2 ($\chi_M T$ = 7.95 cm³ K mol⁻¹) being the ground state and low-lying excited states.
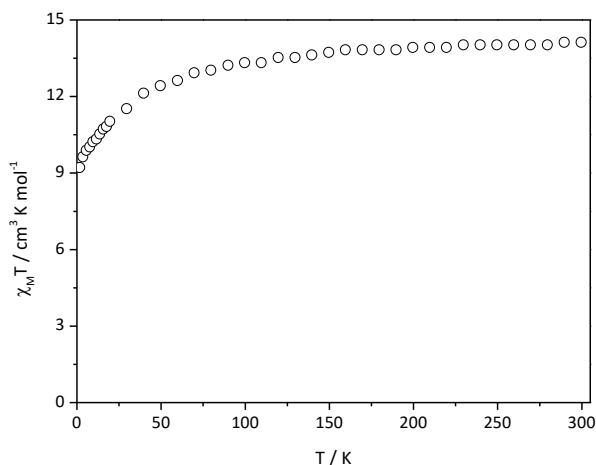
Figure 99 Temperature-dependent magnetic behavior of C22, $\chi_M T$ vs. T plot. ○ experimental data.

At 2 K and 7 T, the magnetization amounts M = 5.55 $N_A\mu_B$ but is not saturated yet. Considering an Ising-like ground doublet, which is well separated from the next excited state, the magnetization saturates to:

$$M_{sat} = 1/4 \cdot g_{eff,z} \cdot N_A\mu_B = 5\ N_A\mu_B \qquad (35)$$

with a pseudo-spin of 1/2. The anisotropic g-factors are assumed to be $g_{eff,x}$ = $g_{eff,y}$ = 0 and $g_{eff,z}$ = 20.[191] The higher value can be attributed to crystal-field effects and low-lying excited states.[330] Nevertheless, the non-superposition of the reduced magnetization indicates the presence of weak magnetic anisotropy which is consistent with the magnetic susceptibility data.
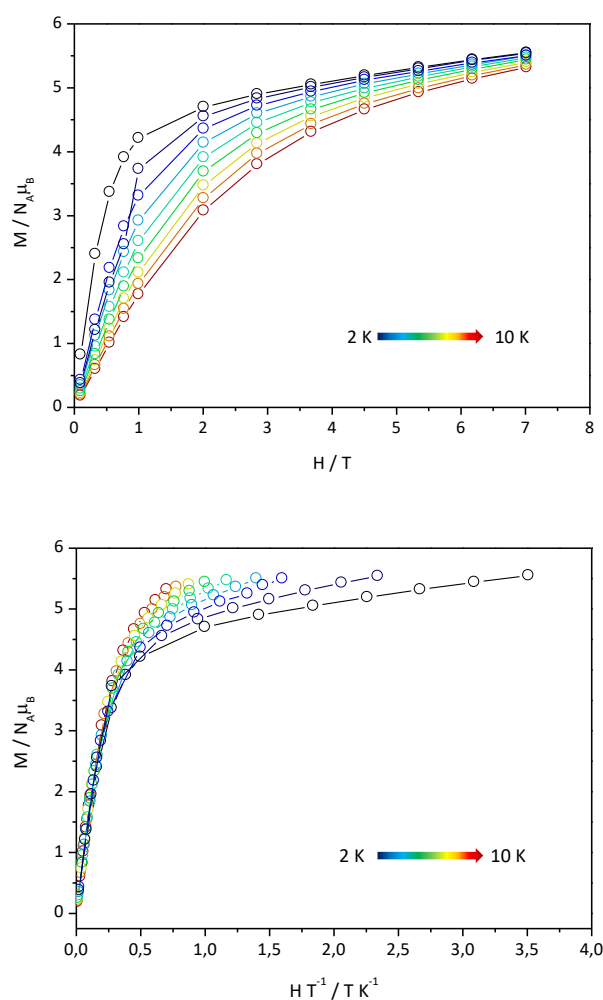

*Figure 100 Field-dependent magnetization measurements of **C22**. Top: M vs. H plot. Bottom: M vs. H/T plot. -○- experimental data.*

In order to investigate the potential SIM behavior, ac susceptibility measurements were performed. An out-of-phase signal was not present at zero-field but observed with an external dc field. Pursuing field-dependent measurements revealed an optimal external field of H_{dc} = 600 Oe. The temperature-dependent scan was performed in the range of 1.9 K to 3.3 K (see Figure 101).
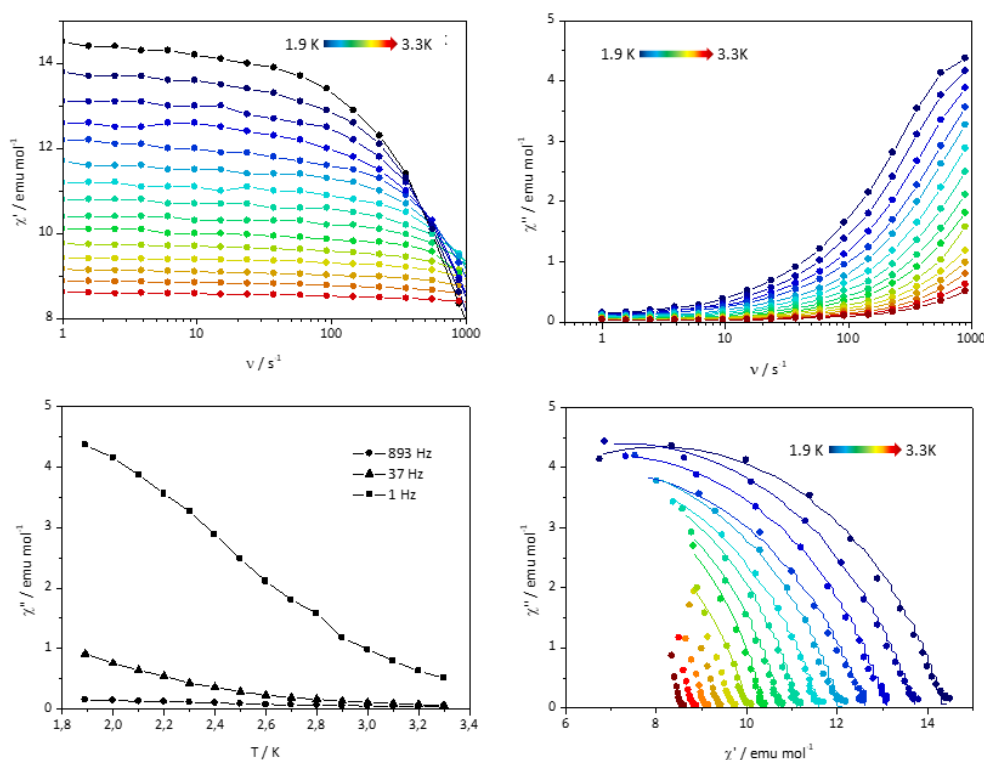

*Figure 101 The ac susceptibility measurements of **C22** at H_{dc} = 600 Oe. Top left: χ' vs. ν plot. Top right: χ'' vs. ν plot. Bottom left: χ'' vs. T plot for 1 Hz, 37 Hz and 893 Hz. -●- experimental data. Bottom right: Cole-Cole plot (1.9 – 3.3 K). ● experimental data, – fit (1.9 – 2.8 K).*

The Cole-Cole plot is shown in the temperature range from 1.9 K to 3.3 K. Due to the absence of a maximum for the higher temperatures, the fit was performed for 1.9 K to 2.8 K using the generalized Debye model (Equation 15). The calculated relaxation times were subsequently plotted as ln(τ) versus 1/*T* plot. The fit was performed considering quantum tunneling and the thermally activated Orbach process (Equation 27) to yield in reasonable values of τ_{QTM} = 3.16 · 10^{-4} s as well as U_{eff} = 15 K (10.4 cm^{-1}) and τ_0 = 1.26 · 10^{-7} s. Both processes were considered. Quantum tunneling could be promoted by dipole-dipole interactions between the Dy(III) ions and the application of the external dc field partly reduces the tunneling process and enables the thermally activated relaxation pathway.
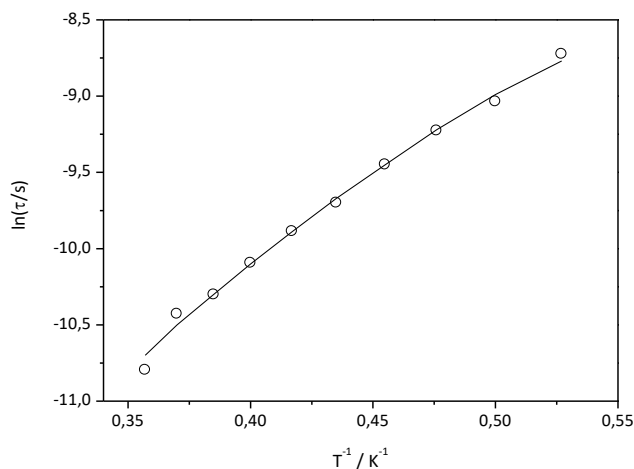
*Figure 102 Arrhenius plot of **C22** with an applied dc field of H_{dc} = 600 Oe. ○ data extracted from the fit of the Cole-Cole plot, − fit including QTM and the Orbach process.*

4.2.3 Evaluation of 'designer' Ligand L5

During the studies, the mononuclear Co(III) (**C21**) and Dy(III) (**C22**) complexes were obtained as single crystals and the desired trinuclear [SIM-SCO-SIM] complex could not be synthesized so far. The pentadentate pocket of the crown ether moiety should be thermodynamically more favorable than the tridentate terpyridine pocket[331,332] and the reported structures with Co(II) or Dy(III) ions with 12-crown-4, 15-crown-5 and 18-crown-6 ligands clearly show the possibility of the desired coordination.[250,333–337] However, the obtained crystal structures demonstrate the preference of the terpyridine pocket as the 15-crown-5 moieties are vacant in both cases. A possible reason could be the rigidity of the terpyridine over the crown ether moiety, which seems to be too flexible to allow the formation of single crystals of the desired trinuclear complexes.

5 Summary and Outlook

This thesis provided an insight into the investigations of the synergy between the spin crossover phenomenon and magnetic exchange coupling as well as single-ion magnet behavior.

Spin Crossover and Magnetic Exchange Coupling

Three di- and polynuclear Cu(II) model complexes for the investigation of the magnetic exchange interaction were successfully synthesized using the 1,3,4-oxadiazole and bis-1,3,4-thiadiazole based ligands **L1** and **L2**.
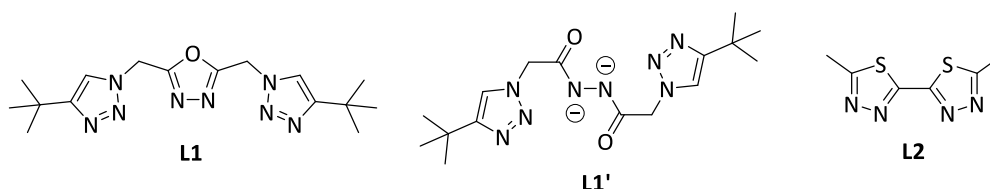

Figure 103 Molecular Structures of the ligands L1, L1' and L2.

In the one-dimensional coordination chain $\{[Cu^{II}(\mu\text{-}\mathbf{L1})Cl_2]\cdot MeCN\}_n$ **C1**, the Cu(II) ions are bridged by the ligand **L1**, which suppresses any magnetic exchange interaction due to the non-conjugated ligand system. In contrast to that, the ring-opened ligand **L1'** allowed the formation of the dinuclear Cu(II) complex $[Cu_2^{II}(\mathbf{L1'})Cl_2(MeOH)_2]$ **C1'** with a central Cu–N–N–Cu moiety and antiferromagnetic exchange coupling of $J = -37.53$ cm^{-1}. Due to the competition between the structural and electronic aspects regarding the planarity and electron density at the nitrogen donor atom, the orbital overlap is not maximal which leads to a comparable weak interaction.
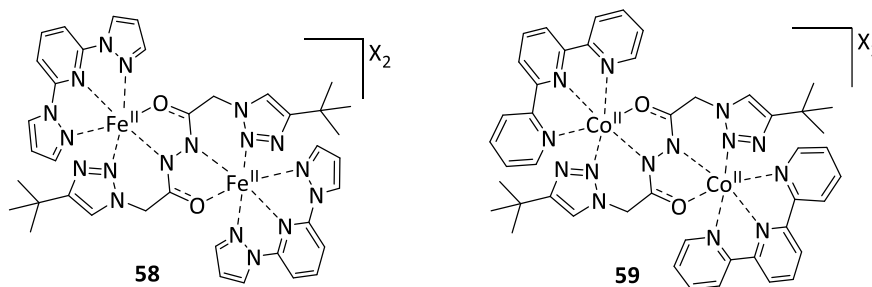

Figure 104 Possible Fe(II) and Co(II) spin crossover complexes with L1' and bpp or terpy co-ligands (X = monovalent non-coordinating anion).

Therefore, ligand **L1'** appears to be suitable to investigate the synergy between SCO and magnetic exchange coupling in Fe(II) or Co(II) complexes. Adequate tridentate meridional coordinating ligands such as bpp or terpy (**58** and **59**) could accomplish the octahedral coordination sphere and provide a suitable ligand field to enable spin crossover behavior.

The magnetic measurements of the polynuclear Cu(II) model complex $\{[Cu^{II}(\mu\text{-}\textbf{L2})_3(H_2O)((CH_3)_2CO)](ClO_4)_2(H_2O)\}_n$ **C2** revealed isolated metal ions in spite of the end-to-end coordination of the bis-1,3,4-thiadiazole based ligand **L2**. With **L2** also several Fe(II) complexes with a comparable coordination mode were synthesized and investigated. The co-crystallized complexes $\{[Fe^{II}(trans\text{-}\mu\text{-}\textbf{L2})_2(H_2O)_4](ClO_4)_2\cdot2H_2O\}_n$ **C3** and $\{[Fe^{II}(\mu\text{-}\textbf{L2})_4(H_2O)_2](ClO_4)_2\cdot\textbf{L2}\}_n$ **C3'** show the formation of a one-dimensional chain and a two-dimensional network. In $\{Fe^{II}(trans\text{-}\mu\text{-}\textbf{L2})_2(\textbf{L2})(SCN)_2\}_n$ **C4**, the Fe(II) ions are bridged by the ligand **L2** forming coordination chains. Due to insufficient amount and quality of the crystals, the magnetic measurements could not be performed. However, the comparable bridging coordination mode of **L2** assumes negligible magnetic exchange interaction. Furthermore, the poly- and mononuclear complexes **C4** and $[Fe^{II}(\textbf{L2})_3](BF_4)_2\cdot3CHCl_3$ **C5** show the ability of **L2** to also coordinate as bidentate chelating ligand. The investigation of the bond distances indicates the HS state in **C3**, **C3'** and **C4**, whereas the LS state is present in complex **C5**. The $\{N_4O_2\}$ and $\{N_6\}$ donor sets in **C3'**, **C4** and **C5** are highly favorable for Fe(II) based SCO complexes and the suitable ligand field of **L2** imply possible spin crossover behavior at low (**C3'**, **C4**) or high temperatures (**C5**).

As the low solubility of **L2** prevents the variation of solvents and full control of the products, other substituents on the 5- and 5'-positions could increase the solubility by inhibiting π-π-stacking of the bis-1,3,4-thiadiazole moieties, for example with *tert*-butyl (**60**) or trifluoromethyl (**61**) functionalities. With the proper choice of the substituent, the ligand field could be further fine-tuned sterically and/or electronically to enable the desired spin crossover behavior. Bulky substituents would cause a larger deviation of the octahedral coordination sphere and could hinder intermolecular interactions such as hydrogen bonds. Electron-withdrawing groups such as the trifluoromethyl (**61**) substituent should stabilize the LS state, whereas electron-donating groups (*tert*-butyl **60**, cyclohexyl **62**, methoxy **63**) favor the HS state.[338]
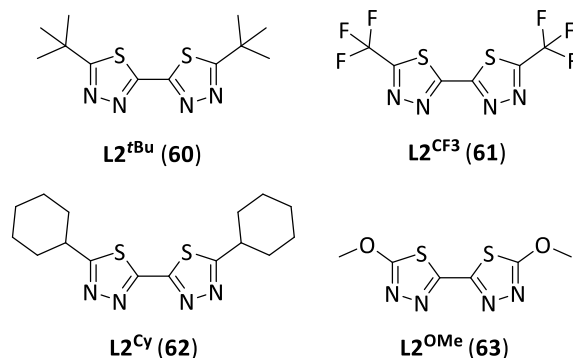

*Figure 105 Possible substituents on the 5- and 5'-positions of the bis-1,3,4-thiadiazole ligand system of **L2**: tert-butyl (**L2^{tBu} 60**), trifluoromethyl (**L2^{CF3} 61**), cyclohexyl (**L2^{Cy} 62**) or methoxy (**L2^{OMe} 63**) substituents.*

As the intramolecular magnetic exchange interaction is negligible, which complexes are highly favorable for the investigation of the influence of intermolecular interactions on the spin crossover behavior. Complex **C3'** could be investigated in terms of possible host-guest functionality due to the formation of the two-dimensional network and the presence of non-coordinating ligand molecules within the cavity.

Furthermore, the corresponding Co(II) coordination chain $\{[Co^{II}(cis\text{-}\mu\text{-}\textbf{L2})_2(H_2O)_4](ClO_4)_2\}_n$ **C6** was obtained by the reaction of cobalt(II) perchlorate and the bis-1,3,4-thiadiazole ligand **L2**. The large bond lengths and the magnetic measurements approved the HS state. Although no spin crossover behavior was observed, the rhombic distortion of the octahedral coordination sphere as well as the strong orbital contribution led to pronounced magnetic anisotropy. The ac susceptibility measurements revealed slow relaxation of magnetization with an effective energy barrier U_{eff} = 7.5 K at 1000 Oe.

The obtained Cu(II), Fe(II) and Co(II) complexes illustrate the high versatility of **L2** concerning the molecular structure and the magnetic properties depending on the metal ion and starting material. Next to the influence on the spin crossover behavior, the variation of the 5- and 5'-substituents of **L2** could also improve the SIM behavior. For example, bulky substituents would cause steric hindrance and thus lead to highly distorted octahedral surroundings, which could further influence the relaxation processes and the height of the effective energy barrier.

Spin Crossover and Single-Ion Magnets

The two synthetic approaches using the CuAAC as well as the 'designer' ligand **L5** to form trinuclear SIM-SCO-SIM complexes were presented in the second part of the thesis. Therefore, the ligands **L3**, **L4** and **L5** were synthesized.
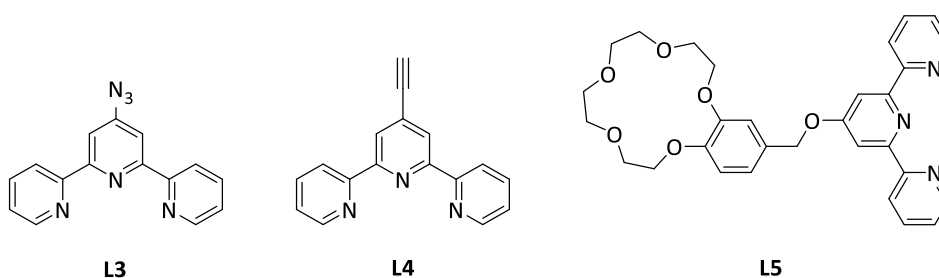

*Figure 106 Molecular structures of the ligands **L3, L4** and **L5**.*

To first investigate the spin crossover behavior of the central moiety, the mononuclear Co(II) complexes with 4'-azido-2,2':6',2''-terpyridine **L3** and various non-coordinating anions were synthesized. The majority exhibits a gradual spin transition, which was confirmed by temperature-dependent solid-state UV-Vis spectroscopy. However, the HS state of $[Co^{II}(\textbf{L3})_2](SCN)_2 \cdot H_2O$ **C11** and the LS state of $[Co^{II}(\textbf{L3})_2](SO_4)$ **C12** were present over the whole temperature range. Surprisingly, the rhombic distortion of the octahedral surrounding in **C11** led to pronounced magnetic anisotropy and SIM behavior, which was approved by ac susceptibility measurements resulting in an effective energy barrier of U_{eff} = 4.4 K at 1600 Oe.

The azide-functionalized SCO complex [Co^{II}(**L3**)$_2$](ClO$_4$)$_2$ **C7** was successfully clicked to the acetylene-substituted SIM [Co^{II}(**L4**)(oda)] **C17**, using equimolar amount of copper(I) iodide in dimethylsulfoxide. The UV-Vis and magnetic measurements corroborated the spin states of the desired trinuclear {Co$^{II}_{HS}$-Co$^{II}_{LS}$-Co$^{II}_{HS}$} complex and weak antiferromagnetic interaction of $J = -2.81$ cm^{-1}. Other solvents and crystallization methods as well as bulkier non-coordinating anions, such as tetraphenylborate and its derivates, could be screened to receive single crystals. The investigation of the crystal structure and the comparison with the precursor SCO and SIM complexes could help to explain the absence of SCO and SIM behavior. So far, the available magnetic data indicate the antagonistic effect of the present antiferromagnetic exchange coupling and SCO/SIM behavior. While this seems to be counterproductive for the trinuclear Co(II) complex, this effect could be used when incorporating a central Fe(II) SCO moiety functioning as molecular switch (**64**). The terpyridine related bpp ligand[339] seems to be a suitable system as a large variability of substituents on the 4'-position of the pyridyl ring is reported.[340–344] Hence, the azide substituent could be introduced and the Fe(II) complex clicked to the SIM **C17**. The spin transition could be promoted by light irradiation.[345] The SIM behavior is switched OFF when irradiating with green light (LIESST, LS→HS) as the paramagnetic HS state couples antiferromagnetically with the terminal Co(II) ions and ON with red light (reverse-LIESST, HS→LS) as the diamagnetic LS state inhibits exchange coupling leading to isolated Co(II) ions.
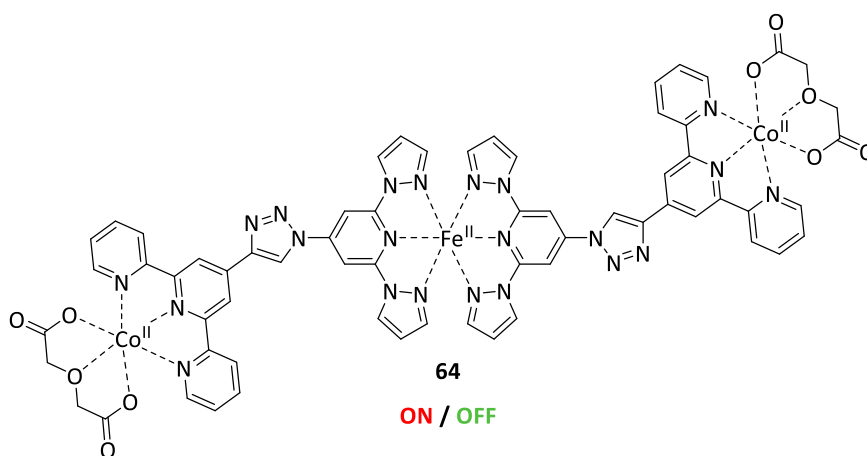

64

ON / **OFF**

Figure 107 Example of a trinuclear [SIM-SCO-SIM] complex with a central [Fe^{II}(bpp)$_2$]$^{2+}$ moiety which functions as molecular switch by light irradiation.

Moreover, the 'designer' ligand 4'-(4'''-benzo-15-crown-5)-methyloxy-2,2':6',2''-terpyridine **L5** was exploited to connect the SCO and SIMs moieties by providing two suitable coordination pockets. The variation of the Co(II) and Dy(III) starting materials led to the formation of the two mononuclear {[Co^{III}(**L5**)]$_2$[Co^{II}(NCS)$_4$]$_3$·6MeCN} **C21** and [Dy^{III}(**L5**)(η^2-NO$_3$)$_2$(η^1-NO$_3$)(H$_2$O)]·MeCN **C22** complexes. In both cases, the 15-crown-5 moieties are vacant. While the Co(II) ion is oxidized to diamagnetic Co(III) in **C21**, the temperature-dependent magnetic susceptibility and field-dependent magnetization measurements of **C22** indicated pronounced axial magnetic anisotropy. The effective energy barrier was found to be $U_{eff} = 15$ K at 600 Oe.

Although no trinuclear [SIM-SCO-SIM] complex could be synthesized with **L5**, the obtained crystal structures give important insight into the reactivity of the ligand. The terpyridine coordination pocket is highly favorable for the coordination of metal ions regardless of 3d or 4f and the crown ether moiety seems to be too flexible to coordinate Co(II) or Dy(III) ions. Therefore, a more rigid ligand system, such as the pentadentate macrocycle shown in Figure 108, could be introduced to enable SCO and SIM behavior. A coordination of Co(II) into such coordination pockets allowing SIM behaviour was already described and might help to overcome the faced problems.[249]
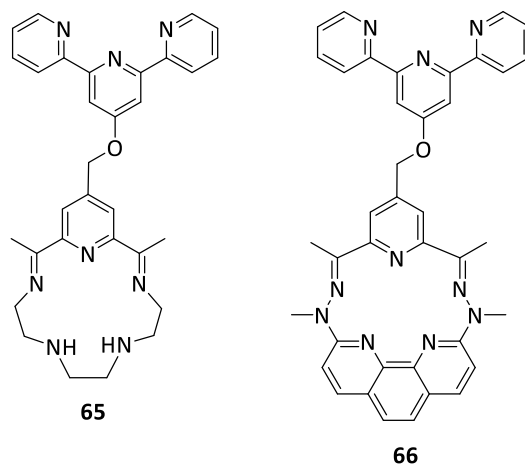

Figure 108 Structures of possible ligands with a terpyridine and a pentadenate macrocyclic coordination pocket to enable spin crossover and SIM behavior.[249]

6 Experimental Section

6.1 General Information

Commercially available chemicals were purchased by abcr, Acros Organics, Alfa Aesar, Deutero, Fisher Scientific, Roth, Sigma Aldrich and TCI and used without further purification. Solvents were dried according to literature procedures.[346] 2,5-Bis[(4-*tert*-butyl-1*H*-1,2,3-triazol-1-yl)methyl]-1,3,4-oxadiazole (**L1**) was synthesized by ■■■■■■■■■■■■■■■■ in his bachelor thesis. 4'-Bromo-2,2':6',2''-terpyridine was synthesized in our group by ■■■■■■■ and ■■■■■■. Reactions with Fe(II) were performed unter inert conditions using Schlenk technique or Glovebox conditions.

6.2 Instrumental Details

6.2.1 Magnetic Measurements

The magnetic data of the direct current (dc) and alternating current (ac) measurements were performed on a Quantum Design SQUID magnetometer MPMS XL at Johannes Gutenberg University Mainz. Temperature-dependent magnetic susceptibility measurements were measured in the range of 2 K to 300 K with an applied dc field of 1000 Oe. Field-dependent magnetization measurements were measured between 2 K to 10 K with an applied static field of 0.1 T to 7 T. In-phase and out-of-phase susceptibilities were measured with an ac field of H_{ac} = 3 Oe and with an applied dc field in the range of H_{dc} = 0 − 3000 Oe with the frequencies of ν = 1 − 1400 Hz. The solid or polycrystalline samples were placed in gelatine capsules, filled with eicosane (**C6**, **C11**, **C19**, **C21** and **C22**) and mounted inside a plastic straw. The diamagnetic contributions of the capsule and eicosane were subtracted from the measured volume magnetization.

$$\chi = \frac{\partial M}{\partial H} \tag{36}$$

$$\chi = \chi_{dia} + \chi_{para} \tag{37}$$

The magnetic data were further corrected considering the diamagnetic contribution close to the Pascal's constants.[347]

$$\chi_{dia} = -M/2 \cdot 10^{-6} \text{ emu mol}^{-1} \tag{38}$$

with the molar mass M. The χT product is described by the Curie law:

$$\chi T = \frac{N_A g^2 \mu_B^2}{3 k_B} S(S + 1) \tag{39}$$

The magnetic susceptibility and magnetization data were fitted with the program PHI.[262] The ac susceptibility data were fitted with the program CC-Fit2,[302] except for **C11**, which was fitted with Origin7.5. The plots were visualized with Origin7.5.

6.2.2 Single Crystal X-Ray Structure Analysis

X-ray crystallographic data were collected by ■■■■■■■■■■■■■ on a STOE IPDS 2T diffractometer at Johannes Gutenberg University Mainz, by ■■■■■■■■ on a STOE STADIVARI at Johannes Gutenberg University Mainz or by STOE & Cie GmbH (Darmstadt) on a STOE STADIVARI device. Further details are given in the Appendix. The crystal structures of **C1**, **C1'**, **C3**, **C3'** and **C6** were solved with SHELXT[348] and refined with SHELXL[349] implemented in the program Olex².[350] The other crystal structures were solved and refined by ■■■■■■■■. The structures were visualized with Mercury3.8, Mercury4.2 and Diamond3. Continuous Shape Measurements (CShM) were performed with SHAPE2.1 and visualized with Diamond3.

6.2.3 Infrared Spectroscopy

IR spectra were recorded at room temperature on a JASCO FT/IR-4200 in form of potassium bromide pellets or on a Nicolet 5700 FT-IR-Spectrometer with an attached Smart Orbit ATR (Diamond) probe head from Thermo Electron Cooperation at Johannes Gutenberg University Mainz. The measurement range was 400 cm^{-1} to 4000 cm^{-1} and the spectra were averaged over 32 measurements. Baseline correction was performed with the software JASCO Spectra Manager or Omnic® from Thermo Electron Cooperation. The spectra were visualized with Origin7.5.

6.2.4 Nuclear Magnetic Resonance Spectroscopy

^{1}H-NMR (400 MHz), ^{13}C-NMR (101 MHz), ^{1}H-^{1}H-COSY, ^{1}H-^{13}C-HMBC and ^{1}H-^{13}C-HSQC spectra were recorded at room temperature on a Bruker DRX-400 at Johannes Gutenberg University Mainz. All compounds were dissolved in an appropriate deuterated solvent. Chemical shifts

were reported in parts per million (ppm) and refer to the used deuterated solvent, relative to the internal standard tetramethylsilane. The references were defined as $CDCl_3$: ^1H – 7.26 ppm (s) and DMSO-d^6: ^1H – 2.50 ppm (quint), ^{13}C – 36.52 ppm (sept).[351] The software MestreNova 14.0 was used for the analyzation of the data.

6.2.5 UV-Vis Spectroscopy

UV-Vis spectra in solution were recorded on a J&M Analytik AG TIDAS CCD UV/NIR spectrometer at Johannes Gutenberg University Mainz. The measurements were performed using a quartz glass cell with an optical path length of 1 cm. The sample was dissolved in an appropriate solvent. First the quartz glass cell and the pure solvent were measured for background information. Measurements and background correction were performed with the software TidasDAQ3. Solid state UV-Vis spectra were recorded on a JASCO V-570 UV/Vis/NIR spectrometer at Johannes Gutenberg University Mainz. Sample preparation was performed by mixing approximately 1 mg of the sample with barium sulfate. The spectrum of pure barium sulfate was used as background. The spectra were processed with the program Jasco Spectra Manager. Temperature-dependent measurements were cooled/heated with a Harrick Low Temperature Reaction Chamber in the range of −30 °C to 80 °C. The spectra were visualized with Origin 7.5.

6.2.6 Mass Spectrometry

ESI mass spectra were recorded by the department of mass spectrometry at Johannes Gutenberg University Mainz on an Agilent 6545 QTOF-MS with positive ion mode. For preparation, the samples were dissolved in appropriate solvents. The spectra were visualized with Origin7.5.

6.2.7 Elemental Analysis

Elemental analysis was performed by the micro-analytical laboratory at Johannes Gutenberg University Mainz on a Foss Heraeus Vario EL elemental analyzer.

6.3 Spin Crossover and Magnetic Exchange Coupling

6.3.1 Ligand L1

1,2-Dichloroacetyl hydrazine (REN-EB-106)[253]
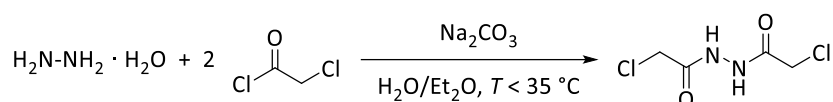
	M [g/mol]	m [g]	n [mol]	eq
Hydrazine hydrate (50-60% aqueous solution)	50.56	25.05	0.50	1.00
Chloroacetyl chloride	112.94	2 x 56.45	2 x 1.00	2 x 2.00
Na_2CO_3	105.99	53.10	0.50	1.00

Chloroacetyl chloride in 150 mL diethyl ether was added dropwise to a solution of hydrazine hydrate in 200 mL diethyl ethyl while cooling ($T < 35\ °C$). The reaction mixture was stirred for 30 min. 100 mL of an aqueous sodium carbonate solution was added and the obtained colorless precipitate was filtered and crystallized in ethyl acetate.

Yield: 22.69 g (0.122 mol, 25%) of a colorless solid. **^{1}H-NMR** (400 MHz, DMSO-d_6, 25 °C, δ/ppm): 10.49 (s, 2H, NH), 4.14 (s, 4H, CH_2). **^{13}C-NMR** (101 MHz, DMSO-d_6, 25 °C, δ/ppm): 164.71 (C^1), 40.87 ($C1'$). **IR** (KBr, $\tilde{v}$/cm^{-1}): 3182.9, 3047.9, 1613.2, 1496.5, 1405.9, 1225.5, 1156.1, 935.3, 794.5, 650.9. **Elemental analysis:** $C_4H_6Cl_2N_2O_2$, calc. C: 25.97%, H: 3.27%, N: 15.14%, exp. C: 26.29%, H: 3.86%, N: 16.58%.

2,5-Bis(chloromethyl)-1,3,4-oxadiazole (REN-EB-107)[253]
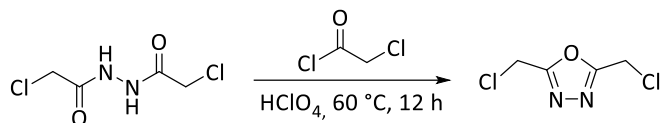
	M [g/mol]	m [g]	n [mol]	eq	V [mL]
1,2-Dichloroacetyl hydrazine	185.01	10.00	0.05	1.00	-
Chloroacetyl chloride	112.94	30.00	0.27	4.90	-
HClO$_4$ (60%)	-	-	-	-	8.75

Chloroacetyl chloride was dissolved in perchloric acid by heating to 60 °C. 1,2-Dichloroacetyl hydrazine was added and the reaction mixture was stirred at 60 °C for 12 h. After cooling, the reaction mixture was poured into ice water and adjusted to pH = 9 with aqueous sodium carbonate solution. The solution was extracted with diethyl ether (4 x 60 mL). The organic solution was washed with aqueous sodium carbonate solution (10%) and dried with potassium carbonate. The solvent was removed under reduced pressure to obtain the product.

Yield: 5.76 g (0.035 mol, 65%) of a yellow liquid. **^{1}H-NMR** (400 MHz, DMSO-d_6, 25 °C, δ/ppm): 5.11 (s, 4H, CH_2). **^{13}C-NMR** (101 MHz, DMSO-d_6, 25 °C, δ/ppm): 163.96 (C^1), 33.01 ($C1'$). **IR** (KBr, $\tilde{v}$/cm^{-1}): 3028.7, 2970.8, 1565.9, 1427.5, 1382.5, 1154.5, 989.5, 760.6, 719.6, 654.9. **Elemental analysis:** C$_4$H$_6$Cl$_2$N$_2$O$_2$, calc. C: 28.77%, H: 2.41%, N: 16.78%, exp. C: 28.27%, H: 2.40%, N: 16.50%.

2,5-Bis(azidomethyl)-1,3,4-oxadiazole (REN-EB-030)[253]
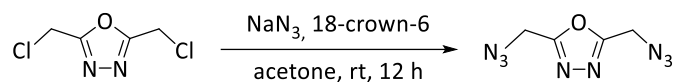
	M [g/mol]	m [g]	n [mol]	eq
2,5-Bis(chloromethyl)-1,3,4-oxadiazole	164.98	19.68	0.11	1.00
NaN$_3$	65.01	41.49	0.64	6.00
18-Crown-6	264.12	2.81	0.01	0.10

2,5-Bis(chloromethyl)-1,3,4-oxadiazole, sodium azide and 18-crown-6 were suspended in 200 mL acetone and stirred for 12 h at room temperature. The reaction mixture was filtered, and the solvent was removed under reduced pressure. The product was isolated by column chromatography (SiO$_2$, dichloromethane/diethyl ether 4:1).

Yield: 18.42 g (0.102 mol, 87%) of a colorless oil. **^{1}H-NMR** (400 MHz, DMSO-d_6, 25 °C, δ/ppm): 4.86 (s, 4H, CH_2). **^{13}C-NMR** (101 MHz, DMSO-d_6, 25 °C, δ/ppm): 163.19 (C^1), 43.54 (*C1'*). **IR** (KBr, $\tilde{v}$/cm^{-1}): 2093.8, 2100.0, 1585.9, 1435.9, 1257.8, 1182.3, 980.1, 890.0, 789.6, 555.0. **Elemental analysis:** C$_4$H$_6$Cl$_2$N$_2$O$_2$, calc. C: 26.67%, H: 2.24%, N: 62.21%, exp. C: 26.77%, H: 2.50%, N: 62.39%.

L1: 2,5-Bis[(4-*tert*-butyl-1*H*-1,2,3-triazol-1-yl)methyl]-1,3,4-oxadiazole (REN-NY-014)[252]
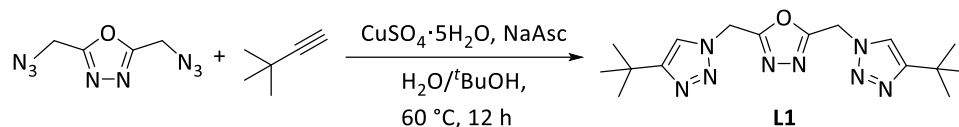
	M [g/mol]	m [g]	n [mol]	eq
2,5-Bis(azidomethyl)-1,3,4-oxadiazole	180.13	2.00	0.011	1.00
tert-Butylacetylene	82.14	2.19	0.027	2.40
CuSO$_4$·5H$_2$O	159.61	0.84	0.003	0.30
Sodium ascorbate	198.11	0.22	0.001	0.10

2,5-Bis(azidomethyl)-1,3,4-oxadiazole, *tert*-butylacetylene, copper(II) sulfate pentahydrate and sodium ascorbate were dissolved in 45 mL water/*tert*-butanol (2:1) and stirred for 12 h at 60 °C. The pale brown precipitate was filtered and dried *in vacuo*.

Yield: 2.13 g (quant.) of a pale brown powder. **^{1}H-NMR** (400 MHz, DMSO-d_6, 25 °C, δ/ppm): 7.98, (s, 2H, $H_{triazole}$), 5.97 (s, 4H, CH_2), 1.26 (s, 18H, CH_3). **^{13}C-NMR** (101 MHz, DMSO-d_6, 25 °C, δ/ppm): 162.49, 156.68, 120.83, 43.40, 30.44, 30.19. **IR** (KBr, $\tilde{v}$/cm^{-1}): **Elemental analysis:** C$_4$H$_6$Cl$_2$N$_2$O$_2$, calc. C: 55.80%, H: 7.02%, 32.53 N: 32.53%, exp. C: 55.86%, H: 7.24%, N: 32.17%. **ESI-MS** (MeOH): *m/z* [M+H]$^+$ calc. 354.2146, exp. 345.2149.

6.3.2 Complexes with L1

C1: {[Cu^{II}(L1)Cl$_2$]·MeCN}$_n$ (REN-EB-219) and C1': [Cu$^{II}_2$(L1')Cl$_2$(MeOH)$_2$] (REN-EB-214-2)
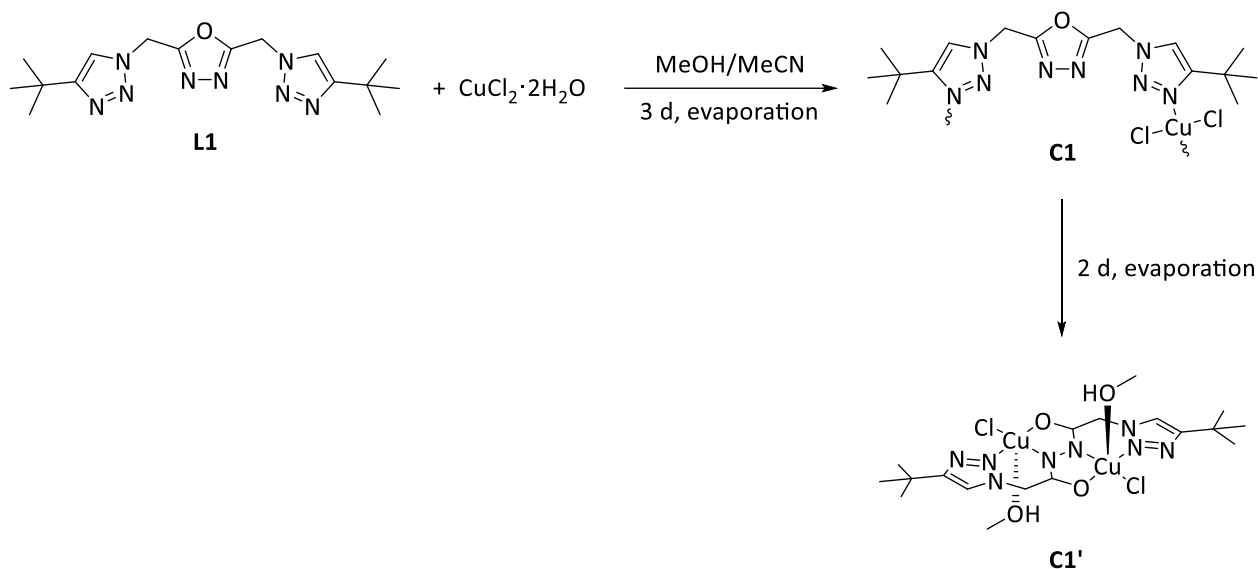
	M [g/mol]	m [mg]	n [mmol]	eq
L1	344.42	34	0.1	1.00
CuCl$_2$·2H$_2$O	170.48	17	0.1	1.00

A solution of copper(II) chloride dihydrate in 6 mL methanol was added to the ligand in 5 mL acetonitrile.

C1: {[Cu^{II}(L1)Cl]·MeCN}$_n$ (REN-EB-219)

After three days of evaporation, violet hexagonal shaped single crystals were obtained.

Yield: 20 mg (484.47 g/mol for one repetition unit, 0.041 mmol, 41%) of violet crystals. **IR** (KBr, $\tilde{v}$/cm^{-1}): 3441.8, 3118.8, 2970.3, 1415.5, 1384.2, 1231.3, 1138.3, 1076.1, 1001.8, 815.7. **Elemental analysis:** C$_{18}$H$_{27}$ClCuN$_9$O, calc. C: 41.58%, H: 5.23%, N: 24.25%, exp. C: 39.59%, H: 5.37%, N: 23.13%.

C1': [Cu$^{II}_2$(L1')Cl$_2$(MeOH)$_2$] (REN-EB-214-2)

After two more days, the violet crystals have turned into green needles.

Yield: 20 mg (622.50 g/mol, 0.032 mmol, 32%) of green needles. **IR** (KBr, $\tilde{\nu}$/cm^{-1}): 3458.2, 3126.0, 2965.5, 1576.0, 1416.9, 1384.2, 1335.5, 1081.9, 1011.5, 771.9. **Elemental analysis:** C$_{18}$H$_{32}$Cl$_2$Cu$_2$N$_8$O$_4$, calc. C: 34.73%, H: 5.18%, N: 18.00%, exp. C: 32.07%, H: 3.55%, N: 18.77%.

6.3.3 Ligand L2

Oxalyl dihydrazide (REN-EB-221)[271]
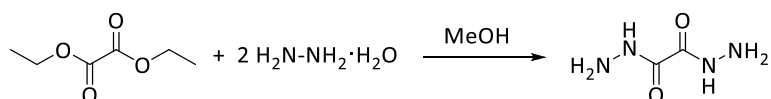
	M [g/mol]	m [g]	n [mol]	eq
Diethyl oxalate	146.14	10.00	0.068	1.00
Hydrazine hydrate (50-60% aqueous solution)	50.06	13.72	0.137	2.00

Hydrazine hydrate was added to a solution of diethyl oxalate in 30 mL methanol and a colorless solid directly precipitated. The reaction mixture was stirred another hour. The colorless precipitate was filtered, washed with methanol, and dried on air.

Yield: 8.00 g (quant.) of a colorless powder. **^{1}H-NMR** (400 MHz, DMSO-d$_6$, 25 °C, δ/ppm): 9.94 (s, 2H, N*H*), 4.48 (s, 4H, N*H$_2$*). **IR** (KBr, $\tilde{v}$/cm^{-1}): 3291.9, 3195.0, 3017.6, 2801.1, 1683.6, 1616.1, 1538.9, 1277.1, 979.7, 535.6.

N,N'-Diacetyloxalhydrazide (REN-EB-223)[272]
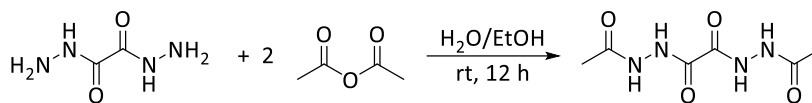
	M [g/mol]	m [g]	n [mol]	eq
Oxalyl dihydrazide	118.09	2.00	0.017	1.00
Acetic anhydride	102.09	3.46	0.034	2.00

Acetic anhydride was dissolved in 2 mL water/ethanol (1:1) and added dropwise to a solution of oxalyl dihydrazide in 60 mL distilled water. The reaction mixture was stirred for 12 h at room temperature. The colorless precipitate was filtered and dried on air.

Yield: 2.68 g (0.013 mol, 78%) of a colorless powder. **¹H-NMR** (400 MHz, DMSO-d$_6$, 25 °C, δ/ppm): 10.54 (s, 2H, NH), 9.88 (s, 2H, NH), 1.87 (s, 6H, CH_3). **IR** (KBr, $\tilde{v}$/cm^{-1}): 3403.3, 3216.2, 3024.3, 1700.9, 1668.1, 1521.6, 1245.8, 996.5, 682.7, 523.6.

L2: 5,5'-Bismethyl-2,2'-di-1,3,4-thiadiazole (REN-EB-229)
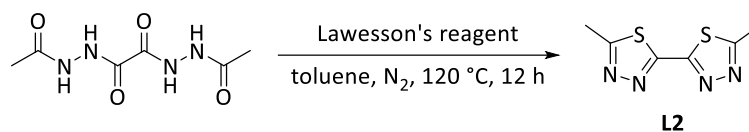
	M [g/mol]	m [mg]	n [mmol]	eq
N,N'-Diacetyloxalhydrazide	202.17	202	1.0	1.00
Lawesson's reagent	404.47	890	2.2	2.20

N,N'-Diacetyloxaldihydrazide and Lawesson's reagent were refluxed in dry toluene for 12 h under nitrogen atmosphere. The solvent was distilled and the product was isolated by column chromatography (SiO$_2$, R$_f$ = 0.5; DCM/Et$_2$O 5:1 to 1:1).

Yield: 134 mg (0.676 mmol, 68%) of a colorless powder. **^{1}H-NMR** (400 MHz, CDCl$_3$, 25 °C, δ/ppm): 2.88 (s, 6H, CH_3). **IR** (KBr, $\tilde{v}$/cm^{-1}): 2924.0, 1466.6, 1414.5, 1383.2, 1206.7, 1190.8, 945.4, 772.8, 653.8, 566.0. **ESI-MS** (MeCN): *m/z* [M+H]$^+$ exp. 199.0108, theo. 199.0107; [M+Na]$^+$ exp. 220.9929, theo. 220.9926.

6.3.4 Complexes with L2

C2: {[Cu^{II}(L2)$_3$(H$_2$O)((CH$_3$)$_2$CO)](ClO$_4$)$_2$(H$_2$O)}$_n$ (REN-EB-451)
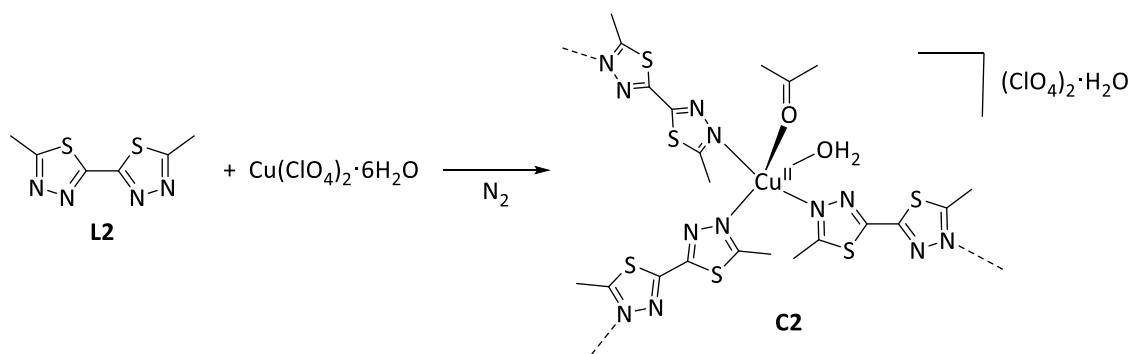
	M [g/mol]	m [mg]	n [mmol]	eq
L2	198.26	30	0.15	3.00
Cu(ClO$_4$)$_2$·6H$_2$O	370.54	19	0.05	1.00

The ligand was dissolved in 16.7 mL dichloromethane. Copper(II) perchlorate hexahydrate was dissolved in 3.3 mL acetone and added to the ligand solution while stirring. The reaction light blue mixture was stirred for 5 min at room temperature and filtered afterwards. After several hours intensive blue single crystals have formed.

Yield: 15 mg (0.023 mmol, 46%) of blue crystals. **IR** (KBr, $\tilde{v}$/cm^{-1}): 3442.8, 2969.8, 2919.2, 1632.5, 1466.1, 1410.2, 1384.2, 1142.6, 1121.4, 1088.6.

C3: {[Fe^{II}(*trans*-μ-L2)(H$_2$O)$_4$](ClO$_4$)$_2$·2H$_2$O}$_n$ (blocks) and C3': {[Fe^{II}(μ-L2)$_4$(H$_2$O)$_2$](ClO$_4$)$_2$·L2}$_n$ (REN-EB-268)
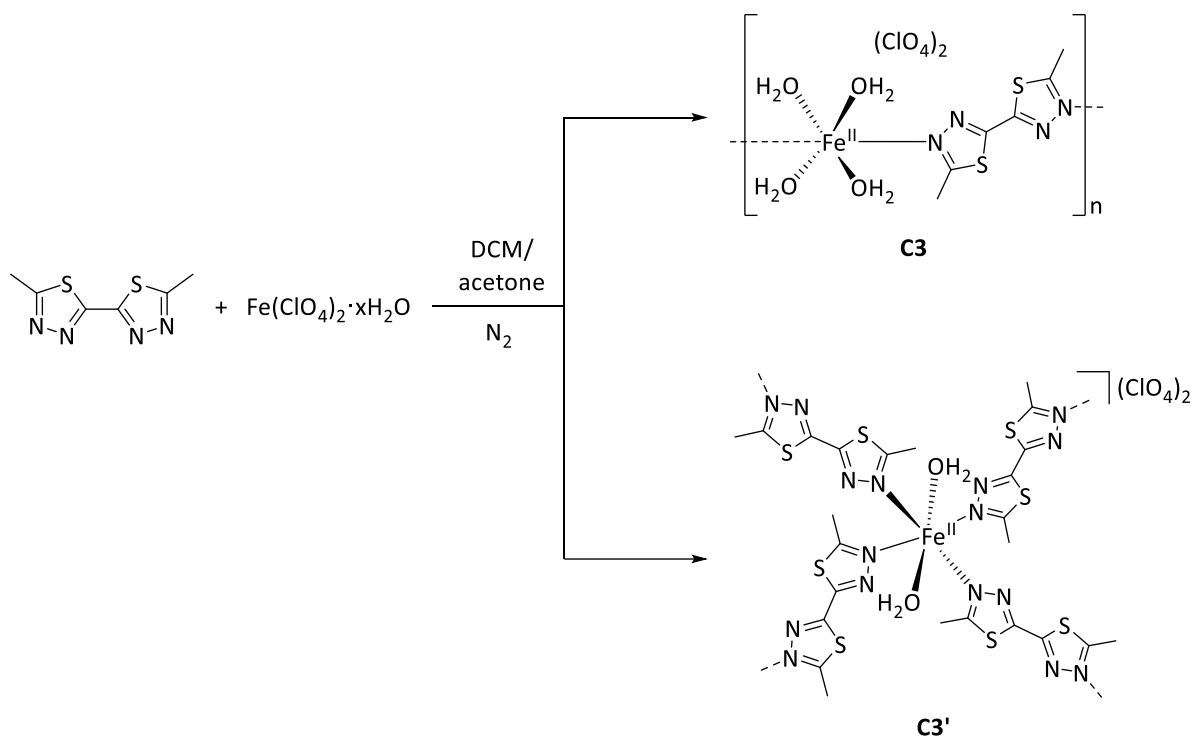
	M [g/mol]	m [mg]	n [mmol]	eq
L2	198.26	30	0.15	3.00
Fe(ClO$_4$)$_2$·xH$_2$O	270.00	14	0.05	1.00

The ligand was dissolved in 5 mL dry and degassed dichloromethane. Iron(II) perchlorate hydrate was dissolved in 1 mL dry and degassed acetone and added to the ligand solution. The reaction mixture was filtered. The next day, yellow single crystals were obtained after evaporation of the solvent (blocks **C3** and plates **C3'**).

C4: {Fe^{II}(*trans*-μ-L2)$_2$(L2)(SCN)$_2$}$_n$ (REN-EB-256)
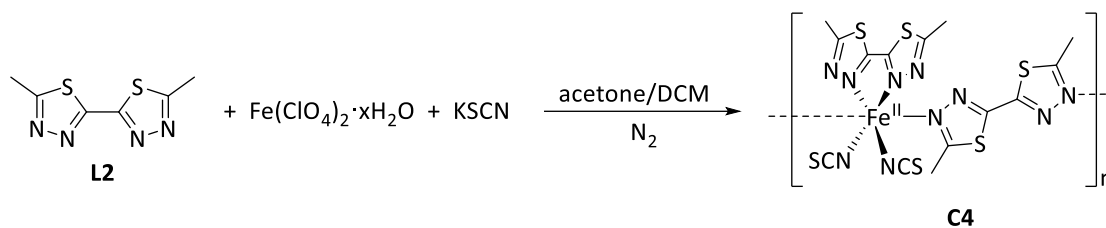
	M [g/mol]	m [mg]	n [mmol]	eq
L2	198.26	40	0.20	2.00
Fe(ClO$_4$)$_2$·xH$_2$O	270.00	27	0.10	1.00
KSCN	97.18	19	0.20	2.00

Iron(II) perchlorate hydrate was dissolved in 6 mL dry and degassed acetone. Potassium thiocyanate was dissolved in 2 mL dry and degassed acetone and added to the iron(II) solution which directly turned intensive red. The solution was stirred for 3 h at room temperature and filtered afterwards. The ligand was dissolved in 6 mL dry and degassed dichloromethane. The freshly prepared iron(II) thiocyanate solution was layered on top of the ligand solution. The next day the vial was opened for evaporation of the solvent. After three weeks, a small amount red block shaped single crystals was obtained in the dried solution.

C5: [Fe^{II}(L2)$_3$](BF$_4$)$_2$·3CHCl$_3$ (REN-EB-367)
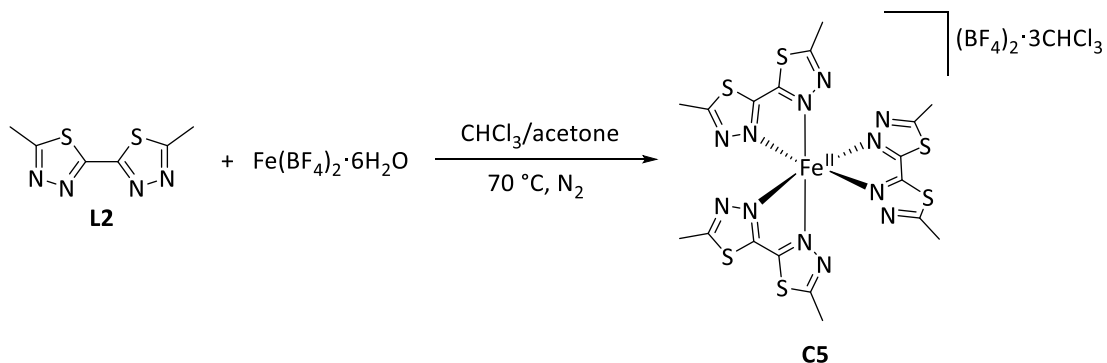
	M [g/mol]	m [mg]	n [mmol]	eq
L2	198.26	60	0.30	3.00
Fe(BF$_4$)$_2$·6H$_2$O	337.55	34	0.10	1.00

The ligand **L2** and iron(II) tetrafluoroborate hexahydrate were suspended in 24 mL chloroform/acetone (5:1) under nitrogen atmosphere and heated to 70 °C for 2 h. After cooling, the suspension was filtered and the filtrate was opened to evaporation. After five months, a small amount brown single crystals was obtained in the dried solution.

C6: {[Co(*cis*-μ-bdtd)₂(H₂O)₄](ClO₄)₂}ₙ (REN-EB-262)
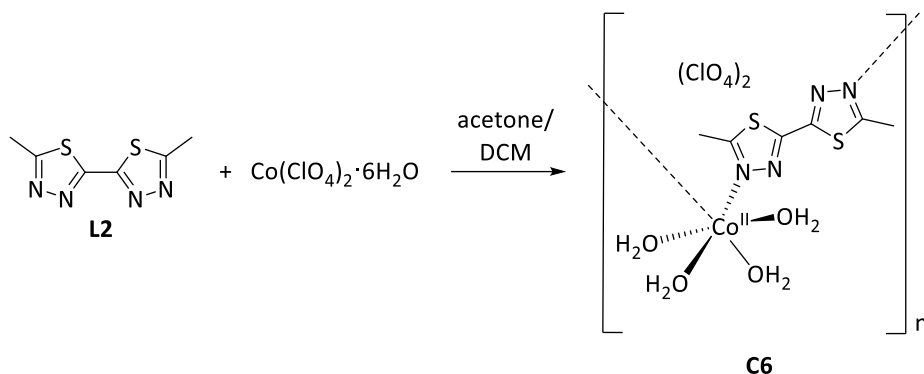
	M [g/mol]	m [mg]	n [mmol]	eq
L2	198.26	30	0.15	3.00
Co(ClO₄)₂·6H₂O	366.74	18	0.05	1.00

The ligand was dissolved in 10 mL dichloromethane. Cobalt(II) perchlorate hexahydrate was dissolved in 2 mL acetone and added to the ligand solution. The reaction mixture was stirred for 5 min and filtered. The solvent was evaporated slowly and the next day red single crystals were obtained.

Yield: 16 mg (0.030 mmol, 60%) of red crystals. **IR** (KBr, $\tilde{v}$/cm⁻¹): 3415.8, 1634.9, 1414.5, 1220.2, 1146.0, 1114.2, 1086.7, 957.5, 636.9, 625.8.

6.4 Spin Crossover and Single-Ion Magnets

6.4.1 Click Reactions

6.4.1.1 Ligands L3 and L4

1,5-Bis(2'-pyridyl)pentane-1,3,5-trione (REN-EB-297)[306]
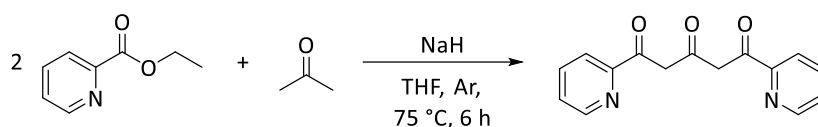
	M [g/mol]	m [g]	n [mmol]	eq	ρ [g/cm^3]	V [mL]
2-Ethyl picolinate	151.16	-	97.5	2.41	1.12	13
Acetone	58.08	-	40.5	1.00	0.79	4
NaH (60% in mineral oil)	24.00	4.00	167	4.12	-	-

Sodium hydride was suspended in dry tetrahydrofuran in a three-necked flask under Argon atmosphere and heated to 75 °C. Dry acetone and 2-ethyl picolinate in 100 mL dry tetrahydrofuran were added dropwise while heating. The grey suspension turned orange. The reaction mixture was heated for 6 h and cooled to room temperature over night. The solvent was removed under reduced pressure and the obtained orange solid was carefully dissolved in 200 mL distilled water, stirred for 1 h and filtered over celite. A pH = 7 was adjusted with diluted hydrochloride acid (3:1) and a yellow precipitate formed. The solid was filtered, washed with cold water and directly dissolved in diethyl ether. The solution was dried over magnesium sulfate and the solvent was removed under reduced pressure to yield the yellow powder.

Yield: 6.24 g (23.26 mmol, 58%) of a yellow powder. **^{1}H-NMR** of bis-enolic form (400 MHz, CDCl$_3$, 25 °C, δ/ppm): 14.58 (s, 1H), 9.10-8.49 (m, 1H), 8.01 (d, J = 7.9 H, 1H), 7.83 (td, J = 7.7, 1.8 Hz, 1H), 7.50-7.29 (m, 1H), 6.80 (s, 1H). **IR** (KBr, $\tilde{v}$/cm^{-1}): 3433.2, 3050.4, 1608.8, 1576.5, 1446.4, 1374.5, 1280.5, 1147.4, 788.7, 586.3.

2,2':6',2''-Terpyridin-4'(1'*H*)-one (REN-EB-375)[306]
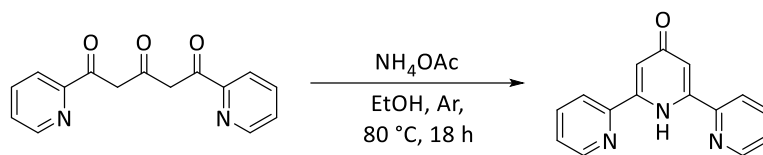
	M [g/mol]	m [g]	n [mmol]	eq
1,5-Bis(2'-pyridyl)pentane-1,3,5-trione	268.27	6.00	22.37	1.00
NH₄OAc	77.08	11.86	153.87	6.88

1,5-Bis(2'-pyridyl)pentane-1,3,5-trione and ammonium acetate were dissolved in 140 mL dry ethanol and heated to 80 °C for 18 h. After cooling to room temperature, the solvent was removed under reduced pressure. The brown solid was washed with cold water to obtain the light brown product.

Yield: 5.00 g (20.14 mmol, 90%) of a light brown powder. **^{1}H-NMR** (400 MHz, DMSO-d_6, 25 °C, δ/ppm): 8.79 (d, *J* = 4.8 Hz, 1H), 7.97 (d, *J* = 7.9 Hz, 1H), 7.90 (td, *J* = 7.7, 1.7 Hz, 1H), 7.45 (dd, *J* = 7.4, 4.9 Hz, 1H), 7.31 (s, 1H). **IR** (KBr, $\tilde{v}$/cm^{-1}): 3345.4, 3269.7, 1637.8, 1526.4, 1317.6, 1277.6, 1116.6, 997.0, 786.8, 622.4.

4'-Chloro-2,2':6',2''-terpyridine (REN-EB-377)[306]
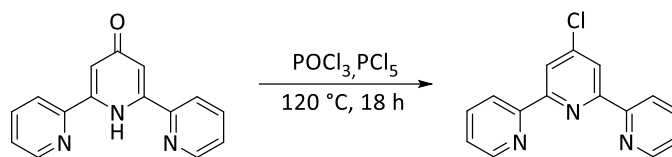
	M [g/mol]	m [g]	n [mmol]	eq	V [mL]
2,2':6',2''-Terpyridin-4'(1'H)-one	248.27	1.50	6.02	1.00	-
POCl₃	153.33	-	-	-	74.60
PCl₅	208.22	2.98	14.31	2.38	-

2,2':6',2''-Terpyridin-4'(1'H)-one, phosphorous oxychloride and phosphorus pentachloride were heated to 120 °C for 18 h. After cooling, the solvent was removed under reduced pressure. 75 mL of distilled water were slowly added to the brown residue. A pH = 12 was adjusted with aqueous potassium hydroxide solution. The brown solution was extracted with chloroform (3 x 70 mL) and dried over magnesium sulfate. The solvent was removed under reduced pressure to obtain the brown powder.

Yield: 1.2 g (4.48 mmol, 75%) of a light brown powder. **¹H-NMR** (400 MHz, CDCl₃, 25 °C, δ/ppm): 8.76-8.67 (m, 1H), 8.60 (d, J = 7.9 Hz, 1H), 8.49 (s, 1H), 7.87 (td, J = 7.7, 1.8 Hz, 1H), 7.43-7.32 (m, 1H). **IR** (KBr, $\tilde{v}$/cm⁻¹): 3088.4, 1557.2, 1466.1, 1393.8, 1064.0, 993.2, 882.3, 816.7, 787.3, 572.3.

4'-Hydrazino-2,2':6',2''-terpyridine (REN-EB-379)[307]
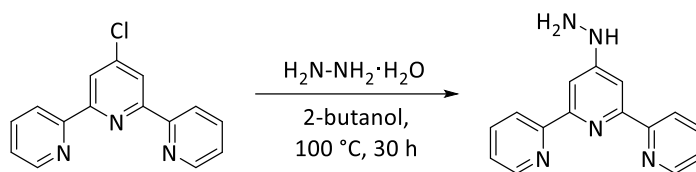
	M [g/mol]	m [g]	n [mmol]	V [mL]
4'-Chloro-2,2':6',2''-terpyridine	267.71	1.10	4.11	-
Hydrazine hydrate (50-60% aqueous solution)	-	-	-	7.32

4'-Chloro-2,2':6',2''-terpyridine was suspended in 23 mL 2-butanol at 60 °C and hydrazine hydrate was added dropwise. The red solution was stirred at 100 °C for 43 h. After cooling to 4 °C, the light brown precipitate was filtered, washed with cold water, and dried *in vacuo*.

Yield: 700 mg (2.66 mmol, 65%) of a light brown powder. **^{1}H-NMR** (400 MHz, CDCl$_3$, 25 °C, δ/ppm): 8.71 (d, *J* = 5.0 Hz, 1H), 8.63 – 8.58 (m, 1H), 8.49 (s, 1H), 7.84 (m, 2H), 7.38 (d, *J* = 6.7 Hz, 1H), 5.78 (s, 1H), 3.82 (s, 1H). **IR** (KBr, $\tilde{v}$/cm^{-1}): 3329.2, 3277.0, 1605.0, 1585.2, 1565.0, 1466.1, 1403.4, 986.4, 786.3, 730.9.

L3: 4'-Azido-2,2':6',2''-terpyridine (REN-EB-248)[307]
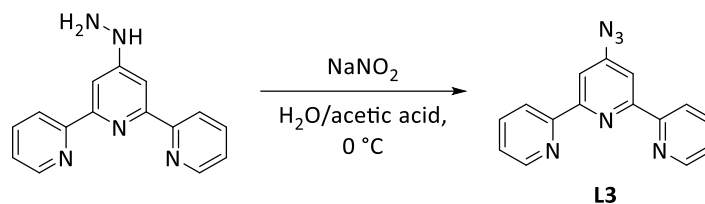
	M [g/mol]	m [g]	n [mmol]	eq
4'-Hydrazino-2,2':6',2''-terpyridine	263.30	0.87	3.29	1.00
NaNO$_2$	69.00	2.27	32.85	10.00

4'-Hydrazino-2,2':6',2''-terpyridine was dissolved in 10.9 mL distilled water/acetic acid (8:2.9) at 0 °C. A solution of sodium nitrite in 5.75 mL distilled water was added dropwise to the solution at 0 °C. The solution was stirred at 0 °C for 30 min and then allowed to warm up to room temperature. A pH = 12 was adjusted with aqueous sodium hydroxide solution. The obtained brownish precipitate was extracted with diethyl ether. The solvent was removed to obtain the product as a light brown solid.

Yield: 145 mg (0.53 mmol, 91%) of a light brown powder. **^{1}H-NMR** (400 MHz, CDCl$_3$, 25 °C, δ/ppm): 8.71 (d, J = 4.8 Hz, 1H), 8.61 (d, J = 7.8 Hz, 1H), 8.16 (s, 1H), 7.95-7.80 (m, 1H), 7.41-7.32 (m, 1H). **IR** (KBr, $\tilde{v}$/cm^{-1}): 3059.0, 2108.8, 1580.9, 1565.0, 1467.6, 1403.9, 1354.8, 1241.9, 787.8, 405.9. **UV-Vis** (MeCN, ε/10^{-6} L mol^{-1} cm^{-1}): 49 261 cm^{-1} (0.21), 40 486 cm^{-1} (0.24), 36 232 cm^{-1} (0.21). **UV-Vis** (MeOH, ε/10^{-6} L mol^{-1} cm^{-1}): 40 323 cm^{-1} (0.26), 37 453 cm^{-1} (0.25).

4'-{[(Trifluormethyl)sulfonyl]oxy}-2,2':6',2''-terpyridine (REN-EB-302)[308]
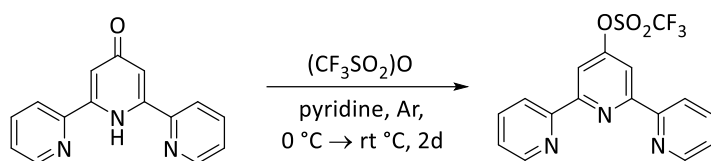
	M [g/mol]	m [mg]	n [mmol]	eq	ρ [g/cm³]	V [mL]
2,2':6',2''-Terpyridin-4'(1'*H*)-one	249.27	700	2.81	1.00	-	-
Trifluoromethanesulfonic anhydride	282.14	872	3.09	1.10	1.68	0.52

2,2':6',2''-Terpyridin-4'(1'*H*)-one was dissolved in 8.75 mL dry pyridine and cooled to 0 °C. Trifluoromethanesulfonic anhydride was added dropwise at 0 °C while stirring and the light brown solution turned dark. The solution was stirred for 30 min at 0 °C and then 2 d at room temperature. The brown solution was poured into ice and stirred for 1 h. The light brown precipitate was filtered and washed with ice cold distilled water. The light brown solid was dissolved in 70 mL *n*-hexane and filtered. The solvent was removed slowly to obtain the product as light brown powder.

Yield: 850 mg (2.23 mmol, 79%) of a light brown powder. **¹H-NMR** (400 MHz, CDCl₃, 25 °C, δ/ppm): 8.73 (d, *J* = 4.8 Hz, 1H), 8.63 (d, *J* = 8.0 Hz, 1H), 8.43 (s, 1H), 7.89 (td, *J* = 7.7, 1.8 Hz, 1H), 7.40 (ddd, *J* = 7.5, 4.8, 1.2 Hz, 1H). **IR** (KBr, ṽ/cm⁻¹): 3107.7, 1563.5, 1426.1, 1403.9, 1199.5, 1139.2, 948.8, 793.6, 606.5, 403.1.

4'-Iodo-2,2':6',2''-terpyridine (REN-EB-309)[308]
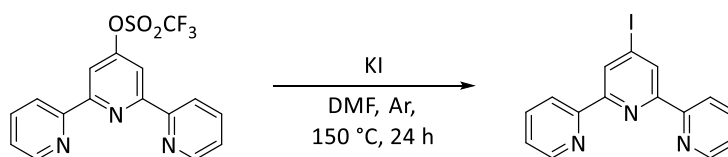
	M [g/mol]	m [g]	n [mmol]	eq
4'-{[(Trifluormethyl)sulfonyl]oxy}-2,2':6',2''-terpyridine	381.32	1.02	2.68	1.00
KI	166.00	0.89	5.35	2.00

4'-{[(Trifluormethyl)sulfonyl]oxy}-2,2':6',2''-terpyridine and potassium iodide were dissolved in 20 mL dry dimethylformamide under Argon atmosphere and heated to 150 °C for 24 h. After cooling to room temperature, the reddish solution was poured into ice water and the yellow suspension was stirred for 30 min. The aqueous suspension was extracted with ethyl acetate and the combined organic solutions were dried over magnesium sulfate. The solvent was removed under reduced pressure to yield a brownish powder as product.

Yield: 285 mg (0.79 mmol, 30%) of a light brown powder. **^{1}H-NMR** (400 MHz, CDCl$_3$, 25 °C, δ/ppm): 8.87 (s, 2H), 8.71 (d, J = 4.9 Hz, 1H), 8.58 (d, J = 8.0 Hz, 2H), 7.91-7.82 (m, 2H), 7.40-7.32 (m, 1H). **IR** (KBr, $\tilde{v}$/cm^{-1}): 3434.6, 3058.6, 1544.7, 1466.6, 1387.1, 1263.2, 1068.9, 993.2, 789.7, 666.8.

4'-[(Trimethylsilyl)-1-ethynyl]-2,2':6',2''-terpyridine (REN-EB-273)[309]
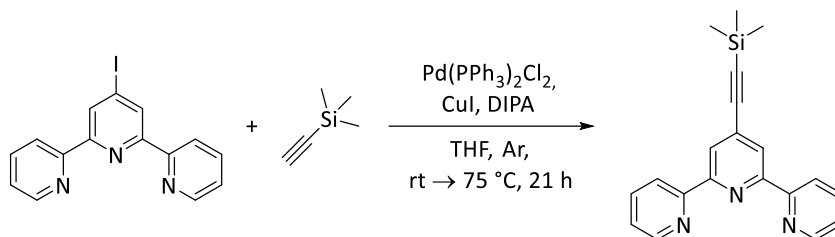
	M [g/mol]	m [mg]	n [mmol]	eq	ρ [g/cm^3]	V [mL]
4'-Iodo-2,2':6',2''-terpyridine	359.27	435	1.21	1.00	-	-
CuI	190.44	23	0.12	0.10	-	-
Pd(PPh$_3$)$_2$Cl$_2$	701.91	25	0.04	0.03	-	-
DIPA	101.19	-	-	-	0.72	4.25
Trimethylsilylacetylene	98.22	180	1.83	1.51	0.71	0.25

4'-Iodo-2,2':6',2''-terpyridine, bis(triphenylphosphine)palladium(II) dichloride, copper(I) iodide and diisopropylamine (DIPA) were suspended in 10 mL dry tetrahydrofuran under Argon atmosphere. Trimethylsilylacetylene was added dropwise to the solution while the color changed from yellow over green to black. The black solution was stirred for 18 h at room temperature and was then heated to 75 °C for 3 h. After cooling to room temperature, the reaction mixture was filtered over celite and washed with tetrahydrofurane and diethylether. The solvent was removed under reduced pressure to obtain a dark brown solid. The product was isolated by flash chromatography (SiO$_2$, chloroform/methanol 99:1).

Yield: 220 mg (0.67 mmol, 55%) of a light brown powder. **^{1}H-NMR** (400 MHz, DMSO-d_6, 25 °C, δ/ppm): 8.74-8.69 (m, 1H), 8.60 (d, J = 7.9 Hz, 1H), 8.51 (s, 1H), 7.87 (td, J = 7.7, 1.9 Hz, 1H).

L4: 4'-Ethynyl-2,2':6'2''-terpyridine (REN-EB-274)[309]
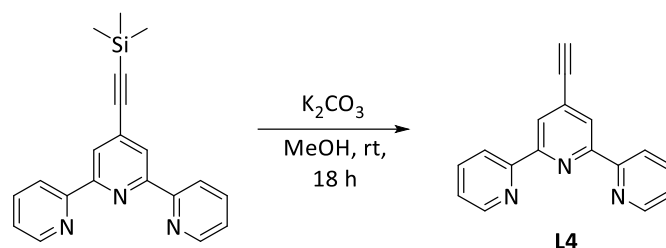
	M [g/mol]	m [mg]	n [mmol]	eq
4'-[(Trimethylsilyl)-1-ethynyl]-2,2':6',2''-terpyridine	329.47	220	0.67	1.00
K$_2$CO$_3$	138.21	111	0.80	1.20

4'-[(Trimethylsilyl)-1-ethynyl]-2,2':6',2''-terpyridine and potassium carbonate were dissolved in 100 mL methanol. The reaction mixture was stirred for 18 h at room temperature. Then 25 mL distilled water were added and the methanol was removed under reduced pressure and the aqueous suspension was extracted with dichloromethane (3 x 18 mL). The organic phase was washed with brine and dried over magnesium sulfate. The solvent was removed under reduced pressure to obtain the light brown product.

Yield: 200 mg (0.67 mmol, quant.) of a light brown powder. **^{1}H-NMR** (400 MHz, CDCl$_3$, 25 °C, δ/ppm 8.72 (d, J = 3.9 Hz, 1H), 8.61 (d, J = 7.9 Hz, 1H), 8.55 (s, 1H), 7.87 (t, J = 7.7 Hz, 1H), 7.36 (t, J = 6.3 Hz, 1H), 3.32 (s, 1H). **IR** (KBr, $\tilde{v}$/cm^{-1}): 3217.7, 2109.3, 1585.2, 1466.6, 1391.9, 1116.6, 883.2, 787.8, 615.2, 408.8.

6.4.1.2 Complexes

Complexes with L3: [Co(L3)₂]X₂

L3

MX₂·nH₂O
solvent

C7-14
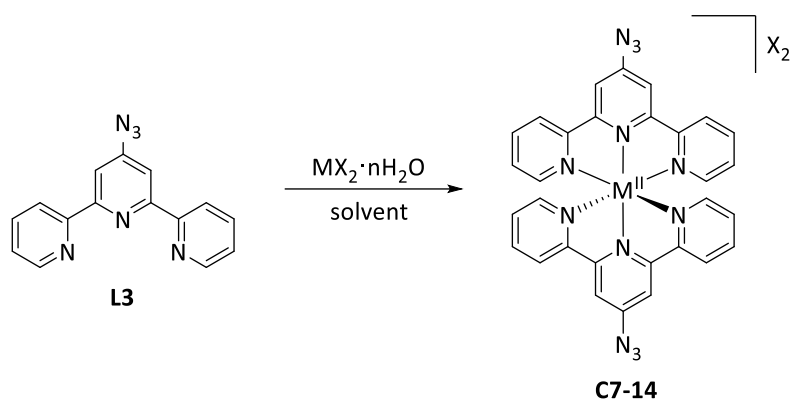
C7: [Co(L3)₂](ClO₄)₂ (REN-EB-270)

	M [g/mol]	m [mg]	n [mmol]	eq
L3	274.28	27	0.10	2.00
Co(ClO₄)₂·6H₂O	366.74	18	0.05	1.00

L3 was dissolved in 10 mL chloroform/methanol (3:2). Cobalt(II) perchlorate hexahydrate was dissolved in 4 mL methanol and added to the ligand solution. The brown precipitate was filtered, washed with chloroform and methanol, and dried *in vacuo.*

Yield: 28 mg (34.77 µmol, 69%) of a brown powder. **IR** (KBr, $\tilde{v}$/cm^{-1}): 3435.6, 3081.7, 2123.2, 1615.1, 1473.8, 1366.3, 1250.1, 1091.5, 792.6, 622.9. **ESI-MS** (MeCN): m/z [Co^{II}(**L3**)₂]$^{2+}$ exp.: 303.5635, theo.: 303.5627; [[Co^{II}(**L3**)(terpy)](ClO₄)]$^+$ exp.: 665.0737, theo.: 665.0732, [[Co^{II}(**L3**)₂](ClO₄)]$^+$ exp.: 706.0750, theo.: 706.0746. **UV-Vis** (MeCN, ε/10^{-6} L mol^{-1} cm^{-1}): 47 847 cm^{-1} (0.45), (0.38), 35 336 cm^{-1} (0.55), 32 051 cm^{-1} (0.27), 31 250 cm^{-1} (0.26), 26 954 cm^{-1} (0.35), 22 124 cm^{-1} (0.16), 19 646 cm^{-1} (0.15).

C8: [Co(L3)₂](PF₆)₂ (REN-EB-342)

	M [g/mol]	m [mg]	n [mmol]	eq
L3	274.28	55	0.20	2.04
Co(OAc)₂·4H₂O	249.08	25	0.10	1.00
NH₄PF₆	163.00	-	-	excess

Cobalt(II) acetate tetrahydrate and **L3** were dissolved in 10 mL chloroform/methanol (9:1) and stirred for 10 min. A saturated methanolic ammonium hexafluorophosphate solution was freshly prepared, filtered over Celite and added dropwise to the reaction solution until a reddish precipitate formed. The red precipitate was filtered and washed with methanol and diethyl ether.

Yield: 15 mg (16.71 μmol, 16%) of a red powder. **IR** (KBr, $\tilde{v}$/cm^{-1}): 3113.0, 3089.9, 2125.2, 1616.54, 1558.68, 1473.4, 1437.2, 1250.6, 835.5, 557.3. **UV-Vis** (MeCN, ε/10^{-6} L mol^{-1} cm^{-1}): 47 847 cm^{-1} (0.46), 35 587 cm^{-1} (0.55), 31 949 cm^{-1} (0.29), 31 153 cm^{-1} (0.28), 27 548 cm^{-1} (0.05), 21 786 cm^{-1} (0.02), 19 841 cm^{-1} (0.02).

C9: [Co(L3)₂]Br₂ (REN-EB-380-2)

	M [g/mol]	m [mg]	n [mmol]	eq
L3	274.28	27	0.10	2.00
CoBr₂·xH₂O	218.75	11	0.05	1.00

L3 was dissolved in 5 mL chloroform. Cobalt(II) bromide hydrate was dissolved in 4 mL methanol and added to the ligand solution. The brown precipitate was filtered, washed with chloroform and methanol and dried *in vacuo*.

Yield: 15 mg (19.55 μmol, 30%) of a brown powder. **IR** (KBr, $\tilde{v}$/cm^{-1}): 3049.9, 2114.6, 1613.2, 1568.3, 1553.4, 1471.9, 1435.3, 1364.4, 1249.2, 794.5. **UV-Vis** (MeOH, ε/10^{-6} L mol^{-1} cm^{-1}): 46 296 cm^{-1} (0.43), 35 336 cm^{-1} (0.43), 32 051 cm^{-1} (0.25), 22 779 cm^{-1} (0.02).

C10: [Co(L3)$_2$]Cl$_2$ (REN-EB-380-5)

	M [g/mol]	m [mg]	n [mmol]	eq
L3	274.28	27	0.10	2.00
CoCl$_2$·6H$_2$O	237.93	12	0.05	1.00

L3 was dissolved in 5 mL chloroform. Cobalt(II) chloride hexahydrate was dissolved in 4 mL methanol and added to the ligand solution. The brown precipitate was filtered, washed with chloroform and methanol, and dried *in vacuo*.

Yield: 12 mg (17.69 μmol, 35%) of a brown powder. **IR** (KBr, $\tilde{v}$/cm^{-1}): 3013.7, 2114.6, 1612.7, 1550.0, 1470.0, 1434.8, 1413.1, 1363.9, 1248.7, 794.5. **UV-Vis** (MeOH, ε/10^{-6} L mol^{-1} cm^{-1}): 45 872 cm^{-1} (0.45), 35 461 cm^{-1} (0.46), 31 746 cm^{-1} (0.27), 22 727 cm^{-1} (0.02).

C11: [Co(L3)$_2$](SCN)$_2$ (REN-EB-380-1)

	M [g/mol]	m [mg]	n [mmol]	eq
L3	274.28	27.43	0.10	2.00
Co(SCN)$_2$	175.10	9	0.05	1.00

L3 was dissolved in 5 mL chloroform. Cobalt(II) thiocyanate was dissolved in 4 mL methanol and added to the ligand solution. The brown precipitate was filtered, washed with chloroform and methanol, and dried *in vacuo*. Red single crystals formed after several weeks by evaporation of the solvent.

Yield: 13 mg (17.96 μmol, 36%) of a brown powder. **IR** (KBr, $\tilde{v}$/cm^{-1}): 3057.6, 2117.9, 2371.1, 1607.9, 1599.2, 1556.3, 1471.9, 1430.9, 1363.9, 1246.3. **UV-Vis** (MeCN, ε/10^{-6} L mol^{-1} cm^{-1}): 47 170 cm^{-1} (0.46), 35 587 cm^{-1} (0.46), 31 847 cm^{-1} (0.23).

C12: [Co(L3)$_2$]SO$_4$ (REN-EB-380-4)

	M [g/mol]	m [mg]	n [mmol]	eq
L3	274.28	27	0.10	2.00
CoSO$_4$·7H$_2$O	281.09	14	0.05	1.00

L3 was dissolved in 5 mL chloroform. Cobalt(II) sulfate heptahydrate was dissolved in 4 mL methanol and added to the ligand solution. The brown precipitate was filtered, washed with chloroform and methanol, and dried *in vacuo*.

Yield: 15 mg (17.69 µmol, 35%) of a brown powder. **IR** (KBr, $\tilde{v}$/cm^{-1}): 2921.6, 2119.9, 2020.1, 1615.6, 1480.1, 1384.2, 1248.7, 1117.1, 790.2, 619.5. **UV-Vis** (MeOH, ε/10^{-6} L mol^{-1} cm^{-1}): 45 455 cm^{-1} (0.48), 35 461 cm^{-1} (0.33), 31 447 cm^{-1} (0.19), 20 576 cm^{-1} (0.23).

C13: [Co(L3)₂](BF₄)₂ (REN-EB-380-3)

	M [g/mol]	m [mg]	n [mmol]	eq
L3	274.28	27	0.10	2.00
Co(BF₄)₂·6H₂O	340.63	17	0.05	1.00

L3 was dissolved in 5 mL chloroform. Cobalt(II) tetrafluoroborate hexahydrate was dissolved in 4 mL methanol and added to the ligand solution. The brown precipitate was filtered, washed with chloroform and methanol, and dried *in vacuo*.

Yield: 13 mg (16.64 µmol, 33%) of a brown powder. **IR** (KBr, $\tilde{v}$/cm^{-1}): 3084.1, 2121.3, 1615.1, 1554.3, 1473.4, 1437.2, 1366.3, 1250.6, 1059.7, 793.1. **UV-Vis** (MeCN, ε/10^{-6} L mol^{-1} cm^{-1}): 47 619 cm^{-1} (0.47), 35 336 cm^{-1} (0.51), 32 154 cm^{-1} (0.28), 22 124 cm^{-1} (0.02).

C14: [Zn(aterpy)₂](ClO₄)₂ (REN-EB-283)

	M [g/mol]	m [mg]	n [mmol]	eq
L3	274.28	27	0.10	2.00
Zn(ClO₄)₂·6H₂O	372.36	19	0.05	1.00

L3 was dissolved in 5 mL chloroform. Zinc(II) perchlorate hexahydrate was dissolved in 3 mL methanol and added to the ligand solution. The yellow precipitate was filtered, washed with chloroform/methanol and dried *in vacuo*.

Yield: 35 mg (43.06 µmol, 86%) of yellow powder. **^{1}H-NMR** (400 MHz, DMSO-d_6, 25 °C, δ/ppm): 8.97 (s, 1H, H^6/H$^{6''}$), 8.81 (s, 1H, H^3/H$^{3''}$), 8.26 (s, 1H, H$^{3'}$/H$^{5'}$), 7.89 (s, 1H, H^4/H$^{4''}$), 7.50 (s, 1H, H^5/H$^{5''}$). **IR** (KBr, $\tilde{v}$/cm^{-1}): 3441.4, 3082.2, 2128.6, 1601.1, 1477. 1435.7, 1252.5, 1086.7, 793.1, 622.4. **ESI-MS** (MeCN): m/z [**L3**+Na]$^+$ exp.: 297.0863, theo.: 297.0859; [2**L3**+Na]$^+$ exp.: 571.1824, theo.: 571.1826; [M+Na]$^+$ exp.: 711.0701, theo.: 711.0705.

Complexes with Brterpy: [Co(Brterpy)₂]X₂

C15, C16
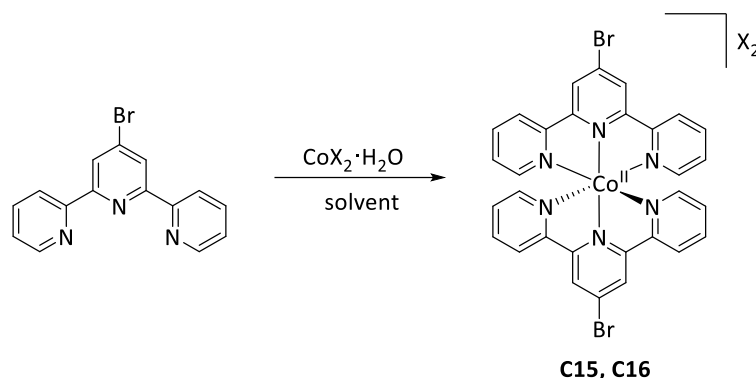
C15: [Co(Brterpy)₂](ClO₄)₂ (REN-EB-351)

	M [g/mol]	m [mg]	n [mmol]	eq
4'-Bromo-2,2':6',2''-terpyridine	312.17	31	0.10	2.00
Co(ClO₄)₂·6H₂O	366.74	18	0.05	1.00

4'-Bromo-2,2':6',2''-terpyridine was dissolved in 4 mL chloroform. Cobalt(II) perchlorate hexahydrate was dissolved in 1 mL methanol and added to the ligand solution. The red precipitate was filtered, washed with chloroform and dried *in vacuo*. Red crystals suitable for X-ray single crystal diffraction were obtained by evaporation of the solvent after several months.

Yield: 11 mg (12.47 μmol, 25%) of a brown powder. **IR** (KBr, $\tilde{v}$/cm⁻¹): 3086.0, 1599.2, 1551.0, 1470.5, 1421.3, 1384.2, 1246.8, 1091.5, 791.2, 622.4. **ESI-MS** (MeCN): m/z [Co(Brterpy)₂]²⁺ exp.: 341.4712, theo.: 341.4708; [Co(Brterpy)₂(ClO₄)]⁺ exp.: 781.8907, theo.: 781.8897. **UV-Vis** (DMF, ε/10⁻⁶ L mol⁻¹ cm⁻¹): 35 971 cm⁻¹ (0.41), 31 546 cm⁻¹ (0.18), 30 769 cm⁻¹ (0.12).

C16: [Co(Brterpy)₂](PF₆)₂ (REN-EB-350)

	M [g/mol]	m [mg]	n [mmol]	eq
4'-Bromo-2,2':6',2''-terpyridine	312.17	59	0.190	2.00
Co(OAc)₂·4H₂O	249.08	23	0.094	1.00
NH₄PF₆	163.00	-	-	excess

4'-Bromo-2,2':6',2''-terpyridine and cobalt(II) acetate tetrahydrate were dissolved in 10 mL methanol. A saturated methanolic ammonium hexafluorophosphate solution was freshly prepared, filtered over Celite and added dropwise until a dark red precipitate appeared. The precipitate was filtered, washed with methanol and dried *in vacuo*. Red crystals suitable for X-ray single crystal diffraction were obtained by evaporation of the solvent after two weeks.

Yield: 19 mg (19.52 μmol, 21%) of a brown powder. **IR** (KBr, $\tilde{v}$/cm^{-1}): 3121.2, 1600.6, 1470.9, 1423.7, 1384.2, 1246.3, 911.7, 829.2, 792.6, 557.8. **ESI-MS** (MeCN): m/z [Co(Brterpy)$_2$]$^{2+}$ exp.: 341.4712, theo.: 341.4708; [Co(Brterpy)$_2$(PF$_6$)]$^+$ theo.: 827.9064, exp.: 827.9065. **UV-Vis** (DMF, ε/10^{-6} L mol^{-1} cm^{-1}): 36 101 cm^{-1} (0.46).

Complexes with L4: [Co(L)(L4)]

C18: [Co(oda)(L4)] (REN-EB-277) [229]
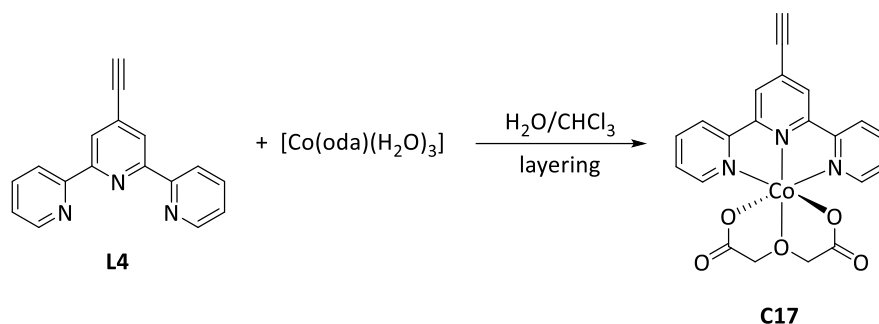
	M [g/mol]	m [mg]	n [μmol]	eq
L4	257.29	23.00	86.30	1.00
[Co(oda)(H₂O)₃]	244.89	21.86	89.30	1.00

L4 was dissolved in 5 mL chloroform and [Co(oda)(H₂O)₃] in 4 mL distilled water (under warming to 50 °C for a few minutes). The aqueous solution was carefully layered on top of the organic layer. The next day, red single crystals formed at the interface. The crystals were filtered, washed with chloroform, and dried.

Yield: 20 mg of red crystals (44.61 μmol, 50%). **IR** (KBr, $\tilde{v}$/cm^{-1}): 3397.0, 3203.6, 3067.2, 2110.2, 1628.6, 1389.1, 1248.7, 1107.4, 910.2, 795.0.

C18: [Co(dipic)(L4)] (REN-EB-395)
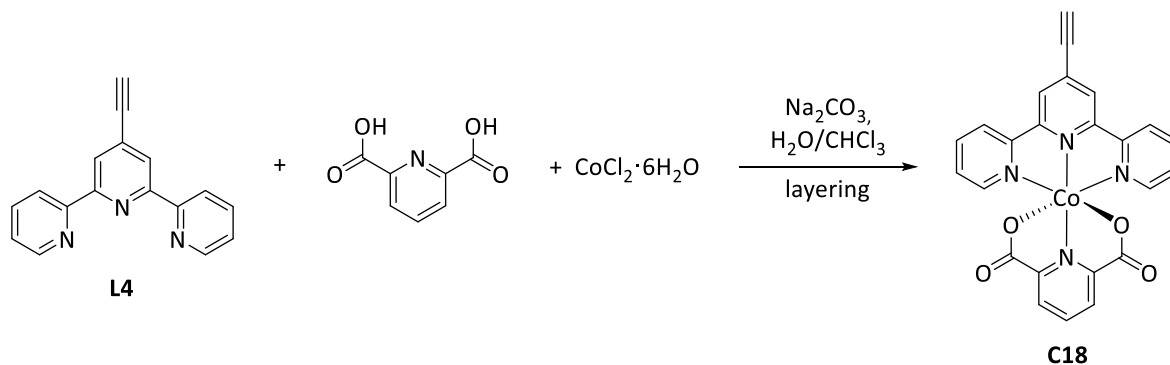
	M [g/mol]	m [mg]	n [mmol]	eq
Pyridine-2,6-dicarboxylic acid	167.12	17	0.1	1.00
L4	257.29	26	0.1	1.00
CoCl$_2$·6H$_2$O	237.93	24	0.1	1.00
Na$_2$CO$_3$	105.99	11	0.1	1.00

Pyridine-2,6-dicarboxylic acid and sodium carbonate were suspended in 2 mL distilled water. A solution of cobalt(II) chloride hexahydrate in 2 mL distilled water was added to the colorless solution and stirred for further five minutes. **L4** was dissolved in 5 mL chloroform. The aqueous solution was layered on top of the ligand solution. After one day, a brownish precipitated had formed at the interface. The precipitate was filtered and dissolved in dimethylformamide/ dichloromethane. After one day, a small amount of yellow crystals formed suitable for single crystal X-ray diffraction.

C19: [Co₃(L3-4)₂(oda)₂](ClO₄)₂ (REN-EB-284)
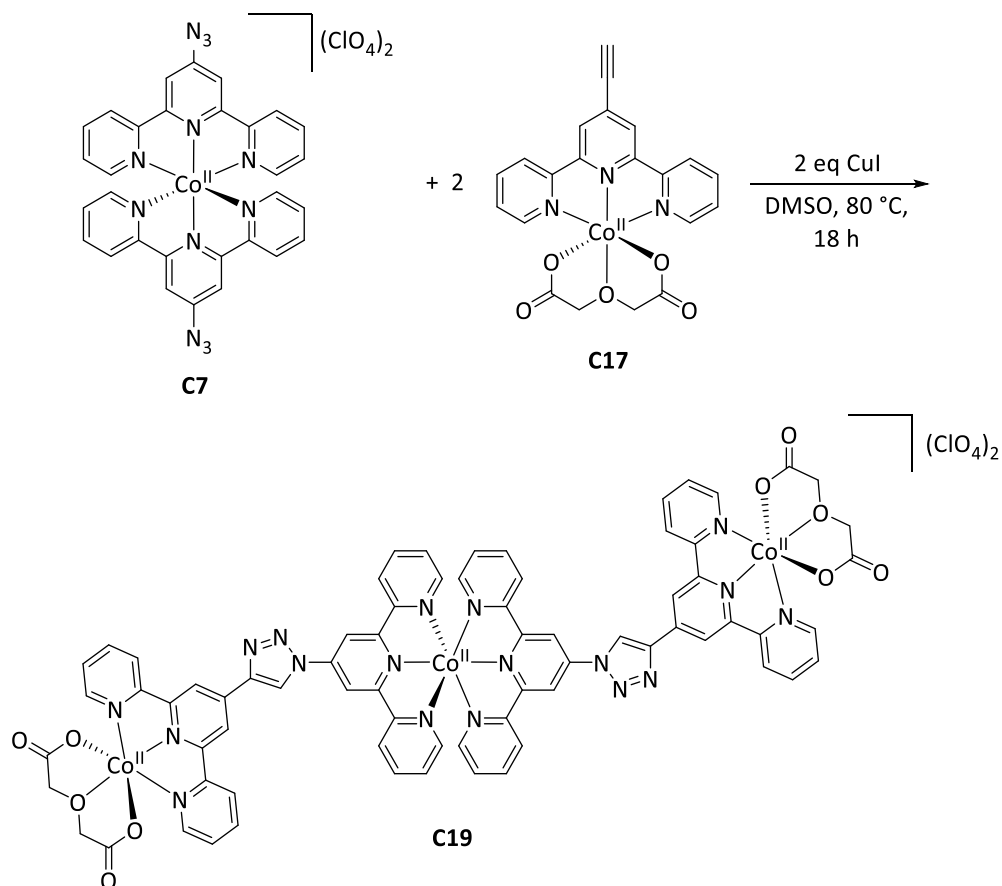
	M [g/mol]	m [mg]	n [μmol]	eq
C7	806.40	8.06	10.00	1.00
C17	448.30	8.97	20.00	2.00
CuI	190.44	3.81	20.00	2.00

C7, **C17** and copper(I) iodide were dissolved in 3.5 mL dimethyl sulfoxide in a 10 mL vial. The solution was stirred at 80 °C for 18 h. The solvent was removed to obtain in a brown powder. The remaining copper(I) iodide could not be removed by aqueous EDTA, potassium iodide or sodium cyanide solution, hence the powder was used for characterization without further purification.

IR (KBr, $\tilde{v}$/cm⁻¹): 3418.2, 3070.6, 1602.6, 1473.4, 1429.5, 1248.2, 1097.3, 1021.6, 791.6, 622.9.
UV-Vis (MeCN): 22 272 cm⁻¹, 19 455 cm⁻¹, 19 084 cm⁻¹.

6.4.2 The 'designer' ligand

6.4.1.3 The Ligand L5

4'-Formylbenzo-15-crown-5 (REN-EB-394)[322]
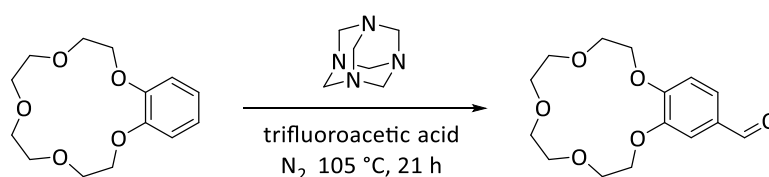
	M [g/mol]	m [g]	n [mmol]	eq
Benzo-15-crown-5	268.31	1.00	3.73	1.00
Urotropine	138.21	0.58	4.17	1.12

Benzo-15-crown-5 and urotropine were dissolved in 3.5 mL trifluoric acid under nitrogen atmosphere. The colorless solution was heated to 105 °C for 21 h. After cooling overnight, the dark reddish solution was poured into 60 g of ice and stirred for 2.5 h. The dark red solution was extracted with chloroform (5 x 25 mL). The organic layers were dried over magnesium sulfate and the solvent was removed under reduced pressure. The dark reddish brown residue was purified by column chromatography (SiO$_2$, CHCl$_3$:MeOH 20:1) and the product was obtained as light yellow solid.

Yield: 700 mg (2.36 mmol, 63%) of a light yellow powder. **^{1}H-NMR** (400 MHz, CDCl$_3$, 25 °C, δ/ppm): 9.84 (s, 1H), 7.45-7.43 (m, 1H), 7.39 (d, J = 1.9 Hz, 1H), 6.94 (d, J = 8.1 Hz, 1H), 4.20 (d, J = 4.0 Hz, 4H), 3.93 (dt, J = 9.2, 3.9 Hz, 4H), 3.77 (d, J = 3.5 Hz, 8H). **IR** (KBr, $\tilde{v}$/cm^{-1}): 3046.0, 2926.5, 2872.9, 1693.7, 1593.4, 1513.4, 1342.2, 1277.6, 1133.0, 936.3.

4'-Hydroxymethylbenzo-15-crown-5 (REN-EB-397)[322]
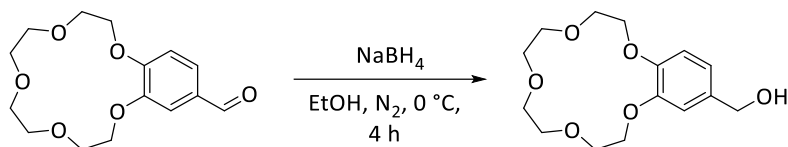
	M [g/mol]	m [mg]	n [mmol]	eq
4'-Formylbenzo-15-crown-5	296.32	700	2.362	1.00
NaBH$_4$	37.83	122	3.221	1.36

4'-Formylbenzo-15-crown-5 was suspended in dry ethanol under nitrogen atmosphere and cooled to 0 °C. Sodium borohydride was added portionwise under nitrogen flow to keep the temperature below 4 °C. Afterwards the colorless solution was stirred at 0 °C for 4 h. The solvent was removed under reduced pressure. The colorless residue was dissolved in 16 mL brine and extracted with dichloromethane (3 x 16 mL). The organic layers were dried over magnesium sulfate and the solvent was removed under reduced pressure to obtain the product.

Yield: 700 mg (2.35 mmol, 71%) of a colorless powder. **^{1}H-NMR** (400 MHz, CDCl$_3$, 25 °C, δ/ppm): 6.92 (d, J = 1.9 Hz, 1H), 6.90-6.81 (m, 2H), 4.60 (s, 1H), 4.14 (td, J = 5.5, 3.3 Hz, 4H), 3.91 (t, J = 4.4 Hz, 4H), 3.76 (s, 8H). **IR** (ATR, $\tilde{v}$/cm^{-1}): 2864.1, 1590.2, 1510.5, 1452.3, 1426.7, 1261.2, 1130.1, 1049.0, 932.9, 807.4.

L5: 4'-(4'''-Benzo-15-crown-5)-methyloxy-2,2'-6',2''-terpyridine L5 (REN-EB-401)[323]
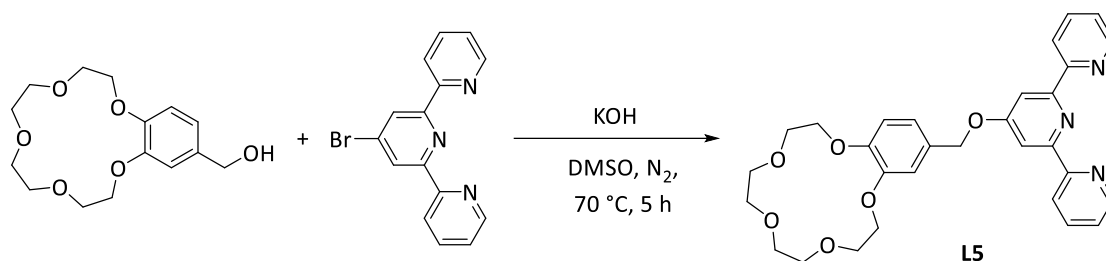
	M [g/mol]	m [g]	n [mmol]	eq
4'-Hydroxymethyl-benzo-15-crown-5	298.33	1.39	4.67	1.00
4'-Bromo-2,2':6',2''-terpyridine	312.16	1.50	4.67	1.00
KOH	56.11	1.35	24.03	5.00

Powdered potassium hydroxide was suspended in 11 mL dimethylsulfoxide under nitrogen atmosphere and heated up to 70 °C. 4'-Hydroxymethyl-benzo-15-crown-5 was dissolved in 11 mL dimethylsulfoxide and added to the suspension. After two hours 4'-bromo-2,2':6',2''-terpyridine was added, whereupon the colorless solution turned dark brown. The reaction mixture was heated for 5 h. After cooling to room temperature, the brown reaction mixture was poured into 300 mL of ice water and a light brown precipitate formed over night. The residue was extracted with chloroform (5 x 80 mL). The combined organic phases were dried over magnesium sulfate and the solvent was removed under reduced pressure. The light brown residue was dissolved in hot methanol and precipitated at −24 °C. The light brown powder was filtered and washed with cold methanol.

Yield: 2.02 g (4.154 mmol, 89 %) of a light brown powder. **^{1}H-NMR** (400 MHz, CDCl$_3$, 25 °C, δ/ppm): 8.72 (s, 2H, H^6/H$^{6''}$), 8.62 (m, 2H, H^3/H$^{3''}$), 8.06 (s, 2H, H$^{3'}$/H$^{5'}$), 8.01 (m, 2H, H^4/H$^{4''}$), 7.51 (m, 2H, H^5/H$^{5''}$), 7.16 (s, 1H, α), 7.05 (m, 1H, β), 6.98 (m, 1H, γ), 5.31 (s, 2H, CH_2), 4.08 (m, 4H, A/A'), 3.77 (m, 4H, B/B'), 3.61 (s, 8H, C/C'/D/D'). **IR** (KBr, $\tilde{v}$/cm^{-1}): 2935.1, 2873.9, 1582.3, 1564.5, 1351.9, 1269.9, 1195.7, 1138.3, 1007.1, 792.1.

6.4.1.4 Complexes

C20: [Co(L5)₂](BF₄)₂ (REN-EB-364)
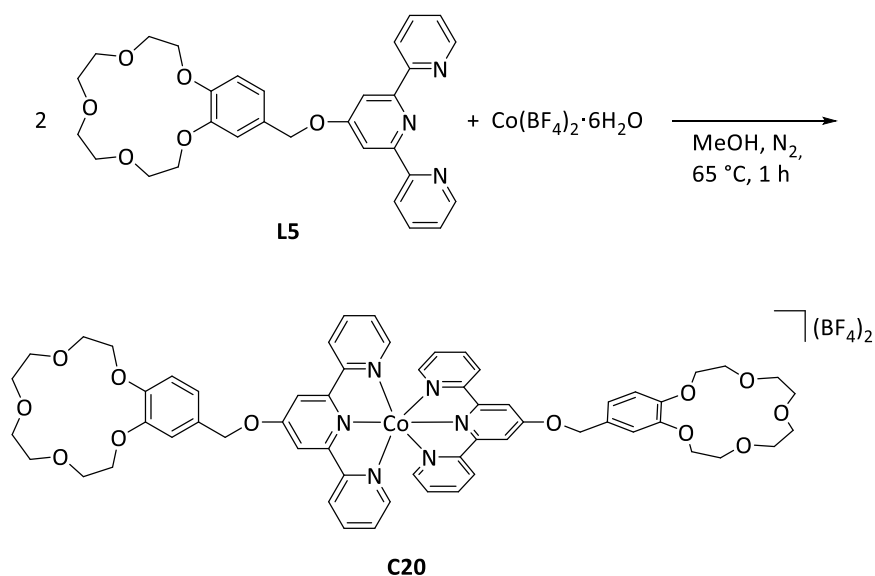
	M [g/mol]	m [mg]	n [mmol]	eq
L5	529.59	158	0.30	2.00
Co(BF₄)₂·6H₂O	340.63	50	0.15	1.00

L5 and cobalt(II) tetrafluoroborate hexahydrate were each suspended in 5 mL methanol under nitrogen atmosphere and heated to 50 °C. The warm cobalt(II) solution was added to the ligand solution and heated to 70 °C for 1 h. After cooling down the solvent was removed and the red solid dried *in vacuo*.

Yield: 208 mg (quant.) of a red powder. **IR** (KBr, $\tilde{v}$/cm⁻¹): 3431.2, 3078.3, 2926.0, 1613.6, 1516.3, 1475.8, 1358.6, 1216.4, 1054.4, 796.9.

C21: [Co^{III}(L5)$_2$][Co^{II}(NCS)$_4$]$_{1.5}$·3MeCN (REN-EB-443-2)

L5

C21
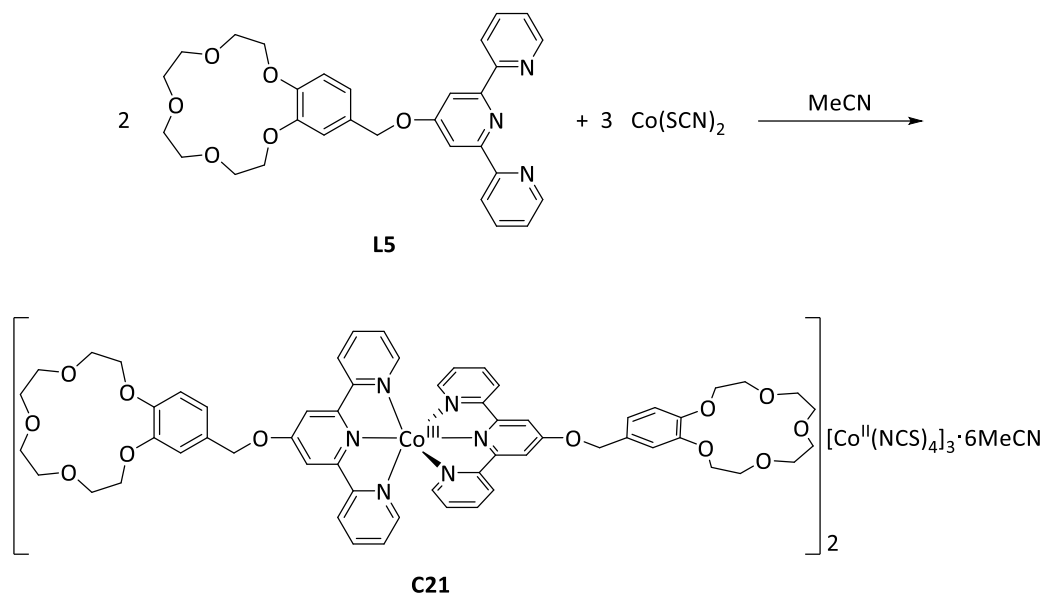
	M [g/mol]	m [mg]	n [mmol]	eq
L5	529.59	53	0.10	2.00
Co(SCN)$_2$	175.10	26	0.15	3.00

L5 was suspended in 6 mL acetonitrile and dissolved by heating to 60 °C. Cobalt(II) thiocyanate was dissolved in 6 mL acetonitrile and added to the warm ligand solution. The solution was stirred for 1 h at 60 °C and turned from red and to green. After cooling, the solution was filtered and the solution opened for evaporation. The next day, green single crystals suitable for X-ray single crystal diffraction were collected.

Yield: 27 mg (8.04 μmol, 16%) of green crystals. **IR** (KBr, ṽ/cm^{-1}): 3072.1, 2864.7, 2062.0, 1614.6, 1482.0, 1384.2, 1360.1, 1267.0, 1215.9, 783.9. **Elemental analysis:** C$_6$H$_{14}$Cl$_2$CoN$_4$O$_{12}$S$_2$, calc. C: 51.53%, H: 4.26%, N: 12.52%, exp. C: 49.00%, H: 4.32%, N: 10.72%.

C22: [Dy(L5)(NO₃)₃(H₂O)] (REN-EB-378)
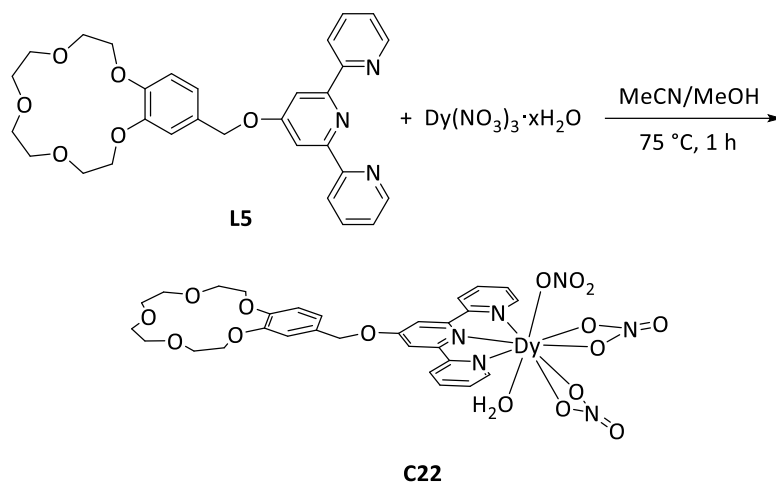
	M [g/mol]	m [mg]	n [mmol]	eq
L5	529.59	26	0.050	1.00
Dy(NO₃)₃·xH₂O	348.51	21	0.059	1.20

The ligand was dissolved in 8 mL acetonitrile/methanol (3:1) and dysprosium(III) nitrate hydrate in 4 mL acetonitrile/methanol (3:1). The metal solution was added to the ligand solution and the reaction mixture was stirred at 75 °C for 1 h. After cooling, the solution was filtered and opened for evaporation. After ten days, colorless single crystals were collected.

Yield: 14 mg (0.0156 mmol, 31%) of colorless crystals. **IR** (KBr, $\tilde{v}$/cm^{-1}): 3477.0, 2911.0, 1611.2, 1515.8, 1484.4, 1384.2, 1316.2, 1138.8, 1017.3, 797.4.

References

[1] P. Gütlich, H. A. Goodwin in *Topics in current chemistry* (Eds.: P. Gütlich, H. A. Goodwin), Springer Berlin Heidelberg, Berlin, Heidelberg, **2004**, pp. 1–47.

[2] L. Cambi, L. Szegö, *Ber. dtsch. Chem. Ges. A/B* **1931**, *64*, 2591.

[3] L. Cambi, L. Szegö, *Ber. dtsch. Chem. Ges. A/B* **1933**, *66*, 656.

[4] L. Cambi, L. Malatesta, *Ber. dtsch. Chem. Ges. A/B* **1937**, *70*, 2067.

[5] A. H. Ewald, R. L. Martin, Ross, I. G. and White, A. H., *Proc. R. Soc. Lond. A* **1964**, *280*, 235.

[6] B. N. Figgis, G. E. Toogood, *J. Chem. Soc., Dalton Trans.* **1972**, 2177.

[7] R. H. Petty, E. V. Dose, M. F. Tweedle, L. J. Wilson, *Inorg. Chem.* **1978**, *17*, 1064.

[8] H. Ohshio, Y. Maeda, Y. Takashima, *Inorg. Chem.* **1983**, *22*, 2684.

[9] B. J. Kennedy, A. C. McGrath, K. S. Murray, B. W. Skelton, A. H. White, *Inorg. Chem.* **1987**, *26*, 483.

[10] M. S. Haddad, W. D. Federer, M. W. Lynch, D. N. Hendrickson, *Inorg. Chem.* **1981**, *20*, 131.

[11] W. A. Baker, H. M. Bobonich, *Inorg. Chem.* **1964**, *3*, 1184.

[12] K. Madeja, E. König, *J. Inorg. Nucl. Chem.* **1963**, *25*, 377.

[13] E. Koenig, K. Madeja, *Inorg. Chem.* **1967**, *6*, 48.

[14] K. S. Murray in *Spin-Crossover Materials* (Ed.: M. A. Halcrow), John Wiley & Sons Ltd, Oxford, UK, **2013**, pp. 1–54.

[15] R. C. Stoufer, D. H. Busch, W. B. Hadley, *J. Am. Chem. Soc.* **1961**, *83*, 3732.

[16] W. Kläui, *Inorg. Chim. Acta* **1980**, *40*, X22-X23.

[17] M. A. Robinson, Curry, J. D., Busch, D. H., *Inorg. Chem.* **1963**, *2*, 1178.

[18] P. G. Sim, E. Sinn, *J. Am. Chem. Soc.* **1981**, *103*, 241.

[19] D. M. Halepoto, D. G. L. Holt, L. F. Larkworthy, G. J. Leigh, D. C. Povey, G. W. Smith, *J. Chem. Soc., Chem. Commun.* **1989**, 1322.

[20] E. König, S. Hüfner, E. Steichele, K. Madeja, *Zeitschrift für Naturforschung A* **1967**, *22*.

[21] E. Knig, S. Kremer, *Theoret. Chim. Acta* **1971**, *22*, 45.

[22] P. Gütlich, H. A. Goodwin (Eds.) *Topics in current chemistry*, Springer Berlin Heidelberg, Berlin, Heidelberg, **2004**.

[23] P. Gütlich, H. A. Goodwin, *Spin Crossover in Transition Metal Compounds II*, Springer, Berlin, Heidelberg, **2004**.

[24] P. Gütlich, H. A. Goodwin, *Spin Crossover in Transition Metal Compounds III*, Springer-Verlag; Springer e-books, Berlin, Heidelberg, **2004**.

[25] P. Gütlich, *Eur. J. Inorg. Chem.* **2013**, *2013*, 581.

References

[26] O. Kahn, *Molecular magnetism*, VCH, New York, NY, **1993**.

[27] A. Hauser in *Topics in current chemistry* (Eds.: P. Gütlich, H. A. Goodwin), Springer Berlin Heidelberg, Berlin, Heidelberg, **2004**, pp. 49–58.

[28] P. Gütlich, Y. Garcia, H. A. Goodwin, *Chem. Soc. Rev.* **2000**, *29*, 419.

[29] P. W. Atkins, M. E. Hagerman, D. F. Shriver, *Inorganic chemistry*, Oxford Univ. Press, Oxford, **2010**.

[30] F. Hund, *Z. Physik* **1927**, *40*, 742.

[31] S. Sugano, Tanabe, Y., Kamimura, H., *Pure and Applied Physics* **1970**.

[32] H. N. Russell, F. A. Saunders, *ApJ* **1925**, *61*, 38.

[33] J. Franck, E. G. Dymond, *Trans. Faraday Soc.* **1926**, *21*, 536.

[34] P. Gütlich, A. Hauser, H. Spiering, *Angew. Chem. Int. Ed. Engl.* **1994**, *33*, 2024.

[35] W. Haberditzl, *Z. Chem.* **1968**, *8*, 119.

[36] L. Wiehl, G. Kiel, C. P. Koehler, H. Spiering, P. Guetlich, *Inorg. Chem.* **1986**, *25*, 1565.

[37] J. A. Real, A. B. Gaspar, M. C. Muñoz, *Dalton Trans.* **2005**, 2062.

[38] M. Sorai, S. Seki, *J. Phys. Chem. Solids* **1974**, *35*, 555.

[39] H. Spiering, T. Kohlhaas, H. Romstedt, A. Hauser, C. Bruns-Yilmaz, J. Kusz, P. Gütlich, *Coord. Chem. Rev.* **1999**, *190-192*, 629.

[40] P. Gütlich, V. Ksenofontov, A. B. Gaspar, *Coord. Chem. Rev.* **2005**, *249*, 1811.

[41] H. G. Drickamer, *Angew. Chem.* **1974**, *86*, 61.

[42] S. Usha, R. Srinivasan, C.N.R. Rao, *Chem. Phys.* **1985**, *100*, 447.

[43] J. J. McGravey, I. Lawthers, *J. Chem. Soc., Chem. Commun.* **1982**, 906.

[44] S. Decurtins, P. Gütlich, C. P. Köhler, H. Spiering, A. Hauser, *Chem. Phys. Lett* **1984**, *105*, 1.

[45] A. Hauser in *Topics in current chemistry*, *Vol. 234* (Eds.: M.-L. Boillot, P. Gütlich), Springer, Berlin, **2004**, pp. 155–198.

[46] J.-F. Létard, P. Guionneau, L. Rabardel, J. A. K. Howard, A. E. Goeta, D. Chasseau, O. Kahn, *Inorg. Chem.* **1998**, *37*, 4432.

[47] G. Chastanet, C. Desplanches, C. Baldé, P. Rosa, M. Marchivie, P. Guionneau, *Chem.Sq.* **2018**.

[48] A. Hauser, *Chem. Phys. Lett* **1986**, *124*, 543.

[49] A. Hauser, *Coord. Chem. Rev.* **1991**, *111*, 275.

[50] A. Hauser, C. Enachescu, M. L. Daku, A. Vargas, N. Amstutz, *Coord. Chem. Rev.* **2006**, *250*, 1642.

[51] D. F. Evans, *J. Chem. Soc.* **1959**, 2003.

[52] B. Weber, F. A. Walker, *Inorg. Chem.* **2007**, *46*, 6794.

[53] J. A. Kitchen, N. G. White, M. Boyd, B. Moubaraki, K. S. Murray, P. D. W. Boyd, S. Brooker, *Inorg. Chem.* **2009**, *48*, 6670.

[54] A. A. Pavlov, G. L. Denisov, M. A. Kiskin, Y. V. Nelyubina, V. V. Novikov, *Inorg. Chem.* **2017**, *56*, 14759.

[55] E. M. Schubert, *J. Chem. Educ.* **1992**, *69*, 62.

[56] L. A. Yatsunyk, F. A. Walker, *Inorg. Chem.* **2004**, *43*, 757.

[57] K. de Buysser, G. G. Herman, E. Bruneel, S. Hoste, I. van Driessche, *Chem. Phys.* **2005**, *315*, 286.

[58] S. Alvarez, *J. Am. Chem. Soc.* **2003**, *125*, 6795.

[59] J. K. McCusker, A. L. Rheingold, D. N. Hendrickson, *Inorg. Chem.* **1996**, *35*, 2100.

[60] P. Guionneau, M. Marchivie, G. Bravic, J.-F. Létard, D. Chasseau in *Topics in current chemistry*, *Vol. 234* (Eds.: M.-L. Boillot, P. Gütlich), Springer, Berlin, **2004**, pp. 97–128.

[61] P. Gütlich, E. Bill, A. X. Trautwein, *Mössbauer Spectroscopy and Transition Metal Chemistry*, Springer Berlin Heidelberg, Berlin, Heidelberg, **2011**.

[62] J. H. Takemoto, B. Hutchinson, *Inorg. Chem.* **1973**, *12*, 705.

[63] P. Gütlich in *Structure and bonding*, Springer Berlin Heidelberg, Berlin, Heidelberg, **1981**, pp. 83–195.

[64] T. Nakamoto, Z. C. Tan, M. Sorai, *Inorg. Chem.* **2001**, *40*, 3805.

[65] E. König in *Structure and bonding* (Eds.: M. J. Clarke, J. B. Goodenough, J. A. Ibers, C. K. Jørgensen, D. M. P. Mingos, J. B. Neilands, G. A. Palmer, D. Reinen, P. J. Sadler, R. Weiss et al.), Springer Berlin Heidelberg, Berlin, Heidelberg, **1991**, pp. 51–152.

[66] B. Papánková, M. Vrbová, R. Boča, P. Šimon, K. Falk, G. Miehe, H. Fuess, *J. Therm. Anal* **2002**, *67*, 721.

[67] M. D. Timken, S. R. Wilson, D. N. Hendrickson, *Inorg. Chem.* **1985**, *24*, 3450.

[68] B. J. Kennedy, K. S. Murray, P. R. Zwack, H. Homborg, W. Kalz, *Inorg. Chem.* **1986**, *25*, 2539.

[69] J. Zarembowitch, O. Kahn, *Inorg. Chem.* **1984**, *23*, 589.

[70] H. Oyanagi, T. Tayagaki, K. Tanaka, *J. Phys. Chem. Solids* **2004**, *65*, 1485.

[71] A. Cannizzo, C. J. Milne, C. Consani, W. Gawelda, C. Bressler, F. van Mourik, M. Chergui, *Coord. Chem. Rev.* **2010**, *254*, 2677.

[72] H. Grünsteudel, H. Paulsen, W. Meyer-Klaucke, H. Winkler, A. X. Trautwein, H. F. Grünsteudel, A.Q.R. Baron, A. I. Chumakov, R. Rüffer, H. Toftlund, *Hyperfine Interactions* **1998**, *113*, 311.

[73] H. Paulsen, H. Grünsteudel, W. Meyer-Klaucke, M. Gerdan, H. F. Grünsteudel, A. I. Chumakov, R. Rüffer, H. Winkler, H. Toftlund, A. X. Trautwein, *Eur. Phys. J. B* **2001**, *23*, 463.

[74] J.-F. Létard, P. Guionneau, L. Goux-Capes in *Topics in current chemistry*, Springer-Verlag, Berlin/Heidelberg, **2004**, pp. 221–249.

[75] H. Spiering, E. Meissner, H. Köppen, E. W. Müller, P. Gütlich, *Chem. Phys.* **1982**, *68*, 65.

[76] N. Willenbacher, H. Spiering, *J. Phys. C: Solid State Phys.* **1988**, *21*, 1423.

[77] H. Spiering, N. Willenbacher, *J. Phys.: Condens. Matter* **1989**, *1*, 10089.

[78] M. Sorai, J. Ensling, P. Gütlich, *Chem. Phys.* **1976**, *18*, 199.

[79] T. Tayagaki, A. Galet, G. Molnar, M. C. Muñoz, A. Zwick, K. Tanaka, J.-A. Real, A. Bousseksou, *J. Phys. Chem. B* **2005**, *109*, 14859.

[80] C. Baldé, C. Desplanches, P. Gütlich, E. Freysz, J. F. Létard, *Inorg. Chim. Acta* **2008**, *361*, 3529.

[81] H. Köppen, E. W. Müller, C. P. Köhler, H. Spiering, E. Meissner, P. Gütlich, *Chem. Phys. Lett* **1982**, *91*, 348.

[82] R. Jakobi, H. Spiering, P. Gütlich, *J. Phys. Chem. Solids* **1992**, *53*, 267.

[83] H. Romstedt, A. Hauser, H. Spiering, *J. Phys. Chem. Solids* **1998**, *59*, 265.

[84] W. Barthel, F. Markwardt, *Biochem. Pharmacol* **1975**, *24*, 1903.

[85] T. Buchen, P. Gütlich, K. H. Sugiyarto, H. A. Goodwin, *Chem. Eur. J.* **1996**, *2*, 1134.

[86] G. Ritter, E. König, W. Ihler, H. A. Goodwin, *Inorg. Chem.* **1978**, *17*, 224.

[87] N. Paradis, G. Chastanet, J.-F. Létard, *Eur. J. Inorg. Chem.* **2012**, *2012*, 3618.

[88] K. S. Murray, C. J. Kepert in *Topics in current chemistry* (Eds.: P. Gütlich, H. A. Goodwin), Springer Berlin Heidelberg, Berlin, Heidelberg, **2004**, pp. 195–228.

[89] R. Hogg, R. G. Wilkins, *J. Chem. Soc.* **1962**, 341.

[90] J. Chambers, B. Eaves, D. Parker, R. Claxton, P. S. Ray, S. J. Slattery, *Inorg. Chim. Acta* **2006**, *359*, 2400.

[91] E. C. Constable, G. Baum, E. Bill, R. Dyson, R. van Eldik, D. Fenske, S. Kaderli, D. Morris, A. Neubrand, M. Neuburger et al., *Chem. Eur. J.* **1999**, *5*, 498.

[92] L. J. Kershaw Cook, R. Kulmaczewski, R. Mohammed, S. Dudley, S. A. Barrett, M. A. Little, R. J. Deeth, M. A. Halcrow, *Angew. Chem. Int. Ed. Engl.* **2016**, *55*, 4327.

[93] S. Kremer, W. Henke, D. Reinen, *Inorg. Chem.* **1982**, *21*, 3013.

[94] J. S. Judge, W. A. Baker, *Inorg. Chim. Acta* **1967**, *1*, 68.

[95] C. Köhler, E. Rentschler, *Eur. J. Inorg. Chem.* **2016**, *2016*, 1955.

[96] P. E. Figgins, D. H. Busch, *J. Am. Chem. Soc.* **1960**, *82*, 820.

[97] S. Hayami, Y. Komatsu, T. Shimizu, H. Kamihata, Y. H. Lee, *Coord. Chem. Rev.* **2011**, *255*, 1981.

[98] H. A. Goodwin in *Topics in current chemistry*, *Vol. 234* (Eds.: M.-L. Boillot, P. Gütlich), Springer, Berlin, **2004**, pp. 23–47.

[99] M.-L. Boillot, P. Gütlich (Eds.) *Topics in current chemistry*, *Vol. 234*, Springer, Berlin, **2004**.

[100] J.S. Griffith, *J. Inorg. Nucl. Chem.* **1956**, *2*, 229.

[101] C. M. Harris, T. N. Lockyer, R. L. Martin, H. R.H. Patil, E. Sinn, *Aust. J. Chem.* **1969**, *22*, 2105.

[102] E. N. Maslen, C. L. Raston, A. H. White, *J. Chem. Soc., Dalton Trans.* **1974**, 1803.

[103] H. Oshio, H. Spiering, V. Ksenofontov, F. Renz, P. Gütlich, *Inorg. Chem.* **2001**, *40*, 1143.

[104] B. N. Figgis, E. S. Kucharski, A. H. White, *Aust. J. Chem.* **1983**, *36*, 1527.

[105] B. N. Figgis, E. S. Kucharski, A. H. White, *Aust. J. Chem.* **1983**, *36*, 1537.

[106] A. B. Gaspar, M. C. Muñoz, V. Niel, J. A. Real, *Inorg. Chem.* **2001**, *40*, 9.

[107] A. Galet, A. B. Gaspar, M. C. Muñoz, J. A. Real, *Inorg. Chem.* **2006**, *45*, 4413.

[108] S. Hayami, K. Murata, D. Urakami, Y. Kojima, M. Akita, K. Inoue, *Chem. Commun. (Camb.)* **2008**, 6510.

[109] S. Hayami, Y. Shigeyoshi, M. Akita, K. Inoue, K. Kato, K. Osaka, M. Takata, R. Kawajiri, T. Mitani, Y. Maeda, *Angew. Chem. Int. Ed.* **2005**, *44*, 4899.

[110] S. Hayami, R. Moriyama, A. Shuto, Y. Maeda, K. Ohta, K. Inoue, *Inorg. Chem.* **2007**, *46*, 7692.

[111] J. Oberhaus, *Dissertation*, Johannes Gutenberg-Universität Mainz, Mainz, **2013**.

[112] O. Kahn, *Science* **1998**, *279*, 44.

[113] S. Brooker, J. A. Kitchen, *Dalton Trans.* **2009**, 7331.

[114] O. Kahn, E. Codjovi, Y. Garcia, P. J. van Koningsbruggen, R. Lapouyade, L. Sommier in *ACS Symposium Series* (Eds.: M. M. Turnbull, T. Sugimoto, L. K. Thompson), American Chemical Society, Washington, DC, **1996**, pp. 298–310.

[115] J. A. Real, A. B. Gaspar, M. C. Muñoz, P. Gütlich, V. Ksenofontov, H. Spiering in *Topics in current chemistry* (Eds.: P. Gütlich, H. A. Goodwin), Springer Berlin Heidelberg, Berlin, Heidelberg, **2004**, pp. 167–193.

[116] J. Olguín, S. Brooker in *Spin-Crossover Materials* (Ed.: M. A. Halcrow), John Wiley & Sons Ltd, Oxford, UK, **2013**, pp. 77–120.

[117] K. S. Murray, *Eur. J. Inorg. Chem.* **2008**, *2008*, 3101.

[118] J. A. Real, H. Bolvin, A. Bousseksou, A. Dworkin, O. Kahn, F. Varret, J. Zarembowitch, *J. Am. Chem. Soc.* **1992**, *114*, 4650.

[119] G. Vos, R. A. Le Febre, R. A. G. de Graaff, J. G. Haasnoot, J. Reedijk, *J. Am. Chem. Soc.* **1983**, *105*, 1682.

[120] J. J. A. Kolnaar, G. van Dijk, H. Kooijman, A. L. Spek, V. G. Ksenofontov, P. Gütlich, J. G. Haasnoot, J. Reedijk, *Inorg. Chem.* **1997**, *36*, 2433.

[121] M. Ruben, E. Breuning, J.-M. Lehn, V. Ksenofontov, F. Renz, P. Gütlich, G. B. M. Vaughan, *Chem. Eur. J.* **2003**, *9*, 4422.

References

[122] A. Real, J. Zarembowitch, O. Kahn, X. Solans, *Inorg. Chem.* **1987**, *26*, 2939.

[123] A. B. Gaspar, V. Ksenofontov, S. Reiman, P. Gütlich, A. L. Thompson, A. E. Goeta, M. C. Muñoz, J. A. Real, *Chem. Eur. J.* **2006**, *12*, 9289.

[124] J. A. Real, I. Castro, A. Bousseksou, M. Verdaguer, R. Burriel, M. Castro, J. Linares, F. Varret, *Inorg. Chem.* **1997**, *36*, 455.

[125] I. Nemec, R. Boča, R. Herchel, Z. Trávníček, M. Gembický, W. Linert, *Monatsh Chem* **2009**, *140*, 815.

[126] A. B. Gaspar, V. Ksenofontov, J. A. Real, P. Gütlich, *Chem. Phys. Lett* **2003**, *373*, 385.

[127] R. Boča, *Coord. Chem. Rev.* **2004**, *248*, 757.

[128] D. Bittner, *Dissertation*, Johannes Gutenberg-Universität Mainz, Mainz, **2018**.

[129] S. R. Batten, J. Bjernemose, P. Jensen, B. A. Leita, K. S. Murray, B. Moubaraki, J. P. Smith, H. Toftlund, *Dalton Trans.* **2004**, 3370.

[130] A. A. Yousif, H. Winkler, H. Toftlund, A. X. Trautwein, I. R. Herbert, *J. Phys.: Condens. Matter* **1989**, *1*, 7103.

[131] F. Grandjean, G. J. Long, B. B. Hutchinson, L. Ohlhausen, P. Neill, J. D. Holcomb, *Inorg. Chem.* **1989**, *28*, 4406.

[132] M. A. Halcrow, *Coord. Chem. Rev.* **2005**, *249*, 2880.

[133] E. König, G. Ritter in *Mössbauer Effect Methodology* (Eds.: I. J. Gruverman, C. W. Seidel, D. K. Dieterly), Springer US, Boston, MA, **1974**, pp. 3–21.

[134] B. A. Leita, B. Moubaraki, K. S. Murray, J. P. Smith, J. D. Cashion, *Chem. Commun.* **2004**, 156.

[135] C. J. Schneider, J. D. Cashion, B. Moubaraki, S. M. Neville, S. R. Batten, D. R. Turner, K. S. Murray, *Polyhedron* **2007**, *26*, 1764.

[136] J. Klingele, S. Dechert, F. Meyer, *Coord. Chem. Rev.* **2009**, *253*, 2698.

[137] M. H. Klingele, B. Moubaraki, J. D. Cashion, K. S. Murray, S. Brooker, *Chem. Commun. (Camb.)* **2005**, 987.

[138] C. F. Herold, L. M. Carrella, E. Rentschler, *Eur. J. Inorg. Chem.* **2015**, *2015*, 3632.

[139] N. Suemura, M. Ohama, S. Kaizaki, *Chem. Commun.* **2001**, 1538.

[140] A. Noble, J. Olguín, R. Clérac, S. Brooker, *Inorg. Chem.* **2010**, *49*, 4560.

[141] C. M. Grunert, S. Reiman, H. Spiering, J. A. Kitchen, S. Brooker, P. Gütlich, *Angew. Chem. Int. Ed. Engl.* **2008**, *47*, 2997.

[142] J. A. Kitchen, J. Olguín, R. Kulmaczewski, N. G. White, V. A. Milway, G. N. L. Jameson, J. L. Tallon, S. Brooker, *Inorg. Chem.* **2013**, *52*, 11185.

[143] J. A. Kitchen, N. G. White, G. N. L. Jameson, J. L. Tallon, S. Brooker, *Inorg. Chem.* **2011**, *50*, 4586.

[144] M. H. Klingele, B. Moubaraki, K. S. Murray, S. Brooker, *Chem. Eur. J.* **2005**, *11*, 6962.

[145] R. W. Hogue, H. L. C. Feltham, R. G. Miller, S. Brooker, *Inorg. Chem.* **2016**, *55*, 4152.

[146] C. F. Herold, S. I. Shylin, E. Rentschler, *Inorg. Chem.* **2016**, *55*, 6414.

[147] F. Fürmeyer, L. M. Carrella, V. Ksenofontov, A. Möller, E. Rentschler, *Inorg. Chem.* **2020**, *59*, 2843.

[148] F. Fürmeyer, L. M. Carrella, E. Rentschler, *Crystals* **2020**, *10*, 448.

[149] F. Fürmeyer, *Master Thesis*, Johannes Gutenberg-Universität Mainz, Mainz, **2017**.

[150] J. Eppelsheimer, *Master Thesis*, Johannes Gutenberg-Universität Mainz, Mainz, **2017**.

[151] M. Carmen Muñoz, J. Antonio Real in *Spin-Crossover Materials* (Ed.: M. A. Halcrow), John Wiley & Sons Ltd, Oxford, UK, **2013**, pp. 121–146.

[152] O. Roubeau, *Chemistry (Weinheim an der Bergstrasse, Germany)* **2012**, *18*, 15230.

[153] O. Roubeau, A. Colin, V. Schmitt, R. Clérac, *Angew. Chem.* **2004**, *116*, 3345.

[154] P. Grondin, O. Roubeau, M. Castro, H. Saadaoui, A. Colin, R. Clérac, *Langmuir : the ACS journal of surfaces and colloids* **2010**, *26*, 5184.

[155] O. Roubeau, B. Agricole, R. Clérac, S. Ravaine, *J. Phys. Chem. B* **2004**, *108*, 15110.

[156] O. Roubeau, E. Natividad, B. Agricole, S. Ravaine, *Langmuir : the ACS journal of surfaces and colloids* **2007**, *23*, 3110.

[157] P. Grondin, D. Siretanu, O. Roubeau, M.-F. Achard, R. Clérac, *Inorg. Chem.* **2012**, *51*, 5417.

[158] O. Kahn, J. Kröber, C. Jay, *Adv. Mater.* **1992**, *4*, 718.

[159] Y. Garcia, O. Kahn, L. Rabardel, B. Chansou, L. Salmon, J. P. Tuchagues, *Inorg. Chem.* **1999**, *38*, 4663.

[160] P. J. van Koningsbruggen, Y. Garcia, O. Kahn, L. Fournès, H. Kooijman, A. L. Spek, J. G. Haasnoot, J. Moscovici, K. Provost, A. Michalowicz et al., *Inorg. Chem.* **2000**, *39*, 1891.

[161] P. J. van Koningsbruggen, Y. Garcia, H. Kooijman, A. L. Spek, J. G. Haasnoot, O. Kahn, J. Linares, E. Codjovi, F. Varret, *J. Chem. Soc., Dalton Trans.* **2001**, 466.

[162] J. A. Real, E. Andrés, M. C. Muñoz, M. Julve, T. Granier, A. Bousseksou, F. Varret, *Science* **1995**, *268*, 265.

[163] W. Vreugdenhil, J. H. van Diemen, R. A.G. de Graaff, J. G. Haasnoot, J. Reedijk, A. M. van der Kraan, O. Kahn, J. Zarembowitch, *Polyhedron* **1990**, *9*, 2971.

[164] N. Moliner, C. Muñoz, S. Létard, X. Solans, N. Menéndez, A. Goujon, F. Varret, J. A. Real, *Inorg. Chem.* **2000**, *39*, 5390.

[165] T. Kitazawa, Y. Gomi, M. Takahashi, M. Takeda, M. Enomoto, A. Miyazaki, T. Enoki, *J. Mater. Chem.* **1996**, *6*, 119.

[166] V. Niel, J. M. Martinez-Agudo, M. C. Muñoz, A. B. Gaspar, J. A. Real, *Inorg. Chem.* **2001**, *40*, 3838.

References

[167] S. Mossin, B. L. Tran, D. Adhikari, M. Pink, F. W. Heinemann, J. Sutter, R. K. Szilagyi, K. Meyer, D. J. Mindiola, *J. Am. Chem. Soc.* **2012**, *134*, 13651.

[168] X. Feng, C. Mathonière, I.-R. Jeon, M. Rouzières, A. Ozarowski, M. L. Aubrey, M. I. Gonzalez, R. Clérac, J. R. Long, *J. Am. Chem. Soc.* **2013**, *135*, 15880.

[169] A. Urtizberea, O. Roubeau, *Chem. Sci.* **2017**, *8*, 2290.

[170] C. Mathonière, H.-J. Lin, D. Siretanu, R. Clérac, J. M. Smith, *J. Am. Chem. Soc.* **2013**, *135*, 19083.

[171] L. Chen, J. Song, W. Zhao, G. Yi, Z. Zhou, A. Yuan, Y. Song, Z. Wang, Z.-W. Ouyang, *Dalton Trans.* **2018**, *47*, 16596.

[172] R. Ababei, C. Pichon, O. Roubeau, Y.-G. Li, N. Bréfuel, L. Buisson, P. Guionneau, C. Mathonière, R. Clérac, *J. Am. Chem. Soc.* **2013**, *135*, 14840.

[173] V. García-López, F. J. Orts-Mula, M. Palacios-Corella, J. M. Clemente-Juan, M. Clemente-León, E. Coronado, *Polyhedron* **2018**, *150*, 54.

[174] B. Drahoš, I. Šalitroš, R. Herchel, *Inorg. Chim. Acta* **2019**, *495*, 118921.

[175] H. L.C. Feltham, S. Brooker, *Coord. Chem. Rev.* **2014**, *276*, 1.

[176] M. Hołyńska (Ed.) *Single-molecule magnets*. *Molecular architectures and building blocks for spintronics*, Wiley-VCH, Weinheim, Germany, **2019**.

[177] R. Sessoli, D. Gatteschi, A. Caneschi, M. A. Novak, *Nature* **1993**, *365*, 141.

[178] G. Christou, D. Gatteschi, D. N. Hendrickson, R. Sessoli, *MRS Bull.* **2000**, *25*, 66.

[179] D. Gatteschi, L. Sorace, *J. Solid State Chem.* **2001**, *159*, 253.

[180] M. Murrie, *Chem. Soc. Rev.* **2010**, *39*, 1986.

[181] R. L. Carlin in *Magnetochemistry* (Ed.: R. L. Carlin), Springer Berlin Heidelberg, Berlin, Heidelberg, **1986**, pp. 19–35.

[182] F. Neese, D. A. Pantazis, *Faraday discussions* **2011**, *148*, 229-38; discussion 299-314.

[183] D. Gatteschi, R. Sessoli, J. Villain, *Molecular Nanomagnets*, Oxford University Press, **2006**.

[184] S. Gómez-Coca, A. Urtizberea, E. Cremades, P. J. Alonso, A. Camón, E. Ruiz, F. Luis, *Nat. Commun.* **2014**, *5*, 4300.

[185] J. Tang, P. Zhang, *Lanthanide Single Molecule Magnets*, Springer Berlin Heidelberg, Berlin, Heidelberg, **2015**.

[186] K. N. Shrivastava, *phys. stat. sol. (b)* **1983**, *117*, 437.

[187] J. M. Zadrozny, M. Atanasov, A. M. Bryan, C.-Y. Lin, B. D. Rekken, P. P. Power, F. Neese, J. R. Long, *Chem. Sci.* **2013**, *4*, 125.

[188] C. Romeike, M. R. Wegewijs, H. Schoeller, *Phys. Rev. Lett.* **2006**, *96*, 196805.

[189] Y.-N. Guo, G.-F. Xu, Y. Guo, J. Tang, *Dalton Trans.* **2011**, *40*, 9953.

[190] M. J. Giansiracusa, A. K. Kostopoulos, D. Collison, R. E. P. Winpenny, N. F. Chilton, *Chem. Commun.* **2019**, *55*, 7025.

[191] J.-L. Liu, Y.-C. Chen, M.-L. Tong, *Chem. Soc. Rev.* **2018**, *47*, 2431.

[192] O. Waldmann, *Inorg. Chem.* **2007**, *46*, 10035.

[193] M. Atanasov, D. Aravena, E. Suturina, E. Bill, D. Maganas, F. Neese, *Coord. Chem. Rev.* **2015**, *289-290*, 177.

[194] N. Ishikawa, *Polyhedron* **2007**, *26*, 2147.

[195] T. Glaser, *Chem. Commun. (Camb.)* **2011**, *47*, 116.

[196] G. Aromí, E. K. Brechin in *Structure and bonding* (Ed.: R. Winpenny), Springer-Verlag, Berlin/Heidelberg, **2006**, pp. 1–67.

[197] S. L. Castro, Z. Sun, C. M. Grant, J. C. Bollinger, D. N. Hendrickson, G. Christou, *J. Am. Chem. Soc.* **1998**, *120*, 2365.

[198] C. Sangregorio, T. Ohm, C. Paulsen, R. Sessoli, D. Gatteschi, *Phys. Rev. Lett.* **1997**, *78*, 4645.

[199] C. J. Milios, A. Vinslava, W. Wernsdorfer, A. Prescimone, P. A. Wood, S. Parsons, S. P. Perlepes, G. Christou, E. K. Brechin, *J. Am. Chem. Soc.* **2007**, *129*, 6547.

[200] M. Murugesu, M. Habrych, W. Wernsdorfer, K. A. Abboud, G. Christou, *J. Am. Chem. Soc.* **2004**, *126*, 4766.

[201] A. M. Ako, I. J. Hewitt, V. Mereacre, R. Clérac, W. Wernsdorfer, C. E. Anson, A. K. Powell, *Angew. Chem. Int. Ed.* **2006**, *45*, 4926.

[202] P. Parois, S. A. Moggach, J. Sanchez-Benitez, K. V. Kamenev, A. R. Lennie, J. E. Warren, E. K. Brechin, S. Parsons, M. Murrie, *Chem. Commun. (Camb.)* **2010**, *46*, 1881.

[203] J. D. Rinehart, J. R. Long, *Chem. Sci.* **2011**, *2*, 2078.

[204] P. Zhang, Y.-N. Guo, J. Tang, *Coord. Chem. Rev.* **2013**, *257*, 1728.

[205] S. N. König, N. F. Chilton, C. Maichle-Mössmer, E. M. Pineda, T. Pugh, R. Anwander, R. A. Layfield, *Dalton Trans.* **2014**, *43*, 3035.

[206] C. R. Ganivet, B. Ballesteros, G. de La Torre, J. M. Clemente-Juan, E. Coronado, T. Torres, *Chem. Eur. J.* **2013**, *19*, 1457.

[207] M.-E. Boulon, G. Cucinotta, J. Luzon, C. Degl'Innocenti, M. Perfetti, K. Bernot, G. Calvez, A. Caneschi, R. Sessoli, *Angew. Chem. Int. Ed. Engl.* **2013**, *52*, 350.

[208] G. Cucinotta, M. Perfetti, J. Luzon, M. Etienne, P.-E. Car, A. Caneschi, G. Calvez, K. Bernot, R. Sessoli, *Angew. Chem. Int. Ed. Engl.* **2012**, *51*, 1606.

[209] Y.-S. Ding, K.-X. Yu, D. Reta, F. Ortu, R. E. P. Winpenny, Y.-Z. Zheng, N. F. Chilton, *Nat. Commun.* **2018**, *9*, 3134.

[210] F.-S. Guo, B. M. Day, Y.-C. Chen, M.-L. Tong, A. Mansikkamäki, R. A. Layfield, *Angew. Chem.* **2017**, *129*, 11603.

References

[211] F.-S. Guo, B. M. Day, Y.-C. Chen, M.-L. Tong, A. Mansikkamäki, R. A. Layfield, *Science* **2018**, *362*, 1400.

[212] K. Randall McClain, C. A. Gould, K. Chakarawet, S. J. Teat, T. J. Groshens, J. R. Long, B. G. Harvey, *Chem. Sci.* **2018**, *9*, 8492.

[213] J. M. Zadrozny, J. Liu, N. A. Piro, C. J. Chang, S. Hill, J. R. Long, *Chem. Commun. (Camb.)* **2012**, *48*, 3927.

[214] R. A. Layfield, *Organometallics* **2014**, *33*, 1084.

[215] D. E. Freedman, W. H. Harman, T. D. Harris, G. J. Long, C. J. Chang, J. R. Long, *J. Am. Chem. Soc.* **2010**, *132*, 1224.

[216] J. M. Zadrozny, D. J. Xiao, M. Atanasov, G. J. Long, F. Grandjean, F. Neese, J. R. Long, *Nat. Chem.* **2013**, *5*, 577.

[217] J. Vallejo, A. Pascual-Álvarez, J. Cano, I. Castro, M. Julve, F. Lloret, J. Krzystek, G. de Munno, D. Armentano, W. Wernsdorfer et al., *Angew. Chem. Int. Ed. Engl.* **2013**, *52*, 14075.

[218] R. Ishikawa, R. Miyamoto, H. Nojiri, B. K. Breedlove, M. Yamashita, *Inorg. Chem.* **2013**, *52*, 8300.

[219] A. Grigoropoulos, M. Pissas, P. Papatolis, V. Psycharis, P. Kyritsis, Y. Sanakis, *Inorg. Chem.* **2013**, *52*, 12869.

[220] R. Ruamps, R. Maurice, L. Batchelor, M. Boggio-Pasqua, R. Guillot, A. L. Barra, J. Liu, E.-E. Bendeif, S. Pillet, S. Hill et al., *J. Am. Chem. Soc.* **2013**, *135*, 3017.

[221] G. A. Craig, M. Murrie, *Chem. Soc. Rev.* **2015**, *44*, 2135.

[222] J. M. Zadrozny, J. R. Long, *Journal of the American Chemical Society* **2011**, *133*, 20732.

[223] T. Jurca, A. Farghal, P.-H. Lin, I. Korobkov, M. Murugesu, D. S. Richeson, *J. Am. Chem. Soc.* **2011**, *133*, 15814.

[224] J. Vallejo, I. Castro, R. Ruiz-García, J. Cano, M. Julve, F. Lloret, G. de Munno, W. Wernsdorfer, E. Pardo, *J. Am. Chem. Soc.* **2012**, *134*, 15704.

[225] D. H. Moseley, S. E. Stavretis, K. Thirunavukkuarasu, M. Ozerov, Y. Cheng, L. L. Daemen, J. Ludwig, Z. Lu, D. Smirnov, C. M. Brown et al., *Nat. Commun.* **2018**, *9*, 2572.

[226] F. Lloret, M. Julve, J. Cano, R. Ruiz-García, E. Pardo, *Inorg. Chim. Acta* **2008**, *361*, 3432.

[227] R. Herchel, L. Váhovská, I. Potočňák, Z. Trávníček, *Inorg. Chem.* **2014**, *53*, 5896.

[228] C. Plenk, J. Krause, E. Rentschler, *Eur. J. Inorg. Chem.* **2015**, *2015*, 370.

[229] J. Krause, *Dissertation*, Johannes Gutenberg-Universität Mainz, Mainz, **2018**.

[230] H. C. Kolb, M. G. Finn, K. B. Sharpless, *Angew. Chem. Int. Ed.* **2001**, *40*, 2004.

[231] L. Liang, D. Astruc, *Coord. Chem. Rev.* **2011**, *255*, 2933.

[232] J. E. Moses, A. D. Moorhouse, *Chem. Soc. Rev.* **2007**, *36*, 1249.

[233] Z.-Q. Liang, C.-X. Wang, J.-X. Yang, H.-W. Gao, Y.-P. Tian, X.-T. Tao, M.-H. Jiang, *New J. Chem.* **2007**, *31*, 906.

[234] C. E. Hoyle, C. N. Bowman, *Angew. Chem. Int. Ed. Engl.* **2010**, *49*, 1540.

[235] D. P. Nair, M. Podgórski, S. Chatani, T. Gong, W. Xi, C. R. Fenoli, C. N. Bowman, *Chem. Mater.* **2013**, *26*, 724.

[236] A. B. Lowe, C. E. Hoyle, C. N. Bowman, *J. Mater. Chem.* **2010**, *20*, 4745.

[237] T. Matsumura, F. Ishiwari, Y. Koyama, T. Takata, *Organic letters* **2010**, *12*, 3828.

[238] R. Huisgen, *Angew. Chem. Int. Ed. Engl.* **1963**, *2*, 565.

[239] R. Huisgen, *Angew. Chem. Int. Ed. Engl.* **1963**, *2*, 633.

[240] A. Michael, *J. Prakt. Chem.* **1893**, *48*, 94.

[241] J. E. Hein, V. V. Fokin, *Chem. Soc. Rev.* **2010**, *39*, 1302.

[242] V. V. Rostovtsev, L. G. Green, V. V. Fokin, K. B. Sharpless, *Angew. Chem. Int. Ed.* **2002**, *41*, 2596.

[243] C. W. Tornøe, C. Christensen, M. Meldal, *J. Org. Chem.* **2002**, *67*, 3057.

[244] M. Meldal, C. W. Tornøe, *Chem. Rev.* **2008**, *108*, 2952.

[245] V. O. Rodionov, V. V. Fokin, M. G. Finn, *Angew. Chem. Int. Ed. Engl.* **2005**, *44*, 2210.

[246] E. C. Constable, C. E. Housecroft, J. R. Price, L. Schweighauser, J. A. Zampese, *Inorg. Chem. Comm.* **2010**, *13*, 495.

[247] C. Plenk, J. Krause, M. Beck, E. Rentschler, *Chem. Commun. (Camb.)* **2015**, *51*, 6524.

[248] C. Schlegel, J. van Slageren, M. Manoli, E. K. Brechin, M. Dressel, *Phys. Rev. Lett.* **2008**, *101*, 147203.

[249] D. Shao, S.-L. Zhang, Le Shi, Y.-Q. Zhang, X.-Y. Wang, *Inorg. Chem.* **2016**, *55*, 10859.

[250] E. L. Gavey, M. Al Hareri, J. Regier, L. D. Carlos, R. A. S. Ferreira, F. S. Razavi, J. M. Rawson, M. Pilkington, *J. Mater. Chem. C* **2015**, *3*, 7738.

[251] E. Bergen, *Click-Reaktionen zum Aufbau neuer Oxadiazol-Liganden für Eisen(II)-SCO-Verbindungen*. *Unpublished Results*. Master Thesis, **2017**.

[252] N. G. Yazdandoost Khosravi, *Oxadiazol-basierte Liganden für Spin-Crossover Verbindungen*. Bachelor Thesis, **2018**.

[253] R. Zhang, R. Jordan, O. Nuyken, *Macromol. Rapid Commun.* **2003**, *24*, 246.

[254] S. Kun, G. Z. Nagy, M. Tóth, L. Czecze, A. N. van Nhien, T. Docsa, P. Gergely, M.-D. Charavgi, P. V. Skourti, E. D. Chrysina et al., *Carbohydr. Res* **2011**, *346*, 1427.

[255] E. Bill, *julX*. *Simulation of Molecular Magnetic data*, **2008**.

[256] S. K. Hoffmann, J. Goslar, S. Lijewski, A. Zalewska, *J. Magn. Reson* **2013**, *236*, 7.

[257] E. Riedel, H.-J. Meyer, C. Janiak, R. Alsfasser (Eds.) *De-Gruyter-Studium*, de Gruyter, Berlin, **2012**.

References

[258] A. Hetzheim, K. Möckel in *Advances in Heterocyclic Chemistry*, Elsevier, **1967**, pp. 183–224.

[259] S. W. Benson, *J. Chem. Educ.* **1965**, *42*, 502.

[260] E. Lippert, *Angew. Chem.* **1960**, *72*, 602.

[261] E. Garribba, G. Micera, *J. Chem. Educ.* **2006**, *83*, 1229.

[262] N. F. Chilton, R. P. Anderson, L. D. Turner, A. Soncini, K. S. Murray, *J. Comput. Chem.* **2013**, *34*, 1164.

[263] A. Palii, B. Tsukerblat, S. Klokishner, K. R. Dunbar, J. M. Clemente-Juan, E. Coronado, *Chem. Soc. Rev.* **2011**, *40*, 3130.

[264] A. Bencini, D. Gatteschi (Eds.) *Electron paramagnetic resonance of exchange coupled systems. With 38 tab*, Springer, Berlin, Heidelberg [u.a.], **2011**.

[265] R. Ishikawa, S. Ueno, Y. Hamatake, Y. Horii, Y. Miyazaki, M. Nakano, T. Noda, M. Uematsu, S. Kawata, *CrystEngComm* **2019**, *21*, 1886.

[266] L. K. Thompson, Z. Xu, A. E. Goeta, J. A. K. Howard, H. J. Clase, D. O. Miller, *Inorg. Chem.* **1998**, *37*, 3217.

[267] Z. Xu, L. K. Thompson, C. J. Matthews, D. O. Miller, A. E. Goeta, C. Wilson, J. A. K. Howard, M. Ohba, H. Ōkawa, *J. Chem. Soc., Dalton Trans.* **2000**, 69.

[268] D. Ajo, A. Bencini, F. Mani, *Inorg. Chem.* **1988**, *27*, 2437.

[269] Z. Xu, L. K. Thompson, D. O. Miller, *Inorg. Chem.* **1997**, *36*, 3985.

[270] P. M. Slangen, P. J. van Koningsbruggen, K. Goubitz, J. G. Haasnoot, J. Reedijk, *Inorg. Chem.* **1994**, *33*, 1121.

[271] R. Arunachalam, C. S. Aswathi, A. Das, R. I. Kureshy, P. S. Subramanian, *ChemPlusChem* **2015**, *80*, 209.

[272] M. Al-Talib, H. Tashtoush, N. Odeh, *Magn. Reson. Chem.* **1990**, *28*, 1072.

[273] Stolle, Kind, *J. prakt. Chem.* **1904**, 428.

[274] K. Dimitrowa, J. Hauschild, H. Zaschke, H. Schubert, *J. Prakt. Chem.* **1980**, *322*, 933.

[275] M. Julve, M. Verdaguer, J. Faus, F. Tinti, J. Moratal, A. Monge, E. Gutierrez-Puebla, *Inorg. Chem.* **1987**, *26*, 3520.

[276] S. ALVAREZ, P. ALEMANY, D. CASANOVA, J. CIRERA, M. LLUNELL, D. AVNIR, *Coord. Chem. Rev.* **2005**, *249*, 1693.

[277] K. Abu-Shandi, H. Winkler, H. Paulsen, R. Glaum, B. Wu, C. Janiak, *Z. anorg. allg. Chem.* **2005**, *631*, 2705.

[278] A. D. Naik, K. Robeyns, C. F. Meunier, A. F. Léonard, A. Rotaru, B. Tinant, Y. Filinchuk, B. L. Su, Y. Garcia, *Inorg. Chem.* **2014**, *53*, 1263.

[279] И. В. Тайдаков, А. Н. Лобанов, А. Г. Витухновский, З. А. Старикова, *Координац. химия* **2013**, *39*, 334.

[280] H. Chicha, A. Kouakou, E. M. Rakib, M. Saadi, L. El Ammari, *Acta Crystallogr. Sect. E Struct. Rep. Online* **2013**, *69*, o1353.

[281] W. Liu, X. Li, H. H. Chen, B. L. Wu, H. Y. Zhang, *Russ J Coord Chem* **2018**, *44*, 72.

[282] E.-C. Yang, Z.-Y. Liu, X.-G. Wang, S. R. Batten, X.-J. Zhao, *CrystEngComm* **2008**, *10*, 1140.

[283] U. Okeke, Y. Gultneh, R. J. Butcher, *Acta Crystallogr. E Crystallogr. Commun.* **2017**, *73*, 1568.

[284] S. Muthu, J. H. K. Yip, J. J. Vittal, *J. Chem. Soc., Dalton Trans.* **2001**, 3577.

[285] B. Weber, *Coord. Chem. Rev.* **2009**, *253*, 2432.

[286] A. E. Thorarinsdottir, A. I. Gaudette, T. D. Harris, *Chem. Sci.* **2017**, *8*, 2448.

[287] N. Moliner, M. C. Muñoz, S. Létard, L. Salmon, J.-P. Tuchagues, A. Bousseksou, J. A. Real, *Inorg. Chem.* **2002**, *41*, 6997.

[288] C. S. Yi, D. W. Lee, Z. He, A. L. Rheingold, K.-C. Lam, T. E. Concolino, *Organometallics* **2000**, *19*, 2909.

[289] P. E. Sues, A. J. Lough, R. H. Morris, *Organometallics* **2011**, *30*, 4418.

[290] B. K. Liebov, C. E. Weigle, K. V. Keinath, J. E. Leap, R. D. Pike, J. M. Keane, *Inorg. Chem.* **2011**, *50*, 4677.

[291] M. Iglesias, D. J. Beetstra, K. J. Cavell, A. Dervisi, I. A. Fallis, B. Kariuki, R. W. Harrington, W. Clegg, P. N. Horton, S. J. Coles et al., *Eur. J. Inorg. Chem.* **2010**, *2010*, 1604.

[292] A. Homs, I. Escofet, A. M. Echavarren, *Org. Lett.* **2013**, *15*, 5782.

[293] A. C. Y. Tay, B. J. Frogley, D. C. Ware, P. J. Brothers, *Dalton Trans.* **2018**, *47*, 3388.

[294] K. S. Low, J. M. Cole, X. Zhou, N. Yufa, *Acta Crystallogr. B* **2012**, *68*, 137.

[295] J. Heilmann, H.-W. Lerner, M. Bolte, *Acta Crystallogr E Struct Rep Online* **2006**, *62*, m1477-m1478.

[296] J. E. Chàvez, C. Crotti, E. Zangrando, E. Farnetti, *Journal of Molecular Catalysis A: Chemical* **2016**, *421*, 189.

[297] S. R. Batten, K. S. Murray, N. J. Sinclair, *Acta Crystallogr C Cryst Struct Commun* **2000**, *56*, e320-e320.

[298] L. M.T. Frija, A. J.L. Pombeiro, M. N. Kopylovich, *Coord. Chem. Rev.* **2016**, *308*, 32.

[299] Y. Rechkemmer, F. D. Breitgoff, M. van der Meer, M. Atanasov, M. Hakl, M. Orlita, P. Neugebauer, F. Neese, B. Sarkar, J. van Slageren, *Nat. Commun.* **2016**, *7*, 10467.

[300] in *Introduction to Molecular Magnetism* (Eds.: C. Benelli, D. Gatteschi), Wiley-VCH Verlag GmbH & Co. KGaA, Weinheim, Germany, **2015**, pp. 25–32.

[301] E. A. Suturina, J. Nehrkorn, J. M. Zadrozny, J. Liu, M. Atanasov, T. Weyhermüller, D. Maganas, S. Hill, A. Schnegg, E. Bill et al., *Inorg. Chem.* **2017**, *56*, 3102.

[302] D. Reta, N. F. Chilton, *Phys. Chem. Chem. Phys.* **2019**, *21*, 23567.

[303] N. V. Prokof'ev, P. C. E. Stamp, *Phys. Rev. Lett.* **1998**, *80*, 5794.

References

[304] S. Vaidya, S. Tewary, S. K. Singh, S. K. Langley, K. S. Murray, Y. Lan, W. Wernsdorfer, G. Rajaraman, M. Shanmugam, *Inorg. Chem.* **2016**, *55*, 9564.

[305] J. Zhou, J. Song, A. Yuan, Z. Wang, L. Chen, Z.-W. Ouyang, *Inorg. Chim. Acta* **2018**, *479*, 113.

[306] E. C. Constable, M. D. Ward, *J. Chem. Soc., Dalton Trans.* **1990**, *12*, 1405.

[307] G. Lowe, A.-S. Droz, J. J. Park, G. W. Weaver, *Bioorg. Chem.* **1999**, *27*, 477.

[308] C.-P. Lin, P. Florio, E. M. Campi, C. Zhang, D. P. Fredericks, K. Saito, W. R. Jackson, M. T.W. Hearn, *Tetrahedron* **2014**, *70*, 8520.

[309] V. Grosshenny, F. M. Romero, R. Ziessel, *J. Org. Chem.* **1997**, *62*, 1491.

[310] A. Baron, C. Herrero, A. Quaranta, M.-F. Charlot, W. Leibl, B. Vauzeilles, A. Aukauloo, *Inorg. Chem.* **2012**, *51*, 5985.

[311] A. Streitwieser, S. Pulver, *J. Am. Chem. Soc.* **1964**, *86*, 1587.

[312] C. Bazzicalupi, A. Bencini, A. Bianchi, A. Danesi, E. Faggi, C. Giorgi, S. Santarelli, B. Valtancoli, *Coord. Chem. Rev.* **2008**, *252*, 1052.

[313] L.-B. Gao, S.-H. Liu, L.-Y. Zhang, L.-X. Shi, Z.-N. Chen, *Organometallics* **2006**, *25*, 506.

[314] C. Enachescu, I. Krivokapic, M. Zerara, J. A. Real, N. Amstutz, A. Hauser, *Inorg. Chim. Acta* **2007**, *360*, 3945.

[315] F. Kobayashi, Y. Komatsumaru, R. Akiyoshi, M. Nakamura, Y. Zhang, L. F. Lindoy, S. Hayami, *Inorg. Chem.* **2020**.

[316] A. Rodriguez, H. Sakiyama, N. Masciocchi, S. Galli, N. Gálvez, F. Lloret, E. Colacio, *Inorg. Chem.* **2005**, *44*, 8399.

[317] C. V. Topping, S. J. Blundell, *J. Condens. Matter Phys.* **2019**, *31*, 13001.

[318] T. T. da Cunha, V. M. M. Barbosa, W. X. C. Oliveira, E. F. Pedroso, D. M. A. García, W. C. Nunes, C. L. M. Pereira, *Inorg. Chem.* **2020**, *59*, 12983.

[319] J. Hudák, R. Boča, Ľ. Dlháň, J. Kožíšek, J. Moncoľ, *Polyhedron* **2011**, *30*, 1367.

[320] L. Zhang, W. Li, J. Zhang, Z.-J. Li, Y.-Y. Qin, J.-K. Cheng, Y.-G. Yao, *Inorg. Chem. Comm.* **2008**, *11*, 279.

[321] A. Majumder, V. Gramlich, G. M. Rosair, S. R. Batten, J. D. Masuda, M. S. El Fallah, J. Ribas, J.-P. Sutter, C. Desplanches, S. Mitra, *Cryst. Growth Des.* **2006**, *6*, 2355.

[322] O. P. Kryatova, A. G. Kolchinski, E. V. Rybak-Akimova, *Tetrahedron* **2003**, *59*, 231.

[323] N. M. Logacheva, V. E. Baulin, A. Y. Tsivadze, E. N. Pyatova, I. S. Ivanova, Y. A. Velikodny, V. V. Chernyshev, *Dalton Trans.* **2009**, 2482.

[324] S. A. Cotton in *Encyclopedia of Inorganic and Bioinorganic Chemistry* (Ed.: R. A. Scott), John Wiley & Sons, Ltd, Chichester, UK, **2011**.

[325] Z. Yu, A. Nabei, T. Izumi, T. Okubo, T. Kuroda-Sowa, *Acta Crystallogr. C* **2008**, *64*, m209-12.

[326] in *Introduction to Molecular Magnetism* (Eds.: C. Benelli, D. Gatteschi), Wiley-VCH Verlag GmbH & Co. KGaA, Weinheim, Germany, **2015**, pp. 69–82.

[327] B. N. Figgis, R. S. Nyholm, *J. Chem. Soc. (resumed)* **1959**, 338.

[328] J. Palion-Gazda, B. Machura, R. Kruszynski, T. Grancha, N. Moliner, F. Lloret, M. Julve, *Inorg. Chem.* **2017**, *56*, 6281.

[329] B. Hussain, D. Savard, T. J. Burchell, W. Wernsdorfer, M. Murugesu, *Chem. Commun. (Camb.)* **2009**, 1100.

[330] S.-D. Jiang, B.-W. Wang, G. Su, Z.-M. Wang, S. Gao, *Angew. Chem.* **2010**, *122*, 7610.

[331] G. Schwarzenbach, G. Anderegg, *Z. anorg. allg. Chem.* **1955**, *282*, 286.

[332] R. D. Hancock, *J. Chem. Educ.* **1992**, *69*, 615.

[333] E. M. Holt, N. W. Alcock, R. R. Hendrixson, G. D. Malpass, R. G. Ghirardelli, R. A. Palmer, *Acta Crystallogr B Struct Sci* **1981**, *37*, 1080.

[334] C. Fiolka, I. Pantenburg, G. Meyer, *Cryst. Growth Des.* **2011**, *11*, 5159.

[335] R. D. Rogers, A. N. Rollins, M. M. Benning, *Inorg. Chem.* **1988**, *27*, 3826.

[336] L. Maxwell, M. Amoza, E. Ruiz, *Inorg. Chem.* **2018**, *57*, 13225.

[337] Y.-S. Ding, T. Han, Y.-Q. Hu, M. Xu, S. Yang, Y.-Z. Zheng, *Inorg. Chem. Front.* **2016**, *3*, 798.

[338] C.-F. Wang, Z.-S. Yao, G.-Y. Yang, J. Tao, *Inorg. Chem.* **2019**, *58*, 1309.

[339] J. M. Holland, C. A. Kilner, M. Thornton-Pett, M. A. Halcrow, J. A. McAllister, Z. Lu, *Chem. Commun.* **2001**, 577.

[340] J. Elhaïk, C. M. Pask, C. A. Kilner, M. A. Halcrow, *Tetrahedron* **2007**, *63*, 291.

[341] M. Nihei, T. Maeshima, Y. Kose, H. Oshio, *Polyhedron* **2007**, *26*, 1993.

[342] M. Haryono, F. W. Heinemann, K. Petukhov, K. Gieb, P. Müller, A. Grohmann, *Eur. J. Inorg. Chem.* **2009**, *2009*, 2136.

[343] C. Rajadurai, F. Schramm, S. Brink, O. Fuhr, M. Ghafari, R. Kruk, M. Ruben, *Inorg. Chem.* **2006**, *45*, 10019.

[344] R. Chandrasekar, F. Schramm, O. Fuhr, M. Ruben, *Eur. J. Inorg. Chem.* **2008**, *2008*, 2649.

[345] G. Chastanet, C. A. Tovee, G. Hyett, M. A. Halcrow, J.-F. Létard, *Dalton Trans.* **2012**, *41*, 4896.

[346] S. Hünig, P. Kreitmeier, G. Märkl, J. Sauer, *Einführung in die apparativen Methoden in der Organischen Chemie*, Inst. für Organische Chemie der Univ. Regensburg, **1994**.

[347] G. A. Bain, J. F. Berry, *J. Chem. Educ.* **2008**, *85*, 532.

[348] G. M. Sheldrick, *Acta Crystallogr. A Found Adv.* **2015**, *71*, 3.

[349] G. M. Sheldrick, *Acta Crystallogr. C Struct. Chem.* **2015**, *71*, 3.

[350] O. V. Dolomanov, L. J. Bourhis, R. J. Gildea, J. A. K. Howard, H. Puschmann, *J Appl Crystallogr* **2009**, *42*, 339.

[351] H. E. Gottlieb, V. Kotlyar, A. Nudelman, *J. Org. Chem.* **1997**, *62*, 7512.

[352] G. Barone, G. Gennaro, A. M. Giuliani, M. Giustini, *RSC Adv.* **2016**, *6*, 4936.

Appendix

A. IR Spectra
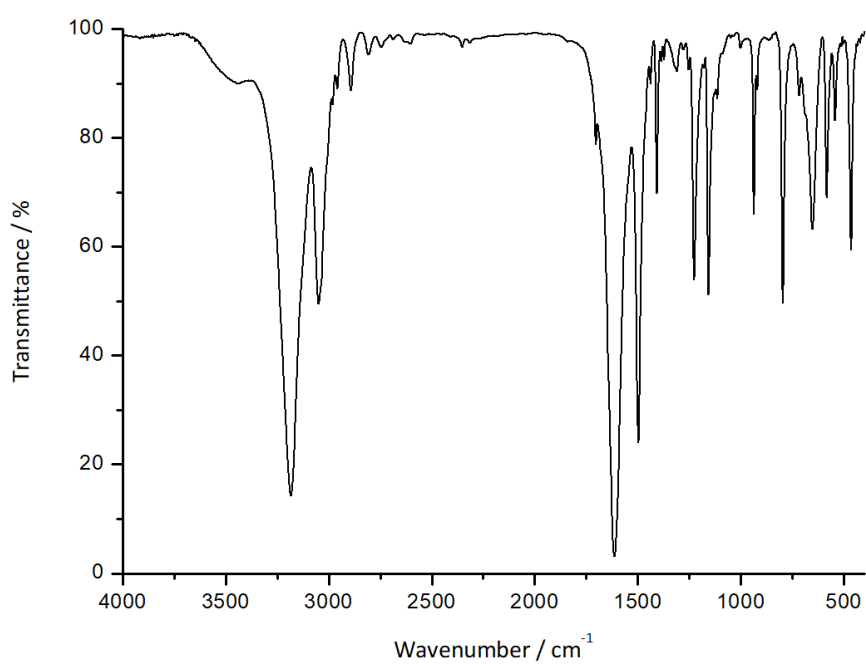
Figure 109 IR spectrum of 1,2-dichloroacetyl hydrazine in KBr (REN-EB-106).
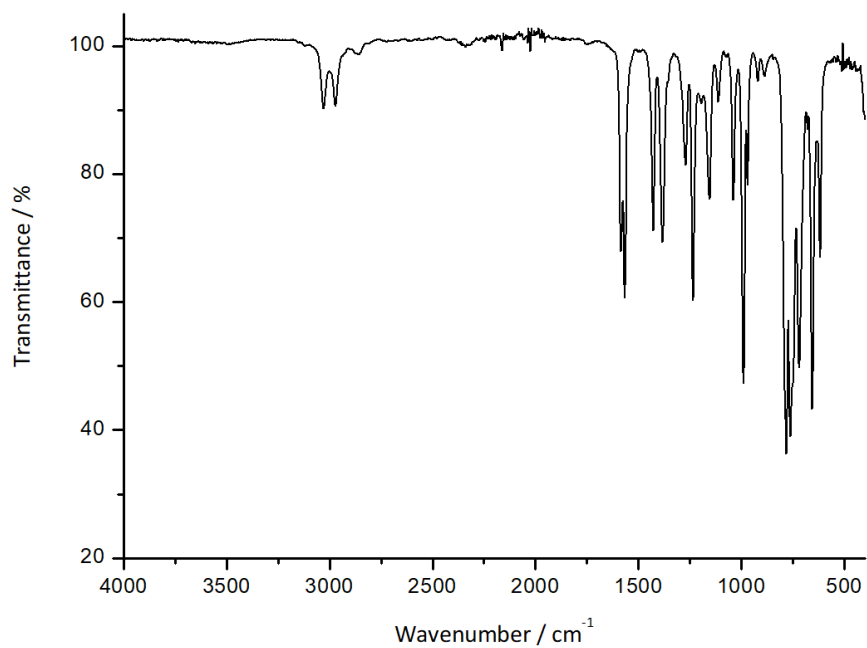
Figure 110 IR spectrum of 2,5-bis(chloromethyl)-1,3,4-oxadiazole in KBr (REN-EB-107).
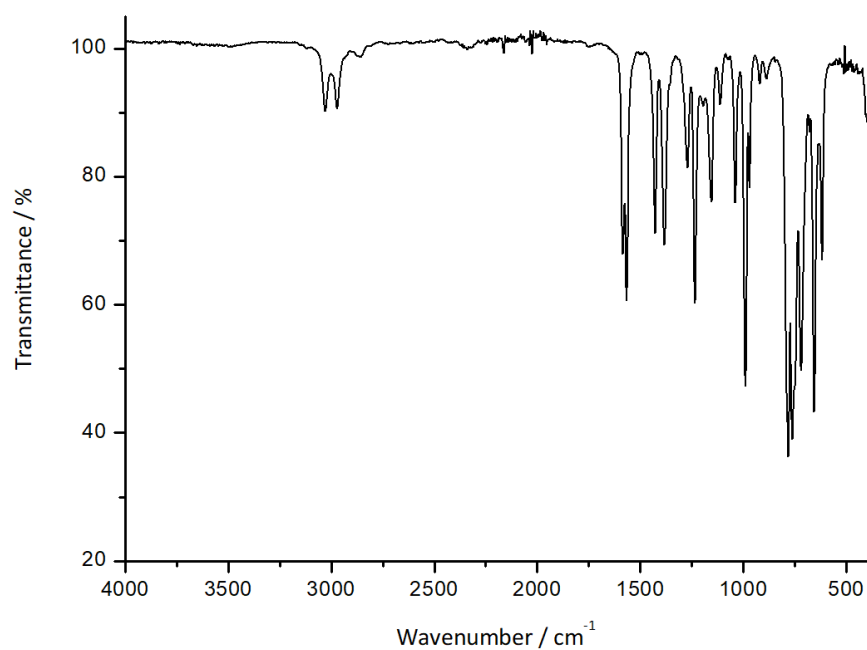
Figure 111 IR spectrum of 2,5-bis(azidomethyl)-1,3,4-oxadiazole in KBr (REN-EB-030).
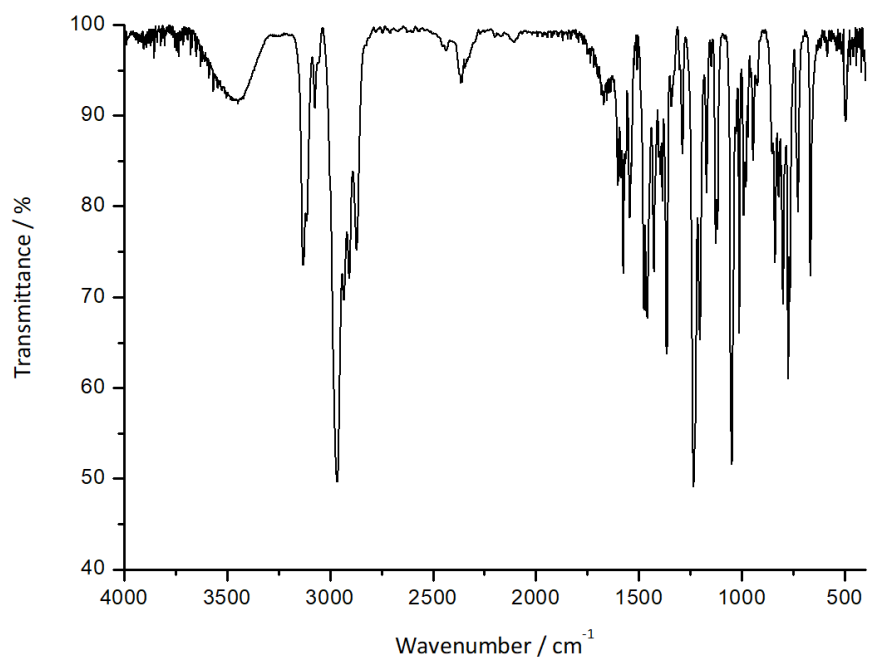
*Figure 112 IR spectrum of **L1** in KBr (REN-NY-014).*
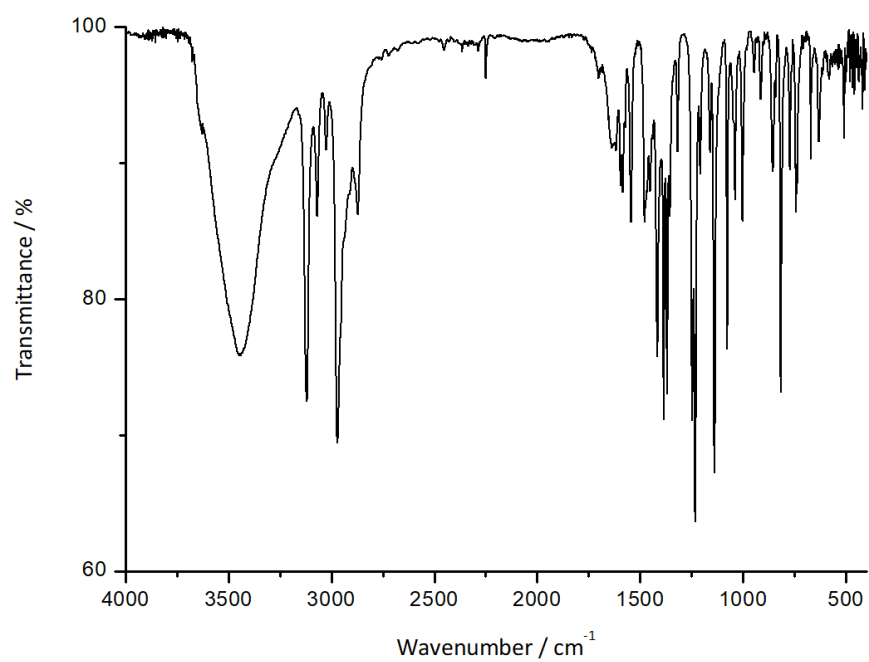
*Figure 113 IR spectrum of **C1** in KBr (REN-EB-219).*
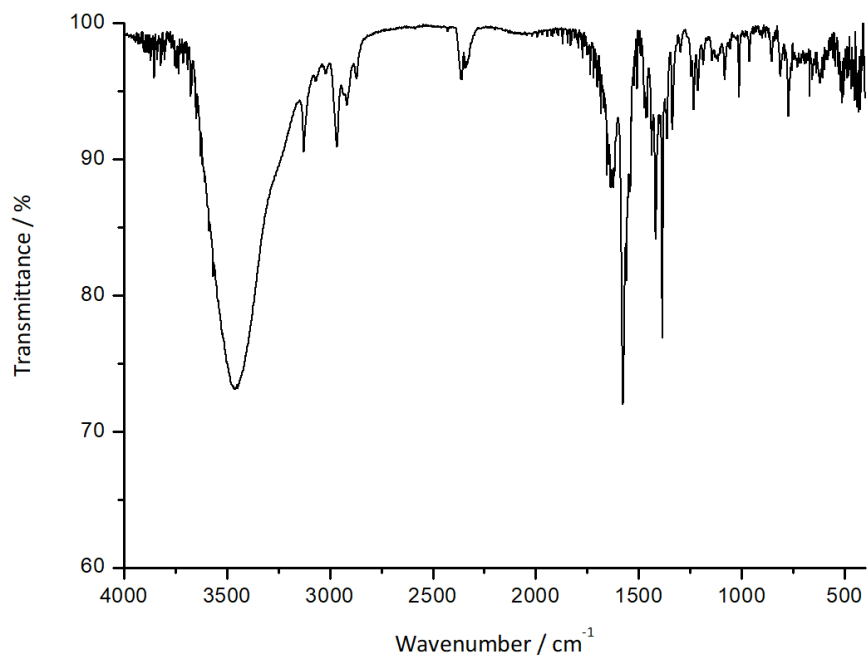
*Figure 114 IR spectrum of **C1'** in KBr (REN-EB-214-2).*
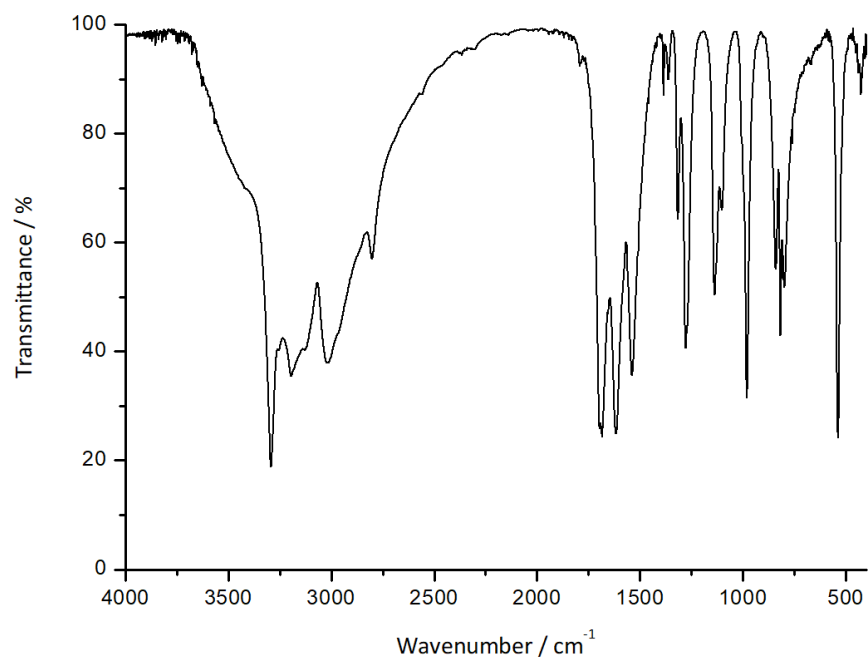
Figure 115 IR spectrum of oxalyldihydrazide in KBr (REN-EB-221)
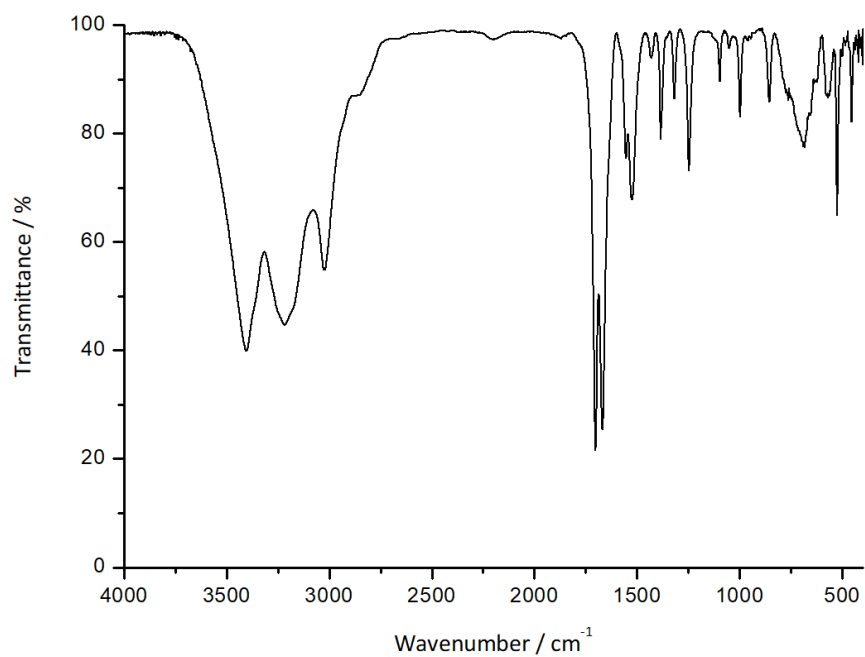
Figure 116 IR spectrum of N,N'-diacetyloxalhydrazide in KBr (REN-EB-225).
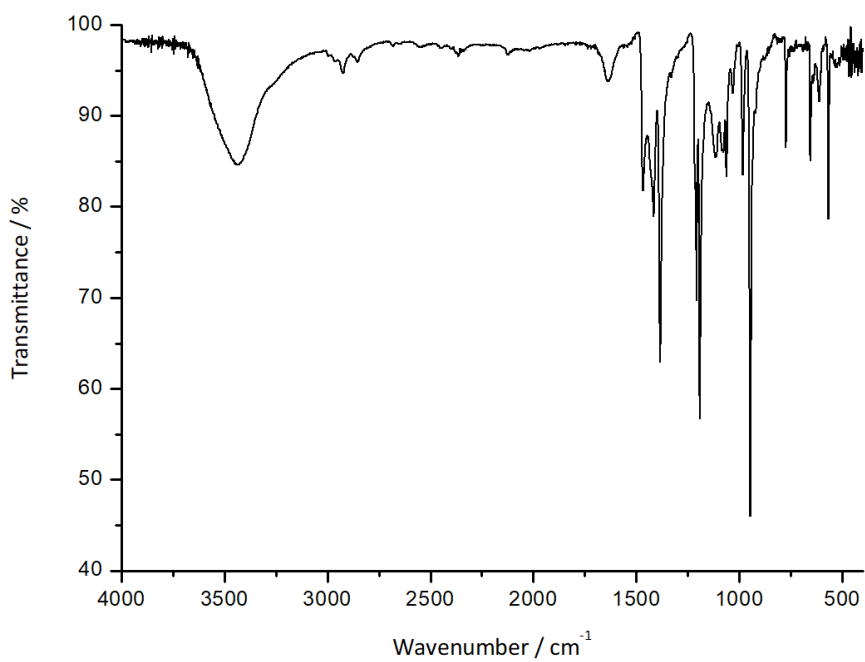
*Figure 117 IR spectrum of **L2** in KBr. (REN-EB-229).*
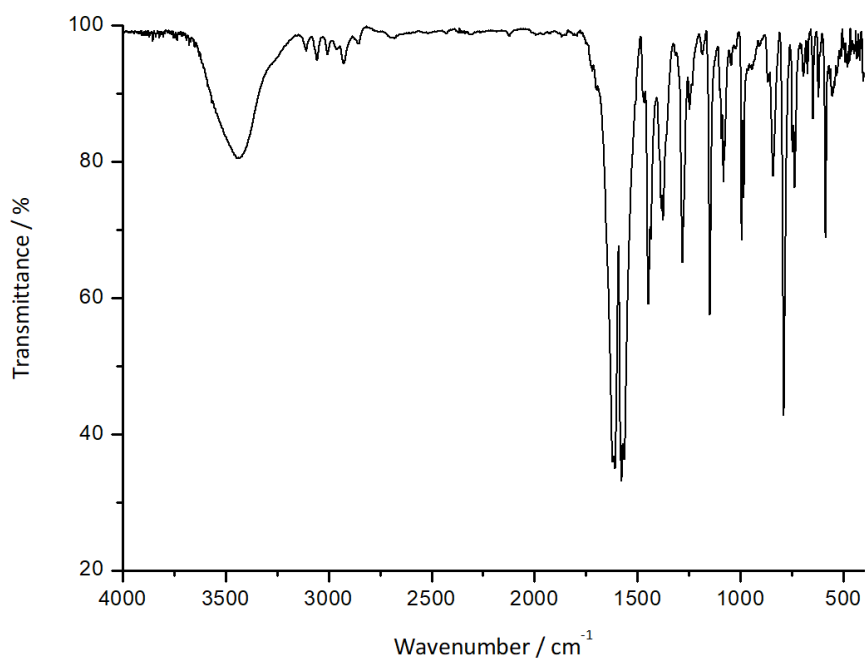
Figure 118 IR spectrum of 1,5-bis(2'-pyridyl)pentane-1,3,5-trione in KBr (REN-EB-397).
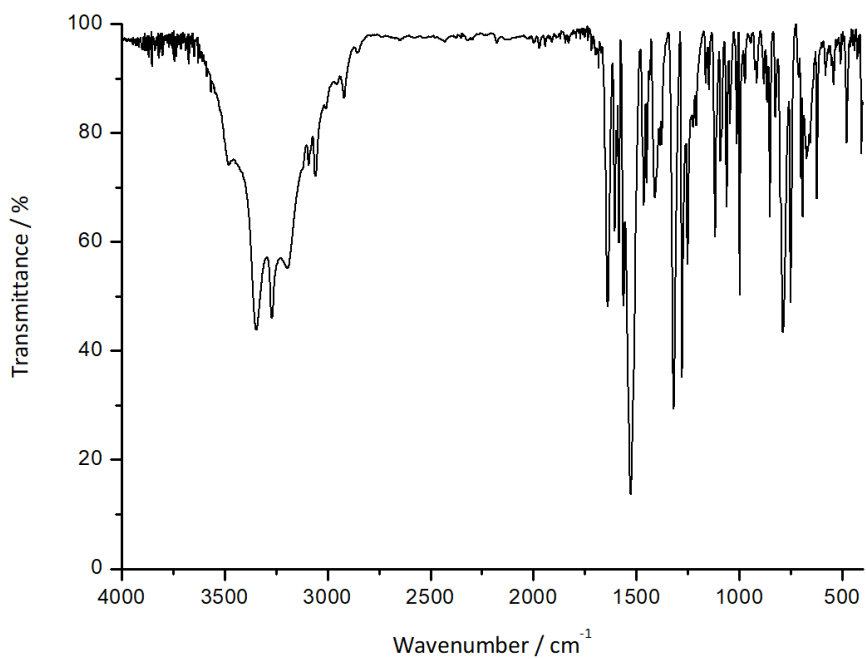
Figure 119 IR spectrum of 2,2':6',2''-terpyridin-4'(1'H)-one in KBr (REN-EB-375).
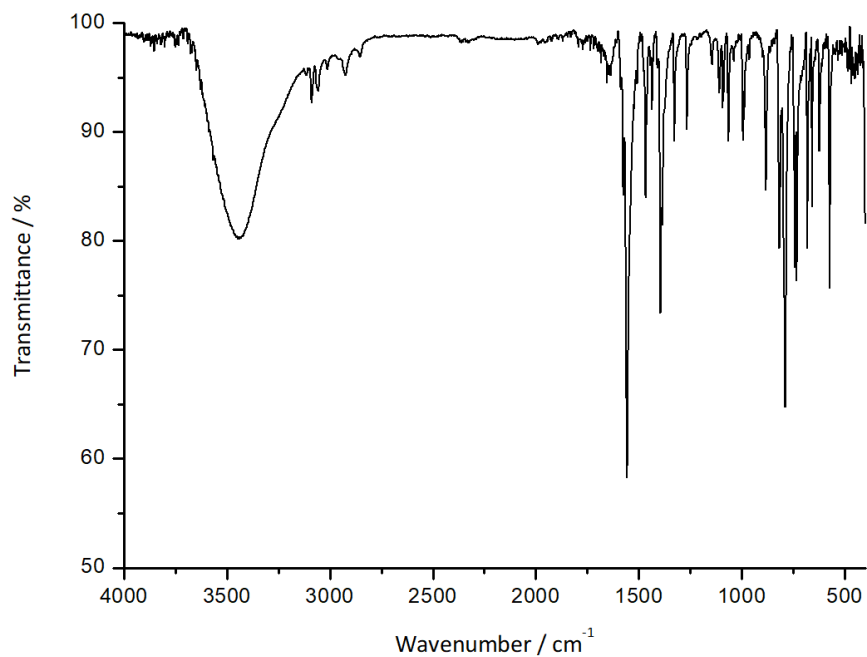
Figure 120 IR spectrum of 4'-chloro-2,2':6',2''-terpyridine in KBr (REN-EB-377).
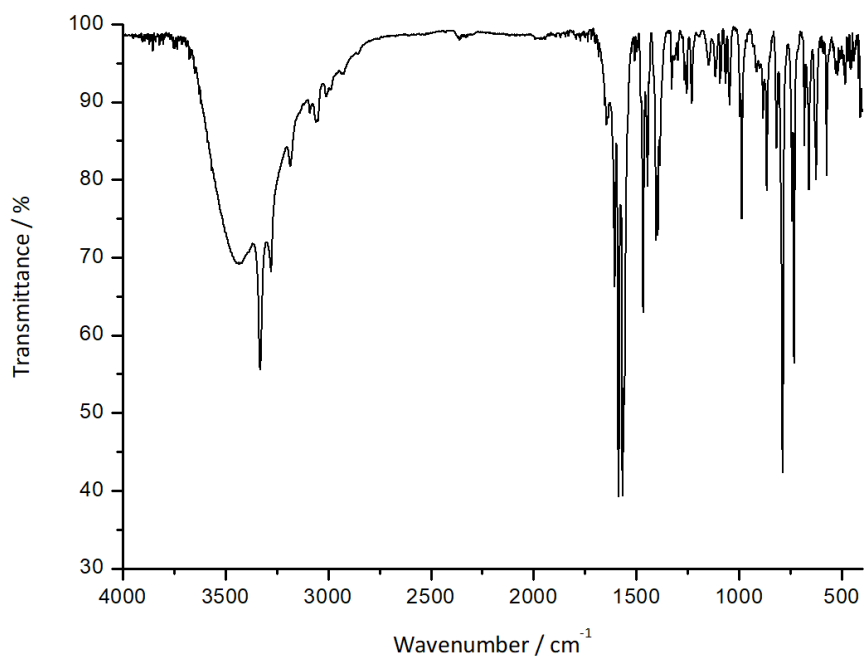
Figure 121 IR spectrum of 4'-hydrazino-2,2':6',2''-terpyridine in KBr (REN-EB-379).
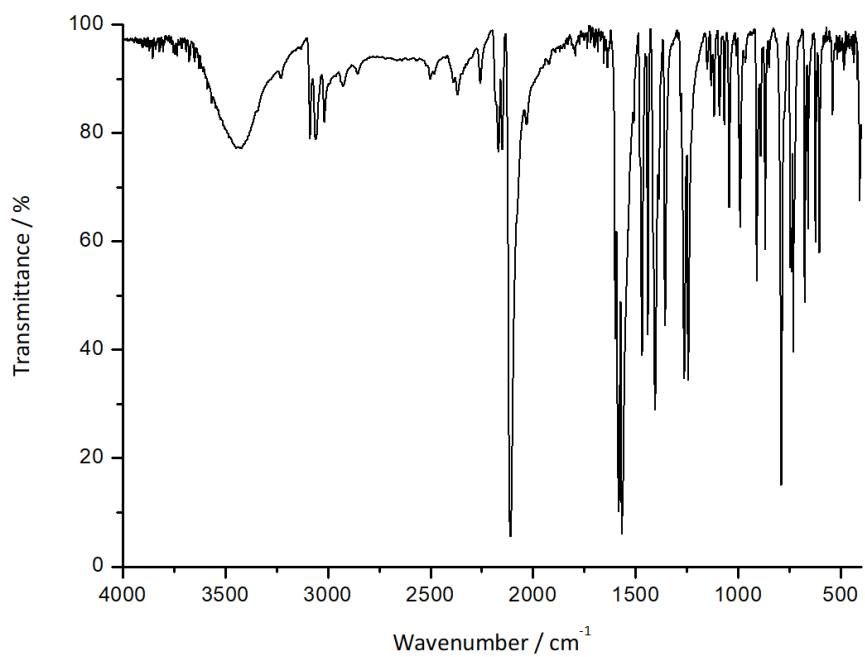
*Figure 122 IR spectrum of **L3** in KBr (REN-EB-248).*
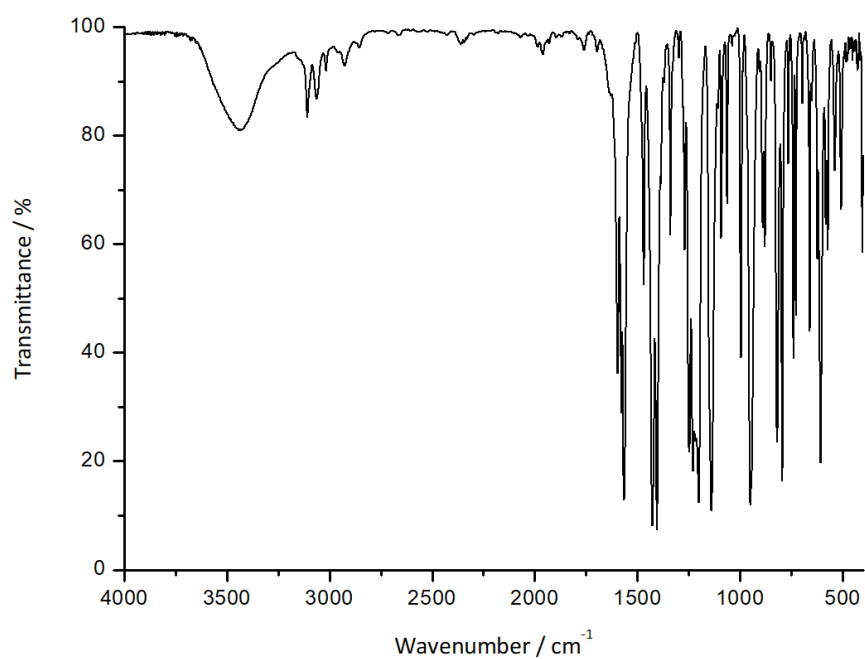
Figure 123 IR spectrum of 4'-{[(trifluormethyl)sulfonyl]oxy}-2,2':6',2''-terpyridine in KBr (REN-EB-302).
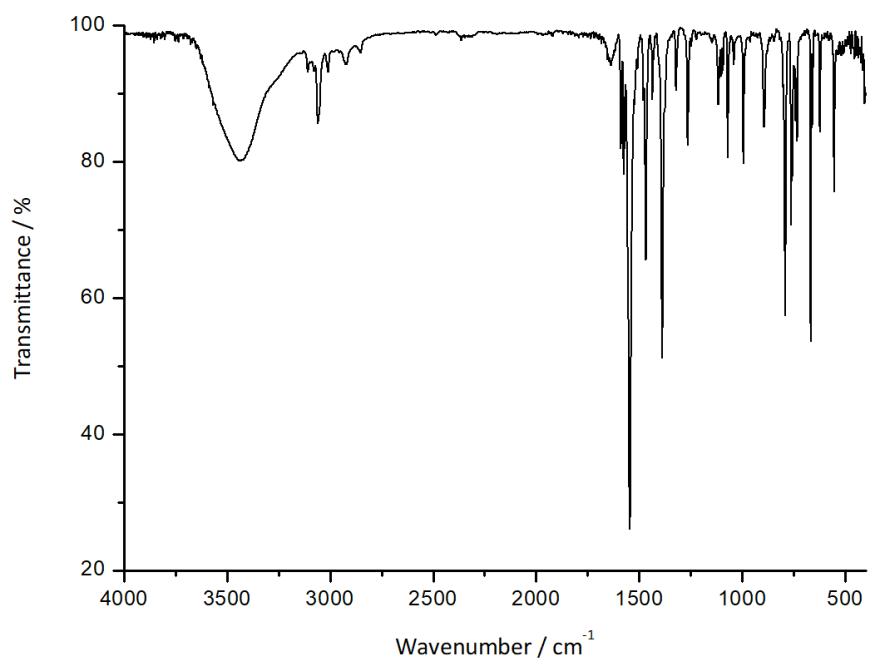
Figure 124 IR spectrum of 4'-iodo-2,2':6',2''-terpyridine in KBr (REN-EB-309).
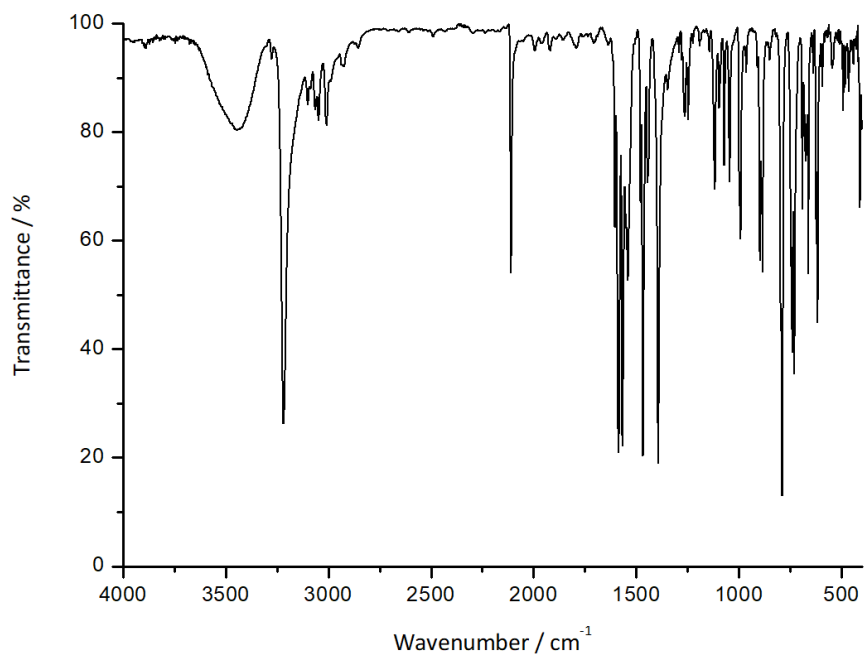
*Figure 125 IR spectrum of **L4** in KBr (REN-EB-274).*
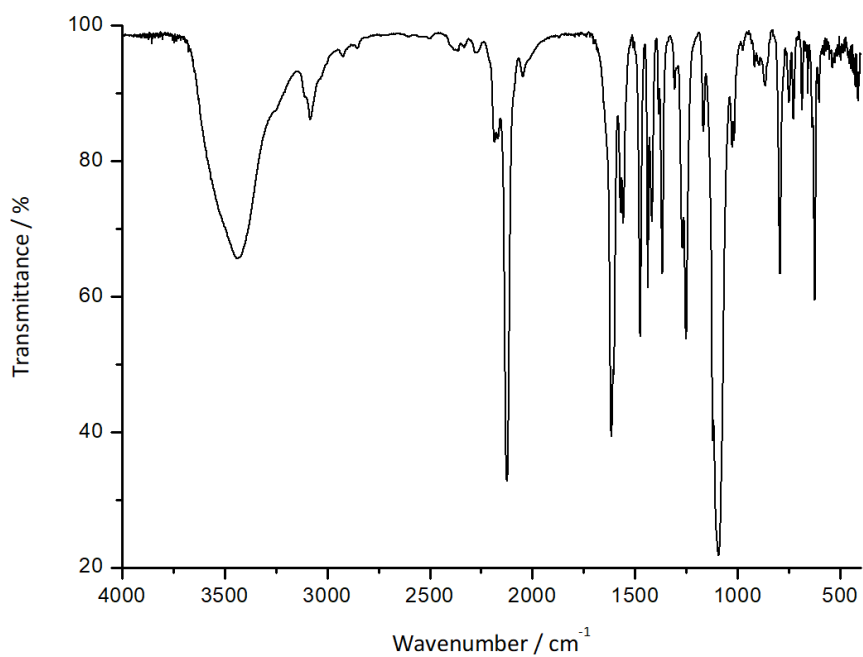
*Figure 126 IR spectrum of **C7** in KBr (REN-EB-270).*
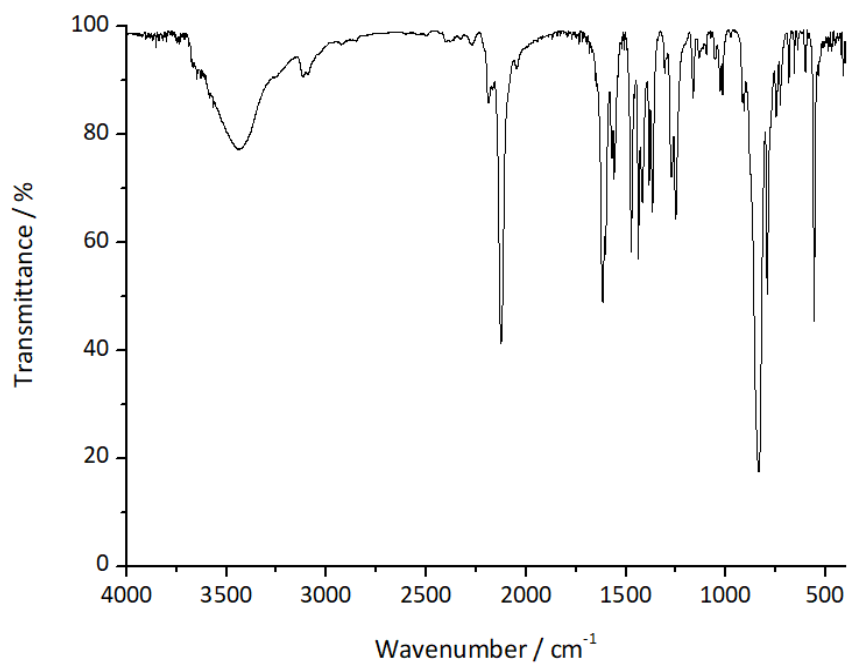
*Figure 127 IR spectrum of **C8** in KBr (REN-EB-342).*
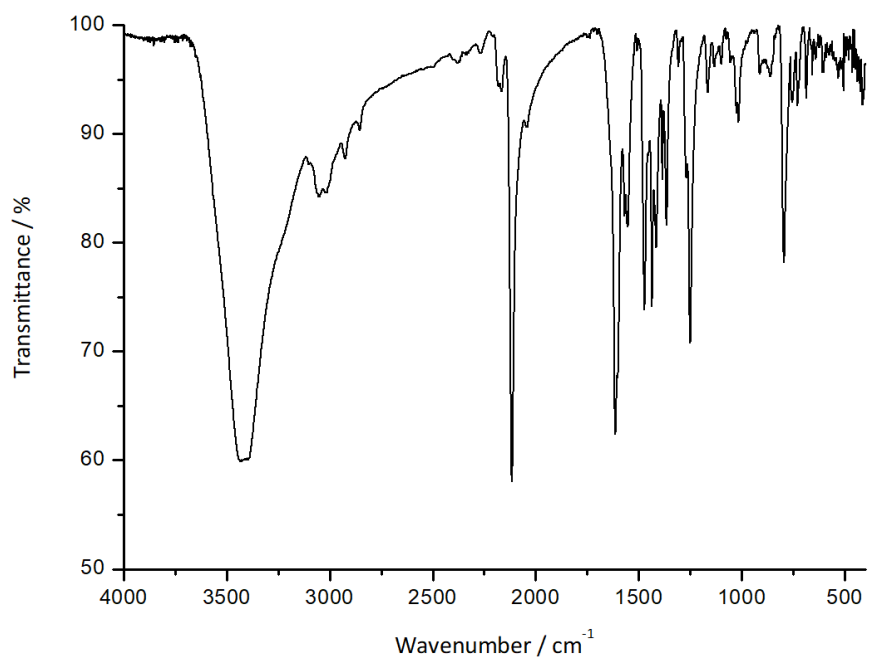
*Figure 128 IR spectrum of **C9** in KBr (REN-EB-380-2).*
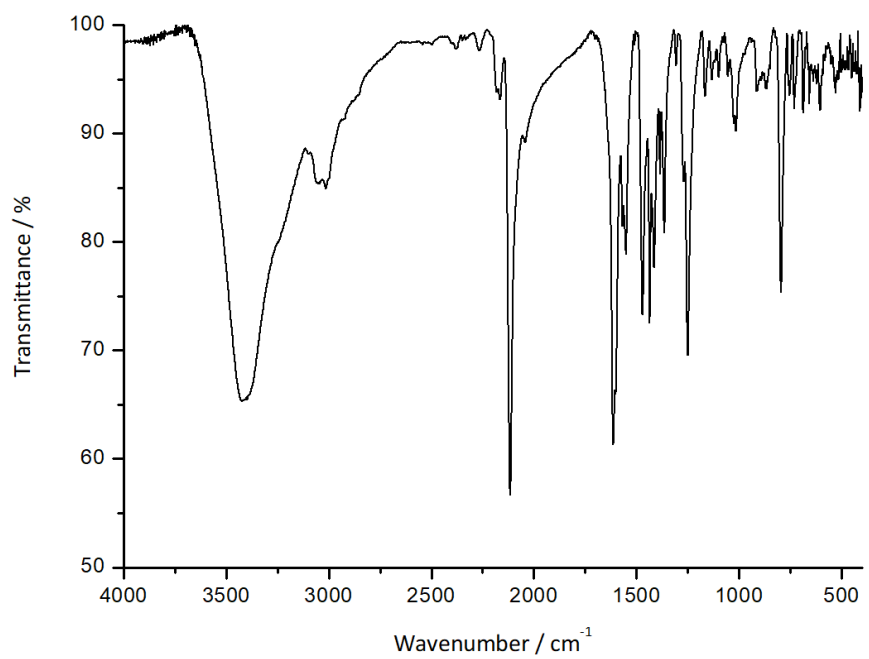
*Figure 129 IR spectrum of **C10** in KBr (REN-EB-380-5).*
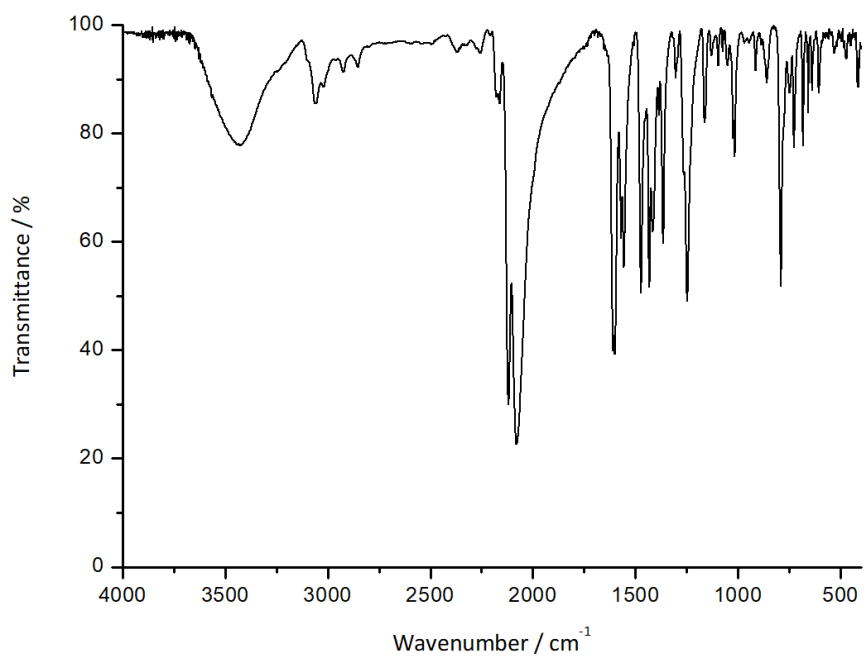
*Figure 130 IR spectrum of **C11** in KBr (REN-EB-380-1).*
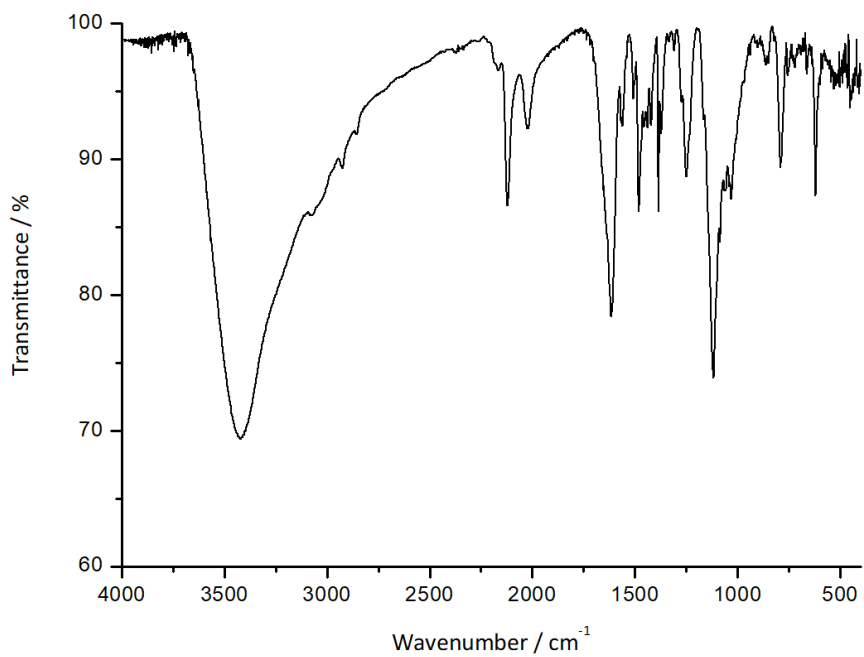
*Figure 131 IR spectrum of **C12** in KBr (REN-EB-380-4).*
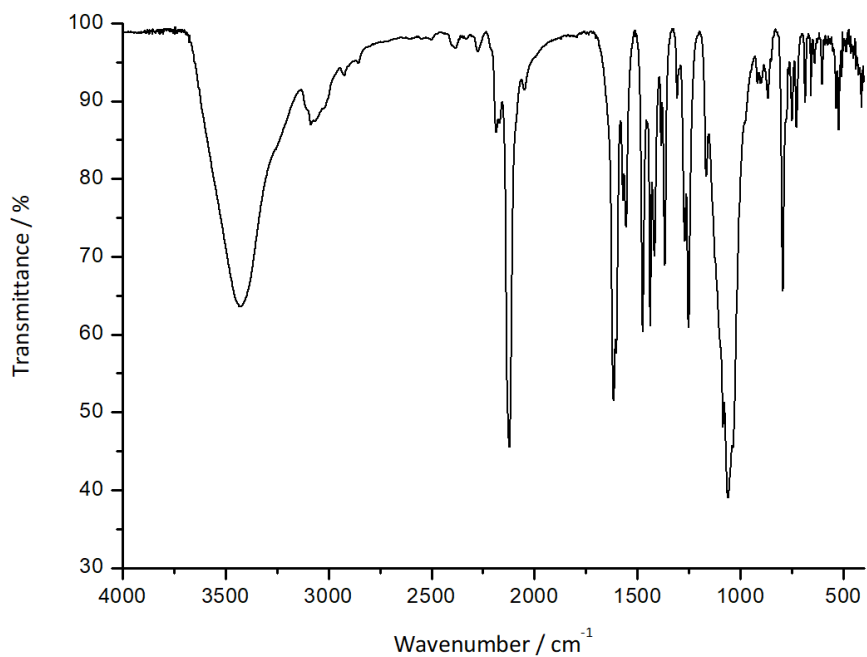
*Figure 132 IR spectrum of **C13** in KBr (REN-EB-380-3).*
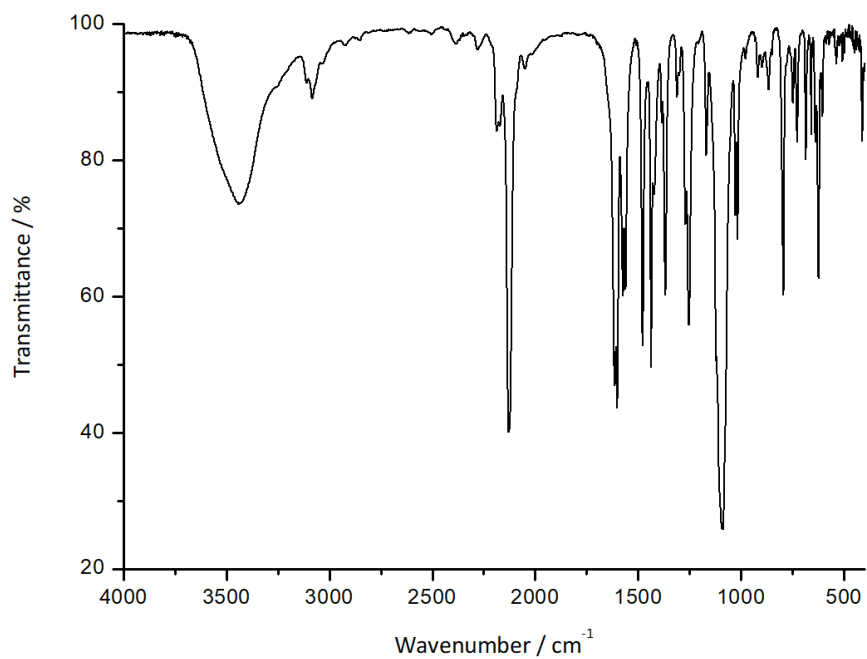
*Figure 133 IR spectrum of **C14** in KBr (REN-EB-283).*
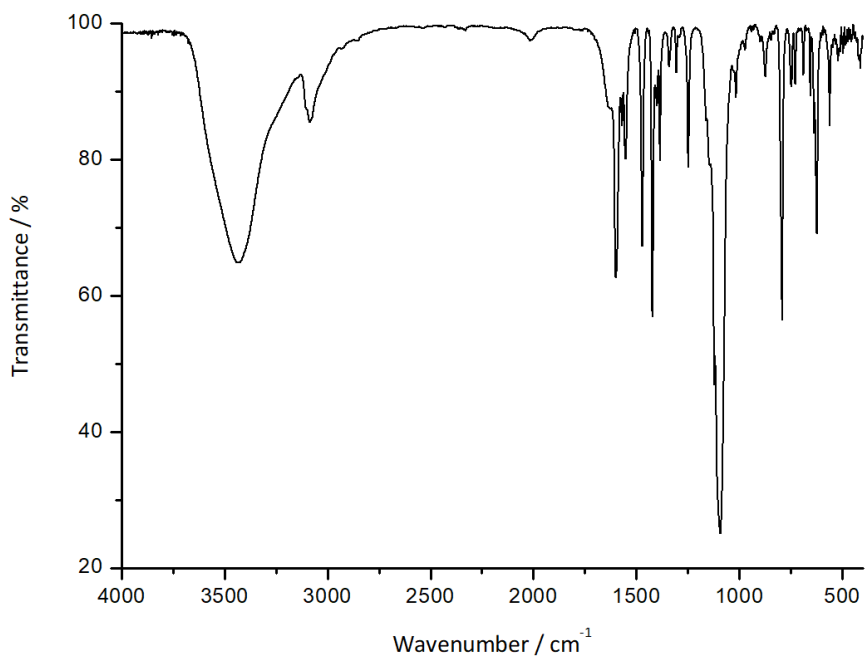
*Figure 134 IR spectrum of **C15** in KBr (REN-EB-351).*
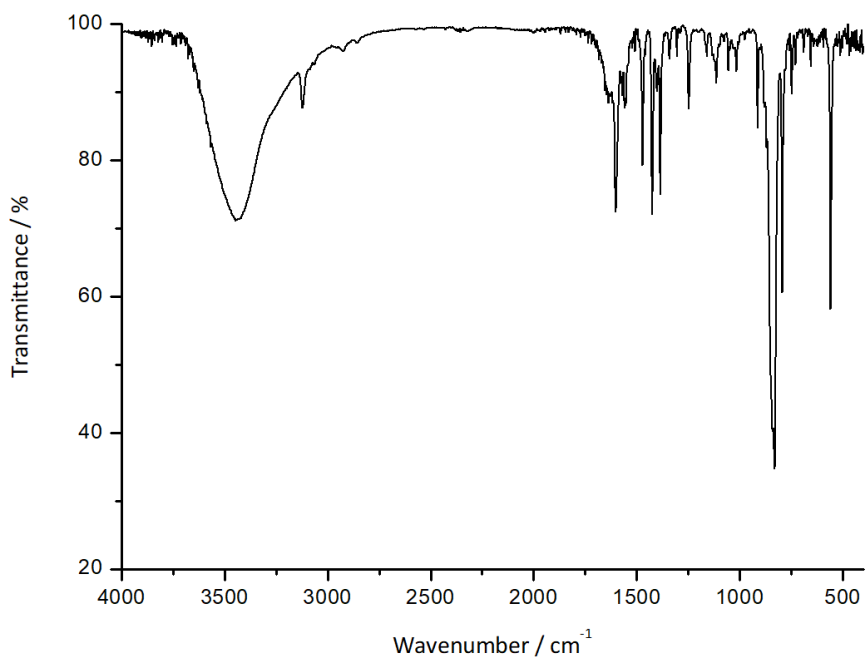
*Figure 135 IR spectrum of **C16** in KBr (REN-EB-350).*
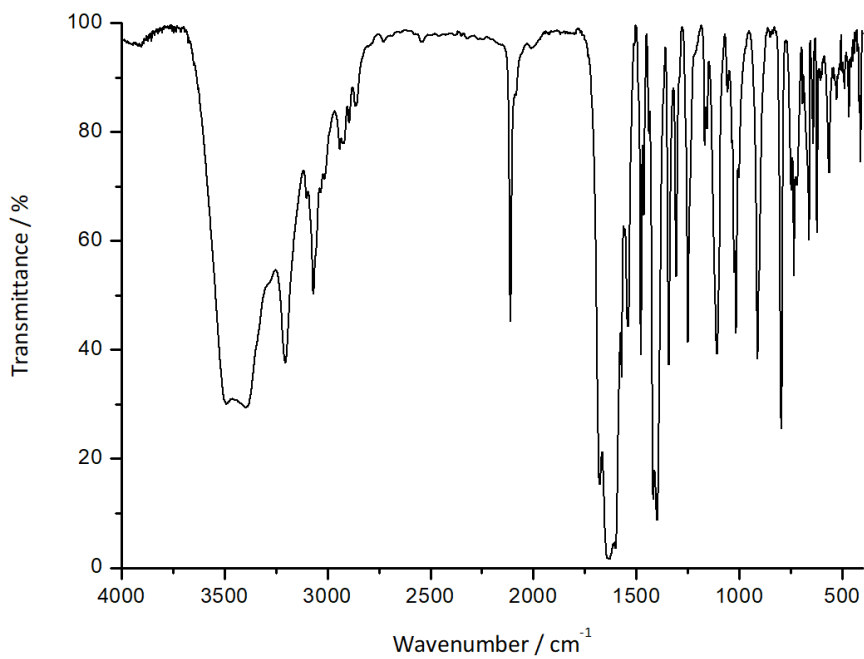
*Figure 136 IR spectrum of **C17** in KBr (REN-EB-277).*
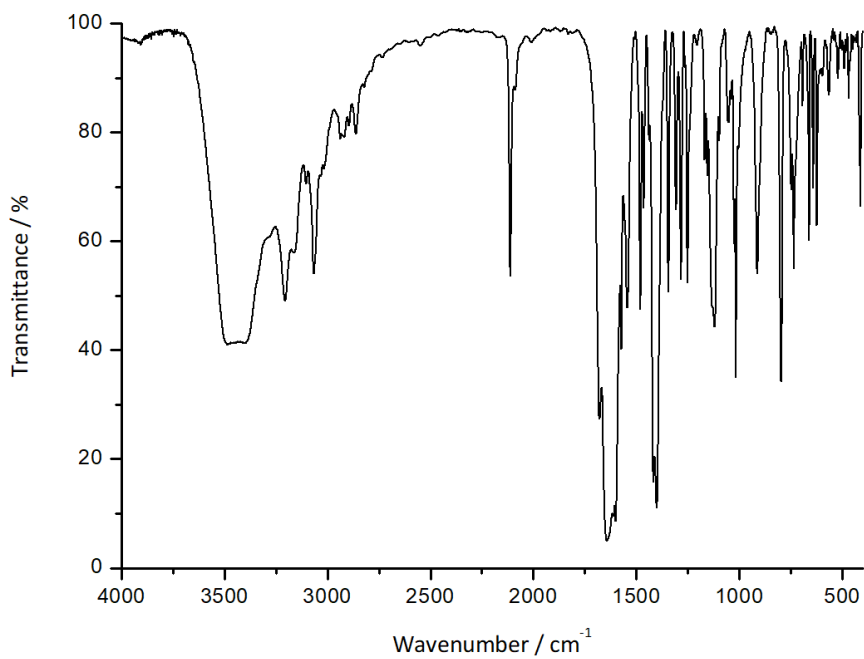
*Figure 137 IR spectrum of **C18** in KBr (REN-EB-395).*
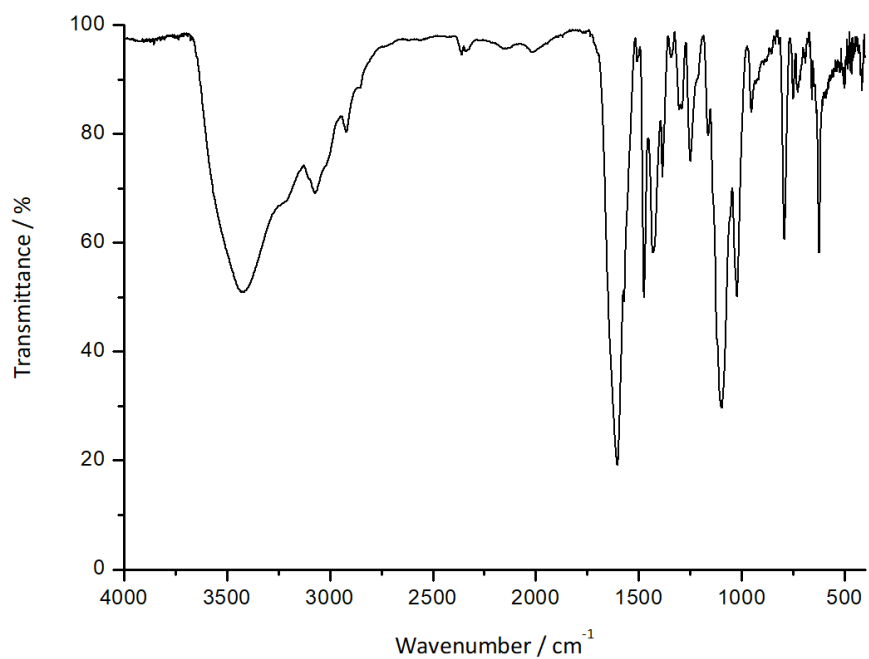
*Figure 138 IR spectrum of **C19** in KBr (REN-EB-284).*
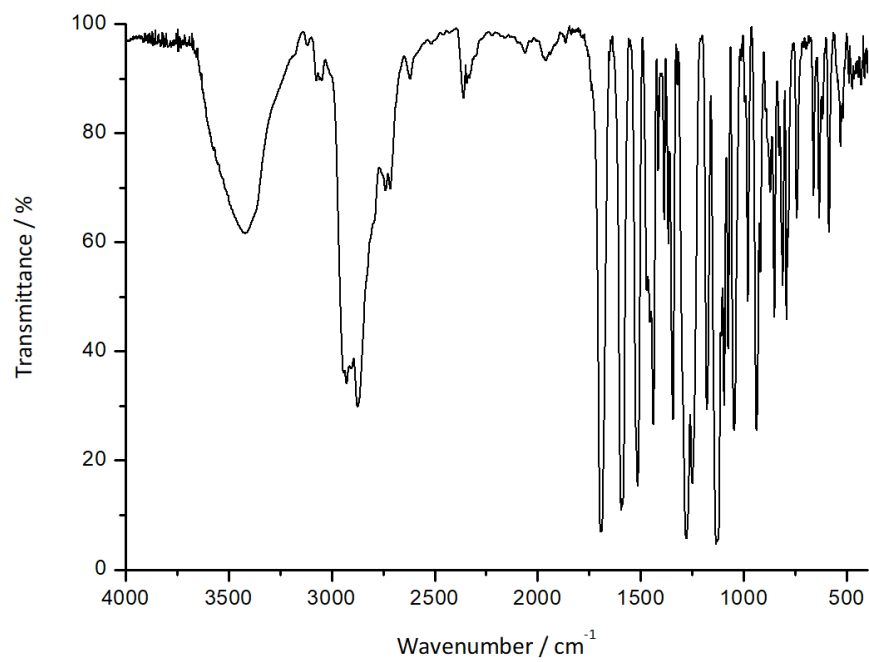
Figure 139 IR spectrum of 4'-formylbenzo-15-crown-5 in KBr (REN-EB-394).
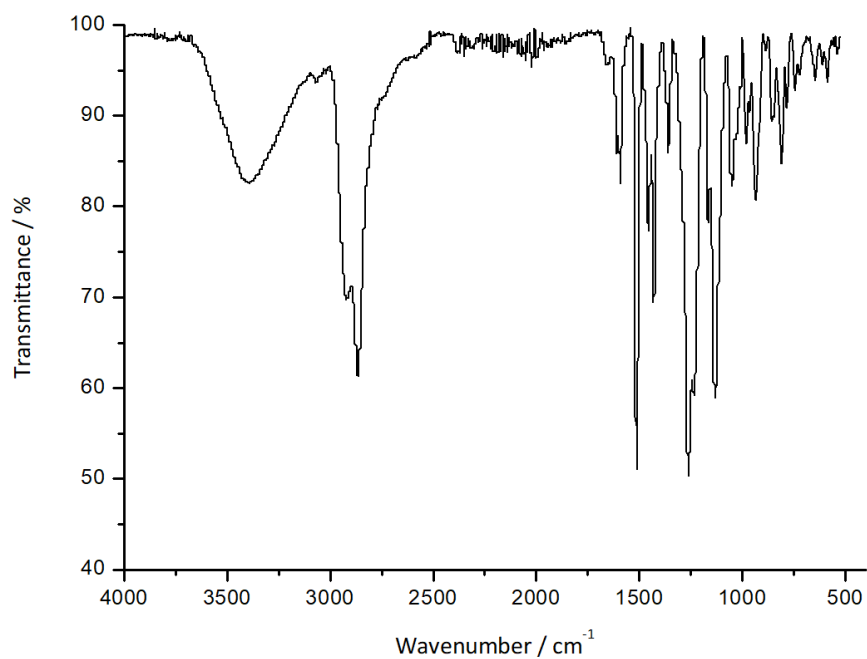
Figure 140 IR spectrum of 4'-hydroxymethylbenzo-15-crown-5 (REN-EB-399).
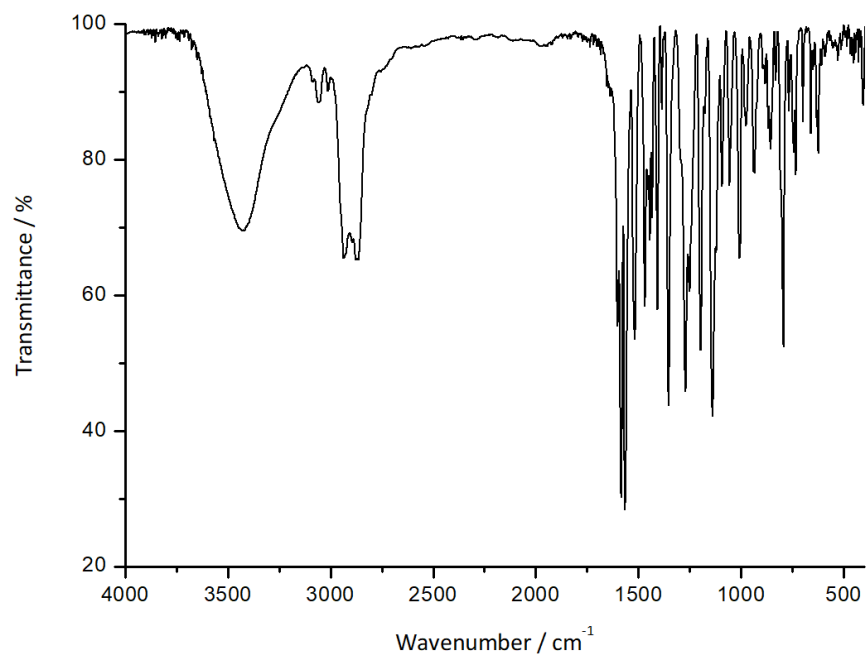
*Figure 141 IR spectrum of **L5** in KBr (REN-EB-401).*
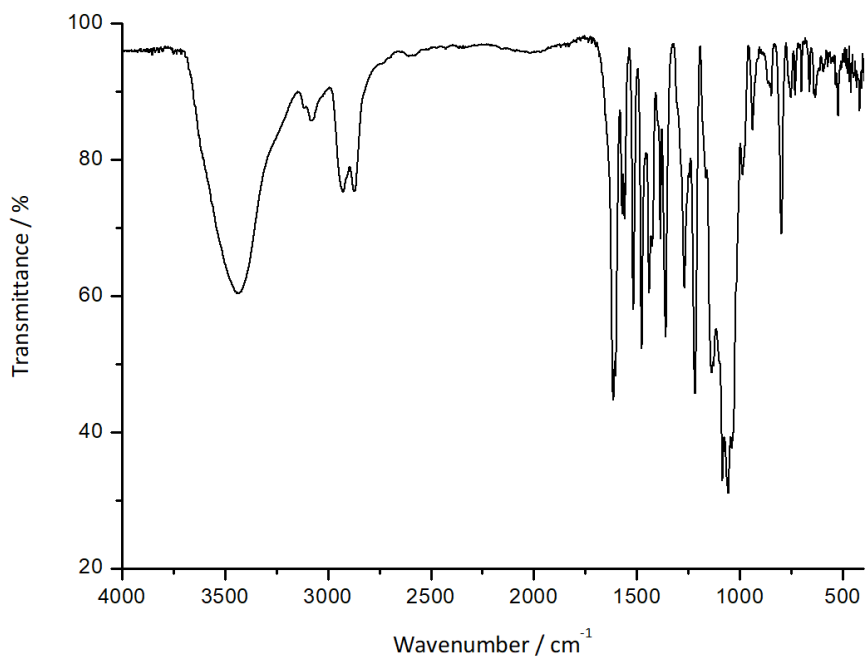
*Figure 142 IR spectrum of **C20** in KBr (REN-EB-364).*
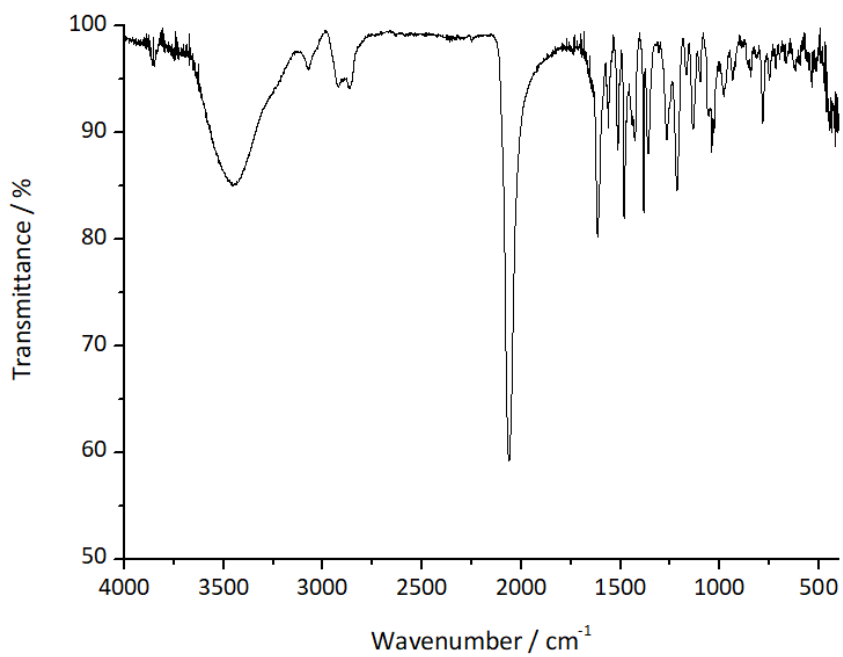
*Figure 143 IR spectrum of **C21** in KBr (REN-EB-443-2).*
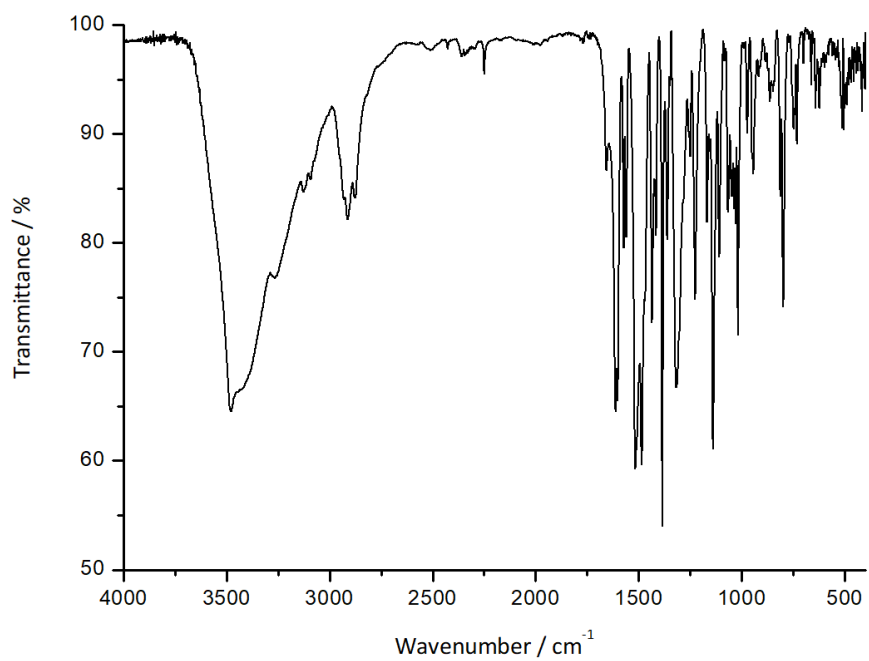
*Figure 144 IR spectrum of **C22** in KBr (REN-EB-378).*

B. NMR Spectra
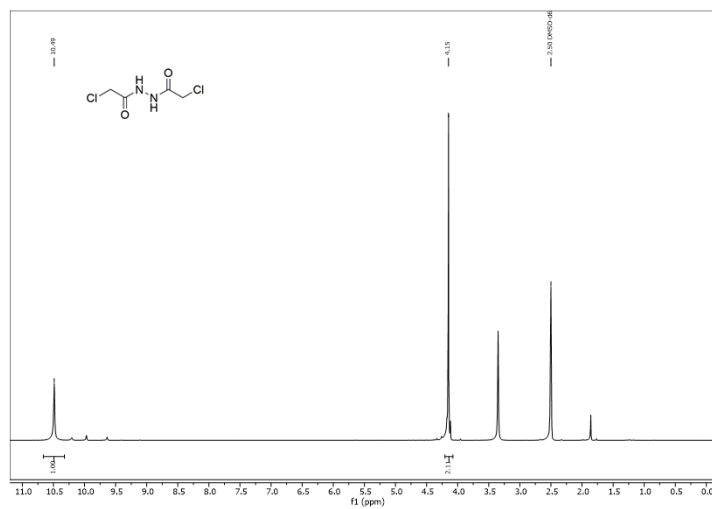
Figure 145 ^{1}H NMR spectrum of 1,2-dichloroacetyl hydrazine in DMSO-d$_6$ (REN-EB-106).
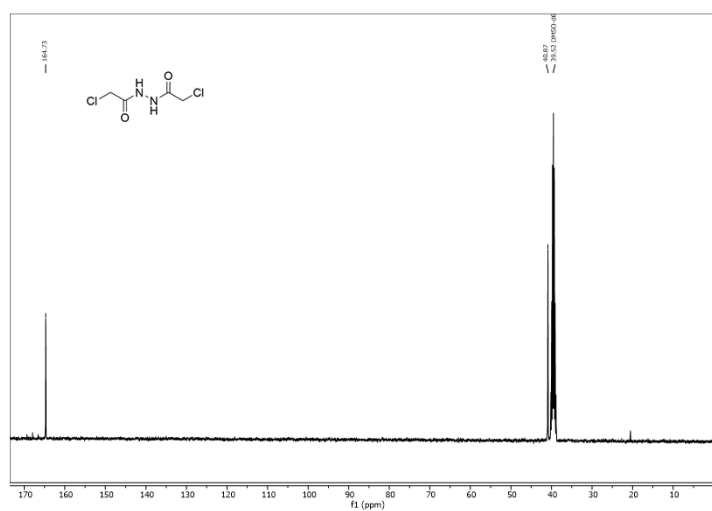
Figure 146 ^{13}C NMR spectrum of 1,2-dichloroacetyl hydrazine in DMSO-d$_6$ (REN-EB-106).
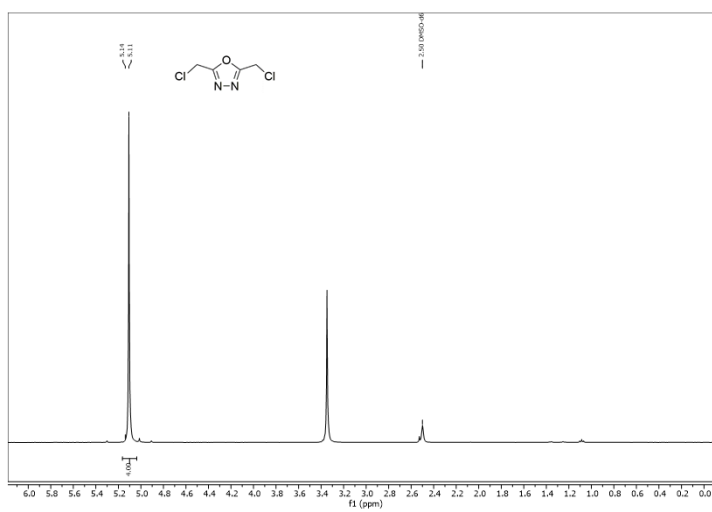
Figure 147 ^{1}H NMR spectrum of 2,5-bis(chloromethyl)-1,3,4-oxadiazole in DMSO-d$_6$ (REN-EB-107).
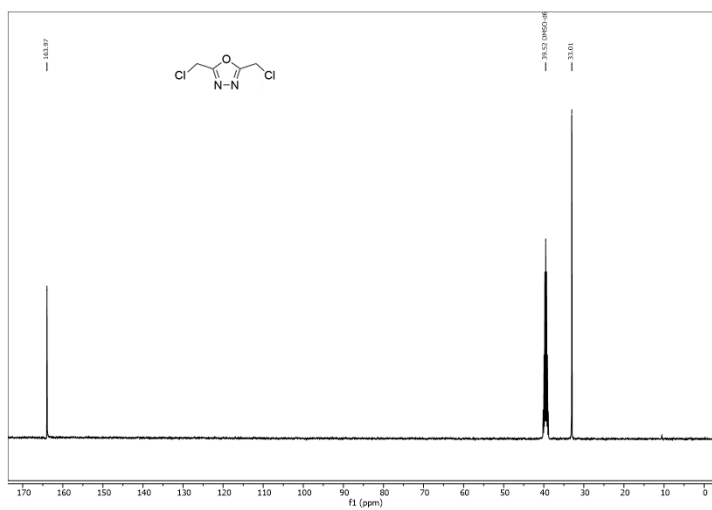
Figure 148 ^{13}C NMR spectrum of 2,5-bis(chloromethyl)-1,3,4-oxadiazole in DMSO-d$_6$ (REN-EB-107).
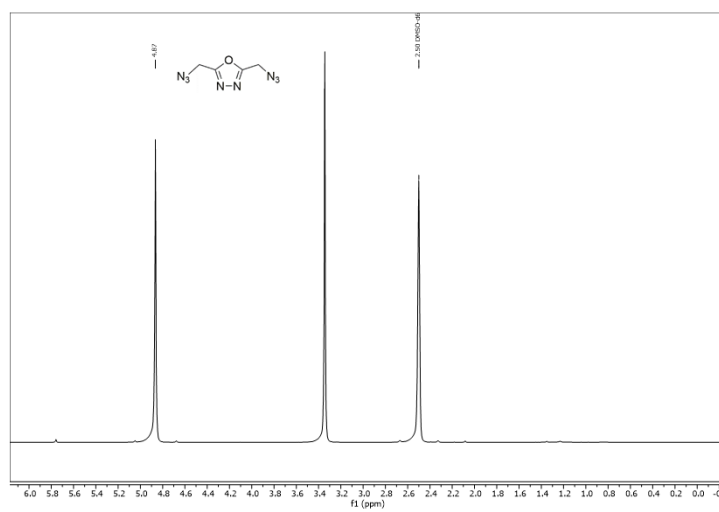
Figure 149 ^{1}H NMR spectrum of 2,5-bis(azidomethyl)-1,3,4-oxadiazole in DMSO-d$_6$ (REN-EB-030).
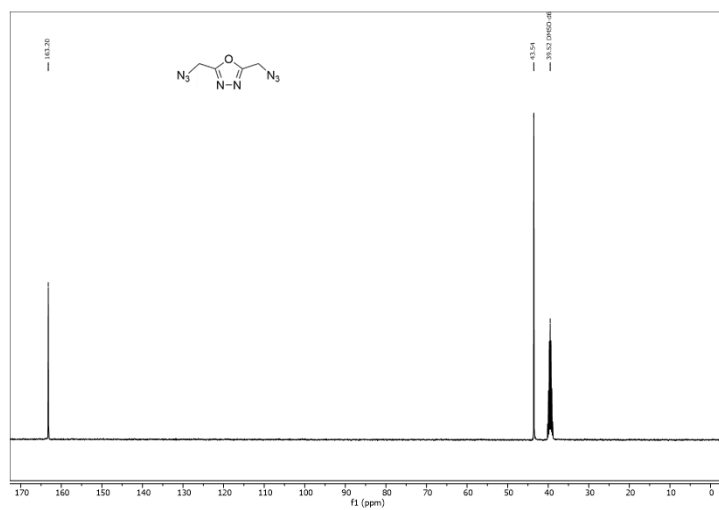
Figure 150 ^{13}C NMR spectrum of 2,5-bis(azidomethyl)-1,3,4-oxadiazole in DMSO-d$_6$ (REN-EB-030).
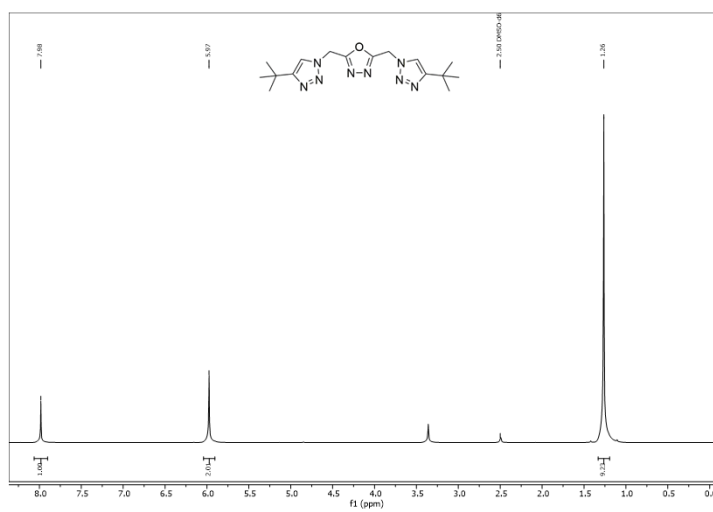
*Figure 151 ^{1}H NMR spectrum of **L1** in DMSO-d$_6$ (REN-NY-014).*
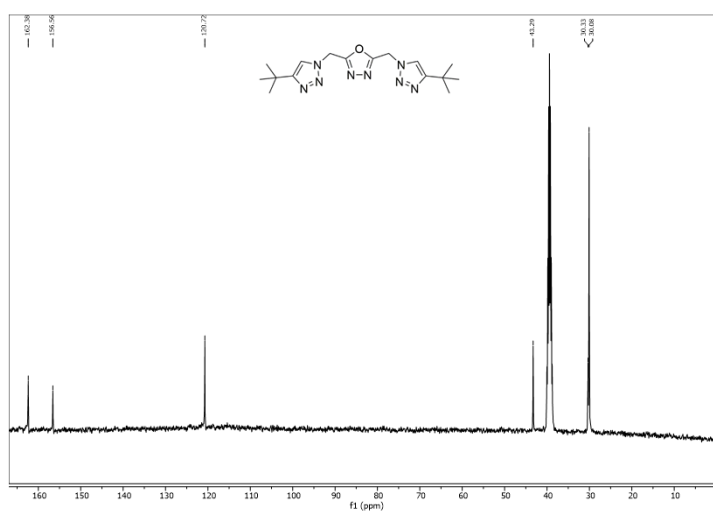
*Figure 152 ^{13}C NMR spectrum of **L1** in DMSO-d$_6$ (REN-NY-014).*
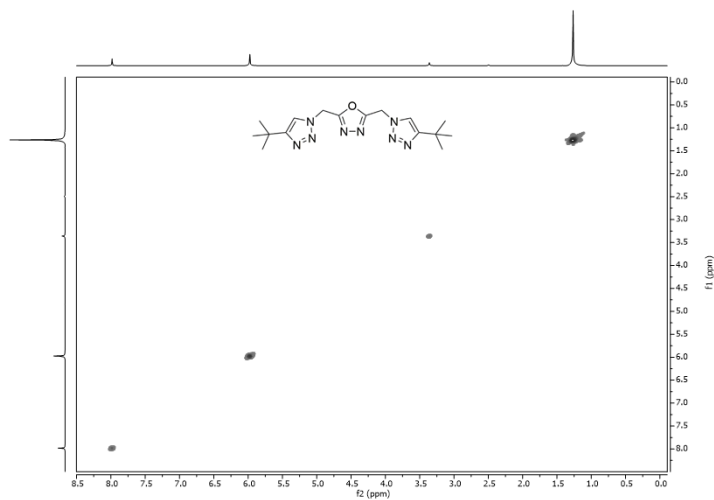
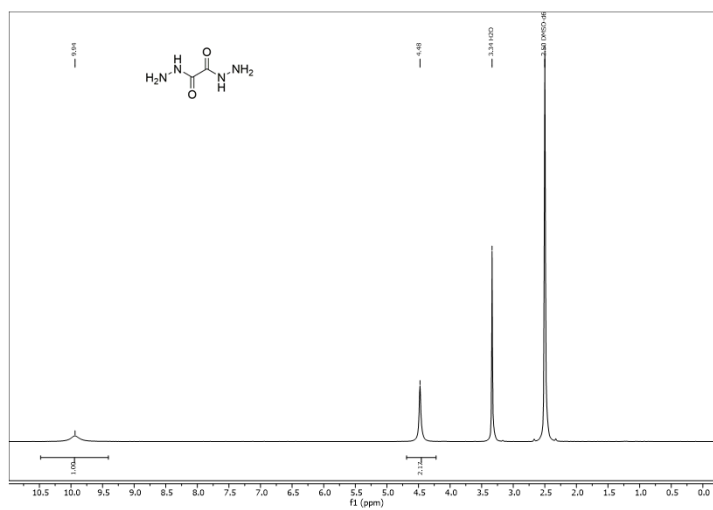*Figure 153 ^{1}H-^{1}H-COSY NMR spectrum of **L1**in DMSO-d$_6$ (REN-NY-014).*
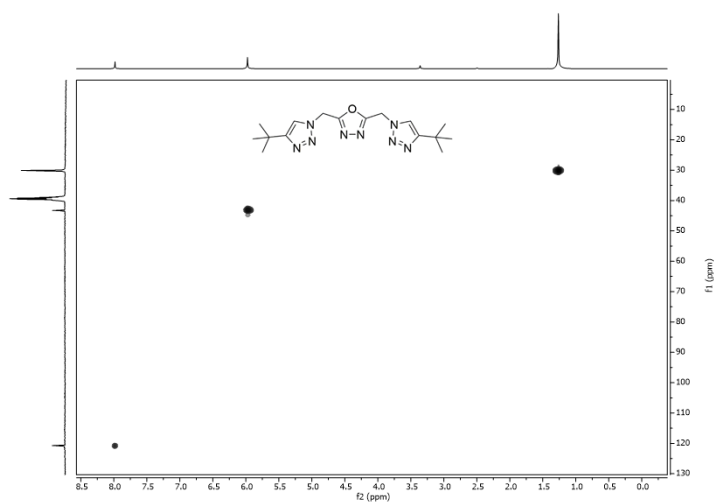
*Figure 154 ^{1}H,^{13}C-HSQC NMR spectrum of **L1** in DMSO-d$_6$ (REN-NY-014).*
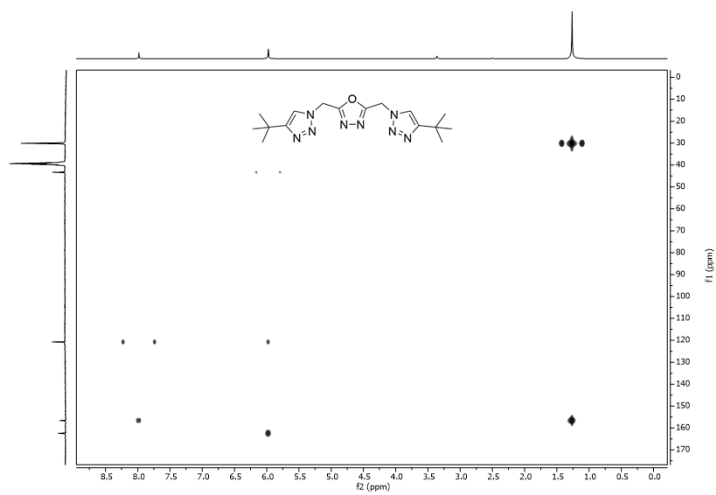
*Figure 155 ^{1}H,^{13}C-HMBC NMR spectrum of **L1** in DMSO-d$_6$ (REN-NY-014).*

Figure 156 ^{1}H NMR spectrum of oxalyl dihydrazide in DMSO-d$_6$ (REN-EB-221).
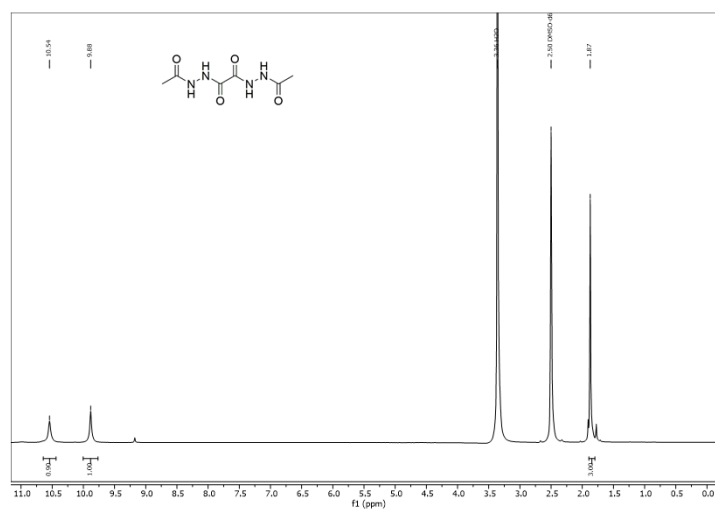
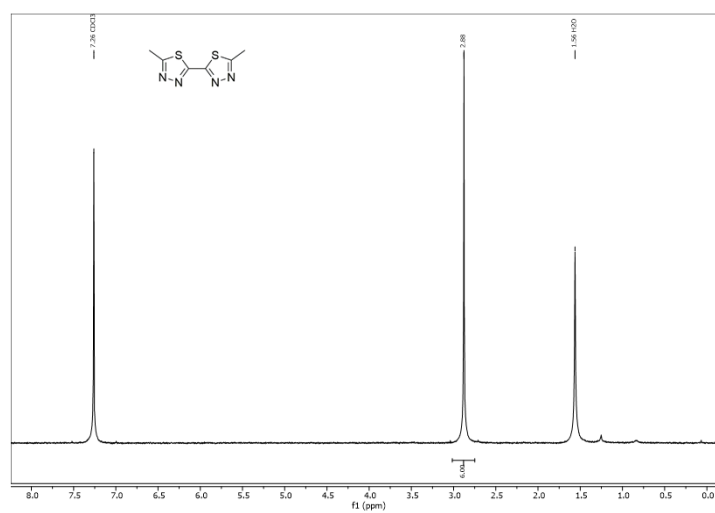*Figure 157 ^{1}H NMR spectrum of N,N-diacetyloxalhydrazide in DMSO-d$_6$ (REN-EB-223).*

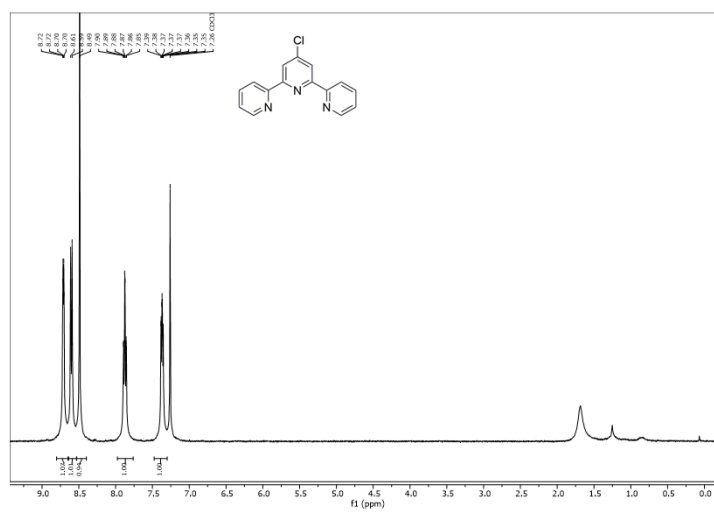*Figure 158 ^{1}H NMR spectrum of 2,2'-bismethyl-5,5'-di-1,3,4-thiadiazole in CDCl$_3$ (REN-EB-229).*

Figure 159 ¹H NMR spectrum of 1,5-bis(2'-pyridyl)pentane-1,3,5-trione in CDCl₃ (REN-EB-297).

Figure 160 ¹H NMR spectrum of 2,2':6',2''-terpyridin-4'(1'H)-one in CDCl₃ (REN-EB-375).

Figure 161 ^{1}H NMR spectrum of 4'-chloro-2,2':6',2''-terpyridine in CDCl$_3$ (REN-EB-377).
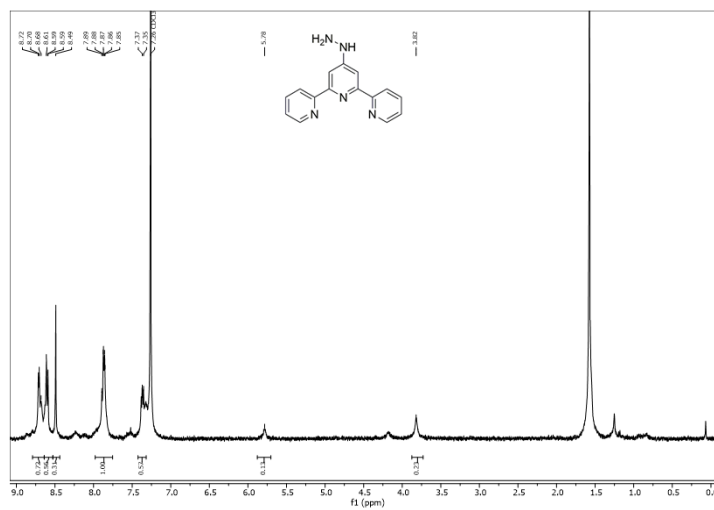

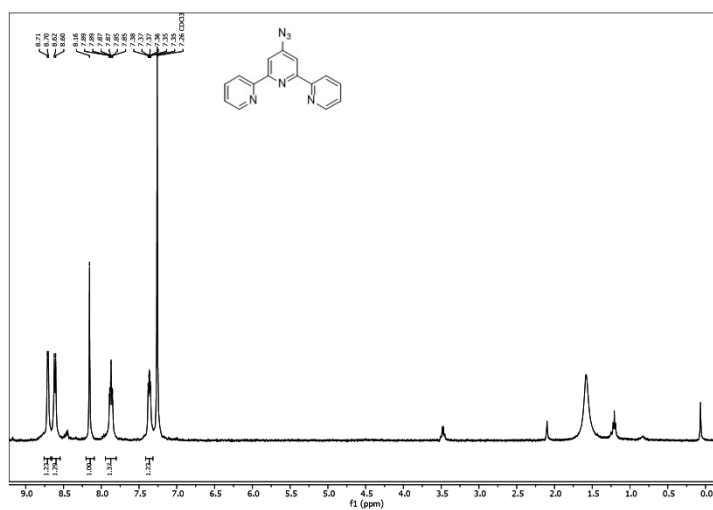*Figure 162 ^{1}H NMR spectrum of 4'-hydrazino-2,2':6',2''-terpyridine in CDCl$_3$ (REN-EB-379).*

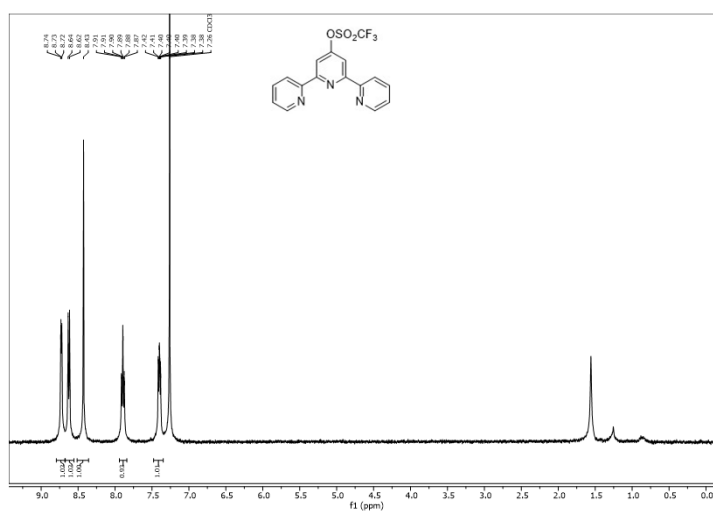*Figure 163 ¹H NMR spectrum of **L3** in CDCl₃ (REN-EB-248).*

Figure 164 ¹H NMR spectrum of 4'-{[(trifluormethyl)sulfonyl]oxy}-2,2':6',2''-terpyridine in CDCl₃ (REN-EB-302).
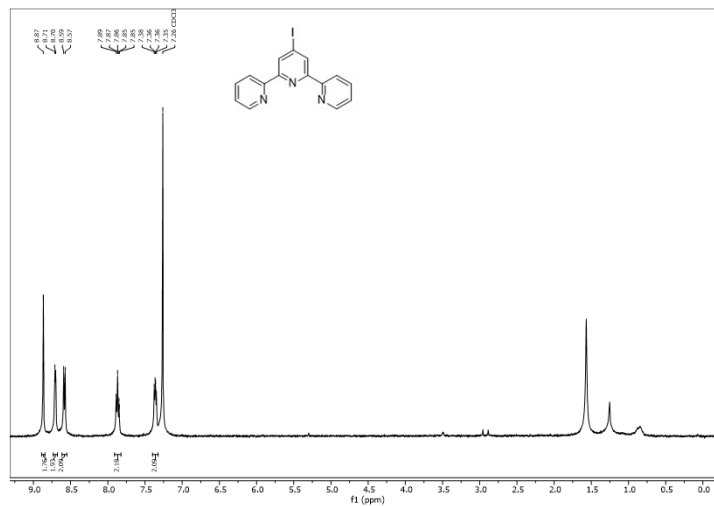
Figure 165 ^{1}H NMR spectrum of 4'-iodo-2,2':6',2''-terpyridine in CDCl$_3$ (REN-EB-309).
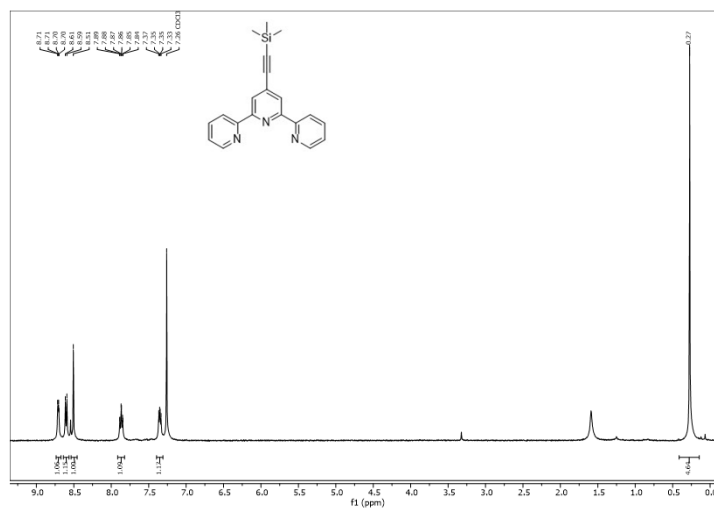

Figure 166 ^{1}H NMR spectrum of 4'-[(trimethylsilyl)-1-ethynyl]-2,2':6',2''-terpyridine in CDCl$_3$ (REN-EB-273).
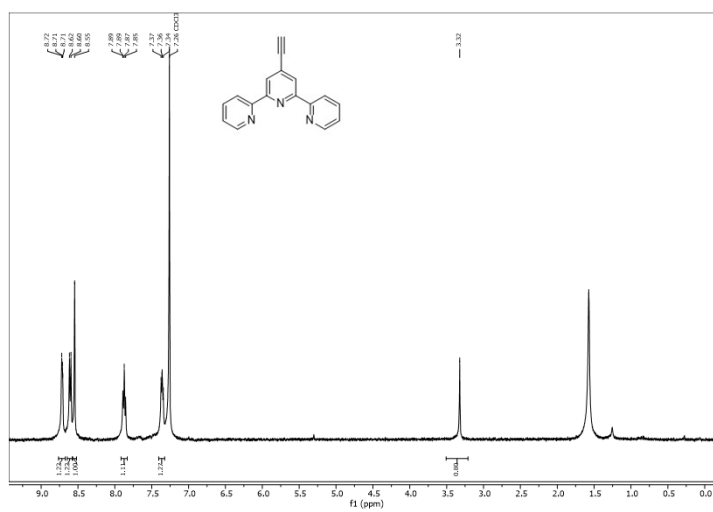
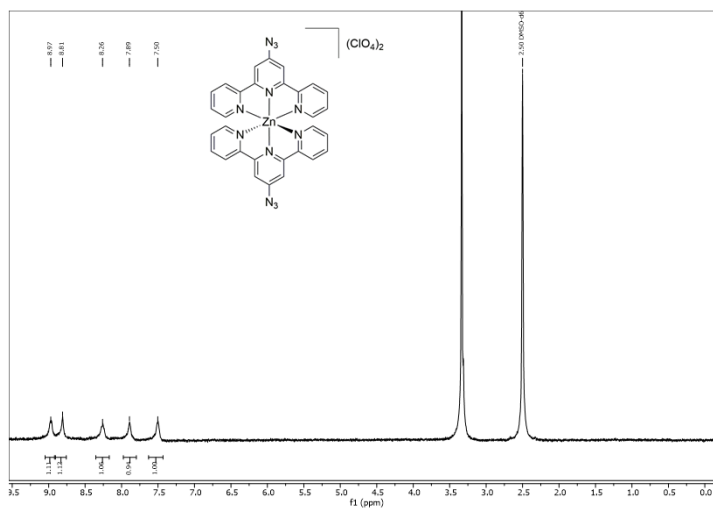*Figure 167 ^{1}H NMR spectrum of **L4** in CDCl$_3$ (REN-EB-274).*

*Figure 168 ^{1}H NMR spectrum of **C14** in DMSO-d$_6$ (REN-EB-283).*
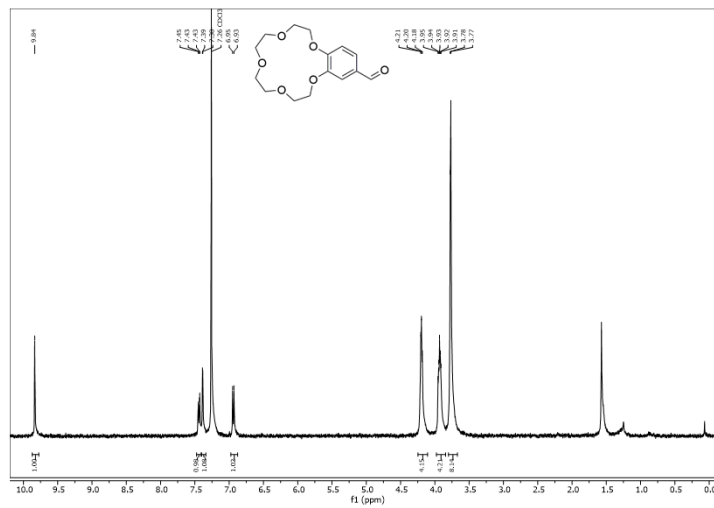
Figure 169 ^{1}H NMR spectrum of 4'-formylbenzo-15-crown-5 in CDCl$_3$ (REN-EB-394).
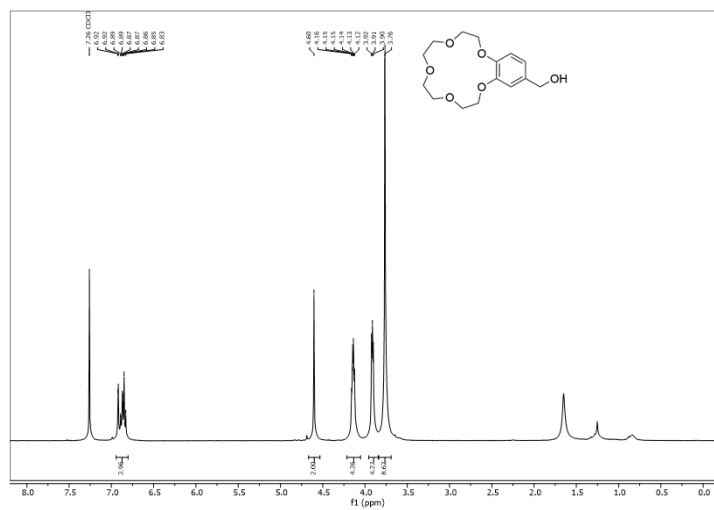
Figure 170 ^{1}H NMR spectrum of 4'-hydroxymethylbenzo-15-crown-5 in CDCl$_3$ (REN-EB-397).
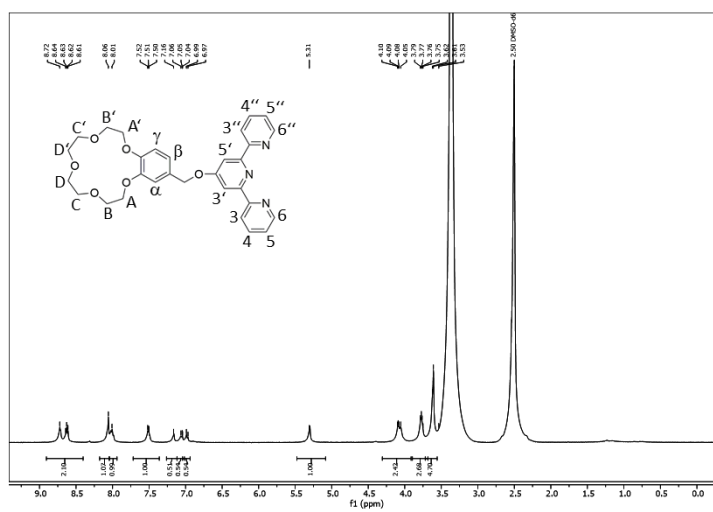
*Figure 171 ^{1}H NMR spectrum of **L5** in DMSO-d$_6$ (REN-EB-401).*

C. ESI-MS Spectra
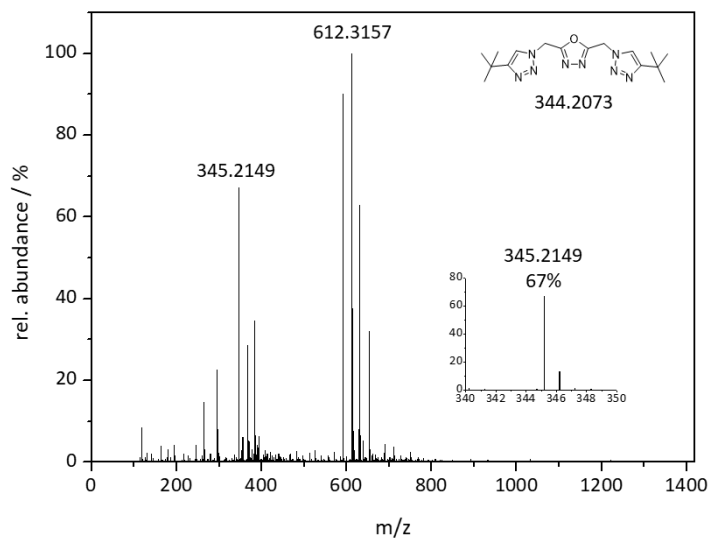
*Figure 172 ESI-MS spectrum of **L1** in MeOH (REN-NY-014).*
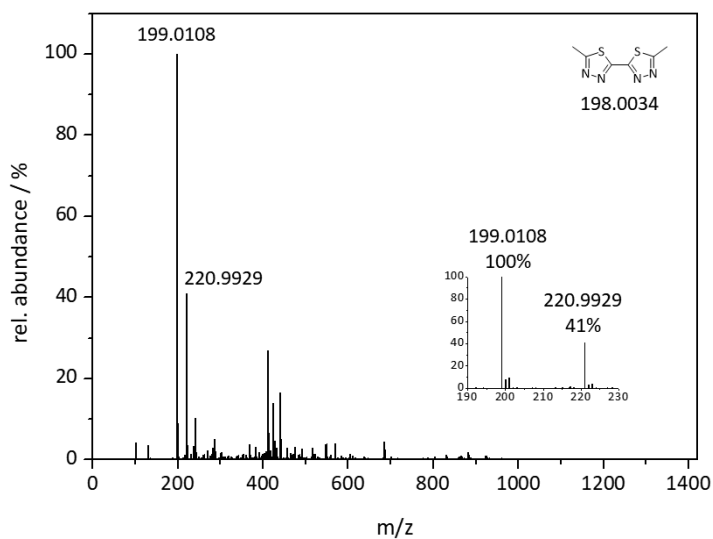
*Figure 173 ESI-MS spectrum of **L2** in MeCN (REN-EB-229).*
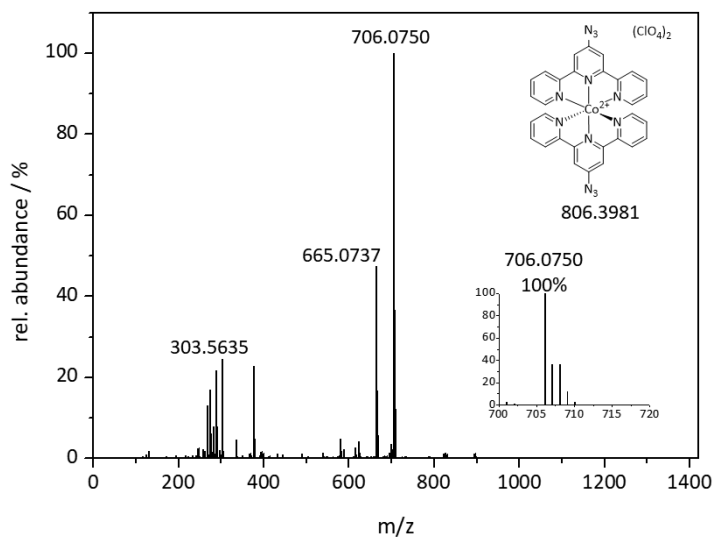
*Figure 174 ESI-MS spectrum of **C7** in MeCN (REN-EB-270).*
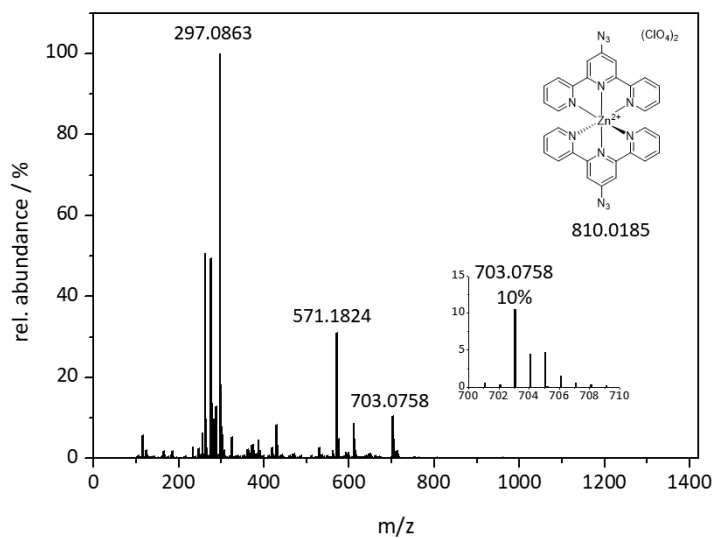
*Figure 175 ESI-MS spectrum of **C14** in MeCN (REN-EB-283).*
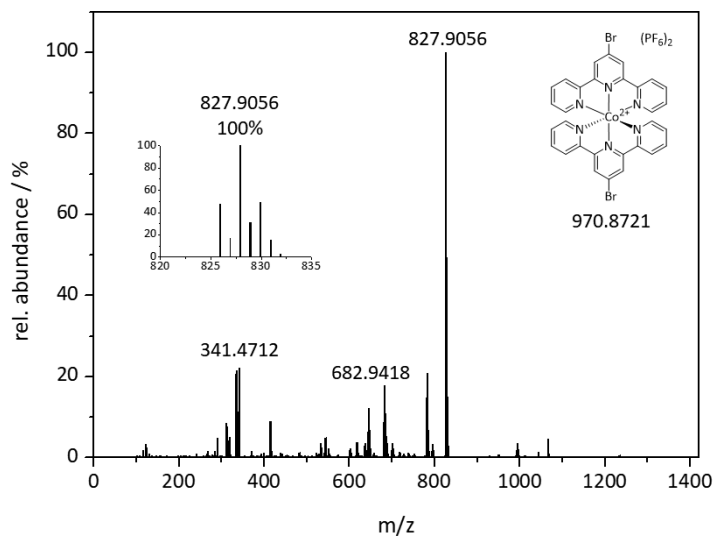
*Figure 176 ESI-MS spectrum of **C15** in MeCN (REN-EB-341).*
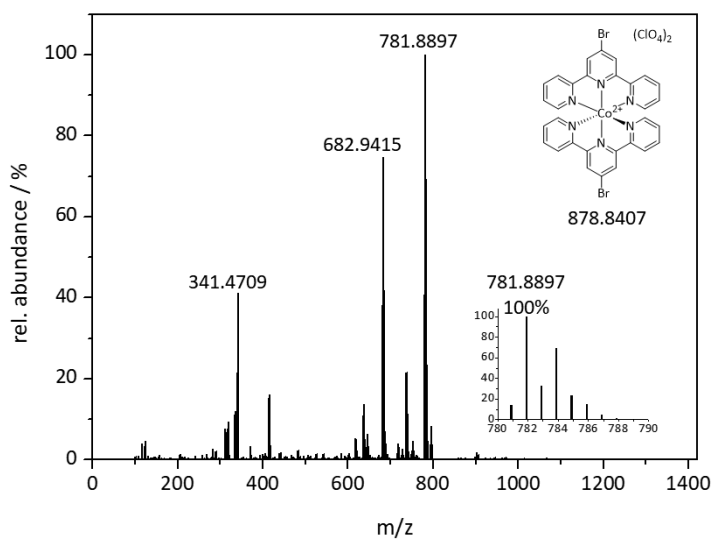
*Figure 177 ESI-MS spectrum of **C16** in MeCN (REN-EB-340).*

D. UV-Vis Spectra
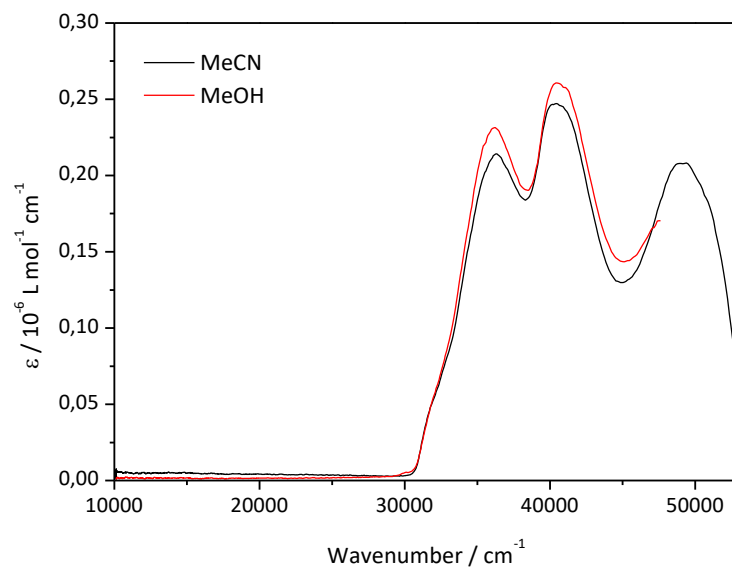
*Figure 178 UV-Vis spectrum of **L3** in MeCN (black) and MeOH (red).*
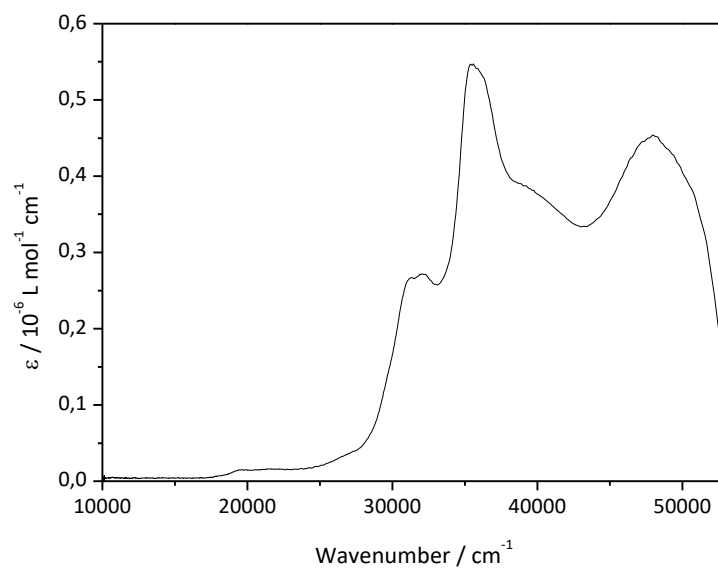
*Figure 179 UV-Vis spectrum of [Co^{II}(**L3**)$_2$](ClO$_4$)$_2$ **C7** in MeCN.*
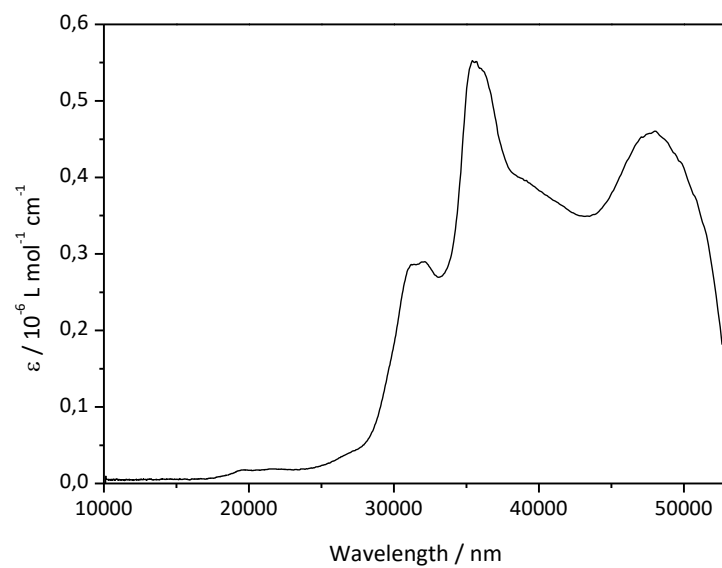
*Figure 180 UV-Vis spectrum of [Co^{II}(**L3**)$_2$](PF$_6$)$_2$ **C8** in MeCN.*
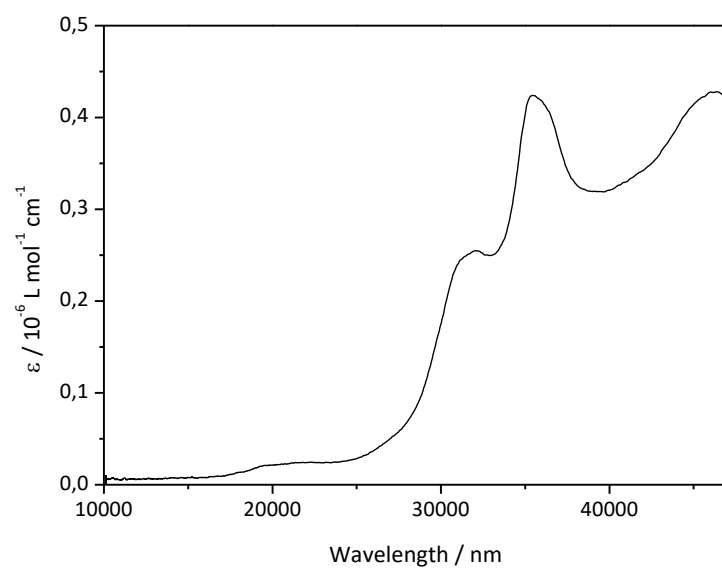
*Figure 181 UV-Vis spectrum of [Co^{II}(**L3**)$_2$]Br$_2$ **C9** in MeCN.*
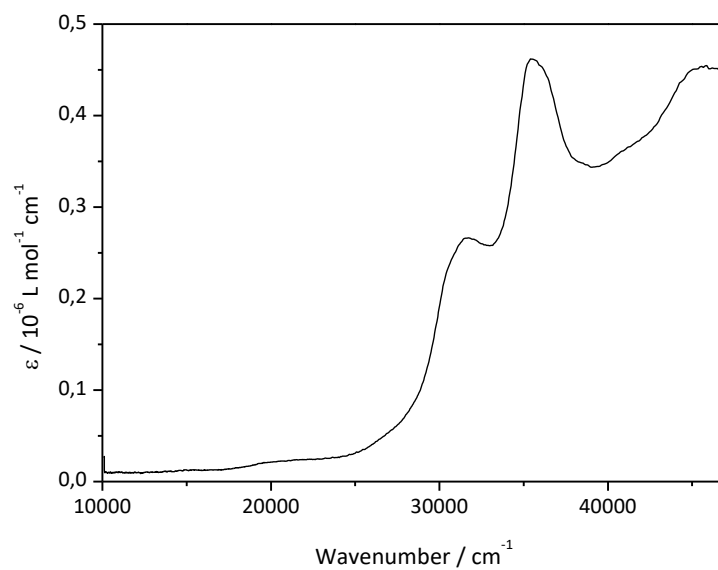
*Figure 182 UV-Vis spectrum of [Co^{II}(**L3**)$_2$]Cl$_2$ **C10** in MeOH.*
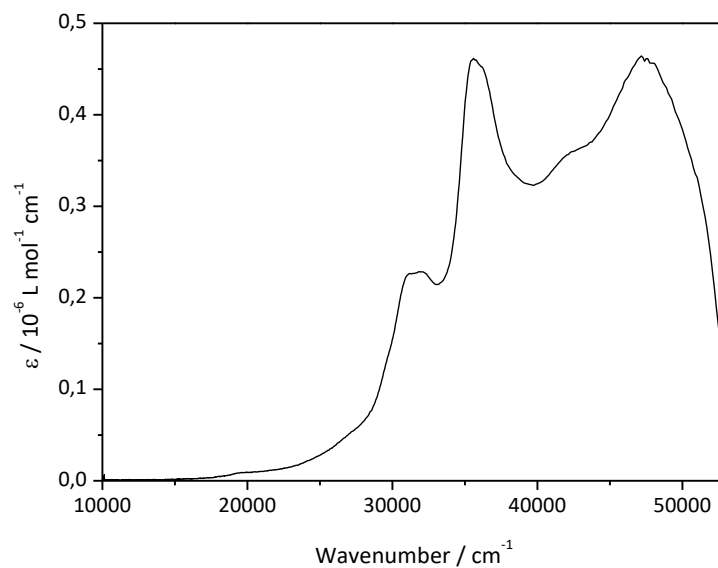
*Figure 183 UV-Vis spectrum of [Co^{II}(**L3**)$_2$](SCN)$_2$ **C11** in MeCN.*
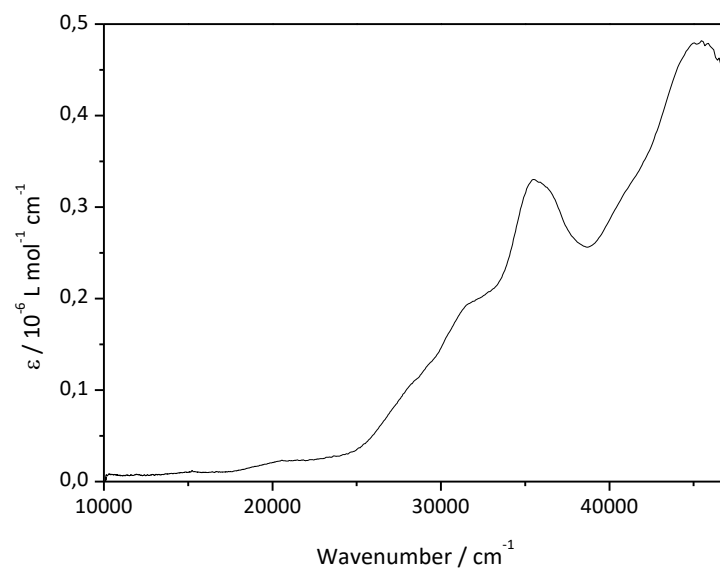
*Figure 184 UV-Vis spectrum of [Co^{II}(**L3**)$_2$]SO$_4$ **C12** in MeOH.*
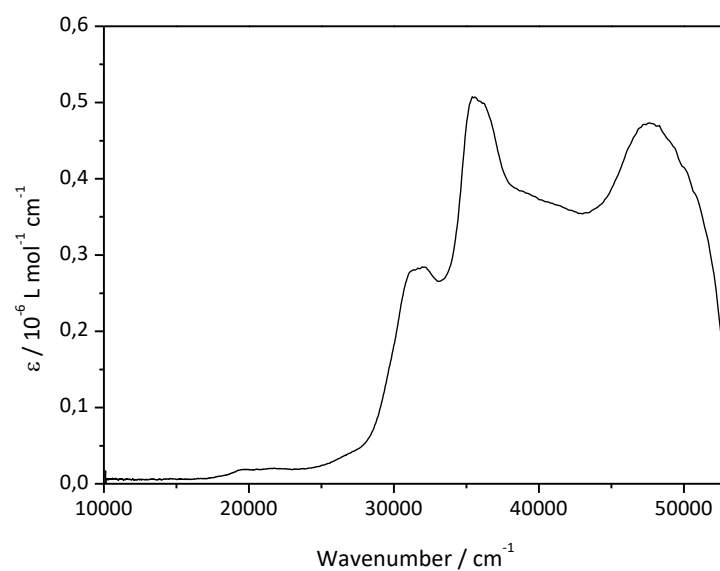
*Figure 185 [Co^{II}(**L3**)$_2$](BF$_4$)$_2$ **C13** in MeCN.*
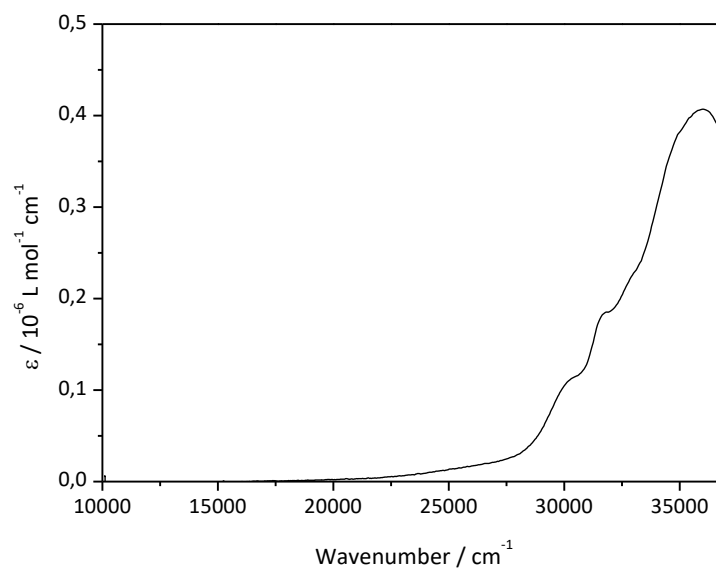
*Figure 186 UV-Vis spectrum of [Co^{II}(Brterpy)$_2$](ClO$_4$)$_2$ **C15** in DMF.*
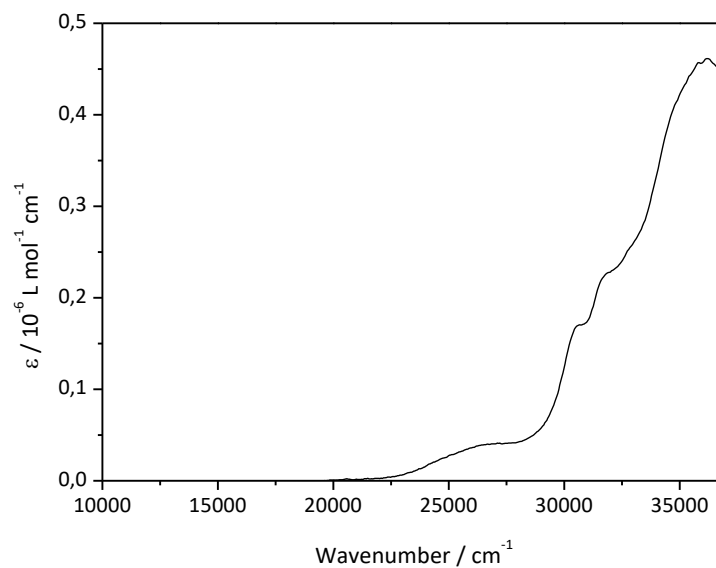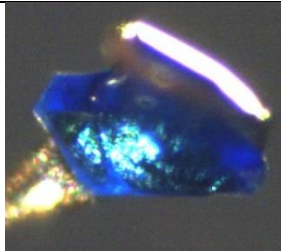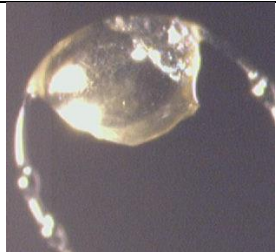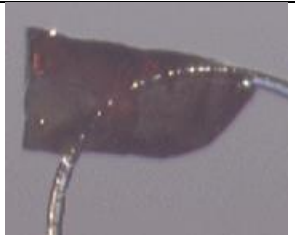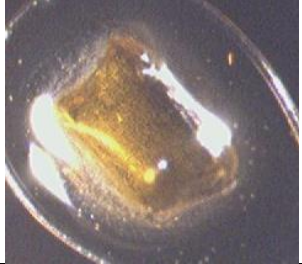
*Figure 187 UV-Vis spectrum of [Co^{II}(Brterpy)$_2$](PF$_6$)$_2$ **C16** in DMF.*

E. Crystallographic Data

	C1: $[Cu(\mu\text{-}L1)_2Cl_2]_n$ REN-EB-219	C1': $[Cu_2(L1')Cl_2(MeOH)_2]$ REN-EB-214-2
Empirical formula	$C_{18}H_{27}Cl_2CuN_9O$	$C18H30Cl2Cu2N8O4$
Formula weight / g mol^{-1}	519.92	620.48
Crystal size / mm	0.15 x 0.11 x 0.05	0.340 x 0.157 x 0.030
Crystal system	Orthorhombic	Orthorhombic
Space group	*Pnma*	*Pbca*
a / Å	8.8223(5)	9.9287(9)
b / Å	20.1430(1)	21.947(3)
c / Å	13.2699(6)	11.8304(10)
a / °	90	90
ß / °	90	90
γ / °	90	90
Volume / Å^3	2358.2(2)	2577.91
Z	4	4
Calc. Density / g cm^{-1}	1.464	1.604
Absorption coefficient μ / mm^{-1}	1.182	1.900
F (000)	1076	1280.0
Temperature / K	120	120
Diffractometer	STOE IPDS 2T	STOE IPDS 2T
Radiation	Mo-Kα	Mo-Kα
Data collection range 2 θ / °	2.77 to 28.38	2.53 to 28.127
Index ranges	$-9 \leq h \leq 11$ $-26 \leq k \leq 22$ $-14 \leq l \leq 17$	$0 \leq h \leq 13$ $0 \leq k \leq 28$ $0 \leq l \leq 15$
Collected reflections	7518	3079
Independent reflections	2882	1025
Data/restaints/parameters	2882/0/152	3079/3/161
Completeness	0.9991	0.976
Max. and min. transmission	0.8390 and 0.9346	0.463 and 0.923
R_{int}	0.0987	0.0711
R_{sigma}	0.0974	0.1027
Goodness-of-Fit on F^2	1.034	1.018
R_1 [$I \geq 4u(I)$]	0.0801	0.0728
wR_2 [$I \geq 4u(I)$]	0.1982	0.1665
R_1 [all data]	0.1199	0.1559
wR_2 [all data]	0.2296	0.2177
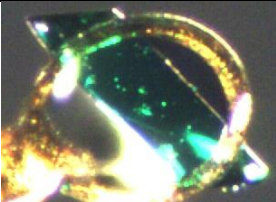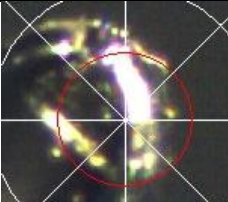
	C2: {[Cu(μ-L2)$_3$(H$_2$O)((CH$_3$)CO)](ClO$_4$)$_2$·H$_2$O}$_n$ REN-EB-451	C3: [Fe(μ-L2)(H$_2$O)$_4$]$_n$ REN-EB-268 blocks
Empirical formula	C$_{12}$H$_{19}$Cl$_2$CuN$_6$O$_{11}$S$_3$	C$_6$H$_{18}$Cl$_2$FeN$_4$O$_{14}$S$_2$
Formula weight / g mol^{-1}	653.95	561.11
Crystal size / mm	0.26 x 0.17 x 0.08	0.35 x 0.303 x 0.21
Crystal system	Triclinic	Monoclinic
Space group	$P\bar{1}$	$P2_1/c$
a / Å	7.7837(4)	7.9066(4)
b / Å	10.2279(6)	13.6816(6)
c / Å	16.0939(9)	9.6368(4)
a / °	84.947(5)	90
ß / °	80.408(5)	103.665(3)
γ / °	83.675(12)	90
Volume / Å³	1252.47(12)	1012.96(7)
Z	2	2
Calc. Density / g cm^{-1}	1.734	1.840
Absorption coefficient μ / mm^{-1}	1.398	1.288
F (000)	664	572
Temperature / K	173	120
Diffractometer	STOE IPDS 2T	STOE IPDS 2T
Radiation	Mo-Kα	Mo-Kα
Data collection range 2 θ / °	2.008 to 30.805	2.636 to 27.880
Index ranges	-10 ≤ h ≤ 10 -14 ≤ k ≤ 14 -23 ≤ l ≤ 22	-10 ≤ h ≤ 10 0 ≤ k ≤ 17 0 ≤ l ≤ 12
Collected reflections	23163	10731
Independent reflections	23163	2405
Data/restraints/parameters	7005/76/362	2405/0/170
Completeness	0.891	1.0
Max. and min. transmission	0.9128 and 0.4858	? and ?
R_{int}	0.0295	0.0172
R_{sigma}	0.0383	0.0173
Goodness-of-Fit on F^2	0.978	1.058
R_1 [$I \geq 2\sigma(I)$]	0.0337	0.0318
wR_2 [$I \geq 2\sigma(I)$]	0.0861	0.0809
R_1 [all data]	0.0417	0.0343
wR_2 [all data]	0.0888	0.0826

	C3′: [Fe(μ-L2)$_2$(H$_2$O)$_2$]$_n$·L2 REN-EB-268 plates	C4: [Fe(L2)(μ-L2)(SCN)$_2$]$_n$ REN-EB-256
Empirical formula	C$_{18}$H$_{22}$Cl$_2$FeN$_{12}$O$_{10}$S$_6$	C$_{14}$H$_{12}$FeN$_{10}$S$_6$
Formula weight / g mol^{-1}	885.58	568.55
Crystal size / mm	0.29 x 0.11 x 0.02	? x ? x ?
Crystal system	Triclinic	Orthorhombic
Space group	$P\bar{1}$	$Pna2_1$
a / Å	9.5904(14)	18.517(2)
b / Å	9.7093(13)	10.6630(8)
c / Å	9.8425(16)	13.7583(9)
a / °	73.194(11)	90
ß / °	80.579(13)	90
γ / °	78.911(11)	90
Volume / Å^3	855.3(2)	2716.5(4)
Z	1	4
Calc. Density / g cm^{-1}	1.719	1.390
Absorption coefficient μ / mm^{-1}	1.031	?
F (000)	450	1152
Temperature / K	193	120
Diffractometer	STOE IPDS 2T	STOE IPDS 2T
Radiation	Mo-Kα	Mo-Kα
Data collection range 2 θ / °	2.662 to 27.941	2.417 to 25.999
Index ranges	-12 $\leq$ h $\leq$ 10 -12 $\leq$ k $\leq$ 12 -12 $\leq$ l $\leq$ 12	-20 $\leq$ h $\leq$ 20 -13 $\leq$ k $\leq$ 12 -16 $\leq$ l $\leq$ 15
Collected reflections	7798	9639
Independent reflections	4069	4956
Data/restraints/parameters	4069/2/253	4956/73/285
Completeness	0.999	0.9287
Max. and min. transmission	? and ?	? and ?
R_{int}	0.0833	0.1812
R_{sigma}	0.1361	0.1732
Goodness-of-Fit on F^2	0.973	1.426
R_1 [$I \geq 2\sigma(I)$]	0.0667	0.1664
wR_2 [$I \geq 2\sigma(I)$]	0.1599	0.3945
R_1 [all data]	0.1528	0.2169
wR_2 [all data]	0.1940	0.4338

	C5: [Fe(**L2**)$_3$](BF$_4$)$_2$·3CHCl$_3$ **REN-EB-367**	C6: [Co(μ-**L2**)(H$_2$O)$_4$]$_n$ **REN-EB-262**
Empirical formula	C1'$_1$H$_{21}$B$_2$C$_{19}$F$_8$FeN$_{12}$S$_6$	C$_6$H$_{14}$Cl$_2$CoN$_4$O$_{12}$S$_2$
Formula weight / g mol^{-1}	1182.38	528.16
Crystal size / mm	0.33 x 0.263 x 0.18	0.38 x 0.25 x 0.10
Crystal system	Triclinic	Monoclinic
Space group	$P\bar{1}$	$P2_n$
a / Å	11.8272(5)	9.6323(7)
b / Å	12.2512(5)	7.5904(4)
c / Å	17.3953(8)	12.6857(11)
a / °	94.787(3)	90
ß / °	107.338(3)	99.869(7)
γ / °	110.656(3)	90
Volume / Å³	2200.59(17)	913.76(12)
Z	2	2
Calc. Density / g cm^{-1}	1.784	1.930
Absorption coefficient μ / mm^{-1}	1.245	1.527
F (000)	1176	534
Temperature / K	120	193
Diffractometer	STOE STADIVARI	STOE IPDS 2T
Radiation	Mo-Kα	Mo-Kα
Data collection range 2 θ / °	1.817 to 30.587	2.46 to 28.51
Index ranges	-16 ≤ h ≤ 16 -17 ≤ k ≤ 17 -23 ≤ l ≤ 24	-12 ≤ h ≤ 12 -9 ≤ k ≤ 9 -16 ≤ l ≤ 13
Collected reflections	56629	4924
Independent reflections	46315	2165
Data/restraints/parameters	46315/0/539	2165/0/126
Completeness	0.881	0.9964
Max. and min. transmission	0.6026 and 0.9275	0.6243 and 0.8617
R_{int}	0.1253	0.0233
R_{sigma}	0.0176	0.0228
Goodness-of-Fit on F^2	1.032	1.058
R_1 [$I \geq 2\sigma(I)$]	0.0293	0.0466
wR_2 [$I \geq 2\sigma(I)$]	0.0750	0.1242
R_1 [all data]	0.0364	0.0507
wR_2 [all data]	0.0819	0.1279

	C11: [Co(**L3**)$_2$](SCN)$_2$·H$_2$O **REN-EB-294-1**	**C15:** [Co(Brterpy)$_2$](ClO$_4$)$_2$ **REN-EB-341**
Empirical formula	C$_2$H$_{22}$CoN$_{14}$OS$_2$	C$_{20}$H$_{20}$Br$_2$Cl$_2$CoN$_6$O$_8$
Formula weight / g mol^{-1}	741.68	882.17
Crystal size / mm	0.09 x 0.06 x 0.05	0.19 x 0.177 x 0.165
Crystal system	Orthorhombic	Monoclinic
Space group	*Pbca*	*Cc*
a / Å	15.1240(4)	12.8102(4)
b / Å	23.7406(6)	12.2097(5)
c / Å	17.8647(6)	20.2668(6)
a / °	90	90
ß / °	90	98.417(2)
γ / °	90	90
Volume / Å³	6414.4(3)	3135.76(19)
Z	8	4
Calc. Density / g cm^{-1}	1.536	1.869
Absorption coefficient μ / mm^{-1}	5.857	3.329
F (000)	3032	1748
Temperature / K	100	173
Diffractometer	STOE STADIVARI	STOE STADIVARI
Radiation	Cu-Kα	Mo-Kα
Data collection range 2 θ / °	4.951 to 69.849	2.31 to 30.48
Index ranges	$-7 \leq h \leq 17$ $-27 \leq k \leq 28$ $-19 \leq l \leq 21$	$-18 \leq h \leq 18$ $-17 \leq k \leq 17$ $-29 \leq l \leq 28$
Collected reflections	28077	39351
Independent reflections	5957	8973
Data/restraints/parameters	5957/36/490	8973/78/480
Completeness	0.981	0.930
Max. and min. transmission	? and ?	0.8964 and 0.5896
R_{int}	0.0385	0.0361
R_{sigma}	0.0268	0.0361
Goodness-of-Fit on F^2	1.056	1.041
R_1 [$I \geq 2\sigma(I)$]	0.0568	0.0422
wR_2 [$I \geq 2\sigma(I)$]	0.1474	0.0949
R_1 [all data]	0.0755	0.0622
wR_2 [all data]	0.1621	0.1043

	C16: [Co(Brterpy)$_2$](PF$_6$)$_2$ **REN-EB-340**	**C18:** [Co(dipic)(**L4**)]·3H$_2$O **REN-EB-395**
Empirical formula	C$_{20}$H$_{20}$Br$_2$CoF$_{12}$N$_6$P$_2$	C$_{24}$H$_{20}$CoN$_4$O$_7$
Formula weight / g mol^{-1}	973.21	535.37
Crystal size / mm	0.1 x 0.1 x 0.09	? x ? x ?
Crystal system	tetragonal	monoclinic
Space group	$P\bar{4}2_1/c$	$P2_1/c$
a / Å	8.9379(2)	15.4399(7)
b / Å	8.9379(2)	14.2620(5)
c / Å	20.3111(6)	11.6525(5)
a / °	90	90
ß / °	90	100.940(4)
γ / °	90	90
Volume / Å^3	1622.57(7)	2519.29(18)
Z	2	4
Calc. Density / g cm^{-1}	1.992	1.42
Absorption coefficient μ / mm^{-1}	8.934	0.731
F (000)	954	1100
Temperature / K	100	120
Diffractometer	STOE STADIVARI	STOE STADIVARI
Radiation	Cu-Kα	Mo-Kα
Data collection range 2 θ / °	14.012 to 139.734	1.961 to 25.999
Index ranges	-9 $\leq$ h $\leq$ 10 -10 $\leq$ k $\leq$ 5 -24 $\leq$ l $\leq$ 23	-19 $\leq$ h $\leq$ 19 -17 $\leq$ k $\leq$ 16 -14 $\leq$ l $\leq$ 14
Collected reflections	14825	35817
Independent reflections	3034	4941
Data/restraints/parameters	3034/0/244	4941/24/355
Completeness	0.9963	1.000
Max. and min. transmission	? and ?	0.4901 and 0.9919
R_{int}	0.0105	0.0897
R_{sigma}	0.0059	0.0579
Goodness-of-Fit on F^2	1.142	1.123
R_1 [$I \geq 2\sigma(I)$]	0.0274	0.0867
wR_2 [$I \geq 2\sigma(I)$]	0.0811	0.2555
R_1 [all data]	0.0292	0.1317
wR_2 [all data]	0.0830	0.2869

	C21: [Co^{III}(L5)$_2$]$_2$[Co^{II}(SCN)$_4$]$_3$·6MeCN REN-EB-443-2	C22: [Dy(L5)(η^2-NO$_3$)$_2$ (η^1-NO$_3$)(H$_2$O)] REN-EB-378
Empirical formula	C$_{144}$H$_{142}$Co$_5$N$_{30}$O$_{24}$S$_{12}$	C$_{22}$H$_{36}$DyN$_7$O$_{16}$
Formula weight / g mol^{-1}	3356.24	937.18
Crystal size / mm	0.21 x 0.117 x 0.04	0.1 x 0.083 x 0.07
Crystal system	Triclinic	Monoclinic
Space group	$P\bar{1}$	$P2_1/c$
a / Å	13.2549(5)	17.8583(5)
b / Å	15.0880(6)	10.7696(2)
c / Å	23.3170(10)	19.4837(5)
a / °	83.299(3)	90
ß / °	78.201(3)	100.155(2)
γ / °	64.640(3)	90
Volume / Å³	4122.5(3)	3688.53(16)
Z	1	4
Calc. Density / g cm^{-1}	1.352	1.688
Absorption coefficient μ / mm^{-1}	?	2.109
F (000)	1735	1884
Temperature / K	173	173
Diffractometer	STOE STADIVARI	STOE STADIVARI
Radiation	Mo-Kα	Mo-Kα
Data collection range 2 θ / °	1.726 to 26.000	2.124 to 30.852
Index ranges	-15 $\leq$ h $\leq$ 16 -18 $\leq$ k $\leq$ 18 -28 $\leq$ l $\leq$ 28	-25 $\leq$ h $\leq$ 24 -15 $\leq$ k $\leq$ 15 -27 $\leq$ l $\leq$ 27
Collected reflections	59350	63582
Independent reflections	16210	10679
Data/restraints/parameters	16210/28/1049	10679/24/554
Completeness	0.999	0.920
Max. and min. transmission	? and ?	0.3507 and 0.9534
R_{int}	0.0469	0.0349
R_{sigma}	0.0412	0.0309
Goodness-of-Fit on F^2	1.127	1.052
R_1 [$I \geq 2\sigma(I)$]	0.1173	0.0381
wR_2 [$I \geq 2\sigma(I)$]	0.3238	0.0785
R_1 [all data]	0.1347	0.0548
wR_2 [all data]	0.3313	0.0838

F. Additional Data

Abbreviations

Physical and other abbreviations

α	orbital reduction parameter
χ	susceptibility
χ'	in-phase susceptibility
χ''	out-of-phase susceptibility
χ_M	molar susceptibility
χ_S	adiabatic susceptibility
χ_T	isothermal susceptibility
Δ	crystal field parameter
Δ_O	energy difference between the t_{2g} and e_g set in an octahedral ligand field
Δ_{HS}	energy difference between the t_{2g} and e_g set in an octahedral ligand field of the high-spin state
Δ_{LS}	energy difference between the t_{2g} and e_g set in an octahedral ligand field of the low-spin state
Δ_C	critical ligand field in an octahedral coordination sphere
ΔE^0_{HL}	zero-point energy difference between the high-spin and low-spin potential wells
ΔE^*_{HL}	activation energy
ΔE_Q	quadrupole splitting
γ_{HS}	high-spin fraction
γ_{LS}	low-spin fraction
δ	isomer shift (Mössbauer); chemical shift (NMR)
Σ_0	deviation of 90° of the twelve *cis*-angles in an octahedral coordination sphere

φ	*cis*-angle
κ	orbital reduction factor
λ	wavelength (UV-Vis); spin-orbit coupling parameter
ν	ordinary frequency
μ	dipole moment
μ_B	Bohr magneton
μ_{eff}	effective magnetic moment
τ	relaxation time
τ_0	pre-exponential factor of the Arrhenius equation
ω	angular frequency
ξ	electron spin-orbit coupling parameter
ac	alternating current
B	Racah parameter of the electron-electron repulsion
C_p	heat capacity
COSY	correlation spectroscopy
CSAPR-9	spherical capped square antiprism
CShM	continuous shape measurements
CuAAC	copper(I)-catalyzed azide-alkyne cycloaddition
D	axial zero-field splitting parameter
dc	direct current
DFT	Density Functional Theory
E	rhombic or transverse zero-field splitting parameter
EPR	Electron Paramagnetic Resonance
eq	equivalents
ESI-MS	Electrospray Ionization Mass Spectrometry
FIR	far infrared
G	Gibbs free energy
H	enthalpy; magnetic field
$\hat{H}_{ZFS}$	zero-field energy operator

HMBC	Heteronuclear Multiple Bond Correlation
HS	high-spin
HSQC	Heteronuclear Single Quantum Coherence
g	Landé factor
I	nuclear spin
IMP	molar fraction of the paramagnetic impurity
IR	Infrared
J	total angular momentum; exchange coupling parameter
k_B	Boltzman constant
L	orbital angular momentum
LIESST	Light Induced Spin State Trapping
LS	low-spin
m	mass
M	molar mass; magnetization
MLCT	metal to ligand charge transfer
n	molar amount
N_A	Avogadro constant
NFS	Nuclear Forward Scattering
NMR	Nuclear Magnetic Resonance
NNoC	*N*-oxide alkyne/alkene cycloaddition
O_h	octahedral coordination sphere
P	spin pairing energy
QTM	quantum tunneling of magnetization
R	ideal gas constant; residual
r	total symmetric stretch vibration
rt	room temperature
S	spin; entropy
SCO	spin crossover
SIM	single-ion magnet
SMM	single-molecule magnet

SQUID	Superconductive Quantum Interference Device
T	temperature
$T_{1/2}$	transition temperature
T_b	blocking temperature
T_d	tetrahedral coordination sphere
TEC	thiol-ene cycloaddition
TIESST	Temperature Induced Spin State Trapping
TIP	Temperature Independent Paramagnetism
TYC	thiol-yne cycloaddition
U	energy barrier of magnetization reversal
U_{eff}	effective energy barrier of magnetization reversal
UV	ultraviolet
Vis	visible
XAS	X-ray absorption spectroscopy
ZFS	zero-field splitting

Chemical abbreviations

1,10-phen	1,10-phenanthroline
2,2'-bipy	2,2'-bipyridine
3-bpp	2,6-pyrazolylpyridine
3,4-lut	3,4-lutidine
abpt	4-amino-3,5-bis(2-pyridyl)-1,2,4-traizole
bptz	3,6-bis(2-pyridyl)tetrazine
bpym	2,2'-bipyrimidine
bpypzH	3,5-bis(2-pyridyl)pyrazole
bpytz	3,6-bis(3,5-dimethylpyrazolyl)-1,2,4,5-tetrazine
bt	2,2'-bi-2-thiazoline
btr	4,4'-bis-1,2,4-triazole
C_p^{ttt}	$1,2,4\text{-}^tBu_3C_5H_2$
DIPA	Diisopropylamine

dmphen	2,9-dimethyl-1,10-phenanthroline
H$_2$dipic	pyridine-2,6-dicarboxylic acid
H$_2$oda	oxydiacetic acid
H$_2$sao	2-hydroxybenz-aldehyde oxime
H$_3$tpa^{Mes}	tris((5-mesityl-1H-pyrrol-2-yl)methyl)amine
H$_4$DOTA	1,4,7,10-tetraazacyclododecene-1,4,7,10-tetra-acetic acid
Htrz	1,2,4-triazole
Ln	lanthanide
Mn$_{12}$	[Mn$_{12}$O$_{12}$(O$_2$CCH$_3$)$_{16}$(H$_2$O)$_4$]·4H$_2$O·2CH$_3$CO$_2$H
NaAsc	sodium ascorbate
Pc	phthalocyanine
PMAPH	3,5-bis{[N-(2-pyridylmethyl)amino]methyl}-1H-pyrazole
PMAT	4-amino-3,5-bis((2-pyridylmethyl)aminomethyl)-1,2,4-triazole
PMOD	2,5-bis((2-pyridylmethyl)aminomethly)1,3,4-oxadiazole
PMTD	2,5-bis((2-pyridylmethyl)aminomethly)1,3,4-thiadiazole
PNP	N[2-P(CHMe$_2$)$_2$-4-methlyphenyl]$_2^-$
py	pyridine
pypzH	3-(2-pyridyl)pyrazole
saltmen	N,N'-(1,1,2,2-tetramethlyethylene)-bis-(salicylideneiminate)
tcmH	tricyanomethane
tp*	hydrotris(dimethlypyrazolyl)borate
tpa	tris(2-pyridylmethyl)amine
TMS	trimethylsilyl
TPyA	tris(2-pyridylmethyl)amine
trz-tetH	5-(4H-1,2,4-triazol-yl)-2H-tetrazole

Crystal Structures

*Figure 188 Molecular structure of **C1**. Color code: grey – C, violet – N, red – O, white – H, orange – Cu(II), green – Cl. ORTEP representation with atomic displacement parameters at 50% level of probability.*
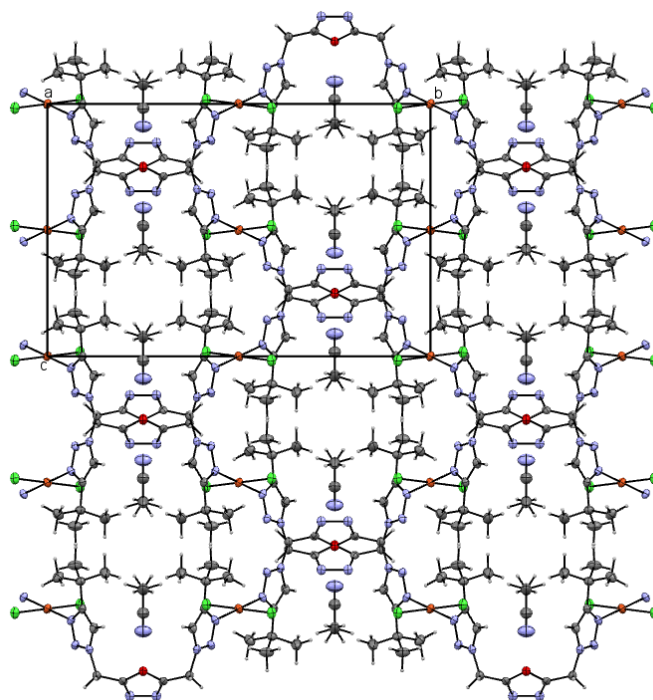
*Figure 189 Packing of **C1** along the b- and c-axis. Color code: grey – C, violet – N, red – O, white – H, orange – Cu(II), green – Cl. ORTEP representation with atomic displacement parameters at 50% level of probability.*
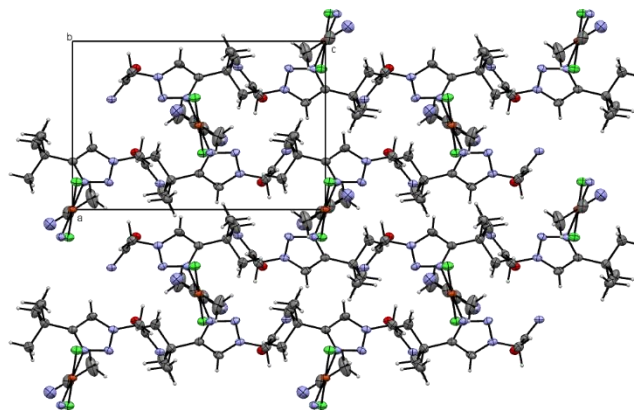
*Figure 190 Packing of **C1** along the a- and c-axis. Color code: grey – C, violet – N, red – O, white – H, orange – Cu(II), green – Cl. ORTEP representation with atomic displacement parameters at 50% level of probability.*

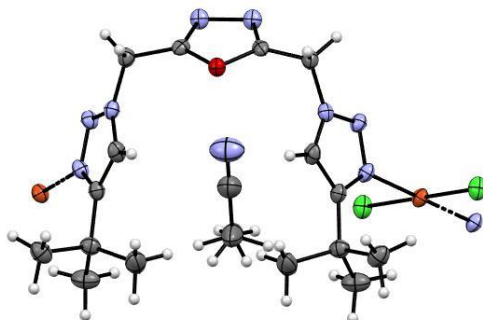*Figure 191 Packing of **C1** along the a- and b-axis. Color code: grey – C, violet – N, red – O, white – H, orange – Cu(II), green – Cl. ORTEP representation with atomic displacement parameters at 50% level of probability.*

*Figure 192 Single chains of **C1**. Left: view along the b-axis, right: view along the c-axis. The colors green, orange and grey represent single chains. Hydrogen atoms and solvent molecules are omitted for clarity. ORTEP representation with atomic displacement parameters at 50% level of probability.*
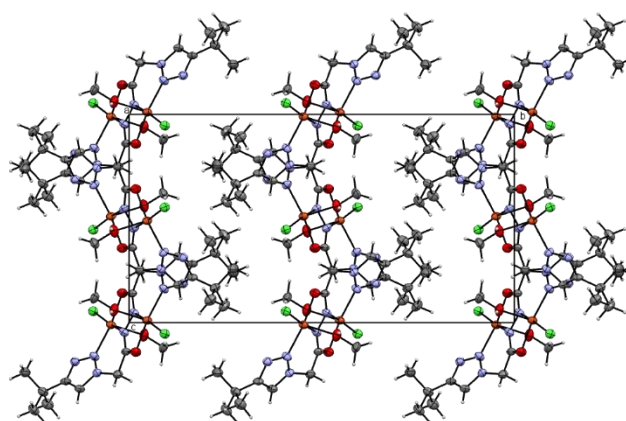
*Figure 193 Packing of **C1'** along the b- and c-axis. Color code: grey – C, violet – N, red – O, orange – Cu(II), green – Cl.. ORTEP representation with atomic displacement parameters at 50% level of probability.*
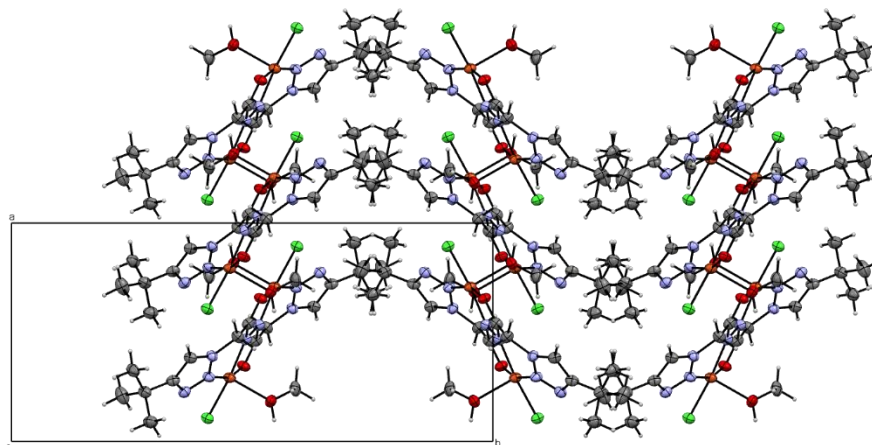
*Figure 194 Packing of **C1'** along the a- and b-axis. Color code: grey – C, violet – N, red – O, orange – Cu(II), green – Cl.. ORTEP representation with atomic displacement parameters at 50% level of probability.*

*Figure 195 Short O-H··Cl contacts between the dinuclear complexes in **C1'** along the a-axis. Color code: grey – C, violet – N, red – O, orange – Cu(II), green – Cl. Hydrogen atoms are omitted for clarity. Dashed lines represent the hydrogen bonds between the complex molecules. ORTEP representation with atomic displacement parameters at 50% level of probability.*

*Figure 196 Packing of **C2** along the a- and c-axis. Color code: grey – C, violet – N, yellow – S, red – O, orange – Cu(II), green – Cl. ORTEP representation with atomic displacement parameters at 50% level of probability.*
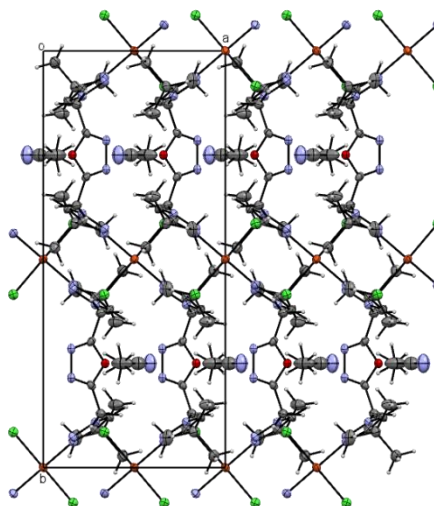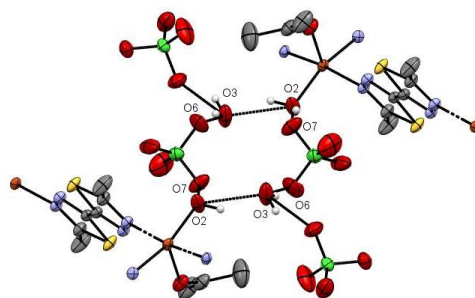

*Figure 197 Hydrogen bond network within the cavity of **C2**. Color code: grey – C, violet – N, yellow – S, red – O, orange – Cu(II), green – Cl. ORTEP representation with atomic displacement parameters at 50% level of probability.*
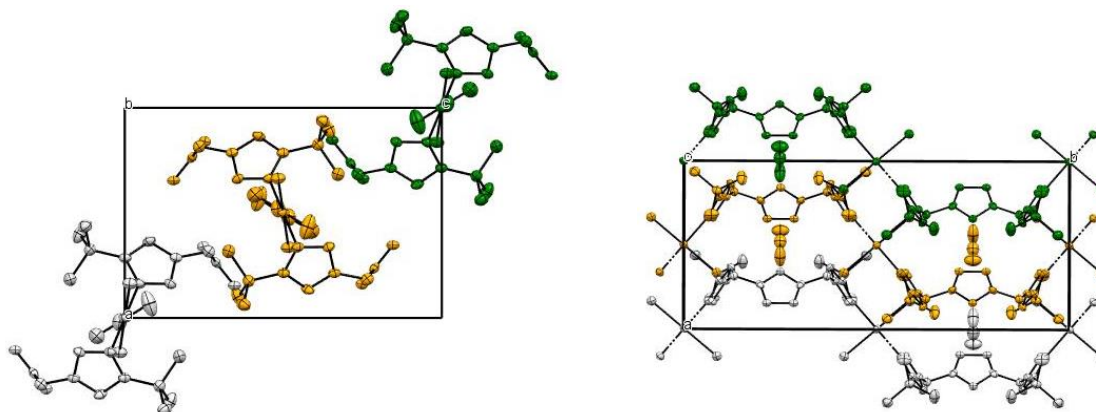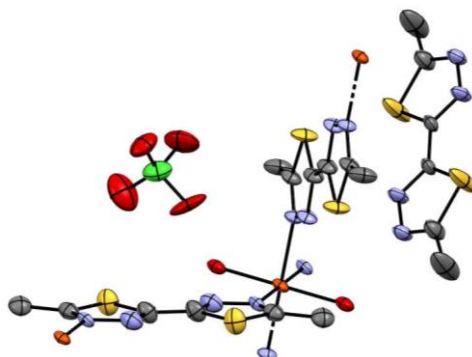
*Figure 198 Asymmetric unit of **C3'**. Color code: grey – C, violet – N, yellow – S, red – O, orange – Fe(II), green – Cl. Hydrogen atoms are omitted for clarity. ORTEP representation with atomic displacement parameters at 50% level of probability.*
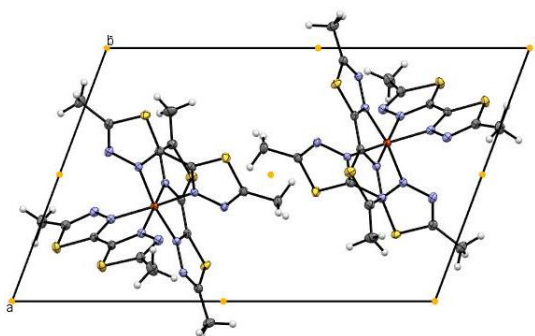

*Figure 199 Unit cell of **C5**. Color code: grey – C, violet – N, yellow – S, red – O, orange – Fe(II), white – H. Solvent molecules and anions are omitted for clarity. The yellow points represent the inversion centers. ORTEP representation with atomic displacement parameters at 50% level of probability.*
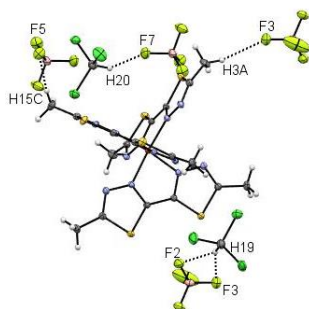
*Figure 200 Molecular structure of **C5** highlighting the hydrogen bonds. Color code: grey – C, violet – N, yellow – S, red – O, orange – Fe(II), green – Cl, light green – F, beige – B, white – H. ORTEP representation with atomic displacement parameters at 50% level of probability.*
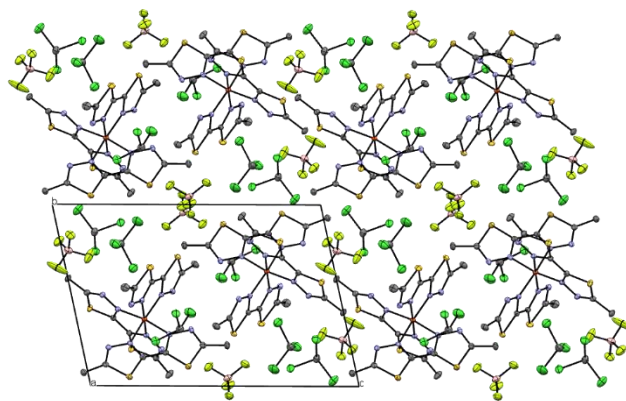
*Figure 201 Packing along the b- and c-axis of **C5**. Color code: grey – C, violet – N, yellow – S, red – O, orange – Fe(II), green – Cl, light green – F, beige – B. Hydrogen atoms are omitted for clarity. ORTEP representation with atomic displacement parameters at 50% level of probability.*
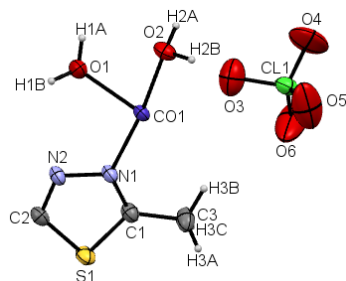
*Figure 202 Asymmetric unit of **C6**. Color code: grey – C, white – H, violet – N, yellow – S, red – O, dark blue – Co(II), green – Cl. ORTEP representation with atomic displacement parameters at 50% level of probability.*
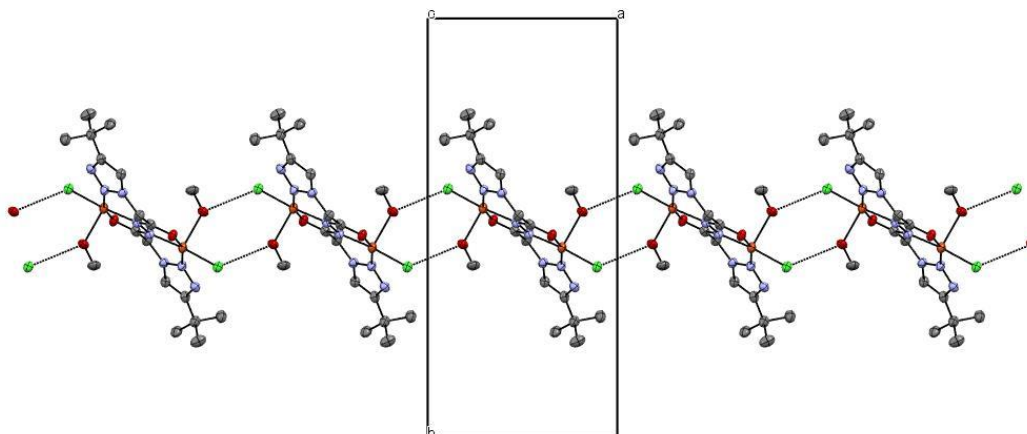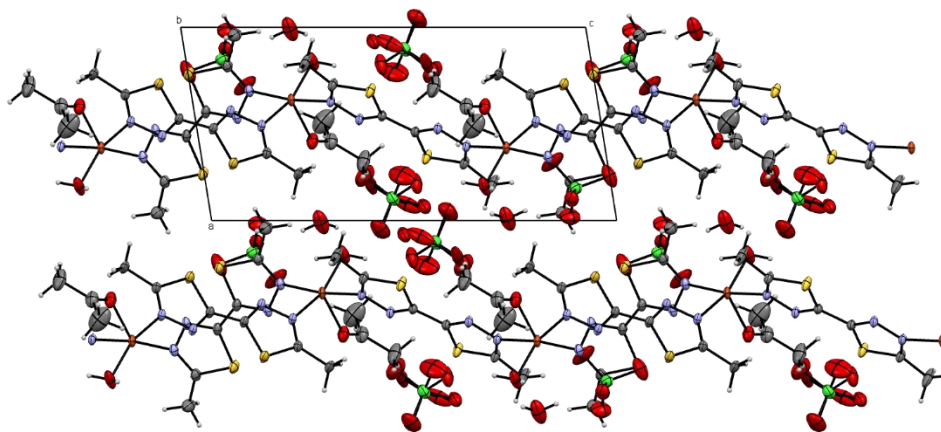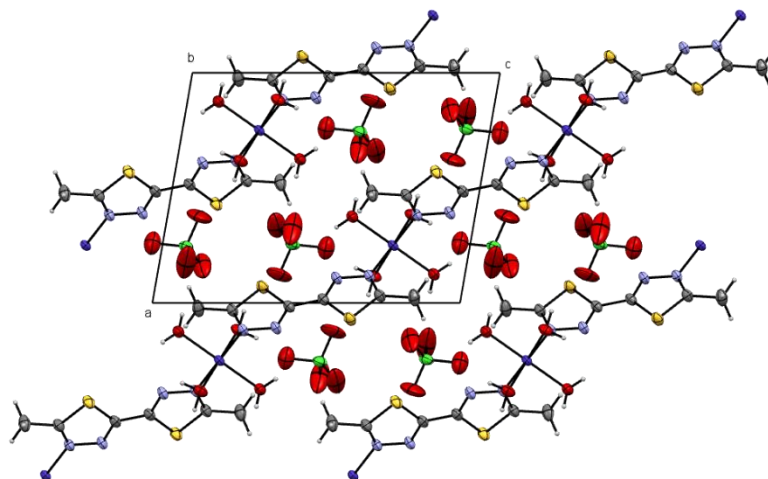

*Figure 203 Packing of **C6** along the a- and c-axis. Color code: grey – C, white – H, violet – N, yellow – S, red – O, dark blue – Co(II), green – Cl. ORTEP representation with atomic displacement parameters at 50% level of probability.*
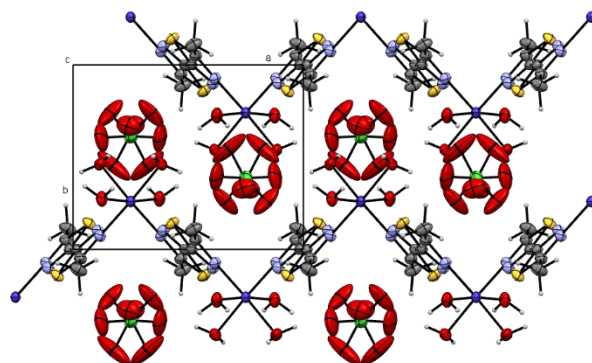
*Figure 204 Packing of **C6** along the a- and b-axis. Color code: grey – C, white – H, violet – N, yellow – S, red – O, dark blue – Co(II), green – Cl. ORTEP representation with atomic displacement parameters at 50% level of probability.*
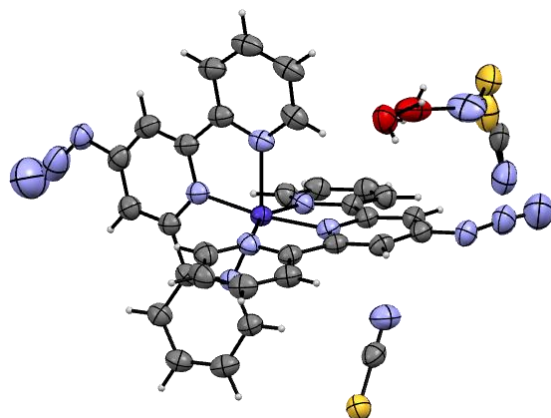

*Figure 205 Molecular structure of **C11** with disordered non-coordinating water molecules and thiocyanate anions. Color code: grey – C, violet – N, yellow – S, red – O, dark blue – Co(II), white – H. ORTEP representation with atomic displacement parameters at 50% level of probability.*
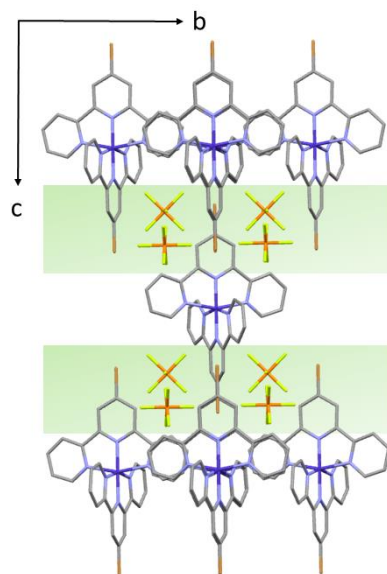
*Figure 206 Packing of the complex cations of **C16** along the a- and c-axis. The colors highlight the layers along the c-axis. ORTEP representation with atomic displacement parameters at 50% level of probability.*
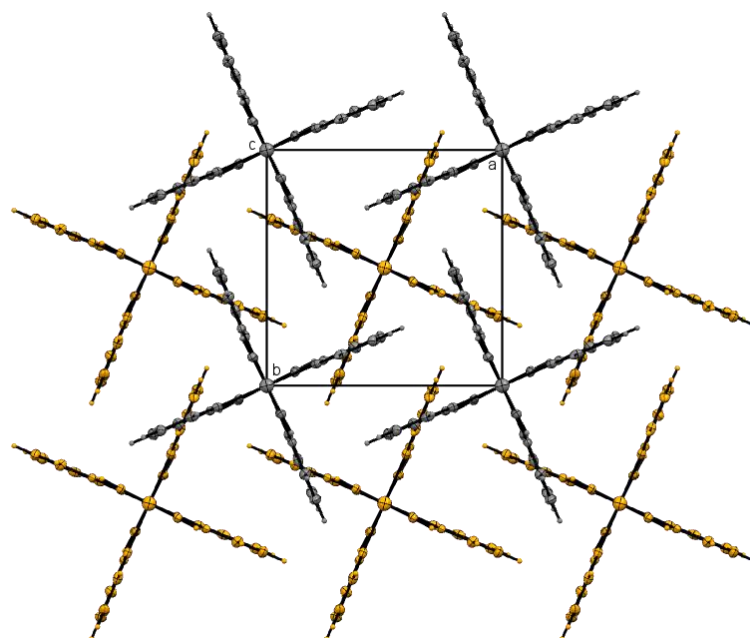
*Figure 207 Packing of the complex cations of **C16** along the a- and b-axis. The colors highlight the layers along the c-axis. ORTEP representation with atomic displacement parameters at 50% level of probability.*
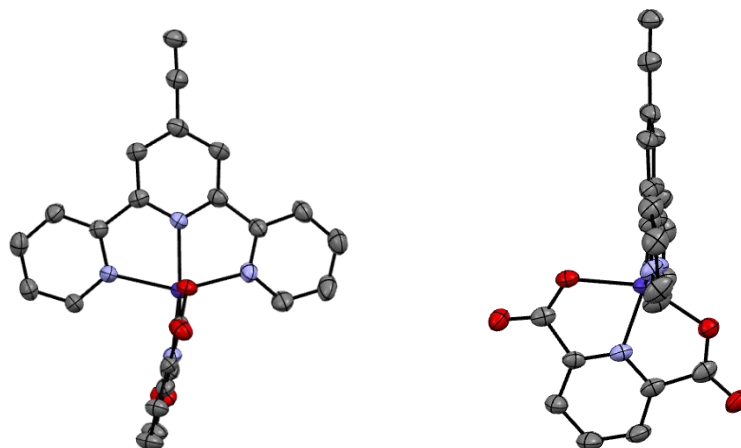
*Figure 208 Molecular structure of complex **C18** highlighting the distortion of the coordination ligands towards each other (164.18°). Color code: grey – C, violet – N, red – O, dark blue – Co(II). Hydrogen atoms are omitted for clarity. ORTEP representation with atomic displacement parameters at 50% level of probability.*
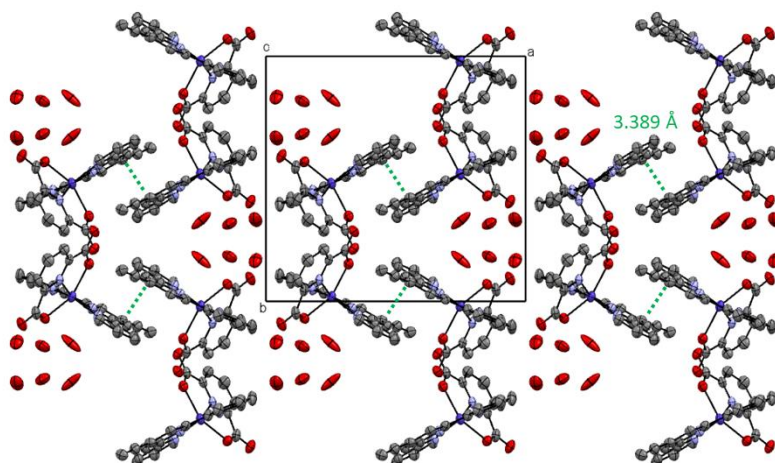
*Figure 209 Packing of the complex **C18** within the ab-plane highlighting the π-π-stacking of the terpyridine ligands. Color code: grey – C, violet – N, red – O, dark blue – Co(II). Hydrogen atoms are omitted for clarity. ORTEP representation with atomic displacement parameters at 50% level of probability.*
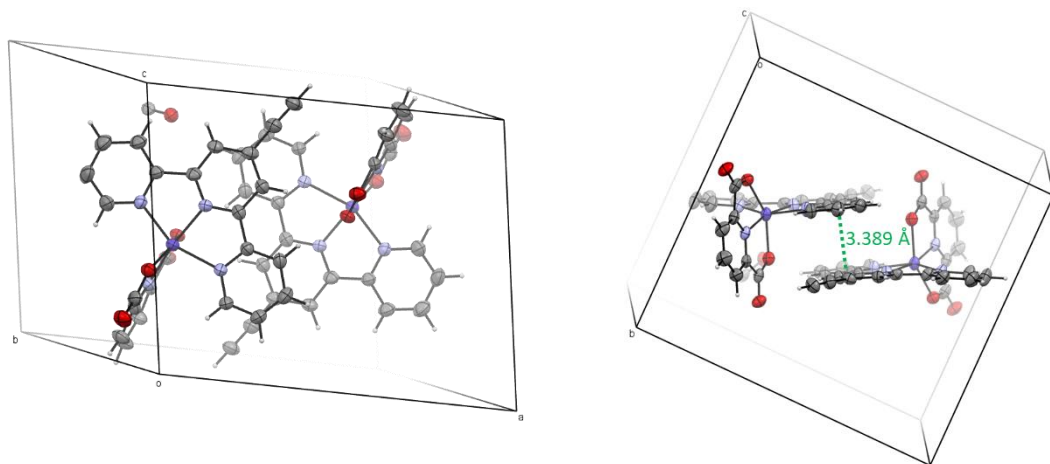
*Figure 210 π-π-stacking of two terpyridine units of **C18**. Color code: grey – C, violet – N, red – O, dark blue – Co(II). Hydrogen atoms are omitted for clarity. ORTEP representation with atomic displacement parameters at 50% level of probability.*
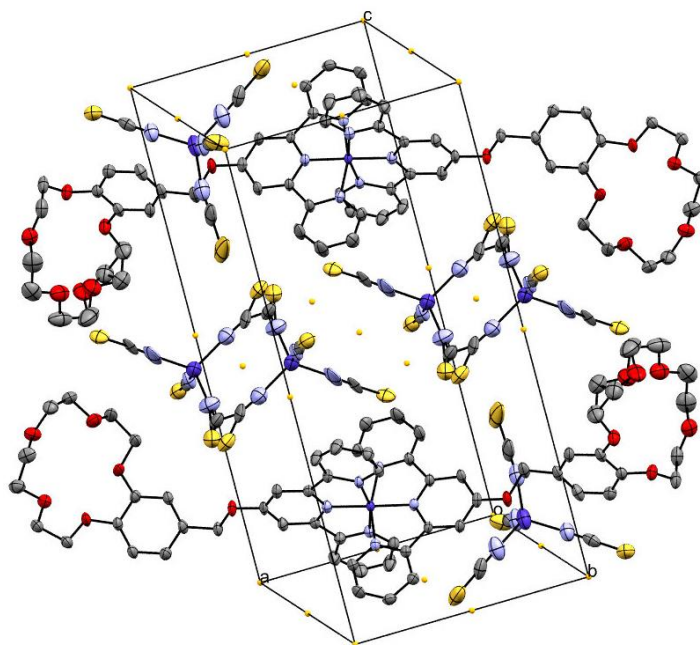
*Figure 211 Molecular structure of **C21**. Color code: grey – C, violet – N, red – O, yellow – S, dark blue – Co. Hydrogen atoms are omitted for clarity. ORTEP representation with atomic displacement parameters at 50% level of probability.*
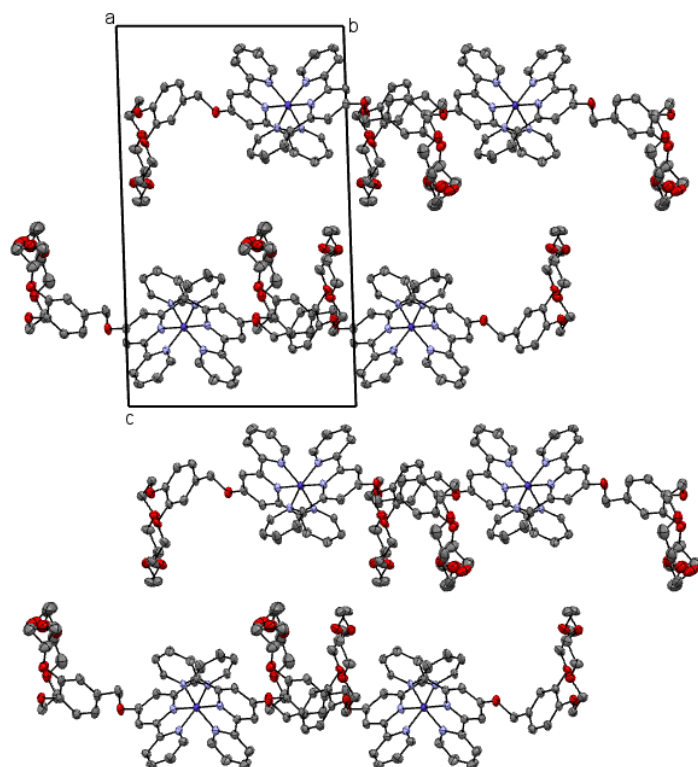
*Figure 212 Packing of the complex cations of **C21**. Color code: grey – C, violet – N, red – O, dark blue – Co(III). Hydrogen atoms are omitted for clarity. ORTEP representation with atomic displacement parameters at 50% level of probability.*
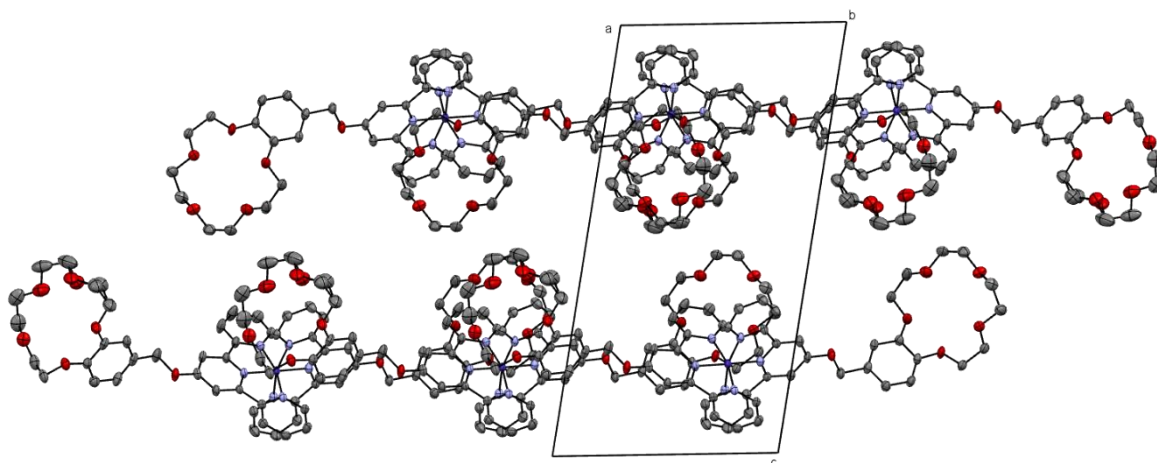
*Figure 213 Packing of the complex cations of **C21**. Color code: grey – C, violet – N, red – O, dark blue – Co(III). Hydrogen atoms are omitted for clarity. ORTEP representation with atomic displacement parameters at 50% level of probability.*

*Figure 214 The {Co2N$_4$} (left) and {Co3N$_4$} (right) cores of **C21** with a tetrahedral structure (T-4) and deviations of 0.197 and 0.243. Continuous shape measurements were performed with SHAPE 2.1. Color code: violet – N, dark blue – Co(II).*
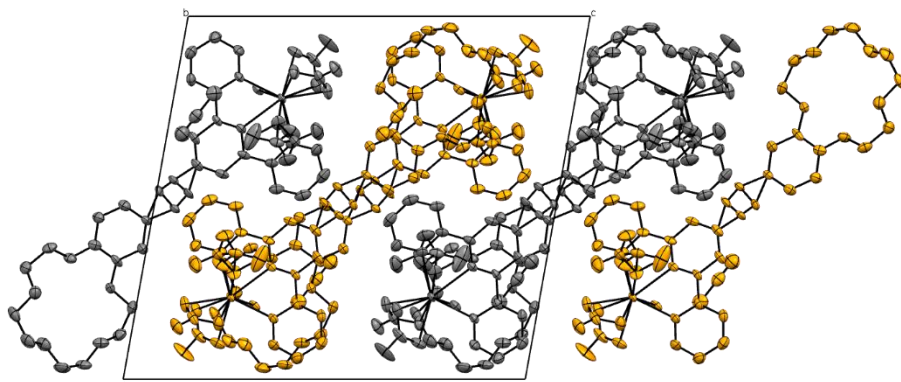
*Figure 215 Packing **C22** along the a- and c-axis.Hydrogen atoms are omitted for clarity. The molecules are colored in grey and orange to highlight the structure. ORTEP representation with atomic displacement parameters at 50% level of probability.*
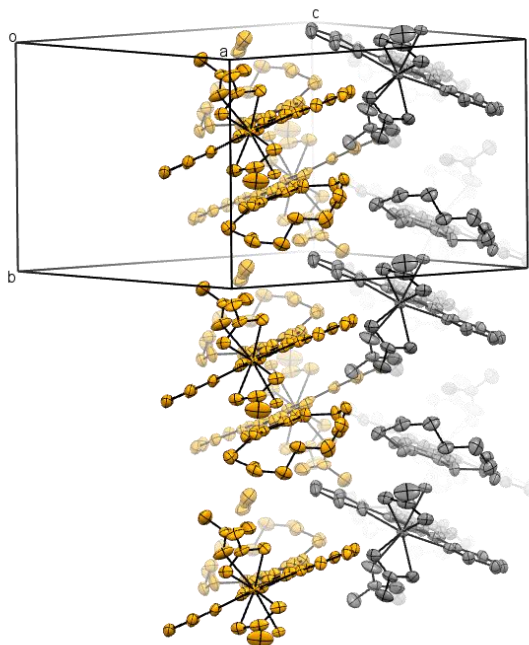
*Figure 216 Packing of **C22**. Hydrogen atoms are omitted for clarity. The molecules are colored in grey and orange to highlight the structure. ORTEP representation with atomic displacement parameters at 50% level of probability.*

Magnetic Data
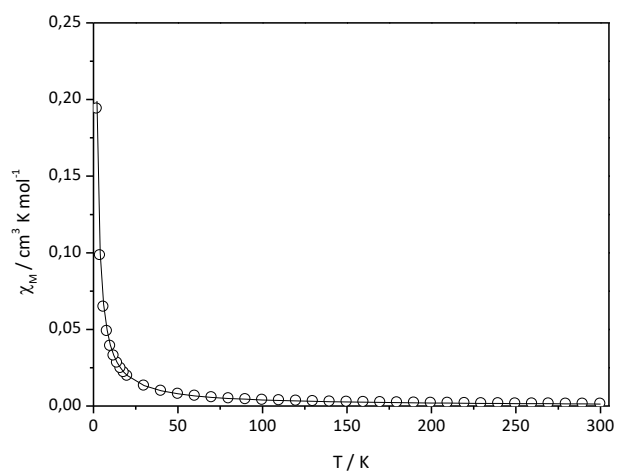
*Figure 217 Temperature-dependent magnetic behavior of **C1**, χ_M versus T plot.*
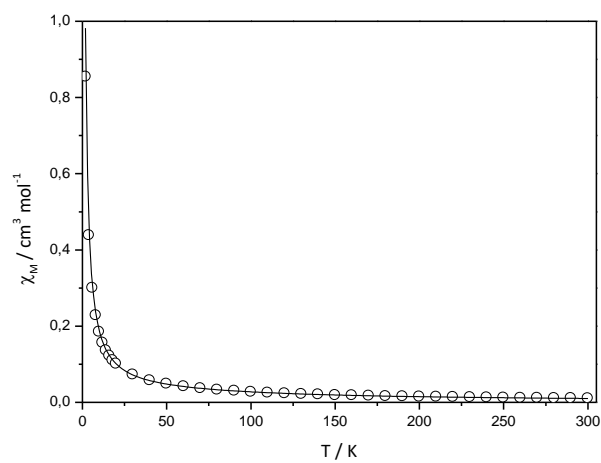
*Figure 218 Temperature-dependent magnetic behavior of **C6**. χ_m vs. T plot. ○ experimental data, − fit.*
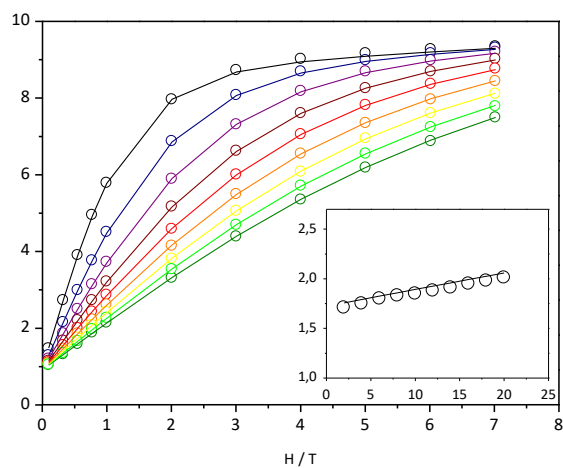
*Figure 219 Field-dependent magnetization, M vs. H plot, and temperature-dependent magnetic behavior of **C6**, $\chi_M T$ vs. T plot. ○ experimental data, − simultaneous fit of magnetization and susceptibility.*
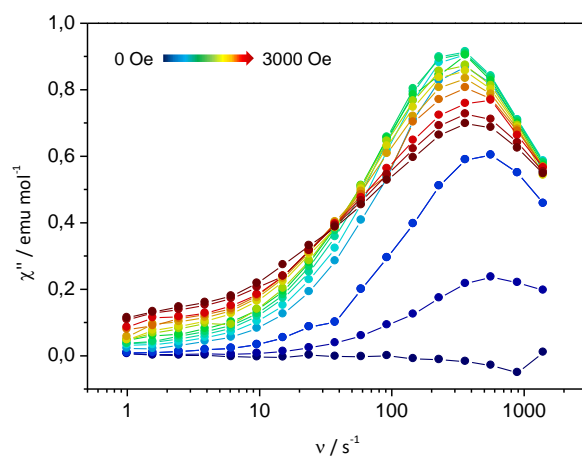
*Figure 220 Frequency-dependent out-of-phase signal χ'' of **C6** at 2 K in the range of 0 − 3000 Oe. -●- experimental data.*
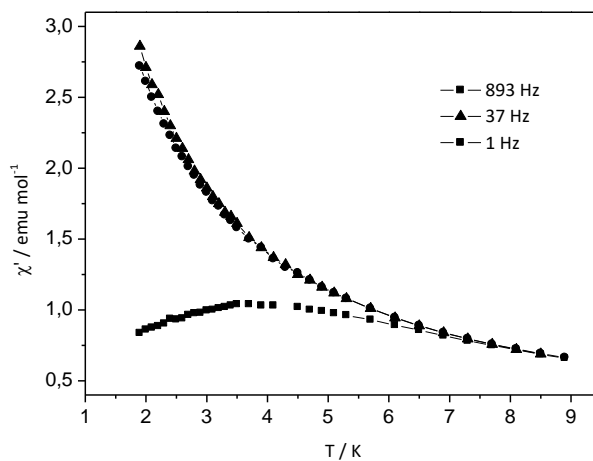
*Figure 221 Temperature-dependent in-phase susceptibility χ' of **C6** at H_{dc} = 1000 Oe in the temperature range of 1.9 − 8.9 K. -•- experimental data.*
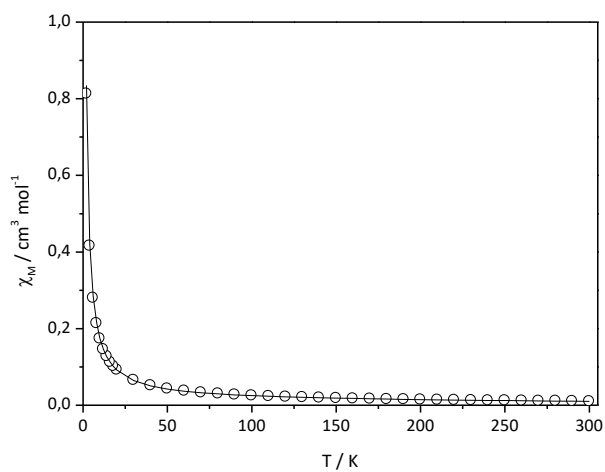
*Figure 222 Temperature-dependent susceptibility of **C11**. χ_M vs. T plot. ○ experimental data, − fit.*
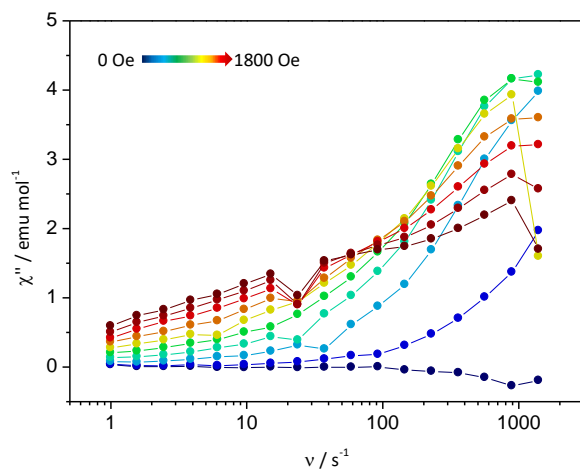
*Figure 223 Frequency-dependent out-of-phase signal χ'' of **C22** at 2 K in the range of 0 – 3000 Oe. -●- experimental data.*
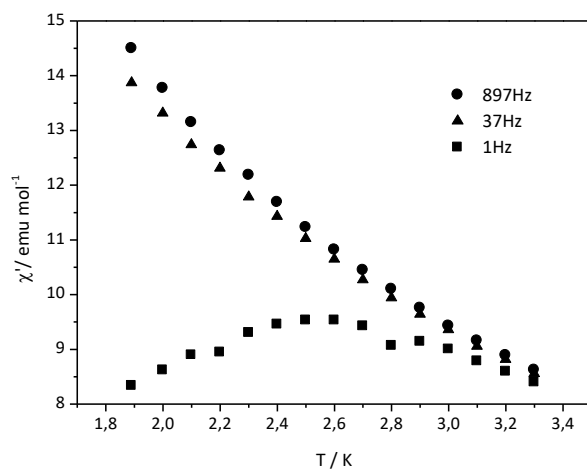
*Figure 224 Temperature-dependent in-phase susceptibility χ' of **C22** at H_{dc} = 600 Oe in the temperature range of 1.9 – 3.3 K. -●- experimental data.*

Tables

*Table 19 Selected bond lengths and angles of **C1'**.*

Distance [Å]		Angle [°]	
Cu1-Cl1	2.237	Cl1-Cu1-O12	93.12
Cu1-N1	2.033	O12-Cu1-N13	80.67
Cu1-N13	1.937	N13-Cu1-N1	88.17
Cu1-O12	1.985	N1-Cu1-Cl1	96.08
Cu1-O14	2.246	O14-Cu1-Cl1	94.43
Cu1-Cu1	4.623	O14-Cu1-O12	95.27
C11-O12	1.282	O14-Cu1-N13	92.79
C11-N13	1.318	O14-Cu1-N1	99.70
N13-N13	1.410	Cu1-N13-N13	113.8

*Table 20 O-H···O and O···O distances and angles of **C2**.*

	C2	
	O2-H2A···O3	1.9
O-H···O [Å]	O2-H2B···O7	1.9
	O3-H3B···O6	2.0
	O3-H3A···O8	2.1
	O2-O3	2.6
O···O [Å]	O2-O7	2.8
	O3-O6	2.8
	O3-O8	2.9
	O2-H2A···O3	145
O-H···O [°]	O2-H2B···O7	165
	O3-H3B···O6	164
	O3-H3A···O8	151

*Table 21 Selected Fe-L bond lengths and L-Fe-L angles of **C4**.*

Fe-L [Å]		L-Fe-L [°]	
Fe1-N1	2.20(2)	N1-Fe1-N3	73.9(7)
Fe1-N3	2.27(2)	N1-Fe1-N5	85.20
Fe1-N5	2.210(19)	N1-Fe1-N8	89.77
Fe1-N8	2.24(3)	N1-Fe1-N10	95.20
Fe1-N9	2.10(3)	N3-Fe1-N5	88.87
Fe1-N10	2.07(3)	N3-Fe1-N8	84.24
Fe1-Fe1	9.592	N3-Fe1-N9	89.10
		N5-Fe1-N8	172.4(8)
		N5-Fe1-N9	88.05
		N5-Fe1-N10	97.99
		N8-Fe1-N9	95.06
		N8-Fe1-N10	88.13
		N9-Fe1-N10	102.5(8)
		N9-C13-S5	176.22
		N10-C14-S6	178.45
		Fe1-N9-C13	158.97
		Fe1-N10-C14	145.61
Σ_0 [°]		63.49	

*Table 22 Selected Fe-L bond lengths and L-Fe-L angles of **C5**.*

	C5	
	Fe1-N1	1.937(18)
	Fe1-N3	1.9536(18)
Fe-L [Å]	Fe1-N5	1.9536(18)
	Fe1-N7	1.9433(18)
	Fe1-N9	1.9515(18)
	Fe1-N11	1.9499(18)
	N1-Fe1-N3	80.53(7)
	N1-Fe1-N5	94.72(7)
	N1-Fe1-N9	93.34(7)
	N1-Fe1-N11	92.64(7)
	N3-Fe1-N5	94.38(7)
	N3-Fe1-N7	95.60(7)
L-Fe-L [°]	N3-Fe1-N9	93.10(7)
	N5-Fe1-N7	80.49(7)
	N5-Fe1-N11	92.96(7)
	N7-Fe1-N9	91.90(7)
	N7-Fe1-N11	91.78(7)
	N9-Fe1-N11	80.42(7)
Σ_0 [°]	58.98	

*Table 23 C-H⋯F bond lengths and angles of **C5**.*

		C5	
	C3⋯F3	3.4
	C15⋯F8	3.3
C⋯F [Å]	C19⋯F2	3.3
	C19⋯F3	3.4
	C20⋯F7	3.0
	C3-H3A⋯F3	2.5
	C15-H15C⋯F8	2.5
C-H⋯F [Å]	C19-H19⋯F2	2.4
	C19-H19⋯F3	2.5
	C20-H20⋯F7	2.1
	C3-H3A⋯F3	144
	C15-H15C⋯F8	133
C-H⋯F [°]	C19-H19⋯F2	146
	C19-H19⋯F3	157
	C20-H20⋯F7	147

*Table 24 Selected hydrogen bond distances of **C6**.*

O-H⋯O Distance [Å]	
O1–H1A⋯O5	2.3
O1–H1B⋯O6	2.0
O2–H2A⋯O4	2.1
O2–H2B⋯O3	2.0

*Table 25 Selected IR stretches of the [Co(**L3**)$_2$]X$_2$ complexes.*

		-N=N=N [cm^{-1}]	CCN ring stretch [cm^{-1}][352]	Non-coordinating anion [cm^{-1}]
L3	4'-azido-2,2':6',2''-terpyridine	2109	1262	-
C7	[Co(**L3**)$_2$](ClO$_4$)$_2$	2123	1250	1092 (ClO$_4^-$)
C8	[Co(**L3**)$_2$](PF$_6$)$_2$	2125	1251	836 (PF$_6^-$)
C9	[Co(**L3**)$_2$]Br$_2$	2115	1249	-
C10	[Co(**L3**)$_2$]Cl$_2$	2115	1249	-
C11	[Co(**L3**)$_2$](SCN)$_2$	2118	1246	2079 (SCN$^-$)
C12	[Co(**L3**)$_2$]SO$_4$	2120	1249	1616 (SO$_4^{2-}$)
C13	[Co(**L3**)$_2$](BF$_4$)$_2$	2121	1251	1060 (BF$_4^-$)
C14	[Zn(**L3**)$_2$](ClO$_4$)$_2$	2129	1253	1087 (ClO$_4^-$)

*Table 26 All twelve cis-anlges of **C18**.*

L–Co1–L [°]	
O1–Co1–N1	75.9(29
O1–Co1–N2	118.4(2)
O1–Co1–N3	93.1(2)
O1–Co1–N4	90.4(2)
O3–Co1–N1	76.1(2)
O3–Co1–N2	90.5(2)
O3–Co1–N3	98.7(2)
O3–Co1–N4	92.4(2)
N1–Co1–N3	97.2(2)
N1–Co1–N4	112.4(2)
N2–Co1–N3	76.3(2)
N2–Co1–N4	76.0(2)

*Table 27 Selected L-Co-L angles of **C21**.*

L–Co1–L [°]		L–Co2–L [°]		L–Co3–L [°]	
N1–Co1–N2	82.4(3)	N7–Co1–N8	104.0(5)	N11–Co1–N12	105.2(9=
N1–Co1–N3	82.0(3)	N7–Co1–N9	111.7(4)	N11–Co1–N13	104.4(8)
N1–Co1–N5	97.1(3)	N7–Co1–N10	111.6(4)	N11–Co1–N14	113.8(8)
N1–Co1–N6	99.2(3)	N8–Co1–N9	111.1(4)	N12–Co1–N13	110.3(8)
N2–Co1–N4	97.2(3)	N8–Co1–N10	113.7(5)	N12–Co1–N14	107.9(7)
N2–Co1–N5	90.6(3)	N9–Co1–N10	105.0(4)	N13–Co1–N14	114.8(9)
N2–Co1–N6	91.9(2)				
N3–Co1–N4	98.4(3)				
N3–Co1–N5	92.8(3)				
N3–Co1–N6	89.1(3)				
N4–Co1–N5	81.8(3)				
N4–Co1–N6	81.9(3)				
N1–Co1–N4	178.8(3)				
N2–Co1–N3	164.3(2)				
N5–Co1–N6	163.6(2)				
$\Sigma_0 = 70.2$		CShM = 0.20		CShM = 0.24	

Table 28 Selected angles of **C22**.

L–Dy–L [°]			
N1–Dy1–N2	66.43(10)	O7–Dy–O8	71.95(9)
N1–Dy1–N3	65.70(9)	O7–Dy–O9	73.53(8)
N1–Dy1–O7	70.92(8)	O8–Dy–O9	52.46(10)
N1–Dy1–O14	76.56(15)	O8–Dy–O11	68.11(10)
N2–Dy1–O7	83.86(9)	O9–Dy–O11	75.51(10)
N2–Dy1–O8	78.93(10)	O9–Dy–O12	73.03(10)
N2–Dy1–O14	69.22(18)	O11–Dy–O12	52.24(10)
N3–Dy1–O7	78.79(9)	O11–Dy–O14	69.80(15)
N3–Dy1–O9	86.33(10)	O12–Dy–O14	74.26(16)
N3–Dy1–O12	72.97(9)		

Continuous Shape Measurements

*Table 29 Calculated values for the continuous shape measurements of **C3**.*

Label	Symmetry	Shape	CShM
HP-6	D_{6h}	Hexagon	32.026
PPY-6	C_{5v}	Pentagonal pyramid	29.520
OC-6	O_h	Octahedron	0.085
TPR-6	D_{3h}	Trigonal prism	16.258
JPPY-6	C_{5v}	Johnson pentagonal pyramid J2	32.834

*Table 30 Calculated values for the continuous shape measurements of **C3'**.*

Label	Symmetry	Shape	CShM
HP-6	D_{6h}	Hexagon	31.807
PPY-6	C_{5v}	Pentagonal pyramid	28.949
OC-6	O_h	Octahedron	0.230
TPR-6	D_{3h}	Trigonal prism	16.521
JPPY-6	C_{5v}	Johnson pentagonal pyramid J2	31.922

*Table 31 Calculated values for the continuous shape measurements of **C4**.*

Label	Symmetry	Shape	CShM
HP-6	D_{6h}	Hexagon	32.202
PPY-6	C_{5v}	Pentagonal pyramid	25.618
OC-6	O_h	Octahedron	0.745
TPR-6	D_{3h}	Trigonal prism	13.503
JPPY-6	C_{5v}	Johnson pentagonal pyramid J2	29.511

*Table 32 Calculated values for the continuous shape measurements of **C5**.*

Label	Symmetry	Shape	CShM
HP-6	D_{6h}	Hexagon	29.869
PPY-6	C_{5v}	Pentagonal pyramid	26.443
OC-6	O_h	Octahedron	0.772
TPR-6	D_{3h}	Trigonal prism	13.293
JPPY-6	C_{5v}	Johnson pentagonal pyramid J2	30.140

*Table 33 Calculated values for the continuous shape measurements of **C3**.*

Label	Symmetry	Shape	CShM
HP-6	D_{6h}	Hexagon	32.026
PPY-6	C_{5v}	Pentagonal pyramid	29.520
OC-6	O_h	Octahedron	0.085
TPR-6	D_{3h}	Trigonal prism	16.258
JPPY-6	C_{5v}	Johnson pentagonal pyramid J2	32.834

*Table 34 Calculated values for the continuous shape measurements of **C6**.*

Label	Symmetry	Shape	CShM
HP-6	D_{6h}	Hexagon	32.602
PPY-6	C_{5v}	Pentagonal pyramid	28.538
OC-6	O_h	Octahedron	0.233
TPR-6	D_{3h}	Trigonal prism	15.213
JPPY-6	C_{5v}	Johnson pentagonal pyramid J2	31.998

*Table 35 Calculated values for the continuous shape measurements of **C11**.*

Label	Symmetry	Shape	CShM
HP-6	D_{6h}	Hexagon	32.915
PPY-6	C_{5v}	Pentagonal pyramid	19.579
OC-6	O_h	Octahedron	3.576
TPR-6	D_{3h}	Trigonal prism	9.457
JPPY-6	C_{5v}	Johnson pentagonal pyramid J2	23.492

*Table 36 Calculated values for the continuous shape measurements of **C15**.*

Label	Symmetry	Shape	CShM
HP-6	D_{6h}	Hexagon	34.129
PPY-6	C_{5v}	Pentagonal pyramid	23.216
OC-6	O_h	Octahedron	2.353
TPR-6	D_{3h}	Trigonal prism	11.884
JPPY-6	C_{5v}	Johnson pentagonal pyramid J2	26.915

*Table 37 Calculated values for the continuous shape measurements of **C16**.*

Label	Symmetry	Shape	CShM
HP-6	D_{6h}	Hexagon	34.765
PPY-6	C_{5v}	Pentagonal pyramid	24.618
OC-6	O_h	Octahedron	2.225
TPR-6	D_{3h}	Trigonal prism	12.704
JPPY-6	C_{5v}	Johnson pentagonal pyramid J2	28.801

*Table 38 Calculated values for the continuous shape measurements of **C18**.*

Label	Symmetry	Shape	CShM
HP-6	D_{6h}	Hexagon	33.171
PPY-6	C_{5v}	Pentagonal pyramid	17.521
OC-6	O_h	Octahedron	5.340
TPR-6	D_{3h}	Trigonal prism	6.728
JPPY-6	C_{5v}	Johnson pentagonal pyramid J2	21.655

*Table 39 Calculated values for the continuous shape measurements of **C21** (Co2).*

Label	Symmetry	Shape	CShM
vTBPY-4	C_{3v}	Vacant trigonal bipyramid	3.594
T-4	T_d	Tetrahedron	0.197

*Table 40 Calculated values for the continuous shape measurements of **C21** (Co3).*

Label	Symmetry	Shape	CShM
vTBPY-4	C_{3v}	Vacant trigonal bipyramid	3.006
T-4	T_d	Tetrahedron	0.243

Table 41 Calculated values for the continuous shape measurements of **C22**.

Label	Symmetry	Shape	CShM
EP-9	D_{9h}	Enneagon	32.722
OPY-9	C_{8v}	Octagonal pyramid	21.572
HBPY-9	D_{7h}	Heptagonal bipyramid	18.855
JTC-9	C_{3v}	Johnson triangular cupola J3	15.832
JCCU-9	C_{4v}	Capped cube J8	9.247
CCU-9	C_{4v}	Spherical-relaxed capped cube	7.959
JCSAPR-9	C_{4v}	Capped square antiprism J10	2.829
CSAPR-9	C_{4v}	Spherical capped square antiprism	1.902
JTCTPR-9	D_{3h}	Tricapped trigonal prism J51	3.351
TCTPR-9	D_{3h}	Spherical tricapped trigonal prism	2.423
JTDIC-9	C_{3v}	Tridiminished icosahedron J63	12.211
HH-9	C_{2v}	Hula-hoop	9.641
MFF-9	Cs	Muffin	2.078

Curriculum Vitae

Date of Birth ■■■■■■■■■■

Place of Birth ■■■■■■

Studies

■■■■■■■■■■■ ■■■ ■■■■■■■■■■■■■■■■■■■■■■■■■■■■■■■■■■■■■■ ■■■■■■■■■■■■■■■■■■■■■■■■■■■■■ ■■■■■■■■■■■■■■■■■■■■■■■■■■■■■■■■■■■■■■

■■■■■■■■■■■■ ■■■■■■■■■■■■■■■■■■■■■■■■■■■■■■■■■■ ■■■■■■■■ ■■■■■■■■■■■■■■■■■■■■■■■■■■■■■■■■■■■■ ■■■■■■■■■■■■■■■■■■■■■■■■■■■■■■

■■■■■■■■■■■ ■■■ ■■■■■■■■■■■■■■■■■■■■■■■■■■■■■■■■■■ ■■■■■■■■ ■■■■■■■■■■■■■■■■■■■■■■■■■■■■■■■■■■■■■■ ■■■■■■■■

■■■■■■■■■■■ ■■■ ■■■■■■■■■■■■■■■■■■■■■■■■■

International Experience

■■■■■■■■■■■■ ■■■■■■■■ ■■■■■■■■■■■■■■■■■■■■■■■■■■■■■■■■■■■ ■■■■■■■■■■■■■■■■■■■■■■■■■■■■ ■■■■■■■■■■■■■■■■■■■■■■■■■■■■■■■■■■

Awards

■■■   ■■■■■■■■■■■■■■■■■■■■■■■■■■
              ■■■■■■■■■■■■■■■■■■■■■■■■■■■■

■■■   ■■■■■■■■■■■■■■■■■■■■■■■■■■■
              ■■■■■■■■■■■■■■■■■■■■■■■■■■

Memberships

■■■■■■■■■■■■   ■■■■■■■■■■■■■■■■■■■■■■■■■■■■■■■
              ■■■■■■■■■■■■■■■■■■■■
              ■■■■■■■■■■■■■■■■■■■■■■■■■■

■■■■■■■   ■■■■■■■■■■■■■■■■■■■■■■■■■■■■■
■■■■■■■   ■■■■■■■■■■■■■■■■■■■■■■■■■■■■■
              ■■■

Training

■■■■■■   ■■■■■■■■■■■■■■■■■■■■■■■■■■

■■■■■■■■■   ■■■■■■■■■■■■■■■■■■■■■■■■■
              ■■■■■■

■■■■■■■■■   ■■■■■■■■■■■■■■■■■■■■■■■■■■■
              ■■■■■■■■

■■■■■■■   ■■■■■■■■■■■■■■■■■■■■■■■■■■■■■

■■■■■■■■■   ■■■■■■■■■■■■■■■■■■■■■■■■■■■■

Conferences & Summer Schools

■■■■■■■   ■■■■■■■■■■■■■■■■■■■■■■■■■■■■■■■
              ■■■■■■■■■■

■■■■■■■■   ■■
               ■■■■■■■■■
               ■■■■■■■■■■■■

■■■■■■■■   ■■
               ■■■■■■■■■■■■■■■■■
               ■■■■■■■■■■■■

■■■■■■■■■   ■■
               ■■
               ■■■■■■■■■■■■■■■■■■■■■■■■

■■■■■■■■   ■■
               ■■■■■■■■■■■■■■■■■■■■■■■■■■■■■■■■■■■